

University of Nottingham
UK | CHINA | MALAYSIA

Earth-abundant Electrocatalytic Materials for the Hydrogen Economy

Matthew Adrian Bird

14304343

Supervisor: Prof Darren A. Walsh

Second Supervisor: Dr Ming Li

School of Chemistry

University of Nottingham

A thesis submitted to the School of Chemistry for the degree of Doctor of Philosophy

Declaration

I, Matthew Adrian Bird, hereby declare that this doctoral thesis, which is approximately 54,000 words in length, is the result of my own investigations and is not being concurrently submitted in candidature for any other degree.

Signed: 

Matthew Adrian Bird

Date: 30/10/2023

University of Nottingham
UK | CHINA | MALAYSIA

Acknowledgements

I offer my sincerest thanks to Prof Darren Walsh for his supervision throughout my PhD and for continuously presenting me with grammatical debates, off-topic discussion, and excellent anecdotes alongside expert electrochemistry. I also thank Dr Graham Newton and Dr Lee Johnson for their continued academic support, especially for the work presented in Chapters 4 and 5. Darren, Graham, and Lee have been instrumental in ensuring that the Nottingham Applied Materials and Interfaces (NAMI) Group is world-class in science, as well as being an inspiring environment in which to work. I thank Dr Ming Li for his role as my secondary supervisor and for the help he provided for the work presented in Chapter 6.

Science is sometimes considered a lonesome discipline. This could not be further from the truth. And so, I offer my wholehearted thanks to everyone past and present in the NAMI Group. I cannot name all the members for the group has grown too large, but special mention will be given to ex-members Dan and Sean who have been sources of inspiration and mentorship throughout my PhD studies. Needless to say, without the amazing friends I have made in the group, my PhD would not have been as enjoyable an experience as it has been, nor would my dependence on caffeine be so high. A PhD extends beyond the lab, and so I thank David, Hannah (Jerry, Nibbler, Gary), Sandy, Conrad, Rory, Chris, and Michael who at various times have lived with me throughout the many trials and tribulations of my PhD. An extra thank you to Rory who selflessly looked after me during the writing of this thesis, ensuring that I ate good food and had good company throughout. To Jo and Donny who I can count on to always be there for support and friendship, thank you for continuing to believe in me even in those times when I did not.

I would like to thank the many people with whom I have done science. Thank you to Will for making carbon nanotubes fun, to Andrzej for zooming in real close to tiny things, to Matt W for showing me the wonders of titanate microspheres, to Matt Cliffe and Andy Jones for refining my understanding of

refinements, and of course to Sean for giving me a life-long dislike of platinum and bubbles.

My time at UoN began in September 2013, and since then I have met many wonderful people and done things I never thought I would. Many thanks to the past and present committees and members of the Creative Writing Society, Impact Magazine, Improv Society, the UoN Skydiving Club, and UoN Sub Aqua. Without these societies my thesis would either have been finished far earlier or, more likely, not at all. Knowing that there is always something fun around the corner is so important when taking on something as massive and consuming as a PhD.

To Mum, Dad, Adam, and Emma, thank you for your continued love and support throughout my quest to be a never-ending student. Finally, a big “who’s a good boy?” to Toby and “who’s a good girl?” to Bella for being the most adorable dogs anyone could wish for.

I love deadlines. I like the whooshing sound they make as they go by.

Douglas Adams

You're mad, bonkers, completely off your head. But I'll tell you a secret. All the best people are.

Lewis Carroll

In loving memory of Grandad,

to whom I dedicate this thesis.

Abstract

The production of hydrogen through sustainable methods is key in the development of a hydrogen economy to help decarbonise society. One such route is through the electrolysis of water. This will require novel electrocatalysts to overcome the sluggish kinetics of the oxygen evolution reaction and to avoid the expensive and rare materials, such as platinum and iridium oxides, currently used to electrocatalyse this reaction.

In the testing of electrocatalysts, Pt and Au are often as counter electrode materials. This thesis shows their use is unsuitable due to the dissolution of the metals when used in the conditions typical of electrocatalytic testing. The dissolved metals diffuse from the counter electrode to the working electrode where they can then deposit. This artificially enhances the measured electrocatalytic activity. The use of a Nafion membrane to prevent the crossover of these contaminants is found to be ineffective. A carbon-based counter electrode separated from the working electrode using a membrane or frit is shown to be the best set-up.

This thesis sets out to explore three strategies that can be used in the design of novel electrocatalysts. Synergistic interactions between Co_3O_4 and single-walled nanotubes (SWNT) are explored through encapsulating the oxide inside the tubes. This interaction leads to an enhancement in the mass activity of the electrocatalyst system towards the oxygen evolution reaction (OER) by altering the surface chemistry of the SWNT. Second, morphological control is examined by modifying titanate microspheres with a sodium titanate layer. This is shown to maintain the underlying structure whilst increasing the specificity of the electrocatalyst towards the 2x2e oxygen reduction reaction (ORR). Heat-treatment then increases the surface area without impacting this specificity. The mechanism of the ORR can also be controlled through doping $BaTiO_3$ with La such that the structure changes from hexagonal to tetragonal. This third design strategy is further explored by increasing the amount of Pr doped into $(Ba_{0.5}Sr_{0.5})_{1-x}Pr_xCo_{0.8}Fe_{0.2}O_{3-\delta}$. This decreases how cubic the structure is, as evidenced through XRD, and is correlated to decreasing OER activity.

Published works and conferences

Bird, M. A., Goodwin, S. E., & Walsh, D. A. (2020). Best Practice for Evaluating Electrocatalysts for the Hydrogen Economy. *ACS Applied Materials & Interfaces*, *12*(68), 20500–20506. https://doi.org/10.1021/acsami.0c03307

Wadge, M. D., Bird, M. A., *et al* (2022). Nanostructured, Alkaline Titanate-Converted, and Heat-Treated Ti6Al4V Microspheres via Wet-Chemical Alkaline Modification and their ORR Electrocatalytic Response. *Adv. Mater. Interfaces, 10(5), 2201523.* https://doi.org/10.1002/admi.202201523

Conference - PRiME 2020: Bird, M., Goodwin, S. E., & Walsh, D. A. (2020). Best Practice for Evaluating Electrocatalysts for the Hydrogen Economy. *ECS Meeting Abstracts*, *MA2020-02*(68), 3677. https://doi.org/10.1149/MA2020-02683677MTGABS

Abbreviations

AC	Activated carbon
AC-TEM	Aberration corrected transmission electron microscopy
AEM	Adsorbate evolution mechanism
AEM	Anion-exchange membrane (as in fuel cells)
AM	Arc-melted
BSCF	$(Ba_{0.5}Sr_{0.5})(Co_{0.8}Fe_{0.2})O_{3-\delta}$
BSD	Back-scatter detector
CCS	Carbon capture and storage
CCS	Carbon capture and storage
CCU	Carbon capture and utilisation
CCUS	Carbon capture, utilisation, and storage
CE	Counter electrode
CNT	Carbon nanotube
CoCp	Cobaltocene
COP	Conference of the Parties
CPS	Counts per second
CV	Cyclic voltammogram
ECSA	Electrochemical surface area
EDTA	Ethylenediaminetetraacetic acid
EDX	Energy dispersive X-ray spectroscopy
Fc	Ferrocene
FC	Fuel cell
FEG-SEM	Field-Emission Gun Scanning Electron Microscope
GC	Glassy carbon
HCP	Hexagonal close-packed
HER	Hydrogen evolution reaction
HOMO	Highest occupied molecular orbital
HOR	Hydrogen oxidation reaction
HOR	Hydrogen oxidation reaction
HR XPS	High resolution X-ray photoelectron spectroscopy
ICDD	International Centre for Diffraction Data
ICP-MS	Inductively coupled plasma mass spectrometry
IEA	International Energy Agency
IHP	Inner Helmholtz plane
IPA	Isopropyl alcohol

IPCC	Intergovernmental Panel on Climate Change
IRENA	International Renewable Energy Agency
K-L	Koutecký-Levich
LOM	Lattice oxygen mediated mechanism
LSV	Linear sweep voltammogram
MOx	Metal oxide
MWNT	Multi-walled nanotube
OER	Oxygen evolution reaction
OHP	Outer Helmholtz plane
ORR	Oxygen reduction reaction
PEM	Proton-exchange membrane
POM	Polyoxometalate
POx	Partial oxidation
ppb	Parts per billion
ppm	Parts per million
PTFE	Polytetrafluoroethylene
PXRD	Powder X-ray diffraction
RDE	Rotating disc electrode
RDS	Rate determining step
RE	Reference electrode
RHE	Reversible hydrogen electrode
SCE	Saturated calomel electrode
SEM	Scanning electron microscopy
SHE	Standard hydrogen electrode
SOMO	Singly occupied molecular orbital
SWNT	Single-walled nanotube
TEM	Transmission electron microscopy
TGA	Thermogravimetric analysis
VC	Vulcan carbon
WE	Working electrode
WGS	Water-gas shift
XPS	X-ray photoelectron spectroscopy
XRD	X-ray diffraction

Symbols

A	Area
a	Intercept of Tafel slope
a_i	Activity of species i
b	Tafel slope
Co	Concentration of oxygen
Do	Diffusion coefficient of oxygen
E	Potential
E	Standard potential
F	Faraday constant, 96485 C
i	Current
i_k	Kinetic current
i_L	Levich current
j	Current density
k	Rate constant
n	Number of electrons transferred
R	Ideal gas constant, 8.314 J K^{-1} mol^{-1}
T	Temperature
z_i	Numerical charge
α	Charge transfer coefficient
δ	Hydrodynamic layer (electrochemistry)
δ	Oxygen non-stoichiometry (perovskites)
ΔH	Change in enthalpy
η	Overpotential
η_x	Overpotential at x mA cm^{-2}
μ	Chemical potential
$\bar{\mu}$	Electrochemical potential
ν	Kinematic viscosity
Φ	Electrostatic potential
ω	Rotation rate / rad s^{-1}

Table of Contents

Declaration i
Acknowledgements ii
Abstract vi
Published works and conferences vii
Abbreviations viii
Symbols x
Table of Contents xi
Chapter 1. Introduction 1
1.1 Carbon Emissions 1
1.2 The Hydrogen Economy 3
1.3 Making Hydrogen 4
1.3.1 Grey Hydrogen 5
1.3.2 Blue Hydrogen 6
1.3.3 Green Hydrogen 8
1.4 Storing and Transporting Hydrogen 12
1.5 Using Hydrogen 14
1.5.1 Fuel Cells 14
1.5.2 Other Uses 15
1.6 Electrocatalyst design 16
1.7 Thesis aims and objectives 20
1.8 References 21
Chapter 2. Theory and Techniques 32
2.1 Fundamentals of Electrochemistry 32
2.2 Electrode Kinetics 38
2.3 Mass Transport Considerations 39
2.4 Theory of Electrocatalysis 43
2.4.1 Hydrogen Evolution Reaction 44
2.4.2 Oxygen Evolution and Reduction Reactions 49
2.5 References 56
Chapter 3. Best Practices for the Use of Counter Electrodes in 3-Electrode Measurements of Hydrogen Evolution Electrocatalysts in Acidic Aqueous Electrolytes 61
3.1 Introduction 61

3.1.1 Operation of a Counter Electrode 61
3.1.2 Concerns Associated with the Counter Electrode 62
3.1.3 Review of Mitigation Strategies 68
3.1.4 Context of the Work Presented in This Chapter 69
3.2 Experimental Section 71
3.2.1 Materials and Apparatus 71
3.2.2 Experimental Methods 72
3.3 Results and Discussion 73
3.3.1 Evidence for Contamination of the WE by CE species 73
3.3.2 Use of Divided Cells to Mitigate Contamination 76
3.3.3 Use of Carbon Counter Electrodes to Mitigate Metallic Contamination 82
3.3.4 Application of Findings 84
3.4 Conclusions 88
3.5 References 90
Chapter 4. The Effect of Encapsulation on the Electrocatalytic Performance of Cobalt Oxide 96
4.1 Introduction 96
4.2 Experimental Section 100
4.2.1 Materials 100
4.2.2 Material Preparation 100
4.2.3 Physical Characterisation 100
4.2.4 Electrochemical and Electrocatalytic Characterisation 101
4.3 Results and Discussion 102
4.3.1 Coating and Encapsulation of Co_3O_4 on and in SWNTs 102
4.3.2 Effect of Encapsulation on the Oxygen Evolution Reaction 106
4.3.3 Effect of Encapsulation on the Stability of the Electrocatalyst 116
4.3.4 OER with Co_3O_4@SWNT in 1 mol dm^{-3} KOH 119
4.4 Conclusions 121
4.5 Future Work 122
4.6 References 124
Chapter 5. The Influence of the Phase and Morphology of Titanate Materials on the Reduction of Oxygen 133
5.1 Introduction 133
5.2 Experimental Section 136
5.2.1 Materials and Apparatus 136

5.2.2 Powder synthesis 136
5.2.3 Physical Characterisation 137
5.2.4 Electrochemical Characterisation 139
5.3 Results and Discussion 140
5.3.1 Physical Characterisation 140
5.3.2 Ink Optimisation for Electrochemical Testing 147
5.3.3 General Electrochemical Characterisation 150
5.3.4 Oxygen Reduction Reaction (ORR) 152
5.4 Conclusions 159
5.5 Future Work 160
5.6 References 161
Chapter 6. Perovskites as Electrocatalysts for the Hydrogen Economy 168
6.1 Introduction 168
6.1.1 Perovskite Materials 168
6.1.2 Synthesis of Perovskites 172
6.1.3 Cation choice as a Design Strategy 172
6.2 Aims of the chapter 176
6.3 Experimental Section 176
6.3.1 Perovskite Synthesis 176
6.3.2 Ink Preparation 177
6.3.3 Electrochemical and Electrocatalytic Measurements 177
6.4 Results and Discussion 178
6.4.1 Praseodymium-doped BSCF 178
6.4.2 Lanthanum-doped $BaTiO_3$ 185
6.5 Conclusions 194
6.6 References 195
Chapter 7. Conclusions 200

Chapter 1. Introduction

"Water will one day be employed as fuel, that hydrogen and oxygen which constitute it, used singly or together, will furnish an inexhaustible source of heat and light, of an intensity of which coal is not capable."

Jules Verne, The Mysterious Island (1875)[1]

It is well established that global warming should be limited to well below 2 °C and preferably no more than 1.5 °C, relative to pre-industrial temperatures. This was unanimously agreed upon at the 21st Conference of Parties (COP21) in 2016 and took the form of the Paris Agreement.[2] However, the pledges made will only limit warming to ~2.7 °C, significantly higher than needed to avoid a global catastrophe.[3] The Glasgow Pact made at COP26 updated these targets, but the most ambitious of these still only have a 50% chance of limiting warming to ~1.8 °C.[4] The latest Intergovernmental Panel on Climate Change (IPCC) reports declare a 'Code Red' for humanity and call for greater action to be taken.[5]

The slow and thus far insufficient response to the climate crisis is due to several interconnected factors. Those of a political or socioeconomic nature are well beyond the scope of this thesis. Some of the technical and scientific challenges, however, will be summarised in this introduction. It should be emphasised that any solution to the crisis will involve a combination of technologies. Although there are benefits and drawbacks to using a given energy storage solution over another, that does not necessarily mean that solution is the only viable one. Certainly, individual technologies will have greater benefits in certain applications, and it is within that framework that technologies should be compared.

1.1 Carbon Emissions

The relationship between atmospheric CO_2 and ground temperature has been known since 1896 when Arrhenius published his paper on the topic.[6] Since

then, human society has pumped ever greater quantities of the gas into the atmosphere as the population grows and demand for energy increases.

The largest proportion of global CO_2 emissions (Figure 1.1) comes from power generation (40 %), with most of that power production coming from coal. Combined, transport and industry emit a similar amount.

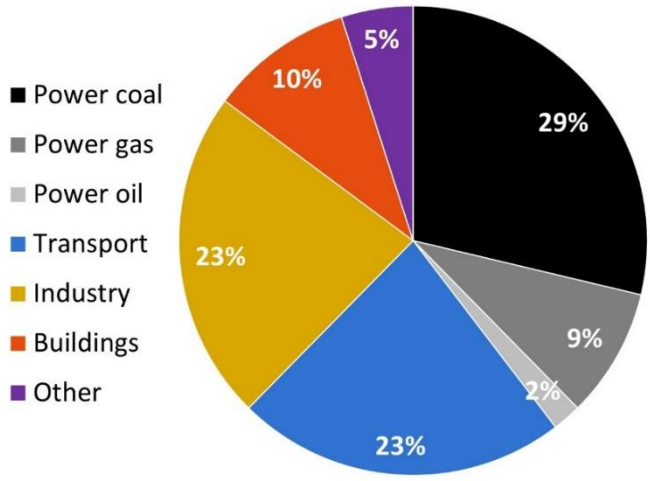


Figure 1.1 Global CO_2 emissions by sector, 2018. Data from the International Energy Agency (IEA).[7]

Power generation is an easily decarbonised area, and as such is one of the sectors which has had the highest amount of focus. Currently, the majority of our electricity comes from using the combustion of fossil fuels to heat water to turn a turbine. This can be replaced with wind turbines, photovoltaic panels, geothermal pumps, and nuclear power and eliminate CO_2 emissions from power generation. In 2020, 28.6 % of electricity was generated from renewable sources, and it is predicted that by 2030 this will need to increase to 61.7 % to achieve the International Energy Agency's Net Zero Scenario.[8] Although this will eliminate a large amount of CO_2 production, it is not enough on its own. Transport decarbonisation is increasingly popular, with companies like Tesla not only proving that electric cars can work, but that they can be desirable. With the UK government set to ban the sale of new petrol cars by 2030[9] and many other countries having proposed similar legislation, the transport sector will see deep cuts in its carbon emissions in the near future.

That leaves the more difficult sectors to decarbonise. Industrial processes often have CO_2 and other greenhouse gas emissions as side products in the reactions they carry out, and often cannot be electrified to remove them. Steel and concrete production are particularly difficult processes to decarbonise through electrification.[10]

Hydrogen has the potential to play a major role in the decarbonisation of processes difficult to decarbonise (see 1.5 Using Hydrogen). However, current hydrogen generation methods have high carbon intensities. Unless hydrogen production is itself decarbonised, using it as part of the solution will only shift carbon emissions rather than act to reduce them. The concept of generating green hydrogen and incorporating it into global systems is known as the hydrogen economy.

1.2 The Hydrogen Economy

Hydrogen is an extremely versatile chemical. It can be combusted to generate heat, combined with oxygen in a fuel cell to generate electricity, and used as a chemical feedstock. This versatility allows hydrogen to help clean-up industries which are otherwise difficult to decarbonise. The technologies used to cleanly generate, transport, store, and use hydrogen are encompassed in the concept of the Hydrogen Economy. This term was first coined in the 1970s by John Bockris, who envisioned hydrogen being generated by nuclear reactors in the sea and then piped to where it was needed.[11]

There are several benefits to using hydrogen as an energy carrier. First, over long distances, the cost of transporting hydrogen through pipes is lower than using cables to transmit electricity of equivalent energy,[12,13] especially for the transmission of energy from off-shore sources.[14] Second, hydrogen temporally and spatially decouples power-generation from power-usage.[13] Without storage, electricity generation by renewables is limited to when the demand for the electricity matches the supply available. Although batteries can be used to store excess electricity, they are not suitable for seasonal storage.[15] If coupled to hydrogen generation, the excess electricity can be stored chemically

rather than wasted. Thus, hydrogen can act as a store of renewable energy which can be used when the wind is not blowing nor the sun shining.

1.3 Making Hydrogen

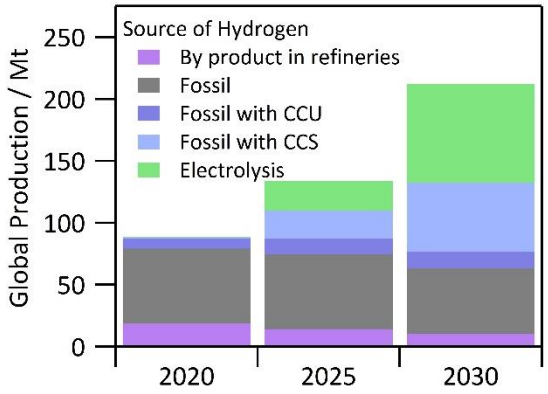


Figure 1.2 Global hydrogen demand by production technology (2025 and 2030 data from the 'net zero emissions by 2050' scenario). CCU: carbon capture and utilisation; CCS: carbon capture and storage. Data from the IEA.[16]

There are many ways of generating hydrogen, with various levels of carbon intensity. The majority of the hydrogen generated today (see Figure 1.2) is grey hydrogen, derived from fossil fuel sources, so called because it has a large and unmitigated carbon footprint. Some of this could be converted to blue hydrogen by incorporating carbon capture technologies into the process. The lowest carbon intensity belongs to that of green hydrogen, which uses renewable energy sources to electrolytically split water to create hydrogen. As the above figure shows, hydrogen production will necessarily shift away from grey sources to blue and green sources in order to reach net zero by 2050. The following sections detail the processes involved for these three main 'colours' of hydrogen. There are other colour descriptors used for sub-types of production which will be mentioned where relevant. However, given the seemingly endless 'colours' of hydrogen, and the lack of consensus over the definitions of those beyond the main three, referring to hydrogen production processes solely by colour perhaps obfuscates understanding rather than aiding it. Grey, blue, and green are the primary colours used to discuss hydrogen and

are part of the EU's CertifHy standard which characterises hydrogen by the associated amount of carbon emissions.[17]

1.3.1 Grey Hydrogen

Nearly 80% of current hydrogen production uses natural gas reforming or coal gasification.[18] Both of these are highly carbon-intensive processes using fossil fuel inputs and outputting significant quantities of CO_2. The first step in natural gas reforming combines methane with high temperature steam:

$$CH_4 + H_2O \rightarrow CO + 3H_2 \qquad \Delta H = 206 \text{ kJ mol}^{-1} \qquad [1.1]$$

Higher hydrocarbons can be also used in this reaction, leading to the more generalised form:

$$C_nH_m + nH_2O \rightarrow nCO + (n + ½m)H_2 \qquad [1.2]$$

The resulting gas mix is known as syngas and has industrial applications in and of itself. The CO can be further reformed through the water-gas shift (WGS) reaction:

$$CO + H_2O \rightarrow CO_2 + H_2 \qquad \Delta H = -41 \text{ kJ mol}^{-1} \qquad [1.3]$$

The heat from the WGS reaction is typically fed back into reaction 1.1, though complete heat recycling is not possible.[19] Additional heat for the first reaction comes from combusting a fraction of the methane which generates additional CO_2. To ensure the reaction proceeds at a useful rate, nickel-based catalysts are used.[20] However, the high temperatures deployed and the formation of solid carbon deposits damage the catalyst over time.

The other common form of grey hydrogen is that produced by coal gasification. This is sometimes referred to as black hydrogen and in 2020 related to 19% of hydrogen generation.[21] A similar process is used for the gasification of biomass which makes so-called brown hydrogen. The coal or biomass is fed into a partial oxidation (POx) reformer where it is transformed into CO through either[22]

$$C_n + ½nO_2 \rightarrow nCO \qquad [1.4]$$

or

$$C_n + nH_2O \rightarrow nCO + nH_2 \quad [1.5]$$

This CO can then be used in the WGS reaction as before. In these equations, coal is presented as containing no hydrogen, though in reality a proportion of the final H_2 product is derived from the coal rather than the water.[22]

The carbon intensity of these methods is extremely high. Coal gasification generates ~20 t CO_2/t H_2.[21] Nearly 900 Mt of direct CO_2 emissions were associated with hydrogen production in 2020 accounting for 2.5% of global energy and industry CO_2 emissions.[21] Given that hydrogen demand is expected to grow, the carbon intensity of hydrogen production must be reduced rapidly.

1.3.2 Blue Hydrogen

Given the maturity of the technologies associated with grey hydrogen, it is natural that the first step in reducing the carbon emissions would be to improve those processes rather than creating new ones. To this end, carbon capture, utilisation, and storage (CCUS) has been heavily investigated as an add-on to currently grey processes. Ostensibly, capturing the CO_2 generated during hydrogen production should solve the emissions problem.

There are several issues with this assumption. First, no carbon capture technique can capture 100 % of the CO_2 produced. Second, some carbon capture utilisation and storage (CCUS) technologies require electricity which can add CO_2 emissions depending on the source of electricity generation.[23] Third, carbon capture typically only refers to CO_2. In the case of steam-methane reforming, a significant amount of CH_4 (~3.5 %) leaks to the atmosphere during the process. According to research by Howarth and Jacobson,[24] CCUS technologies would only reduce carbon emissions by only 9-12%. On a per unit of energy basis, the carbon emissions from using natural gas directly would be lower than using it to create hydrogen even with CCUS (see Figure 1.3).

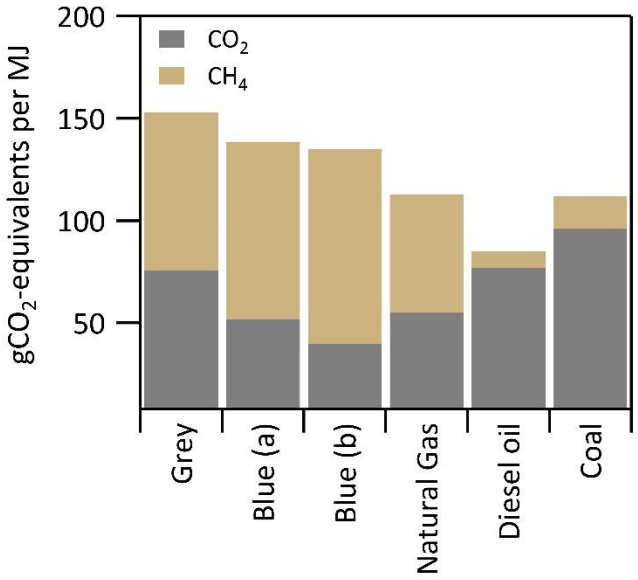


Figure 1.3 Comparison of equivalent CO_2 emissions per unit of heat energy of various fuels including grey and blue hydrogen. Blue (a) is without flue-gas capture. Blue (b) is with flue-gas capture. Data from Howarth and Jacobson.[24]

Despite these issues, blue hydrogen is generally considered necessary as a transitionary technology for hydrogen generation. Grey hydrogen is a mature but dirty technology and green hydrogen a nascent but clean technology. Blue hydrogen could bridge this gap whilst green hydrogen technologies mature. For this reason, the UK Government included CCUS in its Ten Point Plan, with the technology closely associated with hydrogen production.[25]

Another form of hydrogen derived from fossil fuels is produced through pyrolysis (sometimes referred to as turquoise hydrogen[26]) in which pure carbon is the side product rather than CO_2:

$$C_nH_m \rightarrow nC + \tfrac{1}{2}mH_2 \qquad [1.6]$$

Of course, CO_2 emissions are still generated as the process occurs at high temperatures typically produced through the conventional combustion of natural gas. This process can be considered blue if CCUS is used to reduce the carbon emissions associated with that process. This process is not commonly deployed given the quantity of solid carbon produced with limited use. Typically, blue hydrogen processes operate in conditions to avoid pyrolysis as the solid carbon poisons catalysts.[27] However, if demand for the carbon

increases, then this process may increase in popularity.[22] For example, battery electrode production[28] and steel making[22] can use the carbon product produced. Indeed, the high conductivity electrocatalyst support used in this thesis (Vulcan carbon), could be derived from such processes.

Pyrolysis of methane has the added benefit of reduced water requirements compared to methane reforming, water-gas shift reactions, and gasifciation.[26] This is particularly useful for hydrogen production in regions poor in water resources but rich in natural gas, such as Saudi Arabia. Further refinement to the pyrolysis process can be made by using concentrated solar energy as the heat source, which would be especially viable in such places. Doing this would fully transition the process out of the 'blue' bracket, as no CO_2 emissions would be associated with it. Boretti proposes 'aquamarine' as yet another colour code for this process.[29]

1.3.3 Green Hydrogen

The cleanest form of hydrogen production is described as 'green'. Green hydrogen is produced through the splitting of water into its constituent parts, H_2 and O_2. Typically, this is achieved with electricity (electrolysis), though light can also be used for the photocatalytic splitting of water.[30,31] In order to be green, renewable energy must be used as the source of the electricity. If non-renewable electricity sources are used, then the inefficiencies of the processes involved will make it more carbon intensive than grey hydrogen, that uses natural gas directly. Some groups delineate green hydrogen further using the terms yellow hydrogen (when solar power is used) and pink hydrogen (when nuclear power is used).

Globally, there is ample wind and solar energy that could be used to generate clean green hydrogen at a relatively low cost (see Figure 1.4). Countries with fewer renewable resources will inevitably have a higher hydrogen cost, but that assumes no exports of hydrogen. In the truest realisation of the hydrogen economy, a global hydrogen trade network would be established. In this fashion, countries in Africa can 'ship sunlight' in the form of cheaply generated

hydrogen (see Figure 1.4) to cloudier climes, or Scotland could 'truck wind' from the Highlands across the UK. Marco Alvera of Snam, a gas infrastructure company, refers to the solar case as 'long-distance sunlight' and likens the use of hydrogen to transport renewable energy to how natural gas is shipped/piped around the world.[32]

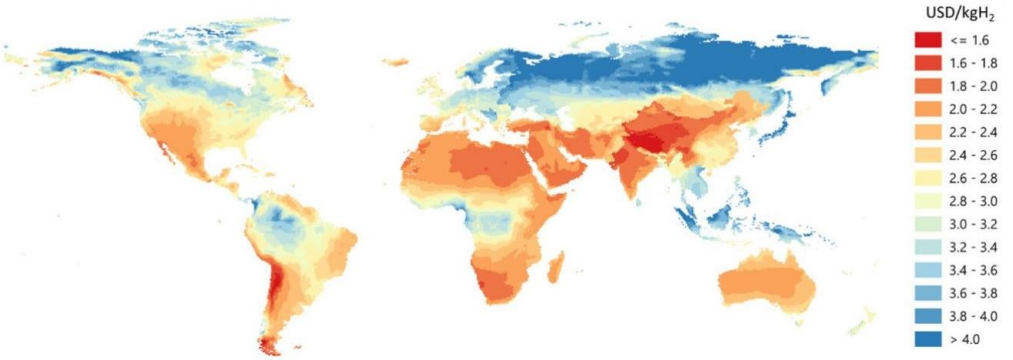


Figure 1.4 Map showing predicted long term hydrogen costs from hybrid solar PV and onshore wind systems. Reproduced from the IEA's Future of Hydrogen report.[33]

Green hydrogen is generated through the electrolysis of water:

$$2H_2O \rightleftharpoons 2H_2 + O_2 \qquad \Delta H = 286 \text{ kJ mol}^{-1} \qquad [1.7]$$

This can be split into the hydrogen and oxygen evolution reactions (HER and OER, respectively), which in turn are split into multiple elemental steps. The details of these reactions and the electrocatalysis of them is given in the next chapter and in the relevant chapters throughout this thesis. For now, it is enough to say that it is difficult to achieve high gas fluxes (directly related to the current flow) with low applied overpotentials.

By far the most mature and widely used technology (see Figure 1.5) is alkaline electrolysis. After this, acidic proton-exchange membrane (PEM) electrolysis is second, with anion-exchange membrane-based (AEM), and solid oxide electrolyser (SOECs) slowly increasing as the technologies improve.[18,34]

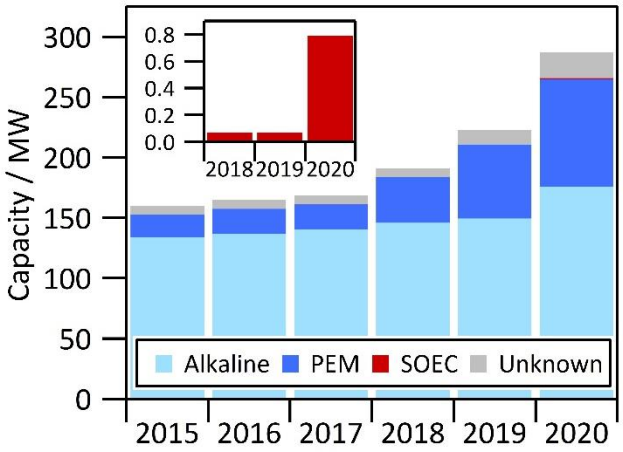


Figure 1.5 Global installed water electrolysis capacity by technology 2015-2020. Inset shows the contribution of SOECs 2018-2020. Data from the IEA Global Hydrogen Review.[18]

Each technology has its own benefits and drawbacks. All electrolysis technologies have the advantage of a far purer stream of hydrogen (~99.999 vol%)[35] than the grey and blue hydrogen production methods. A major reason for this is the lack of combustion side products.

All electrolyser technologies require the oxygen and hydrogen products be kept separate. If not, they could recombine (potentially explosively) to form water and reduce the efficiency of the cell. For this reason, separators are required. Alkaline electrolysis uses a diaphragm to separate the cathodic and anodic sides of the cell. The diaphragm is designed to prevent the crossover of gasses, allow ion transport to balance the charge during electrolysis, and withstand the highly caustic environment (30 % KOH). The first diaphragm material was asbestos, but owing to the associated health risks, less harmful materials are now used. The most common material in use today is Zirfon™ based on porous zirconium dioxide.[36]

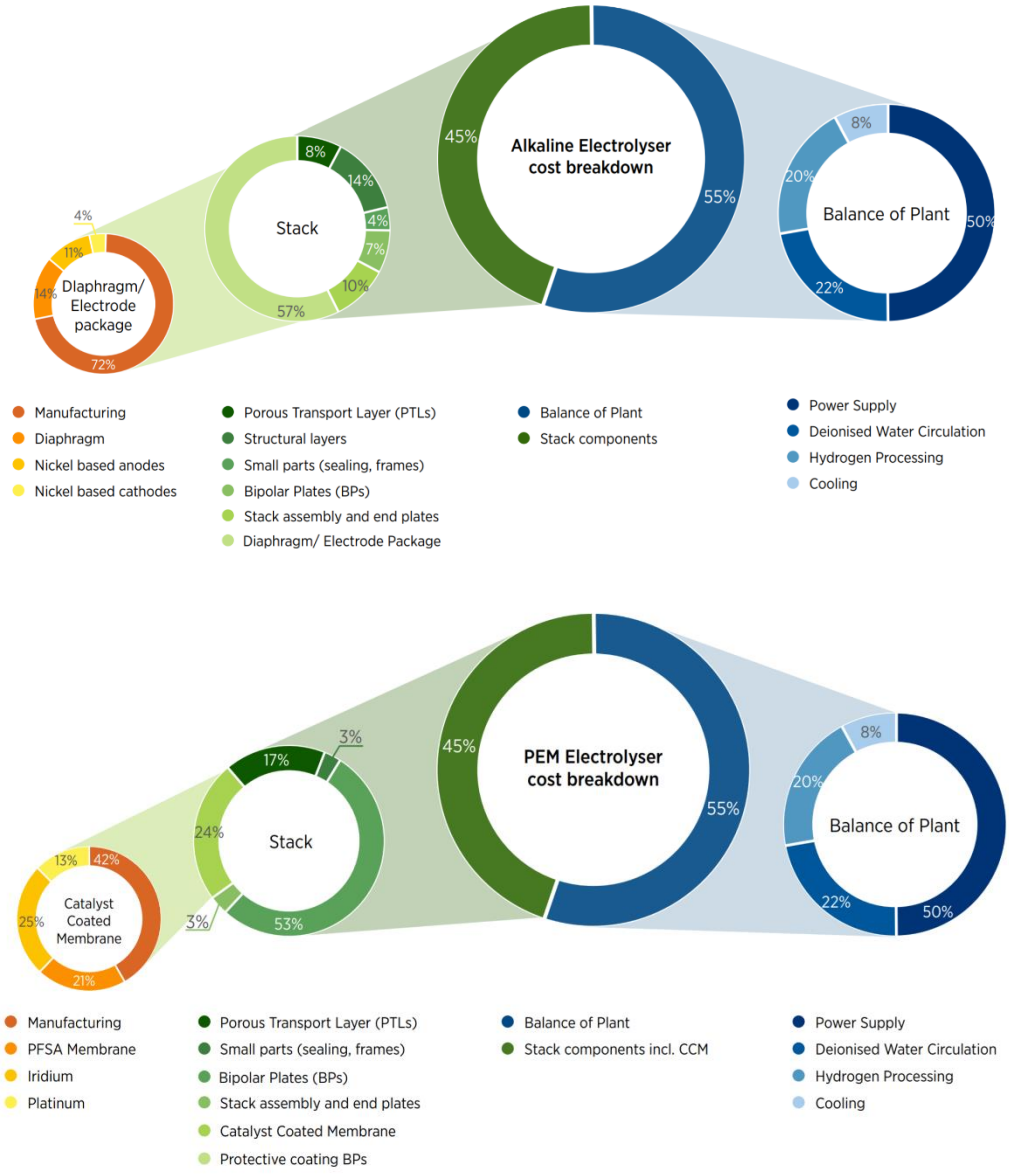
The membrane in PEM electrolysers is selective to cations (preferably with a high specificity for H^+). The most common of these is Nafion, a perfluorinated sulfonate ionomer.[37] By contrast, for AEM electrolysers the membrane is selective to the crossover of anions (specifically OH^-). Given that AEM electrolysis is a nascent field, there is currently no preferred membrane

material and research is ongoing. In SOECs, the cathode and anode are separated by a solid electrolyte through which gasses cannot permeate. The charge is balanced through the diffusion of O^{2-} ions via oxygen vacancies.

The prevalence of alkaline electrolysers for the chloralkali process (to generate Cl_2 at the anode and H_2 as the side product at the cathode), makes this technology currently the most scalable.[35] PEM electrolysis systems operate at a lower temperature than alkaline electrolysers and can withstand a higher working pressure.

The primary issue with using electrolysis to generate hydrogen is the high energy requirements of the process. A minimum energy input of at least 286 kJ $mol^{-1}{}_{H2}$ (the thermoneutral voltage for water splitting is 1.48 V vs RHE)[38] is required. In reality, due to the need for an activation overpotential, the energy requirement will be higher.

The cost of the electricity is a major contributor to the overall cost for both alkaline and PEM electrolysers, though not the only large cost (see Figure 1.6). Overall, a PEM electrolyser is 50-60% more expensive than an alkaline one.[39] Notably, the cost of the electrocatalysts account for a relatively small portion of the overall cost of an electrolyser, especially in the case of alkaline electrolysers. That is not to say that there is no benefit in changing the electrocatalysts. Global iridium supply and demand is low, with much production concentrated in South Africa as a by-product of other mining projects.[40] This means a sudden increase in the demand for the metal will be difficult to meet with current production capabilities. Centralised production capacity makes the resource geopolitically fraught. Platinum production is higher owing to its use in a wider range of applications, but production is also highly linked to South Africa. Both metals had significant price increases in 2021 because of pandemic-related production outages in the country.[40] Electrocatalysts which rely on materials produced in larger quantities and in a wider variety of locations will aid the transition to a hydrogen economy even if those materials have only a small overall influence on the cost of the electrolyser.



Note: The specific breakdown varies by manufacturer, application and location, but values in the figure represent an average.

Figure 1.6 Breakdown of the costs of an average 1 MW alkaline (top) or PEM (bottom) electrolyser. Reproduced from IRENA.[39]

1.4 Storing and Transporting Hydrogen

Once hydrogen has been made, whether through grey, blue, or green methods, it must be stored and transported. The small size of the hydrogen molecule poses several problems for storage. H_2 will escape through any cracks or imperfections rapidly.

Many metals (such as steel) cannot be used to store H_2. The molecule penetrates the metal and leads to 'hydrogen embrittlement', resulting in cracks in the metal due to hydride formation.[41,42] This in turn leads to the leakage of H_2. In order to store hydrogen in cylinders, alternative designs must be used. For example, cylinders can be spun from carbon fibres or made from resin materials,[43] or traditional gas cylinders can be lined with those materials.[44] An interesting case of hydrogen being stored in a cylinder-like container has been demonstrated by the National Renewable Energy Laboratory (NREL) who have used the inside of a wind turbine tower to store the hydrogen made using wind power.[45]

Hydrogen can also be stored cryogenically as a liquid. In this form nearly twice as much hydrogen can be stored in the same volume as with gaseous hydrogen pressurised to 70 MPa.[44] However, cooling H_2 to a liquid requires energy equivalent to about 30% of the energy stored in the H_2 reducing efficiency. Thus, cryogenic H_2 only makes sense in situations where the gains in efficiency from a lighter storage method outweigh the energy losses from cooling. For example, liquid H_2 has been considered as a shipping fuel (see next section). If it is going to be used shortly after cooling, then active refrigeration is not required, and good insulation can be relied on. Any hydrogen that evaporates off as a gas can be captured and burnt to recover those energy losses. If it needs to be stored long-term as a liquid, then active refrigeration leads to further efficiency losses.

Pure hydrogen or hydrogen mixed with other gases can be stored underground. This can either be in the pores of sedimentary rocks (such as depleted gas or oil fields) or in caverns.[43,46–48] Such large-scale storage can be useful for seasonal storage of H_2. This is made in the summer months through solar green hydrogen and can then be used in the winter. This is far more cost-effective than using a battery with equivalent energy storage and charging/discharging it once a year.[48]

A heavily researched field for hydrogen storage is that of metal hydrides.[49,50] Here, a metal or alloy chemisorbs hydrogen to form a hydride. An ideal material

for this kind of storage is one which can take on the hydrogen at close to ambient conditions and then release the hydrogen after a small change in the temperature and/or pressure.[49]

Another method for storing and transporting H_2 is in pipes.[51,52] Much of the gas pipe infrastructure was previously used to carry town gas and so is already suitable to carry up to 20% H_2.[53] To carry 100% may require extensive pipe changes, though in the UK much of this has already been carried out anyway as the network upgrades from iron pipes to plastic pipes. Although this was done as a cost-saving and modernisation exercise, it has the fortunate consequence of readying the network for H_2. Although it may seem that pipes are primarily a transport mechanism, the built-in flexibility of gas networks makes them ideal for storage.[51] In a high-renewable scenario with much of electricity coupled to hydrogen production, sunny and windy days will result in a lot of hydrogen generation. On days with less useful weather conditions, hydrogen generation will be low. Rather than requiring storage capacity match that needed for the days of most generation, the pressure of the gas grid can be leveraged instead. When production is low, the pressure is reduced; when production is high, more H_2 is pumped into the grid at higher pressure.[32,51] Thus, the same volume of pipes can store variable amounts of gas. This is already done with natural gas grids; in the winter the network is at a significantly higher pressure to keep up with higher demand.[51]

It is not a case that one of these methods will 'win'. Each has its own benefits and drawbacks. The hydrogen economy will depend on a versatile network of various storage and transport systems.

1.5 Using Hydrogen

1.5.1 Fuel Cells

Where splitting water requires an energy input, forming water from its constituent elements generates a flow of electrons. The reverse of the OER is the oxygen reduction reaction (ORR), and the reverse of the HER is the hydrogen oxidation reaction (HOR). The ORR and HOR are thus the reactions

which occur at the cathode and anode of a fuel cell, respectively. Overall, the reaction is:

$$2H_2 + O_2 \rightleftharpoons 2H_2O \quad [1.8]$$

In much the same way as electrolysers can be split into different families, so too can fuel cells. Alkaline fuel cells (AFCs) operate at high pH values and have an efficiency of 60 – 70 %. PEM fuel cells (PEMFCs) operate in acidic conditions and generally have a lower efficiency of 43 – 68 %. Solid oxide fuel cells (SOFCs) use solid electrolytes and have efficiencies between 55 – 65 %.[54] The membranes and electrolytes previously discussed for electrolysers can also be used in fuel cells.

PEMFCs are the preferred class of fuel cells for fuel cell electric vehicles (FCEV). It is unlikely that fuel cells will be used for passenger cars to anywhere near the extent that batteries are. However, for heavy-goods vehicles, the enhanced gravimetric density of hydrogen compared to batteries may make fuel cell options more attractive as a greater proportion of the truck's weight can be dedicated to goods storage. In addition, trucking companies will want to minimise refuelling times. It is inefficient to wait for a truck to charge up and it would not always be possible to coincide recharging with rest stops. Thus, being able to refuel with hydrogen presents time (and cost) savings to a trucking company.[55]

Precious metal electrocatalysts account for 42 % of the cost of a current fuel cell.[56] As will be discussed in greater detail later in this thesis, there is a push towards non-precious metals to be used as the electrocatalysts in fuel cells.[57] It is hoped that if the cost of the electrocatalysts used in fuel cells dops, then the FCEVs may become cost competitive.[58]

1.5.2 Other Uses

As discussed in the opening of this introduction, there are significant emissions associated with industrial processes that cannot be electrified. Given this, fuel cells will not help solve those issues. However, hydrogen molecules are more versatile than electrons. Hydrogen is a commonly used feedstock material in

the chemical industry. Ammonia requires large quantities of hydrogen and given ammonia's widespread use as a fertiliser, this presents an opportunity to not just greenify an industrial process, but indirectly make agriculture cleaner.[59]

Iron and steel production accounts for 7% of global CO_2 emissions globally (greater than that of aviation, for example).[60] Although parts of the steel production process can be electrified (such as using electric arc furnaces), the biggest gains are to be made through hydrogen involved in the direct reduced iron (DRI) process.[61,62] To use hydrogen in this process only makes sense when it is green, otherwise this would simply shift emissions elsewhere. Green hydrogen used in the DRI process could lead to a 97% reduction in the CO_2 emissions associated with steel production.[10]

Natural gas can be combusted either for electricity generation or to use the heat directly (for cooking and residential heating, for example). Although hydrogen can create electricity through its use in fuel cells, it can also be used to replace natural gas in heat generation. The materials and geometries used in natural gas turbines will have to be adjusted to account for hydrogen's higher chemical reactivity and higher burn temperatures. But otherwise, hydrogen can be used either as a pure gas or mixed in with natural gas to lower the carbon intensity of this kind of heat generation.[52] There are many island communities which use hydrogen as for heating their homes and cooking without converting the hydrogen into electricity.[63]

1.6 Electrocatalyst design

The design and optimisation of electrocatalysts for water-splitting and fuel cell applications is vital to reduce the dependence on precious metals. Ideally dependence on conflict minerals should also be avoided. Thus, researchers have deployed numerous strategies to enhance the performance of the electrocatalysts they design.[64–70]

Although there are many more strategies available,[65,71,72] this thesis focuses primarily on three: synergistic interactions with another material, morphological control of the electrocatalyst, and cationic doping. Specific

details will be given in the relevant chapters, but a broad overview of the strategies is given here.

1.6.1.1 Synergistic Interactions

Introducing synergistic interactions to the electrocatalyst is a commonly explored strategy.[65] Here, rather than changing the active material, a separate material is introduced. The activity of the combined material is greater than the activity of either material on its own. This means it is not just the more active material being the cause of the good performance; the interaction between, or the proximity of, the two materials lead to the enhancement.[73]

One method to induce a synergistic interaction is to decorate one material with another. For example, Zhu *et al* electrochemically generated Ru nanoparticles from a bulk Sr_2RuO_4 perovskite oxide and found that the Ru nanoparticles on the surface offered an alternative active site to which intermediates could adsorb.[74] The close proximity to the perovskite active sites led to a synergistic interaction enhancing the activity beyond that achieved by the base perovskite oxide.[74]

Decoration of perovskites (ABO_3, defined in section 1.6.1.3) with Ni,[75] Co,[75–77] and Co-Ni bimetallic[78] nanoparticles derived from the base perovskite has also been demonstrated to synergistically boost the activity of the electrocatalyst. For the HER, the traditional electrocatalytic active sites of the perovskite are the octahedra formed by the B-site cations and the oxygen atoms (more details in Chapter 6). When the perovskite is decorated with metallic nanoparticles, the perovskite B-site acts as the active site for the water dissociation step and the nanoparticles decorating the surface provide a more energetically favourable hydrogen adsorption site.[75–78] Zhu *et al* demonstrated this synergistic interaction by comparing the base perovskite $(La_{0.4}Sr_{0.4})(Ti_{0.9})O_{3-\delta}$ (LST) with a Ni nanoparticle decorated form (e-LSNT) generated by exsolving Ni from $(La_{0.4}Sr_{0.4})(Ti_{0.9}Ni_{0.1})O_{3-\delta}$ (LSTN).[75] They showed that e-LSNT had enhanced HER activity compared to both the LST base perovskite and the LSTN from which the Ni nanoparticles were derived, indicating a synergistic interaction.[75]

Another common synergistic route taken in electrocatalyst design is to combine the electrocatalyst with carbonaceous materials which on their own are not considered to be excellent electrocatalysts for the HER, OER, or ORR.[79–85]

For example, Deng *et al* encapsulated Fe nanoparticles within peapod like carbon nanotubes. They found that the Fe interacted with the nanotube from the inside, altering the activity of the exterior active sites on the nanotube surface. This led to the material being more active than nanotubes without the encapsulated Fe, despite the intermediates not being able to directly interact with the Fe.[85]

Chapter 4 investigates similar synergistic interactions between cobalt oxide and single-walled nanotubes (SWNTs). In this case, we show that the confinement of the oxide alters the surface chemistry of the SWNTs, enhancing electrocatalytic performance towards the OER. This allows for an electrocatalyst to be designed that can use significantly less cobalt whilst maintaining electrocatalytic activity.

1.6.1.2 Morphological Control

Morphology refers to the physical structure of a material as opposed to its chemical structure. By controlling the morphology, the exposed surface area is also controlled. However, morphological control can go beyond simply increasing the surface area—it can also allow for more efficient movement of reactants and products.

There are many ways to change the morphology of a material.[86] It can be achieved through simple grinding the material,[87] or through more complex procedures such as chemical-[88,89] or heat-treatments[90] which enhance the porosity of the material, and in turn the activity.[90–92]

Specific morphologies have also been investigated, including nanohorns,[93] nanoflowers,[94] nanocabbages,[95] and nanopomegranates,[96] to name but a few nanoforms of many.[86] Regardless of the nanoanalogy, such structures often have greater activity than their bulk counterparts, even when normalised to the enhanced surface area. At the nanoscale, there can be stresses and strains

which enhance the activity of the active site.[86,97–99] There has recently been work that shows even across an individual nanostructure there is variation in activity: Mefford *et al* used a comprehensive set of *operando* methods to demonstrate, amongst other things, the basal plane of a hexagonal platelet of β-$Co(OH)_2$ was inactive towards the OER, whereas the edge sites were highly active.[100] Designing materials with more edge sites thus increases the activity more rapidly than would be expected from surface area enhancements alone. Indeed, this was discovered to be entirely the origin of the electrocatalytic activity for MoS_2 electrocatalysts.[101,102]

Chapter 5 explores the use of titanate-based microspheres as an interesting morphology for oxygen reduction electrocatalysts. Chemically processing these microspheres to create a porous surface layer is also explored.

1.6.1.3 Cationic Doping

Families of materials are often explored together for their electrocatalytic properties. Changing the identity of the elements or chemical moieties present, or by doping them with varying amounts of another element, can lead to enhancements in the activity towards a given electrocatalytic reaction.[65–67,70,103–105]

Chapter 6 discusses this in the context of perovskite electrocatalysts. These are a broad material family characterised by an ABO_3, where A is generally a rare-earth or alkali earth metal and B is typically a transition metal. By incorporating multiple elements, the crystal structure can be altered.[106,107] This can expose different active sites which may be better optimised to the adsorption of intermediates involved in the reaction. It is possible to change the oxidation state of one element in the electrocatalyst by changing the identity of another. This, in turn, can alter the activity of the material.[108]

An example of changing the activity through doping the material is presented by Guan *et al.* They synthesised a range of perovskites with a consistent B-site, but a varied A-site. Although the B-site octahedron is considered the primary active site for perovskite electrocatalysts, varying the A-site led to changes in

the activity of the material towards the HER because the electronegativity of the A-site can induce a change in the valence of the B-site.[109,110]

1.7 Thesis aims and objectives

The overall objective of this body of work is to further understand how synergistic interactions, morphological control, and cationic doping can be used to alter the activity of a given electrocatalyst family towards reactions pertinent to the hydrogen economy.

First, Chapter 3 explores the use of counter electrodes (CE) in electrocatalytic measurements and strives to elucidate the best practice when working in this area. Typically, Pt or Au CEs are used, but this is demonstrated to lead to the artificial enhancement of electrocatalyst materials due to the dissolution of metals from the CE and subsequent deposition on the working electrode. Although experimental design is not itself a strategy for the design of an electrocatalyst, it underpins the ability to discern whether or not a deployed strategy has an impact.

Chapter 4 sets out to improve our understanding of the synergistic interactions between electrocatalysts and single-walled nanotubes (SWNTs).[111] Specifically, Co_3O_4 is chosen as the benchmark electrocatalyst to be explored due to its prominence in the literature.

Chapter 5 examines the control of electrocatalyst morphologies. Specifically, the chapter focuses on titanate microspheres for their mechanical properties and investigates how the growth of a chemically different layer over the surface of the nanoparticle impacts the activity of the ORR. Titanate structures are chosen as the underlying material as they have previously been demonstrated to offer interesting microspherical structures.[112]

Chapter 6 assesses the impact of various doping strategies on perovskite oxide electrocatalysts. This class of materials was chosen for the investigation as they are well known to accept a wide range of dopants.[113] Through use of the measured XRD patterns, the physical changes that arise from these doping strategies are correlated to changes in electrocatalytic performance.

1.8 References

1. Verne, J. *The Mysterious Island*. (Pierre-Jules Hetzel, 1875).

2. UNFCCC. *Adoption of the Paris Agreement, FCCC/CP/2015/L.9/Rev.1*. (United Nations Framework Convention on Climate Change, 2015).

3. UNEP. *Emissions Gap Report 2021: The Heat Is On – A World of Climate Promises Not Yet Delivered*. (2021).

4. Simon Evans *et al.* COP26: Key outcomes agreed at the UN climate talks in Glasgow - Carbon Brief. https://www.carbonbrief.org/cop26-key-outcomes-agreed-at-the-un-climate-talks-in-glasgow.

5. IPCC. *Climate Change 2021: The Physical Science Basis. Contribution of Working Group I to the Sixth Assessment Report of the Intergovernmental Panel on Climate Change*. (2021).

6. Arrhenius, S. On the Influence of Carbonic Acid in the Air upon the Temperature of the Ground. *Lond. Edinb. Dublin Philos. Mag. J. Sci.* **5**, 237–276 (1896).

7. IEA. *The role of CCUS in low-carbon power systems*. (2020).

8. Renewables - Fuels & Technologies - IEA. https://www.iea.org/fuels-and-technologies/renewables.

9. Harrabin, R. Ban on new petrol and diesel cars in UK from 2030 under PM's green plan. *BBC News* (2020).

10. Fennell, P., Driver, J., Bataille, C. & Davis, S. J. Cement and steel — nine steps to net zero. *Nature* **603**, 574–577 (2022).

11. Bockris, J. O. A Hydrogen Economy. *Science* **176**, 1323 (1972).

12. Bockris, J. O. M. The hydrogen economy: Its history. *Int. J. Hydrogen Energy* **38**, 2579–2588 (2013).

13. Smeets, F. & Vaes, J. Electrolysis Systems for Grid Relieving. in *Hydrogen Science and Engineering Materials, Processes, Systems and Technology Volume 1* (eds. Emonts, B. & Stolten, D.) (Wiley-VCH Verlag GmbH & Co. KGaA, 2016).

14. Miao, B., Giordano, L. & Chan, S. H. Long-distance renewable hydrogen transmission via cables and pipelines. *Int. J. Hydrogen Energy* **46**, 18699–18718 (2021).

15. Pellow, M. A., Emmott, C. J. M., Barnhart, C. J. & Benson, S. M. Hydrogen or batteries for grid storage? A net energy analysis. *Energy Environ. Sci.* **8**, 1938–1952 (2015).

16. IEA. Global hydrogen demand by production technology in the Net Zero Scenario, 2020-2030. https://www.iea.org/data-and-statistics/charts/global-hydrogen-demand-by-production-technology-in-the-net-zero-scenario-2020-2030 (2021).

17. HOME - CERTIFHY. https://www.certifhy.eu/.

18. IEA. *Hydrogen*. (2021).

19. Sorensen, B. & Spazzafumo, G. *Hydrogen and Fuel Cells*. (Academic Press, 2018).

20. Matsumura, Y. & Nakamori, T. Steam reforming of methane over nickel catalysts at low reaction temperature. *Appl. Catal. A Gen.* **258**, 107–114 (2004).

21. IEA. *Global Hydrogen Review 2021*. (2021).

22. Nikolaidis, P. & Poullikkas, A. A comparative overview of hydrogen production processes. *Renew. Sustain. Energy Rev.* **67**, 597–611 (2017).

23. Gabrielli, P., Gazzani, M. & Mazzotti, M. The Role of Carbon Capture and Utilization, Carbon Capture and Storage, and Biomass to Enable a Net-Zero-CO2 Emissions Chemical Industry. *Ind. Eng. Chem. Res.* **59**, 7033–7045 (2020).

24. Howarth, R. W. & Jacobson, M. Z. How green is blue hydrogen? *Energy Sci. Eng.* **9**, 1676–1687 (2021).

25. HM Government. *The Ten Point Plan for a Green Industrial Revolution*. https://www.gov.uk/government/publications/the-ten-point-plan-for-a-green-industrial-revolution/title (2020).

26. Boretti, A. A perspective on the production of hydrogen from solar-driven thermal decomposition of methane. *Int. J. Hydrogen Energy* **46**, 34509–34514 (2021).

27. Peters, R. Fuel Processing for Utilization in Fuel Cells. in *Hydrogen Science and Engineering Materials, Processes, Systems and Technology Volume 1* (eds. Stolten, D. & Emonts, B.) (Wiley-VCH Verlag GmbH & Co. KGaA, 2016).

28. Clarke, R. & Abánades, A. Briefing: Pyrolysis of natural gas to hydrogen: A key energy transition tool. *Proc. Inst. Civ. Eng. Energy* **174**, 98–102 (2021).

29. Boretti, A. There are hydrogen production pathways with better than green hydrogen economic and environmental costs. *Int. J. Hydrogen Energy* **46**, 23988–23995 (2021).

30. Yin Tee, S. *et al.* Recent Progress in Energy-Driven Water Splitting. *Adv. Sci.* **4**, 1600337 (2017).

31. Ma, Y., Lin, L., Takata, T., Hisatomi, T. & Domen, K. A perspective on two pathways of photocatalytic water splitting and their practical application systems. *Phys. Chem. Chem. Phys.* **25**, 6586–6601 (2023).

32. Alvera, M. *The Hydrogen Revolution*. (Hodder Studio, 2021).

33. IEA. *The Future of Hydrogen*. (2019).

34. Dawood, F., Anda, M. & Shafiullah, G. M. Hydrogen production for energy: An overview. *Int. J. Hydrogen Energy* **45**, 3847–3869 (2020).

35. Abdin, Z. *et al.* Hydrogen as an energy vector. *Renew. Sustain. Energy Rev.* **120**, 109620 (2020).

36. Brauns, J. *et al.* Evaluation of Diaphragms and Membranes as Separators for Alkaline Water Electrolysis. *J. Electrochem. Soc.* **168**, 014510 (2021).

37. Mauritz, K. A. & Moore, R. B. State of Understanding of Nafion. *Chem. Rev.* **104**, 4535–4586 (2004).

38. Li, W. *et al.* Electrolyzer Design for Flexible Decoupled Water Splitting and Organic Upgrading with Electron Reservoirs. *Chem* **4**, 637–649 (2018).

39. IRENA. *Green Hydrogen Cost Reduction: Scaling Up Electrolysers To Meet The 1.5°C Climate Goal*. (2020).

40. Johnson Matthey. *PGM market report May 2021*. (2021).

41. Dwivedi, S. K. & Vishwakarma, M. Hydrogen embrittlement in different materials: A review. *Int. J. Hydrogen Energy* **43**, 21603–21616 (2018).

42. Eliezer, D. & Silverstein, R. Recent Studies of Hydrogen Embrittlement in Structural Materials. *Procedia Struct. Integr.* **13**, 2233–2238 (2018).

43. Elberry, A. M., Thakur, J., Santasalo-Aarnio, A. & Larmi, M. Large-scale compressed hydrogen storage as part of renewable electricity storage systems. *Int. J. Hydrogen Energy* **46**, 15671–15690 (2021).

44. Sheffield, J. W., Martin, K. B. & Folkson, R. Electricity and hydrogen as energy vectors for transportation vehicles. in *Alternative Fuels and Advanced Vehicle Technologies for Improved Environmental Performance: Towards Zero Carbon Transportation* 117–137 (Woodhead Publishing, 2014).

45. Ramesh Bapu, B. R., Karthikeyan, J. & Vijay Kumar Reddy, K. Hydrogen storage in wind turbine tower - A review. in *Proc. Int. Conf. Front. Automob. Mech. Eng.* 308–312 (2010).

46. Liebscher, A., Wackerl, J. & Streibel, M. Geologic Storage of Hydrogen - Fundamentals, Processing, and Projects. in *Hydrogen Science and Engineering: Materials, Processes, Systems and Technology* vol. 2 629–658 (Wiley-VCH Verlag GmbH & Co. KGaA, 2016).

47. Portarapillo, M. & Di Benedetto, A. Risk Assessment of the Large-Scale Hydrogen Storage in Salt Caverns. *Energies* **14**, 2856 (2021).

48. Elberry, A. M., Thakur, J. & Veysey, J. Seasonal hydrogen storage for sustainable renewable energy integration in the electricity sector: A case study of Finland. *J. Energy Storage* **44**, 103474 (2021).

49. Modi, P. & Aguey-Zinsou, K. F. Room Temperature Metal Hydrides for Stationary and Heat Storage Applications: A Review. *Front. Energy Res.* **9**, 128 (2021).

50. Chen, P., Akiba, E., Orimo, S., Zuettel, A. & Schlapbach, L. Hydrogen Storage by Reversible Metal Hydride Formation. in *Hydrogen Science and Engineering: Materials, Processes, Systems and Technology* vol. 2 763–790 (Wiley-VCH Verlag GmbH & Co. KGaA, 2016).

51. Clegg, S. & Mancarella, P. Storing renewables in the gas network: modelling of power-to-gas seasonal storage flexibility in low-carbon power systems. *IET Gener. Transm. Distrib.* **10**, 566–575 (2016).

52. Griebel, P. Gas Turbines and Hydrogen. in *Hydrogen Science and Engineering : Materials, Processes, Systems and Technology* vol. 2 1011–1032 (Wiley-VCH Verlag GmbH & Co. KGaA, 2016).

53. Everett, B. & Boyle, G. Integrating Renewable Energy. in *Renewable Energy* (ed. Boyle, G.) 461–526 (Oxford University Press, 2012).

54. Fan, L., Tu, Z. & Chan, S. H. Recent development of hydrogen and fuel cell technologies: A review. *Energy Reports* **7**, 8421–8446 (2021).

55. Nugroho, R., Rose, P. K., Gnann, T. & Wei, M. Cost of a potential hydrogen-refueling network for heavy-duty vehicles with long-haul application in Germany 2050. *Int. J. Hydrogen Energy* **46**, 35459–35478 (2021).

56. Osmieri, L. *et al.* Status and challenges for the application of platinum group metal-free catalysts in proton-exchange membrane fuel cells. *Curr. Opin. Electrochem.* **25**, 100627 (2021).

57. Cui, J., Chen, Q., Li, X. & Zhang, S. Recent advances in non-precious metal electrocatalysts for oxygen reduction in acidic media and PEMFCs: an activity, stability and mechanism study. *Green Chem.* **23**, 6898–6925 (2021).

58. Thompson, S. T. & Papageorgopoulos, D. Platinum group metal-free catalysts boost cost competitiveness of fuel cell vehicles. *Nat. Catal.* **2**, 558–561 (2019).

59. Ghavam, S., Vahdati, M., Wilson, I. A. G. & Styring, P. Sustainable Ammonia Production Processes. *Front. Energy Res.* **9**, 34 (2021).

60. IEA. *Tracking Industry 2021*. (2021).

61. IEA. *Iron and Steel*. (2021).

62. Toktarova, A., Walter, V., Göransson, L. & Johnsson, F. Interaction between electrified steel production and the north European electricity system. *Appl. Energy* **310**, 118584 (2022).

63. Barbir, F. Hydrogen Islands - Utilization of Renewable Energy for an Autonomous Power Supply. in *Hydrogen Science and Engineering: Materials, Processes, Systems and Technology* vol. 2 1075–1096 (Wiley-VCH Verlag GmbH & Co. KGaA, 2016).

64. Hong, W. T. *et al.* Toward the rational design of non-precious transition metal oxides for oxygen electrocatalysis. *Energy Environ. Sci.* **8**, 1404–1427 (2015).

65. Wang, Y., Zheng, X. & Wang, D. Design concept for electrocatalysts. *Nano Res.* **15**, 1730–1752 (2022).

66. Doyle, R. L. & Lyons, M. E. G. The Oxygen Evolution Reaction: Mechanistic Concepts and Catalyst Design. in *Photoelectrochemical Solar Fuel Production: From Basic Principles to Advanced Devices* (eds. Giménez, S. & Bisquert, J.) (Springer International Publishing, 2016).

67. Jiao, Y., Zheng, Y., Jaroniec, M. & Qiao, S. Z. Design of electrocatalysts for oxygen- and hydrogen-involving energy conversion reactions. *Chem. Soc. Rev.* **44**, 2060–2086 (2015).

68. Wang, H. & Liu, D. J. Rational design of platinum-group-metal-free electrocatalysts for oxygen reduction reaction. *Curr. Opin. Electrochem.* **28**, 100724 (2021).

69. Wang, X. *et al.* Review of Metal Catalysts for Oxygen Reduction Reaction: From Nanoscale Engineering to Atomic Design. *Chem* **5**, 1486–1511 (2019).

70. Seh, Z. W. *et al.* Combining theory and experiment in electrocatalysis: Insights into materials design. *Science* **355**, eaad4998 (2017).

71. Liu, F. *et al.* Rational Design of Better Hydrogen Evolution Electrocatalysts for Water Splitting: A Review. *Adv. Sci.* **9**, 2200307 (2022).

72. Linnemann, J., Kanokkanchana, K. & Tschulik, K. Design Strategies for Electrocatalysts from an Electrochemist's Perspective. *ACS Catal.* **11**, 5318–5346 (2021).

73. Zhuang, L., Jin, J. & Abruña, H. D. Direct observation of electrocatalytic synergy. *J. Am. Chem. Soc.* **129**, 11033–11035 (2007).

74. Zhu, Y. L. *et al.* Unusual synergistic effect in layered Ruddlesden - Popper oxide enables ultrafast hydrogen evolution. *Nat. Commun.* **10**, 9 (2019).

75. Zhu, Y. *et al.* Synergistically enhanced hydrogen evolution electrocatalysis by in situ exsolution of metallic nanoparticles on perovskites. *J. Mater. Chem. A* **6**, 13582–13587 (2018).

76. Zhang, Y. Q. *et al.* In situ grown cobalt phosphide (CoP) on perovskite nanofibers as an optimized trifunctional electrocatalyst for Zn-Air batteries and overall water splitting. *J. Mater. Chem. A* **7**, 26607–26617 (2019).

77. Hua, B. *et al.* A coupling for success: Controlled growth of Co/CoOx nanoshoots on perovskite mesoporous nanofibres as high-performance trifunctional electrocatalysts in alkaline condition. *Nano Energy* **32**, 247–254 (2017).

78. Islam, Q. A., Majee, R. & Bhattacharyya, S. Bimetallic nanoparticle decorated perovskite oxide for state-of-the-art trifunctional electrocatalysis. *J. Mater. Chem. A* **7**, 19453–19464 (2019).

79. Wan, W. *et al.* Transition metal electrocatalysts encapsulated into N-doped carbon nanotubes on reduced graphene oxide nanosheets: efficient water splitting through synergistic effects. *J. Mater. Chem. A* **7**, 15145–15155 (2019).

80. Wang, A. *et al.* Insights into the synergistic effect of multi-walled carbon nanotube decorated Mo-doped CoP2 hybrid electrocatalysts toward efficient and durable overall water splitting. *J. Mater. Chem. A* **8**, 17621–17633 (2020).

81. Melchionna, M., Fornasiero, P. & Prato, M. Into the carbon: A matter of core and shell in advanced electrocatalysis. *APL Mater.* **8**, 20905 (2020).

82. Sun, L., Wang, X., Wang, Y. & Zhang, Q. Roles of carbon nanotubes in novel energy storage devices. *Carbon* **122**, 462–474 (2017).

83. Sheng, J. & Li, Y. Applications of Carbon Nanotubes in Oxygen Electrocatalytic Reactions. *ACS Appl. Mater. Interfaces* **14**, 20455–20462 (2021).

84. Deng, J. *et al.* Highly active and durable non-precious-metal catalysts encapsulated in carbon nanotubes for hydrogen evolution reaction. *Energy Environ. Sci.* **7**, 1919–1923 (2014).

85. Deng, D. *et al.* Iron Encapsulated within Pod-like Carbon Nanotubes for Oxygen Reduction Reaction. *Angew. Chemie Int. Ed.* **52**, 371–375 (2013).

86. Mistry, H., Varela, A. S., Kühl, S., Strasser, P. & Cuenya, B. R. Nanostructured electrocatalysts with tunable activity and selectivity. *Nat. Rev. Mater.* **1**, 1–14 (2016).

87. Zhu, Y. *et al.* SrNb0.1Co0.7Fe0.2O3− δ Perovskite as a Next-Generation Electrocatalyst for Oxygen Evolution in Alkaline Solution. *Angew. Chemie Int. Ed.* **54**, 3897–3901 (2015).

88. Wan, L. *et al.* A Mild CO2Etching Method to Tailor the Pore Structure of Platinum-Free Oxygen Reduction Catalysts in Proton Exchange Membrane Fuel Cells. *ACS Appl. Mater. Interfaces* **13**, 45661–45669 (2021).

89. Shin, D., An, X., Choun, M. & Lee, J. Effect of transition metal induced pore structure on oxygen reduction reaction of electrospun fibrous carbon. *Catal. Today* **260**, 82–88 (2016).

90. Bandosz, T. J. Revealing the impact of small pores on oxygen reduction on carbon electrocatalysts: A journey through recent findings. *Carbon* **188**, 289–304 (2022).

91. Trogadas, P. & Coppens, M. O. Nature-inspired electrocatalysts and devices for energy conversion. *Chem. Soc. Rev.* **49**, 3107–3141 (2020).

92. Qi, J., Zhang, W. & Cao, R. Porous Materials as Highly Efficient Electrocatalysts for the Oxygen Evolution Reaction. *ChemCatChem* **10**, 1206–1220 (2018).

93. Kagkoura, A. & Tagmatarchis, N. Carbon Nanohorn-Based Electrocatalysts for Energy Conversion. *Nanomaterials* **10**, 1–26 (2020).

94. Han, S. J. *et al.* Catalytic Evaluation of Nanoflower Structured Manganese Oxide Electrocatalyst for Oxygen Reduction in Alkaline Media. *Catalysts* **10**, 822 (2020).

95. Ikkurthi, K. D., Srinivasa Rao, S., Ahn, J. W., Sunesh, C. D. & Kim, H. J. A cabbage leaf like nanostructure of a NiS@ZnS composite on Ni foam with excellent electrochemical performance for supercapacitors. *Dalt. Trans.* **48**, 578–586 (2019).

96. Chen, Y. Y. *et al.* Pomegranate-like N,P-Doped Mo2C@C Nanospheres as Highly Active Electrocatalysts for Alkaline Hydrogen Evolution. *ACS Nano* **10**, 8851–8860 (2016).

97. Zhou, M. *et al.* Enhancing the Intrinsic Activity and Stability of Perovskite Cobaltite at Elevated Temperature Through Surface Stress. *Small* **17**, 2104144 (2021).

98. Mavrikakis, M., Hammer, B. & Nørskov, J. K. Effect of Strain on the Reactivity of Metal Surfaces. *Phys. Rev. Lett.* **81**, 2819 (1998).

99. Strasser, P. *et al.* Lattice-strain control of the activity in dealloyed core–shell fuel cell catalysts. *Nat. Chem.* **2**, 454–460 (2010).

100. Mefford, J. T. *et al.* Correlative operando microscopy of oxygen evolution electrocatalysts. *Nature* **593**, 67–73 (2021).

101. Jaramillo, T. F. *et al.* Identification of active edge sites for electrochemical H2 evolution from MoS2 nanocatalysts. *Science* **317**, 100–102 (2007).

102. Seo, B. & Joo, S. H. Recent advances in unveiling active sites in molybdenum sulfide-based electrocatalysts for the hydrogen evolution reaction. *Nano Converg.* **4**, 1–11 (2017).

103. Gupta, S. *et al.* Quaternary FeCoNiMn-Based Nanocarbon Electrocatalysts for Bifunctional Oxygen Reduction and Evolution: Promotional Role of Mn Doping in Stabilizing Carbon. *ACS Catal.* **7**, 8386–8393 (2017).

104. Wygant, B. R. *et al.* Structural and Catalytic Effects of Iron-and Scandium-Doping on a Strontium Cobalt Oxide Electrocatalyst for Water Oxidation. *ACS Catal.* **6**, 1122–1133 (2016).

105. Jiang, M. *et al.* Double Perovskites as Model Bifunctional Catalysts toward Rational Design: The Correlation between Electrocatalytic Activity and Complex Spin Configuration. *ACS Appl. Mater. Interfaces* **10**, 19746–19754 (2018).

106. Chen, D., Chen, C., Baiyee, Z. M., Shao, Z. & Ciucci, F. Nonstoichiometric Oxides as Low-Cost and Highly-Efficient Oxygen Reduction/Evolution Catalysts for Low-Temperature Electrochemical Devices. *Chem. Rev.* **115**, 9869–9921 (2015).

107. Xu, X. *et al.* A Perovskite Electrocatalyst for Efficient Hydrogen Evolution Reaction. *Adv. Mater.* **28**, 6442–6448 (2016).

108. Chen, H. *et al.* Activating Lattice Oxygen in Perovskite Oxide by B-Site Cation Doping for Modulated Stability and Activity at Elevated Temperatures. *Adv. Sci.* **8**, 2102713 (2021).

109. Guan, D. *et al.* Searching General Sufficient-and-Necessary Conditions for Ultrafast Hydrogen-Evolving Electrocatalysis. *Adv. Funct. Mater.* **29**, 1900704 (2019).

110. Guan, D. *et al.* Screening highly active perovskites for hydrogen-evolving reaction via unifying ionic electronegativity descriptor. *Nat. Commun.* **10**, 1–8 (2019).

111. Iglesias, D. & Melchionna, M. Enter the Tubes: Carbon Nanotube Endohedral Catalysis. *Catalysts* **9**, 128 (2019).

112. Wadge, M. D. *et al.* Developing highly nanoporous titanate structures via wet chemical conversion of DC magnetron sputtered titanium thin films. *J. Colloid Interface Sci.* **566**, 271–283 (2020).

113. Sun, H., Dai, J., Zhou, W. & Shao, Z. Emerging Strategies for Developing High-Performance Perovskite-Based Materials for Electrochemical Water Splitting. *Energy Fuels* **34**, 10547–10567 (2020).

Chapter 2. Theory and Techniques

2.1 Fundamentals of Electrochemistry

Electrochemistry is "the branch of chemistry concerned with the interrelation of electrical and chemical effects."[1] In this sense, either a chemical change brings about an electrical effect (as in a fuel cell) or an electrical input brings about a chemical change (as in an electrolyser). When carrying out an electrochemical measurement one can control or measure the electron flow of the system. When electrons transfer from the Fermi level of an electrode to the LUMO of a species, the species is said to be reduced. Conversely, when the electrons transfer from the HOMO of a species into the Fermi level of the electrode, the species is said to be oxidised. Schematically this is shown in Figure 2.1. The movement of the electrons is measured as a current. The position of the Fermi level is measured as a potential.

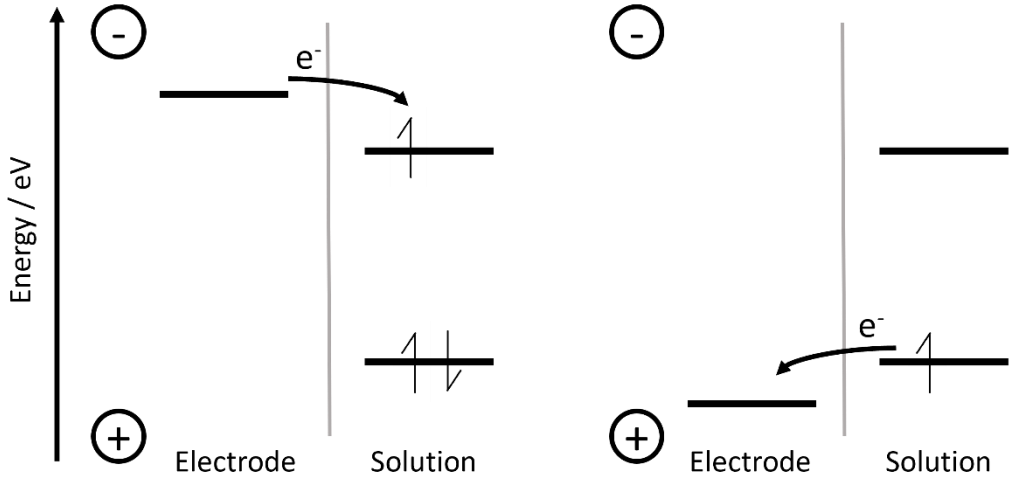


Figure 2.1 A schematic representation of a reduction (left) and an oxidation (right). The y-axis represents energy (eV). The single-headed arrows represent electrons moving from or to the fermi level of the electrode. The + and – represent the potential of the electrode. A more negative potential represents a higher electrochemical potential. Adapted from Bard and Faulkner.[1]

The current observed due to an electron transfer is known as Faradaic current. Non-Faradaic currents arise due to adsorption-desorption events at the electrode, which changes the electrode-solution interface. Of greatest relevance here is the case of the electrical double layer which is shown schematically in Figure 2.2 for the case of a negatively charged electrode. The double layer is so named for the distinct formation of an inner and an outer Helmholtz plane (IHP and OHP). The IHP forms at the centre of the charges of the solvent molecules oriented at the electrode surface and any specifically adsorbed desolvated ions.[1,2] The IHP effectively acts as the minimum distance a cation can approach a negatively charged electrode (or a positively charged electrode for an approaching anion), despite the opposite charges of the ion and electrode. A layer of solvated ions forms next to the IHP. The centre of these solvated ions is the OHP. Beyond the OHP, the solvent molecules and ions 'feel' the effect of the electrode less and so there is less orientation of these. The diffuse double layer extends out until its composition matches that of the bulk.[1]

No electrons pass from the electrode to the double layer (nor vice versa) in its formation. However, a current is still measured due to the redistribution of charge. In the context of the work presented in this thesis, the current that flows due to the formation of the double-layer capacitance is significantly smaller than the Faradaic currents that flow due to the HER, OER, or ORR. However, in systems with low concentrations of electroactive species the charging currents can be of similar (or greater) magnitudes to the Faradaic ones.[1] By measuring the non-Faradaic current that passes due to the charging of this layer, the electrochemical surface area (ECSA) can be determined as the contours of the double-layer will follow that of the electrode surface.[3]

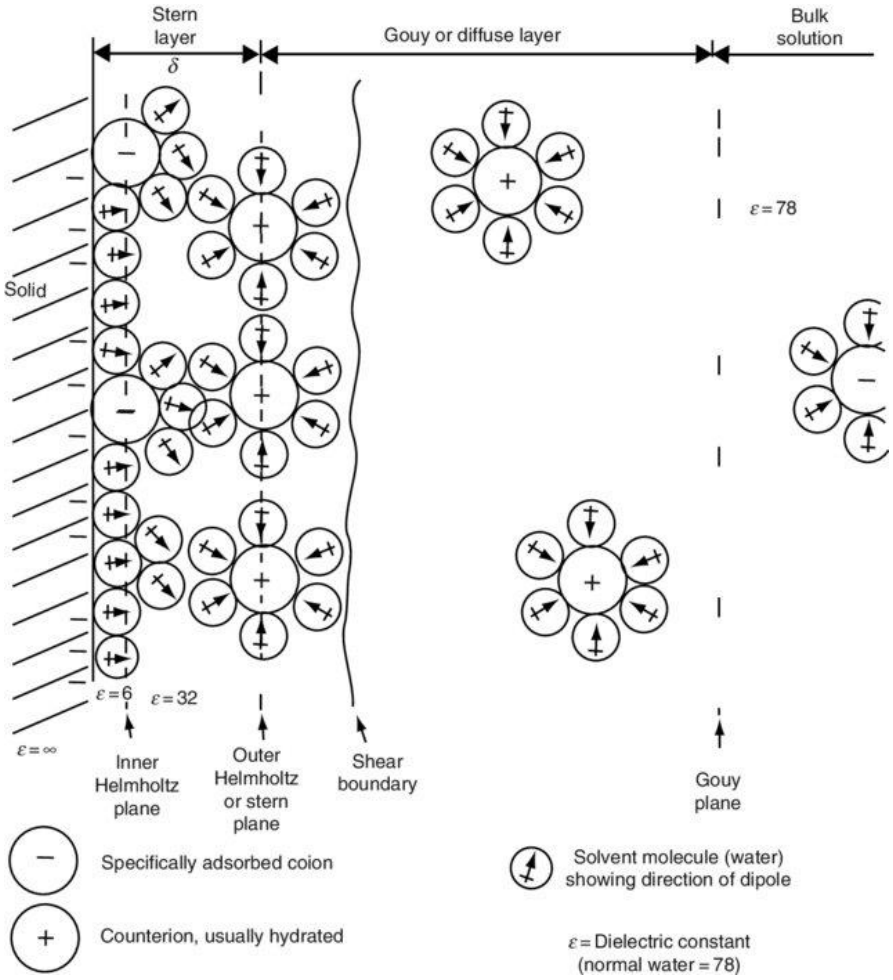


Figure 2.2 Schematic representation of the electrical double layer reproduced from Somasundaran et al.[4] *Solvent molecules electrostatically align at the electrode surface forming the IHP and solvated cations are attracted to the negative electrode forming the OHP. Beyond this a concentration gradient (diffuse layer) extends out to the bulk.*

The ability to accurately measure currents and potentials is a fundamental requirement for electrochemistry. The potential describes the driving force for a reaction. From a chemical perspective such driving forces are described by the chemical potential μ which is defined as

$$\mu_i = \mu_i^0 + RT \ln a_i \qquad [2.1]$$

In which a_i is the activity of the species *i.* The electrochemical equivalent of this is the electrochemical potential $\bar{\mu}$ which uses the following definition to account for the potential (ϕ) on a charged species *i*

$$\bar{\mu}_i = \mu_i + z_i F \phi \qquad [2.2]$$

Here z_i is the numerical charge of the species and F is the Faraday constant (96485 C mol^{-1}). Clearly, if one wishes to know the electrochemical driving force, then knowledge of the potential is required. The definition of the ϕ is the energy required to bring a unit positive test charge from infinity to the interface.[5] To measure this directly would require taking the measurement within a homogenous phase. However, this is impossible as to make the measurement necessitates creating a phase boundary at which to measure. For instance, to measure the potential of a solution would require introducing a metal|solution (where ϕ_m is the potential at the metal and ϕ_s is the potential at the surface) interface. The potential of the interface is given by

$$^{M}\Delta^{S}\phi = \phi_M - \phi_S \qquad [2.3]$$

The difference described in equation [2.3] is for the inner potentials: that is the transfer of charge from within one phase to within another. This difference can only be measured in the case of two identical phases in contact with each other.[6] Experimentally, it is only possible to measure the differences in the outer (or Volta) potentials from the surface of one phase to the surface of the next phase.[6] However, this brings up an obvious issue. If the potential of neither phase can be individually known, then taking the difference of the outer potentials provides no way to make comparisons. This leads to the requirement of a reference electrode.[1,2,5–7]

Clever experimental design allows the potential of one interface to be set as constant, and thus any measured changes ascribed to the interface of interest. The first requirement for such a setup is that the terminals be of identical composition. This is typically achieved through having copper metal connecting both the working (i.e., the electrode with the interface of interest) and reference electrodes to the measurement device (e.g., a voltmeter or potentiostat).[6] If the interface of the reference electrode in solution is at equilibrium and this equilibrium is not disturbed during the measurement then one could say that this potential is arbitrarily set to 0 V.[6,7] Thus, any measured potential is ascribed to the working electrode interface. Note that this is not

the same as saying the potential of the working electrode interface is known: it is not. Nor is there any thermodynamic or chemical meaning behind saying the reference interface is at 0 V. However, the usefulness here comes when the working electrode interface is changed, and the reference electrode interface remains in the same equilibrium as before. The difference in the two measured potential differences can be said to be the difference between the two different working electrode interfaces. And so, comparisons can be made between systems without ever needing directly measure the potential of any individual material.

The prototypical reference electrode is the standard hydrogen electrode (SHE). This is a platinised platinum flag submerged in an acid with a proton activity of 1 mol dm^{-3}. Over this flag hydrogen gas is bubbled at 1 atm. The Pt catalyses the defining equilibrium reaction: $2H^+ (aq) + 2e^- \rightleftharpoons H_2 (g)$. The equilibrium potential of this reaction is defined as 0 V in the defined conditions. A closely related reference system is the reversible hydrogen electrode (RHE). The equilibrium here is identical however, the restriction of the proton activity is lifted. The RHE equilibrium potential is defined as 0 V at all pH values. Thus, if 1 mol dm^{-3} HCl is used or 1 mol dm^{-3} KOH, the potential is still 0 V.[6,7]

The requirement of 1 atm of H_2 gas bubbling over a platinum flag makes this setup impractical for many experimental setups. For this reason, 'electrodes of the second kind' can be used.[7] These electrodes still have a well-defined equilibrium, but their potentials are defined against the SHE (or RHE). In this thesis, two reference electrodes of the second kind are used: Ag/AgCl (defined by [2.4][6]) and Hg/HgO (defined by [2.5][6]).

$$AgCl + e^- \rightleftharpoons Ag + Cl^- \qquad [2.4]$$

$$HgO + H_2O + 2e^- \rightleftharpoons Hg + 2OH^- \qquad [2.5]$$

All reference electrodes must meet the following criteria:[8]

1. Chemically and electrochemically reversible (Nernstian)

2. Must be ideally non-polarisable (potential constant with a small change in current)
3. Thermal coefficient of potential must be small.

Assuming the electrode meets those criteria, the theoretical potential can be calculated from the Nernst equation. This equation takes the form of [2.6], where C_R^* and C_O^* are the bulk concentrations of the reduced and oxidised species, respectively.[1]

$$E = E^0 - \left(\frac{RT}{nF}\right) \ln \frac{C_R^*}{C_O^*} \quad [2.6]$$

Using the Nernst equation, one can see that a unit change in pH results in a 59 mV change in the potential. If E^0 is known for a reference electrode vs SHE, the potential can be adjusted to be vs RHE using that relationship.

Better still, the potential of a reference electrode used in an experiment should be experimentally measured vs a lab-made RHE. Alternatively, a sealed RHE unit with a hydrogen cartridge can be used as a portable RHE. In this thesis both lab made and portable RHEs from Gaskatel are used. Experimentally measuring the reference potential is preferable to using literature values for the equilibrium potential and using the Nernst equation to adjust for pH as non-idealities in the reference electrode and inaccurate assumptions about the pH could lead to the used reference potential being significantly different to the actual reference potential.[9]

For the second requirement, all reference electrodes should be able to withstand a small change in the current passing through them. But large currents will adjust the equilibrium making the reference electrode potential change. For this reason, in electrochemical setups a counter electrode is used.[5] The current flows between the working and counter electrodes meaning no current needs to flow through the reference electrode. In reality, the measurement of the potential requires a small current to flow, but this is sufficiently small to not affect the potential. Further details on the use of a

counter electrode are given in the next chapter. The use of a working, reference, and counter electrode is known as a three-electrode setup. [5]

When using a three-electrode setup, the electrolyte and electrode interfaces each have a resistance. This will lead to a drop in the measured potential.[10–12] Accounting for this is known as iR-compensation and is carried out automatically following the method set out by He and Faulkner.[12] The resistance of the system is initially measured at a potential at which there are no Faradaic processes occurring. The potentiostat applies a 50 mV step around this potential and measures the current response over a short span of time. Through the simple V = iR relationship, the resistance is then calculated.[12] The level of compensation applied is 85% for all experiments in this thesis. Total, or near total, compensation is not applied as this can lead to potentiostat oscillations.[12,13]

The Nernst equation is the fundamental thermodynamic relationship in electrochemistry. A system is said to be under Nernstian control when it follows the relationship. This will be true when the system is in equilibrium. If the system is significantly perturbed towards an oxidation or reduction reaction, then the Nernst equation is no longer valid.[1]

2.2 Electrode Kinetics

The measurement of potential can generally be considered a measurement of the thermodynamic properties of a system: how much energy is required to cause an oxidation or a reduction. The measurement of current, on the other hand, provides information about the kinetics of a system.

The current density is directly proportional to the rate of the reaction taking place at a given interface.[5] The amount of energy beyond the equilibrium potential that is applied is known as the overpotential η.

The relationship between the applied overpotential and the kinetics of the reaction (and thus the current) is described by the Butler-Volmer equation [2.7].[1]

$$i = FAk^0\left[C_O(0,t)e^{-\alpha f\eta} - C_R(0,t)e^{(1-\alpha)f\eta}\right] \text{ where } f = \frac{F}{RT} \qquad [2.7]$$

Here, A is the area of the electrode, k^0 is standard rate constant, and η is the overpotential. In this equation, α is the electron transfer coefficient and represents the symmetry of the reaction. When α = 0.5, the reduction and oxidation reactions are equally far apart from the transition state along the reaction coordinate. It is often assumed that this is the case.[1]

The Butler-Volmer equation is true across all overpotentials and at equilibrium, though strictly only for simple 1 electron processes.[1,14] However, it can be simplified. When the overpotential is sufficiently positive or negative, either the reduction or oxidation term can be eliminated. Rearrangement then leads to the Tafel relationship:[14]

$$\eta = a + b\log j \qquad [2.8]$$

A plot of overpotential against the log of the current density. The slope b gives information about the rate determining steps of the reaction due to the inclusion of α (equation [2.9])[15]. However, it should be noted that the α in the Tafel equation is only equivalent to that in the Butler-Volmer equation for simple electrochemical reactions.[14]

$$b = \frac{2.3RT}{\alpha F} \qquad [2.9]$$

The intercept of a Tafel slope, *a*, is the log of the current at zero overpotential. This current is the exchange current and is the current that flows in the absence of net electrocatalysis.[16] It is important to use iR-compensated measurements when carrying out Tafel analyses for the underlying Butler-Volmer theory to be valid.[16] Details of the use of the Tafel slopes are given in the chapters where relevant.

2.3 Mass Transport Considerations

Any current that flows is related to the flux of reactants and products to and from the electrode surface. This allows the current to be broken down into three constituent parts: diffusion, convection, and migration.[1] In strong acids

and bases, migratory currents can be neglected. In less conductive solvents, supporting electrolyte is added to negate this contribution to the current density. In stationary systems, the experiments must be done over short enough time scales that thermally convective flows do not influence the measurement. This results in only diffusive currents being of concern, and so the previously discussed equations can be used, and diffusion properties be calculated.

However, convection currents can be used to discern further information about the system. The convection can be carefully controlled by rotating the electrode at defined rotation rates. There will be no depletion of the analyte, as the rotation leads to a laminar flow of reactant and product to and from the electrode surface. Material from the bulk (which is rotating from the perspective of the electrode) enters into a stagnant region close to the electrode surface known as the hydrodynamic layer, δ_H. Once in this layer, the final movement of the material to the electrode is through diffusion. The size of this layer is proportional to the square root of the rotation rate, ω, and depends on the kinematic viscosity, ν, of the liquid as well as the diffusion coefficient of the analyte in the electrolyte, D_O, and its bulk concentration, C_O.[1]

By varying the rotation rate of the electrode, the rate of flux of material to the electrode is also changed and so the current varies. A plot of the square root of rotation rate against the measured current is known as a Levich plot, the slope of which is defined by equation [2.10], where A is the geometric surface area of the electrode, n is the number of electrons transferred, and F is Faraday's constant.[1]

$$i_L = 0.620nFAD_O^{2/3}\nu^{-1/6}\omega^{1/2}C_O \qquad [2.10]$$

This equation is only valid for kinetically facile reactions, whereby the measured current equals the Levich current. In the case of slower reactions such as those studied in this thesis, Koutecký–Levich analysis is used instead. This is given by the following equation:

$$\frac{1}{i} = \frac{1}{i_k} + \frac{1}{i_L} \qquad [2.11]$$

Where i is the measured current, i_k is the kinetic current and i_L is the Levich current. The kinetic current is the current that would flow if the electrode rotated with infinite rotation rate (and thus have an infinite rate of mass transfer to and from the electrode surface). For reactions that follow the Levich equation, this current is infinite as kinetics never limit the reaction. For every other reaction, the kinetic current will have a finite value and is an indicator of the kinetics of the reaction. The inverse of the current against the inverse square root of the rotation rate gives K-L plot. The gradient of this plot is the inverse Levich current and can be used to determine the number of electrons transferred, n, assuming all other constants are known.[1,2]

The currents used in Levich and K-L analyses are governed by mass transport. This is related to the hydrodynamic layer, the cross-sectional area of which is given by the geometric area of the electrode. As such, this should be used as the area, A when carrying out and presenting Levich and K-L analyses. The kinetic current, however, relates to electron transfer dynamics.[17] This is affected by the specific surface area and so the kinetic current can be normalised to the ECSA as opposed to the geometric area after the analyses are carried out.

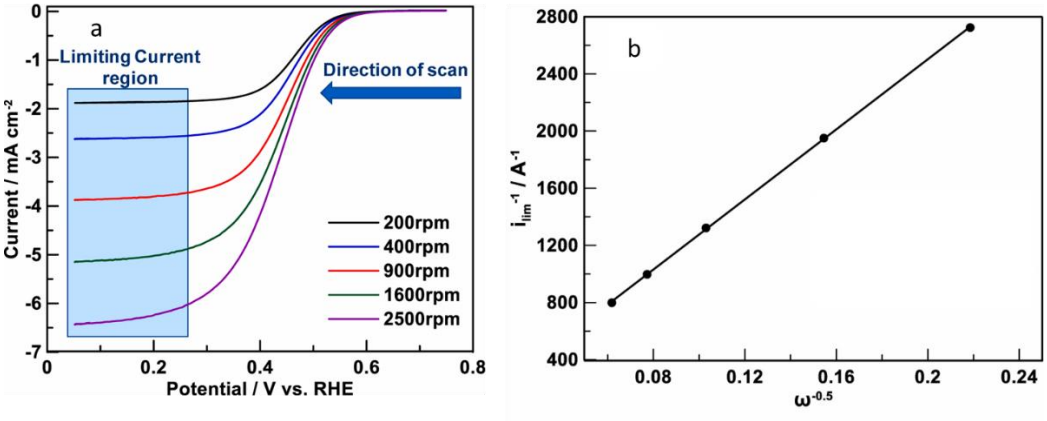


Figure 2.3 An example of a K-L study in which RDE voltammograms were measured at various rotation rates (a). In (b) the inverse of the current (in A) at a particular potential (0.1 V) from the plateau region is plotted against the inverse rotation rate (in rad s^{-1}). The slope in (b) is the inverse of the Levich current. Reproduced from Fruehwald et al.[18]

An underlying assumption of the K-L analysis is that the electrode has a flat geometry. However, in the field of electrocatalysis electrodes are typically coated with the electrocatalyst of interest. Especially, when these are supported on high surface area carbon materials, the real surface area can be greater than that of the geometric area of the electrode. Additionally, the coating will have a three-dimensional structure which can interfere with the mass transport of reactants and products. Studies by Masa *et al*[19] and Ward *et al*[20,21] have investigated the significance of this. They found that high surface areas relative to the geometric area shifts the kinetic-controlled region of the RDE voltammogram positive, giving the appearance of better kinetics. As such, it is recommended that the kinetic parameters not be extracted through K-L analysis in these cases.[19,20] However, Masa *et al* note that the plateau remains unchanged and thus extraction of properties such as the electron transfer number, n, as described previously is still valid.[19]

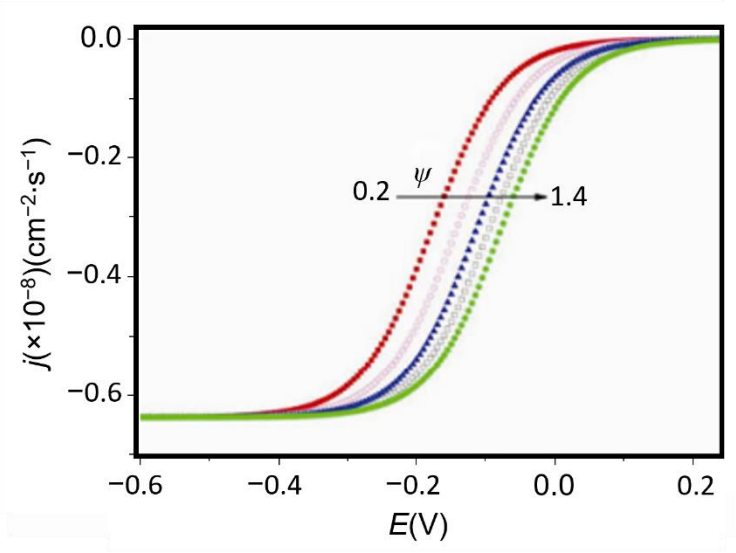


Figure 2.4 Theoretical RDE voltammograms for oxygen reduction with varying real surface areas. $\psi = \frac{A_{real}}{A_{geo}}$ *Increasing values of ψ leads the electrocatalyst appearing more active (shift to more positive currents) despite no changes to the intrinsic activity. Reproduced from Masa* et al.[19]

2.4 Theory of Electrocatalysis

Overall, electrolysing water is an inefficient process. At the cathode is a 2-electron reaction (hydrogen evolution, HER) and at the anode is a 4-electron process (oxygen evolution, OER). Neither of these occur at a significant rate at the thermodynamic voltage, and so an overpotential must be applied. A simplified view of the various losses that lead to an overpotential for an overall electrolysis cell is presented in Figure 2.5 (left). Below 1.23 V the electrolysis of water is thermodynamically unfavourable, and so is the absolute minimum potential required to drive the reaction. The activation region represents losses associated with the formation of intermediates associated with the rate determining step (RDS) of the reaction. For example, in an alkaline electrolyser, this could be the adsorption of OH^- onto the anode surface, or the dissociation of water at the cathode. Losses in the ohmic region result from the summation of the various resistances associated with the electrolyser construction such as the conductivity of the electrodes and current collectors, formation of bubbles, and the conductivity of the electrolyte and membrane (or diaphragm). Beyond the ohmic region are losses associated with mass transport limitations, referred to as concentration overpotentials. These occur when the rate of gaseous product formation is faster than the removal of the product.[22]

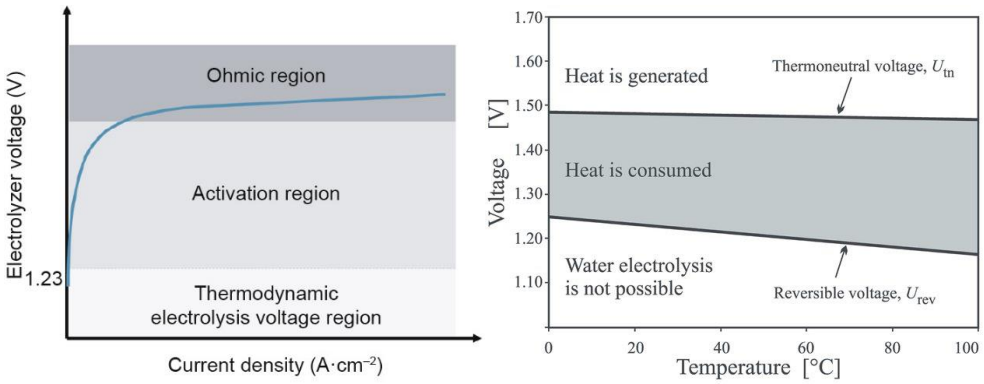


Figure 2.5 (Left) Losses within an electrolysis cell are associated with activation and resistances within the cell. Figure reproduced from Peng et al.[23] *(Right) The variation of the reversible voltage with temperature for the electrolysis of water. The thermoneutral voltage is nearly constant for all temperatures. Reproduced from Mori* et al.[24]

Although electrolysis thermodynamically occurs at 1.23 V (under standard conditions) it initially proceeds endothermically. This means heat from the environment must be consumed for the reaction to proceed isothermally. At atmospheric pressures, the thermoneutral voltage for water-splitting is 1.48 V (the thermoneutral voltage is only slightly dependant on temperature).[25] Above this voltage, the electrolysis is exothermic and so heat must be removed from the system in order to be isothermal. Given the high overpotentials that electrolysers typically operate at, it can be assumed the electrolysis occurring will be exothermic and that heat management systems must be deployed to remove the excess heat generated.

Within the context of lab-scale research, the various losses and heat management systems are too complicated and interconnected to optimise as a whole. As such, the problem can be broken down into its constituent parts. This thesis is preoccupied with minimising the losses within the activation region by enhancing the activity of the electrocatalysts on which the OER, ORR and HER occur. The following two sections break down these reactions into their elementary steps.

2.4.1 Hydrogen Evolution Reaction

The HER is the faster of the two reactions involved in water-splitting. This is due to it only requiring the transfer of two electrons per hydrogen molecule (in contrast to the four electrons required for the OER). These two electron transfers take place through elementary steps, the nature of which depends on the pH of the system. These are described below and summarised in Table 2.1.

*Table 2.1 The elementary steps and overall reaction for the hydrogen evolution reaction in acidic and basic electrolytes. An asterisk * denotes a surface site on the electrocatalyst.*

Step	Acid	Alkaline and neutral
Volmer	$H^+ + e^- + * \rightarrow H^*$	$H_2O + e^- + * \rightarrow H^* + OH^-$
Heyrovsky	$H^+ + e^- + H^* \rightarrow H_2 + *$	$H_2O + H^* + e^- \rightarrow H_2 + OH^- + *$
Tafel	$H^* + H^* \rightarrow H_2 + 2*$	$H^* + H^* \rightarrow H_2 + 2*$
Overall	$\mathbf{2H^+ + 2e^- \rightarrow H_2}$	$\mathbf{2H_2O + 2e^- \rightarrow H_2 + 2OH^-}$

In acidic electrolytes, a proton adsorbs onto a vacant active site on the electrocatalyst surface (Volmer step). Another proton can then react with this to form H_2 (Heyrovsky step). Alternatively, a second proton can adsorb onto an adjacent active site and then these two adsorbed intermediates chemically react to form H_2 (Tafel step).

In basic electrolytes, H_2O must first dissociate leaving an adsorbed H intermediate (Volmer). The Heyrovsky step requires that intermediate to interact with an aqueous proton to form H_2 and OH^-. Similarly to the acidic case, there can be a second Volmer step followed by a chemical Tafel step.

Depending on the last step, HER mechanisms are categorised as either Volmer-Heyrovsky or Volmer-Tafel. Historically, the HER is one of the most studied reactions with Julius Tafel proposing the Tafel step as far back as 1905.[26] Despite this, there is still debate as to the precise mechanism on various electrocatalyst surfaces.

Given that the HER involves intermediates adsorbing onto a vacant active site on the electrocatalyst surface, it is thus described as an inner-sphere reaction. As such, one of the main focuses in electrocatalyst design is the optimisation of the interaction between the surface and the intermediates. An ideal electrocatalyst will neither bind the intermediate too strongly nor too weakly, as per the Sabatier principle. This relationship manifests as a volcano-style plot, in which the energy of intermediate adsorption is correlated to some kinetic parameter associated with the reaction.

For the HER, the adsorption is described by ΔG_{H^*} (the free energy of adsorption of H onto a vacant site) and the exchange current density of HER. The latter was popularised by Trasatti and co-workers in 1972,[27] though this relationship has been discussed in the literature for far longer.[28] A more complete description of its relation to ΔG_{H^*} was further described by Nørskov and co-workers in 2005 in what is considered a seminal text on the topic.[29] Nørskov and co-workers described an ideal HER electrocatalyst (that is, one with the highest exchange current density) as being thermoneutral across the full reaction. So, $\Delta G_{H^*} = 0$

meaning there is neither an energy barrier to adsorbing the intermediate nor for its desorption. In cases where $\Delta G_{H^*} \ll 0$ eV, the hydrogen will readily adsorb onto the electrocatalyst surface (i.e., the Volmer step is fast), but there is a large energy barrier to its desorption making the Heyrovsky or Tafel step(s) rate limiting. Conversely a $\Delta G_{H^*} \gg 0$ eV would make the Volmer step rate limiting due to the unfavourable interaction between the electrocatalyst surface and the hydrogen intermediate, though the second step would be quick. In this sense, Pt is close to ideal with only a small deviation from thermoneutral binding of intermediates as shown in Figure 2.6. Likewise, this figure suggests Au has too high a free energy change, whereas Mo and Ni are too low. Given the mechanism of the HER, ΔG_{H^*} is the only adsorption energy of interest. As such, this free energy is used as the *x*-axis of the volcano in Figure 2.7.

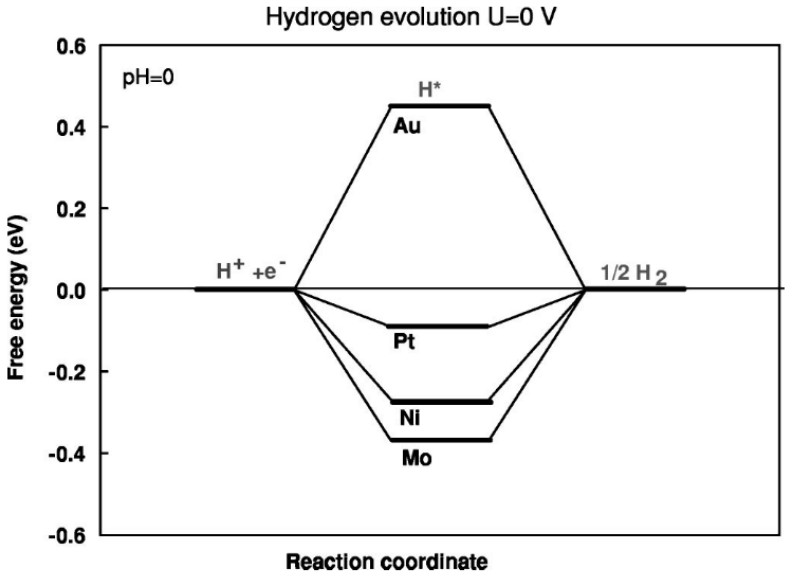


Figure 2.6 Free energy diagram for the HER at equilibrium at pH = 0 and T = 300 K for metallic Au, Pt, Ni, and Mo. Free energies are given at θ = ¼. Figure reproduced from Nørskov et al.[29]

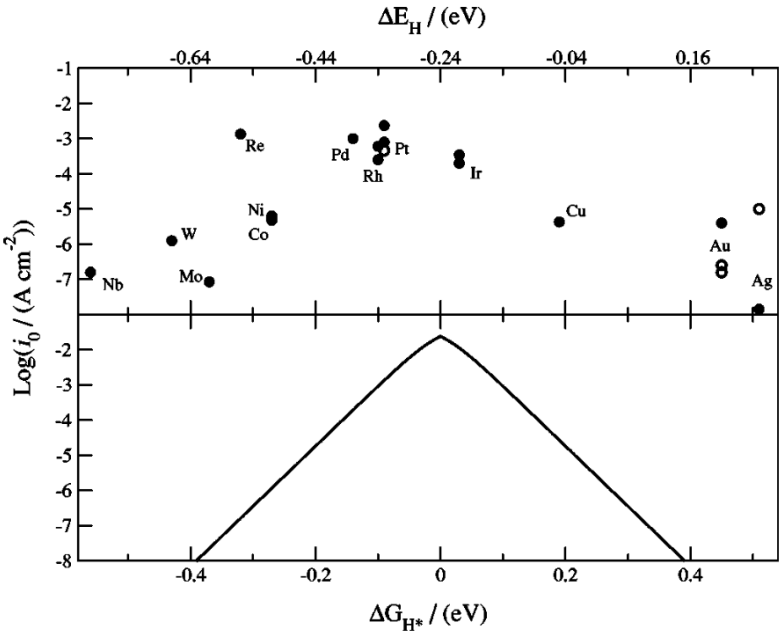


Figure 2.7 Experimental exchange current densities against the theoretically determined ΔG_{H^*}, with the approximate volcano shape shown at the bottom. Reproduced from Nørskov et al.[29]

A description of an ideal HER electrocatalyst was given by Santos and co-workers in 2012. They used a combination of DFT and electron transfer theories to elucidate three key properties:[30]

1. $\Delta G_{H^*} \approx 0$ eV (at pH 0)
2. The d-band of the electrocatalyst should span the Fermi level
3. The d-band of the electrocatalyst should interact strongly with the 1s orbital of hydrogen.

In base and neutral media, the mechanism for the HER is more complicated; water must first dissociate at the electrocatalyst surface. As such a bifunctional mechanism is proposed, in which water adsorbs to the surface and is dissociated leaving an HO* which must subsequently desorb.[31,32] For this reason there is a significant reduction in the kinetics of the HER in basic or neutral electrolytes versus acidic ones. In base, the source of protons to eventually form hydrogen is water as opposed to the hydronium ion (which readily gives up its proton). For this reason, in basic electrolytes an additional two properties should be considered for rational electrocatalyst design:

4. Good water dissociation ability

5. Optimal OH^- desorption energies

The exact quantification of these parameters is up for debate, though their applicability is well-known.[32]

Thus far, the discussion has focused on metallic electrocatalysts. This thesis focuses on the use of metal oxide-based electrocatalysts. The 5 properties described above for good electrocatalysts are still valid for oxide-based electrocatalysts.[33] However, the active sites are no longer necessarily metallic, and so the elementary steps presented in Table 2.1 may occur on either metallic or oxide sites. The elementary steps for the HER as they pertain to an oxide system is shown in Figure 2.8.

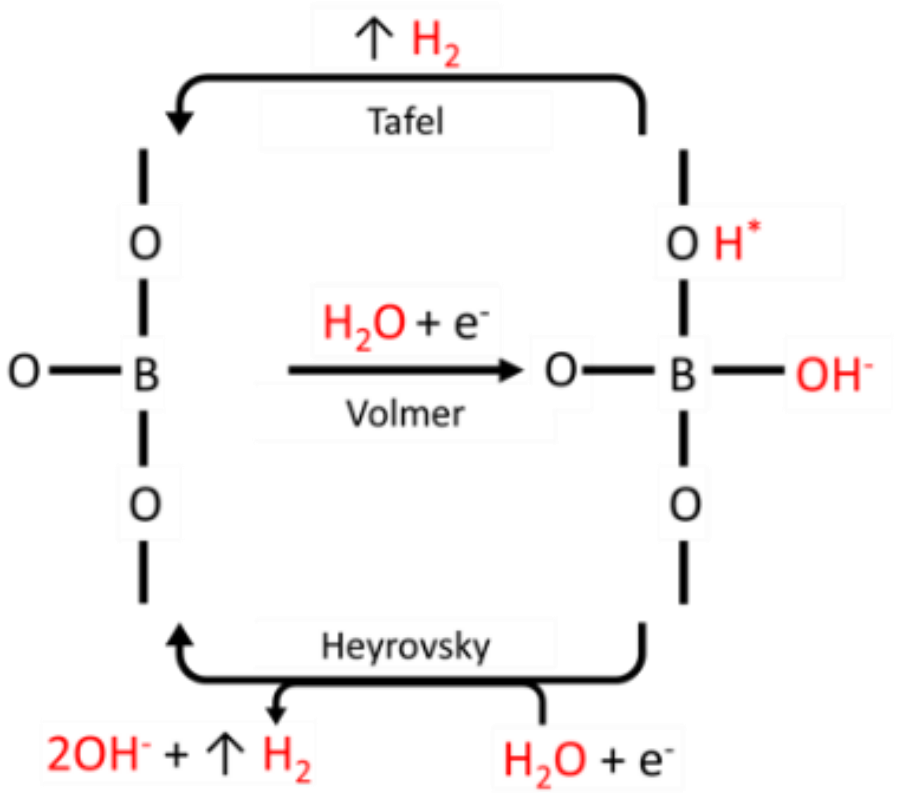


*Figure 2.8 HER mechanism in basic conditions as proposed by Xu[34] and Zhu[35]. Species from the perovskite lattice are in black and from the electrolyte are in red. B = transition metal, * refers to adsorbed species. In this example adsorption of H to a lattice oxygen site is more favourable than adsorption onto the metal.*

In basic conditions, oxygen vacancies in the oxide structure can assist with the dissociation of H_2O.[36] The oxygen in the lattice structure of an oxide electrocatalyst can participate in the HER by adsorbing a proton (the Volmer step), [34–37] whereas the metal cation can adsorb the OH^-.[34] In contrast to the mono-metallic materials described previously, an oxide effectively has two active sites in close proximity to each other.[36]

2.4.2 Oxygen Evolution and Reduction Reactions

The OER and ORR are far more complicated reactions than the HER. This is mainly due to the requirement of a concerted transfer of 4 electrons (as opposed to 2 for the HER). However, the theory developed for the HER is still a strong starting point for discussion of the OER and ORR.

The ORR has two possible routes. There is the dissociative route which involves 2 two-electron (2x2) steps and an associative route which involves 4 one-electron (4x1) steps.

The 2x2 mechanism proceeds as follows (* represents a catalytic site):[38–40]

$$O_2 + 2* \rightarrow 2O* \quad [2.12]$$

$$2O* + 2H^+ + 2e^- \rightarrow 2OH* \quad [2.13]$$

$$2OH* + 2H^+ + 2e^- \rightarrow 2H_2O + 2* \quad [2.14]$$

Alternatively, the 4x1 pathway proceeds as:

$$O_2 + * \rightarrow O_2* \quad [2.15]$$

$$O_2* + H^+ + e^- \rightarrow OOH* \quad [2.16]$$

$$OOH* + H^+ + e^- \rightarrow O* + H_2O \quad [2.17]$$

$$O* + H^+ + e^- \rightarrow OH* \quad [2.18]$$

$$OH* + H^+ + e^- \rightarrow H_2O + * \quad [2.19]$$

Regardless of which pathway is followed, the strength of the oxygen-catalyst interaction is of great importance. Pt/C is generally considered the best electrocatalyst for the ORR, and Ir- and Ru-based electrocatalysts for the OER. For an electrocatalyst to have good activity for the ORR the strength of the O—

catalyst interaction must be sufficiently strong that it is stable, but not so strong that the proton-transfer steps are slow.

Nørskov *et al* constructed a free-energy diagram from DFT calculations of the dissociative 2x2 mechanism for three different metals (Figure 2.9).[40] From the diagram, it can be seen that Ni binds very strongly with O and OH. This means the initial step is extremely rapid, but the proceeding proton transfer steps are slow due to the highly endothermic nature of those steps.[40]

The reverse is true for Au. The proton transfer steps are favourably exothermic, however the activity is low due to activation energy of the Au—O bond formation.[40] Contrast these to Pt which has favourable Pt—O bond formation (though not as strong as that for Ni) and a small energy barrier for the proton transfer steps. The free energy of the oxygen binding is therefore a good predictor of catalytic activity.

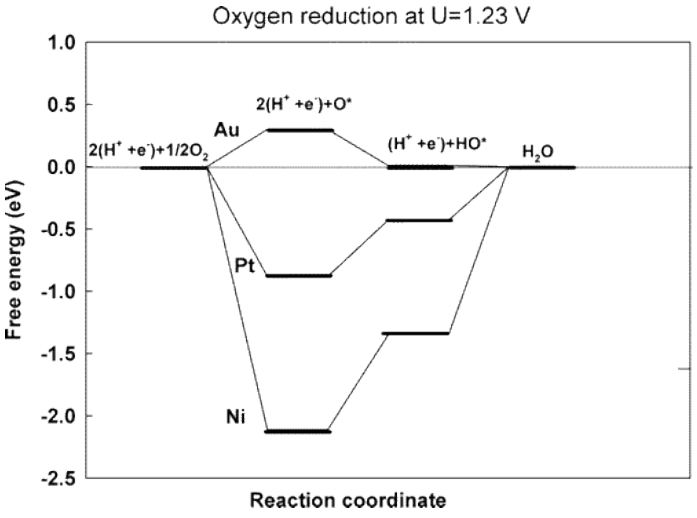


Figure 2.9 Free energy diagram of ORR for Pt, Au and Ni. Reproduced from Nørskov et al.[40]

Volcano plots of the activity (often indicated by the overpotential η needed to produce a specific current density) versus the binding energy of oxygen to the surface (ΔE_O) or the difference between the energies of O binding and OH binding ($\Delta G_{O*} - \Delta G_{OH*}$) can be generated. This relationship is expected as per the Sabatier Principle as described for the HER.

It has been observed that the stability of O* correlates strongly to OH* so either can be used as an indicator of activity.[38,40–42] Indeed, the ΔE of any of the intermediate states (OOH*, OH* or O*) are strongly correlated to activity due to the scaling relationship that exists between the intermediate states. In an ideal situation there would be no energy difference between the intermediate states of the OER reaction as this would mean spontaneous transitions between states. However, as outlined by Hong *et al* in their review, the energies of the intermediate states are strongly correlated: ΔE_{OOH*} is correlated to ΔE_{OH*} in a 1:1 relationship with a difference of ~3.2-3.4 eV, whilst ΔE_{O*} is correlated by 2:1 relationship with the states.[41] This means that there will always be a non-zero difference between the lowest and highest energy intermediates. This scaling relationship is also a major issue for the OER as the reaction intermediates are similar.[43,44] The result is that there is a minimum overpotential of at 300 – 400 mV in the reduction of oxygen to bring about the evolution of oxygen.[43]

Oxide-based electrocatalyst materials follow the same elementary steps as for the metallic case[45,46] but are not restricted in the same way that mono-metallic electrocatalysts are. Work from Man *et al* showed that the scaling relationship still holds in oxides.[46] However, unlike in the purely metallic case, some oxides can overcome the scaling relationship,[43,45,47] so long as the structure allows for two active sites in close proximity.[45] Given that a single active site cannot be optimised beyond the limits of the scaling relationship, one strategy is to introduce more types of active site into the same electrocatalyst. For example, Shen *et al*, designed a SnO_x/Pt-Cu-Ni composite electrocatalyst. *OOH forms on the tin oxide, whereas the adjacent Pt is active towards the proceeding steps. Once *OOH forms, it transfers across to the locally adjacent Pt site for the next steps.[47]

Volcano plots for the activity of oxide based electrocatalysts for the OER can be produced as shown in Figure 2.10. Although Pt-, Ru- and Ir-oxides are present towards the top of the plot, so too are oxides containing more abundant elements such as Co and Ni.

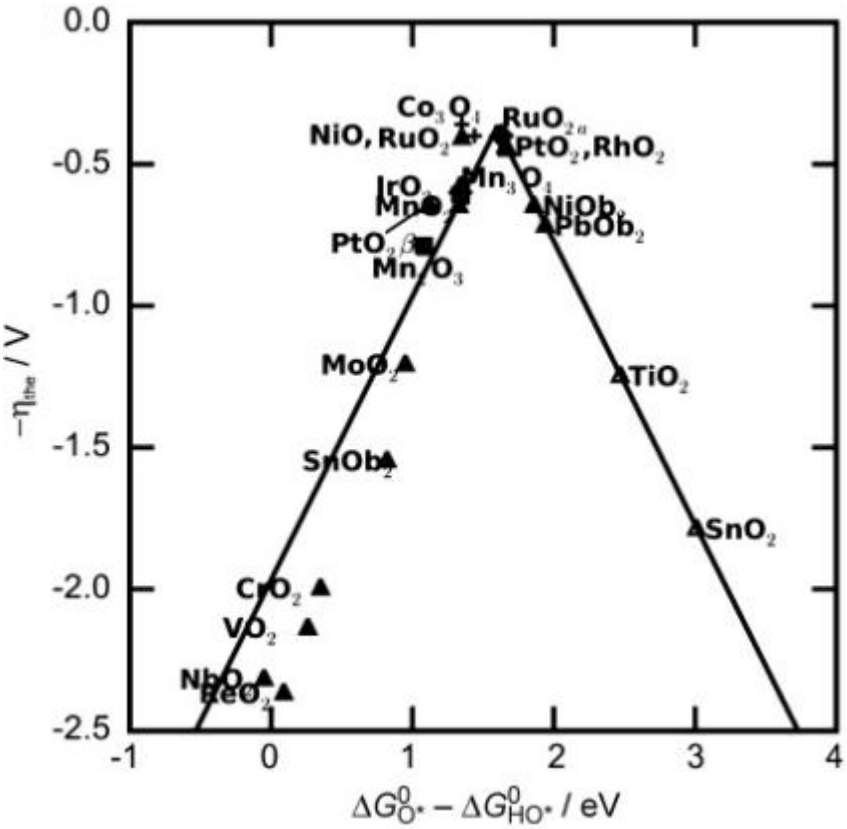


Figure 2.10 Volcano plot for a selection of oxide-based electrocatalysts shows $-\eta_{the}$ against $[\Delta G_{O^*} - \Delta G_{HO^*}]$. η_{the} is the theoretical overpotential. Reproduced from Man et al.[46]

There have been several proposed mechanisms by which the OER can take place on an oxide-based electrocatalyst.[47–51] For example, the OER can be mediated by the redox reactions of the adsorbed species in the so-called adsorbate evolution mechanism (AEM). Alternatively, the OER can involve oxygen atoms in the oxide lattice (lattice oxygen mediated, LOM). Both mechanisms can be observed in perovskite oxides and are represented in Figure 2.11.[48,50,52] In the case of the AEM, the resultant O_2 evolved is entirely derived from oxygen atoms which were previously in the electrolyte. However, with the LOM mechanism one of the oxygen atoms in the resulting O_2 is from the oxide lattice.[48]

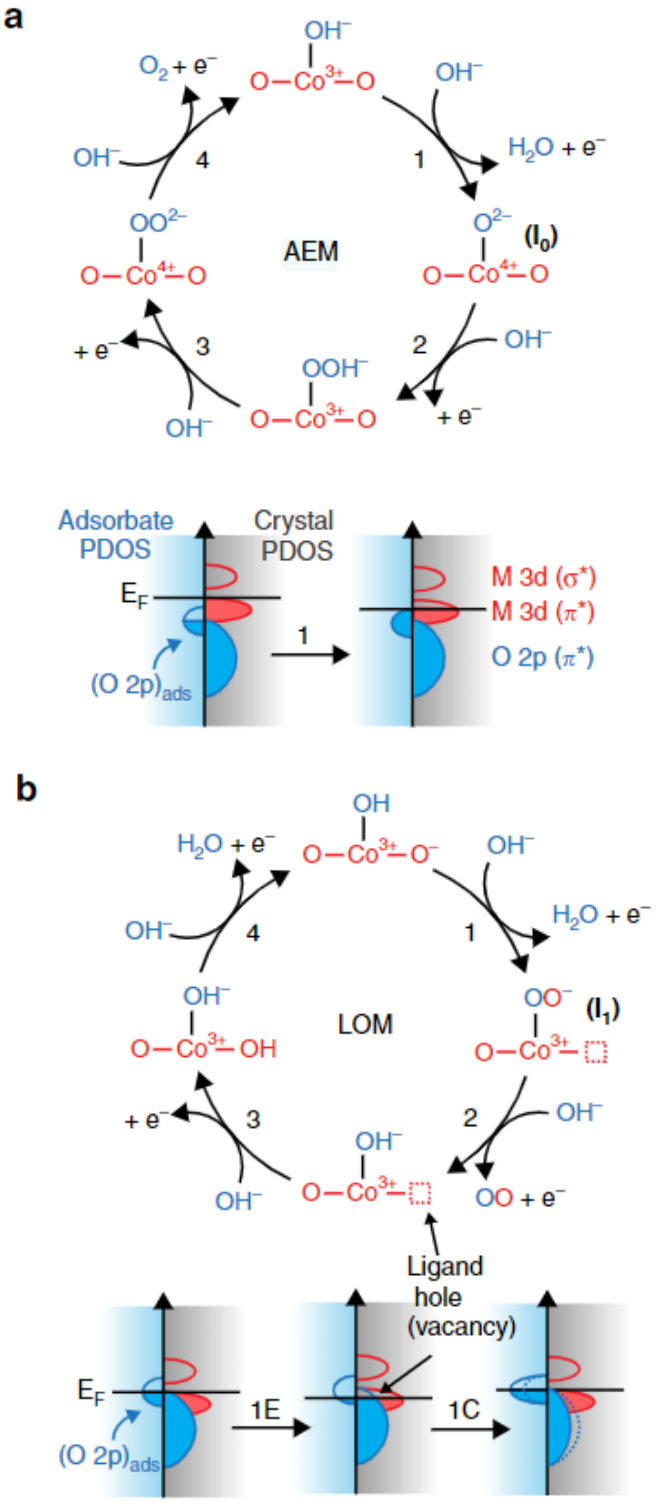


Figure 2.11 Schematics of the a) general adsorbate evolution mechanism (AEM) and b) lattice-oxygen mediated mechanism (LOM for the OER). Red and blue atoms are from the lattice and solvent, respectively. In this example the metallic cation within the oxide is Co. Reproduced from Mefford et al.[48]

A similar mechanism to the AEM for the OER has been proposed for the ORR at oxide electrocatalysts. Using a perovskite oxide as an example, Figure 2.12 shows that the intermediates for the ORR at an oxide are similar to those for the OER.[53] This mechanism can be considered to hold for the more general metal oxide case.[54] Given that the intermediates are similar, the ideal parameters for an OER and ORR electrocatalyst may, too, be similar. Indeed, this was observed by Suntivich *et al* who proposed that the filling of the e_g orbital of the was a useful predictor for activity both for the OER[50] and the ORR[53]. An e_g orbital with 1 electron has been deemed close to ideal. Slight differences were observed between the OER and ORR, however, with the work by Suntivich *et al* showing that an average e_g orbital filling of just under 1 electron was ideal for the ORR and just over 1 was ideal for the OER, resulting in the volcano plots shown in Figure 2.13.[50]

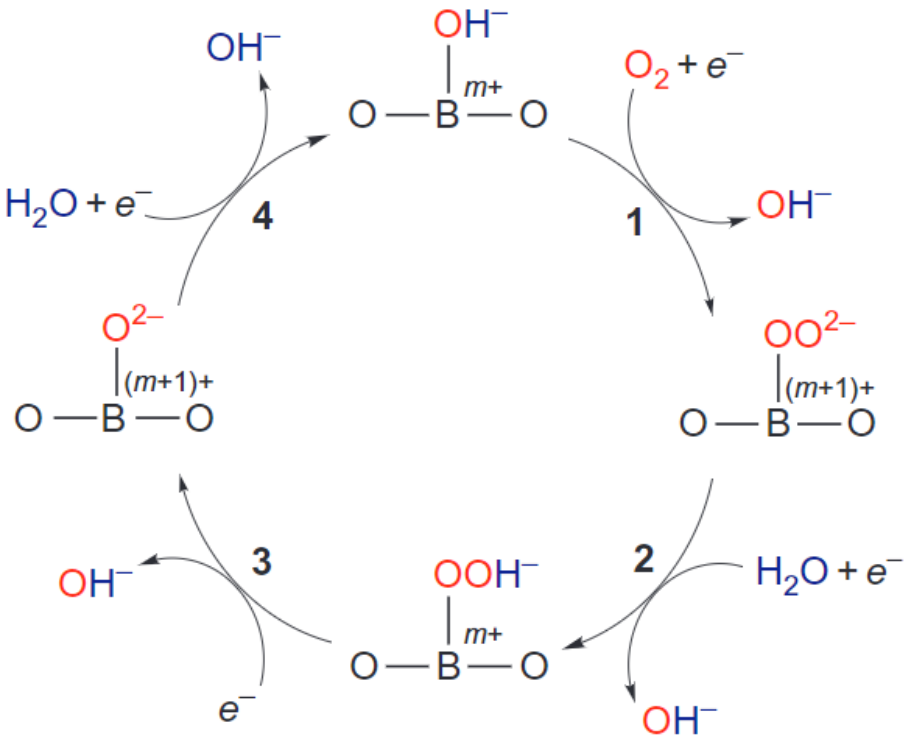


Figure 2.12 ORR mechanism at a perovskite oxide electrocatalyst. Red atoms represent atoms belonging to the oxide lattice. Blue atoms belong to the electrolyte. B = transition metal. Reproduced from Suntivich et al.[53]

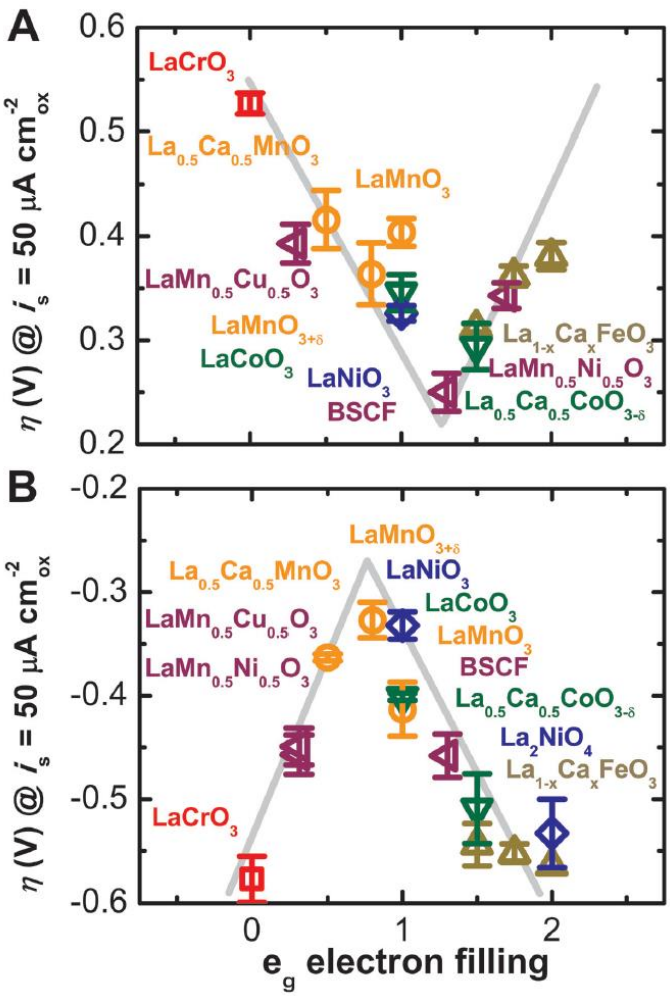


Figure 2.13 Volcano plots showing the overpotential vs *the e_g occupancy for the (A) OER and (B) ORR. Reproduced from Suntivich et al.*[50]

2.5 References

1. Bard, A. J. & Faulkner, L. R. *Electrochemical Methods*. (John Wiley & Sons, Inc., 2001).

2. Hamann, C. H., Hamnett, A. & Vielstich, W. *Electrochemistry*. (Wiley-VCH, 2007).

3. Ott, S. *et al.* Seven steps to reliable cyclic voltammetry measurements for the determination of double layer capacitance. *J. Phys. Energy* **3**, 034013 (2021).

4. Somasundaran, P., Mehta, S. C., Yu, X. & Krishnakumar, S. Colloid Systems and Interfaces Stability of Dispersions through Polymer and Surfactant Adsorption. in *Handbook of Surface and Colloid Chemistry, Third Edition* (ed. Birdi, K. S.) 155–196 (CRC Press, 2008).

5. Gileadi, E. *Physical Electrochemistry: Fundamentals, Techniques and Applications*. (Wiley-VCH, 2011).

6. Inzelt, G., Lewenstam, A. & Scholz, F. *Handbook of Reference Electrodes*. (Springer, 2013).

7. Ives, D. J. G. & Janz, G. J. *Reference electrodes, theory and practice*. (Academic Press, 1961).

8. Kahlert, H. Reference Electrodes. in *Electroanalytical Methods* 261–278 (Springer Berlin Heidelberg, 2005).

9. Niu, S., Li, S., Du, Y., Han, X. & Xu, P. How to Reliably Report the Overpotential of an Electrocatalyst. *ACS Energy Lett.* **5**, 1083–1087 (2020).

10. Heenan, A. R., Hamonnet, J. & Marshall, A. T. Why Careful iR Compensation and Reporting of Electrode Potentials Are Critical for the CO_2 Reduction Reaction. *ACS Energy Lett.* **7**, 2357–2361 (2022).

11. Anantharaj, S. & Noda, S. iR drop correction in electrocatalysis: everything one needs to know! *J. Mater. Chem. A* **10**, 9348–9354 (2022).

12. He, P. & Faulkner, L. R. Intelligent, Automatic Compensation of Solution Resistance. *Anal. Chem.* **58**, 517–523 (1986).

13. Zheng, W. iR Compensation for Electrocatalysis Studies: Considerations and Recommendations. *ACS Energy Lett.* **8**, 1952–1958 (2023).

14. Shinagawa, T., Garcia-Esparza, A. T. & Takanabe, K. Insight on Tafel slopes from a microkinetic analysis of aqueous electrocatalysis for energy conversion. *Sci. Rep.* **5**, 1–21 (2015).

15. Fang, Y. H. & Liu, Z. P. Tafel Kinetics of Electrocatalytic Reactions: From Experiment to First-Principles. *ACS Catal.* **4**, 4364–4376 (2014).

16. Anantharaj, S. & Noda, S. How properly are we interpreting the Tafel lines in energy conversion electrocatalysis? *Mater. Today Energy* **29**, 101123 (2022).

17. Chen, W. *et al.* Quantifying intrinsic kinetics of electrochemical reaction controlled by mass transfer of multiple species under rotating disk electrode configuration. *J. Electroanal. Chem.* **872**, 114042 (2020).

18. Fruehwald, H. M., Zenkina, O. V. & Easton, E. B. A new spin on electrochemistry in the undergraduate lab. *Chem. Teach. Int.* **4**, 23–37 (2022).

19. Masa, J., Batchelor-McAuley, C., Schuhmann, W. & Compton, R. G. Koutecky-Levich analysis applied to nanoparticle modified rotating disk electrodes: Electrocatalysis or misinterpretation. *Nano Res.* **7**, 71–78 (2014).

20. Ward, K. R., Gara, M., Lawrence, N. S., Hartshorne, R. S. & Compton, R. G. Nanoparticle modified electrodes can show an apparent increase in electrode kinetics due solely to altered surface geometry: The effective electrochemical rate constant for non-flat and non-uniform electrode surfaces. *J. Electroanal. Chem.* **695**, 1–9 (2013).

21. Gara, M., Ward, K. R. & Compton, R. G. Nanomaterial modified electrodes: evaluating oxygen reduction catalysts. *Nanoscale* **5**, 7304–7311 (2013).

22. Amores, E., Rodríguez, J., Oviedo, J. & De Lucas-Consuegra, A. Development of an operation strategy for hydrogen production using solar PV energy based on fluid dynamic aspects. *Open Eng.* **7**, 141–152 (2017).

23. Peng, L. & Wei, Z. Catalyst Engineering for Electrochemical Energy Conversion from Water to Water: Water Electrolysis and the Hydrogen Fuel Cell. *Engineering* **6**, 653–679 (2020).

24. Mori, M., Mržljak, T., Drobnič, B. & Sekavčnik, M. Integral characteristics of hydrogen production in alkaline electrolysers. *Journal of Mechanical Engineering* **59**, 585–594 (2013).

25. Zhang, D. & Zeng, K. Status and Prospects of Alkaline Electrolysis. in *Hydrogen Science and Engineering Materials, Processes, Systems and Technology Volume 1* (eds. Stolten, D. & Emonts, B.) 283–308 (Wiley-VCH Verlag GmbH & Co. KGaA, 2016).

26. Tafel, J. Über die Polarisation bei kathodischer Wasserstoffentwicklung. *Zeitschrift für Phys. Chemie* **50U**, 641–712 (1905).

27. Trasatti, S. Work function, electronegativity, and electrochemical behaviour of metals. III. Electrolytic hydrogen evolution in acid solutions. *J. Electroanal. Chem.* **39**, 163–184 (1972).

28. Parsons, R. The rate of electrolytic hydrogen evolution and the heat of adsorption of hydrogen. *Trans. Faraday Soc.* **54**, 1053–1063 (1958).

29. Nørskov, J. K. *et al.* Trends in the Exchange Current for Hydrogen Evolution. *J. Electrochem. Soc.* **152**, J23–J23 (2005).

30. Santos, E., Quaino, P. & Schmickler, W. Theory of electrocatalysis: hydrogen evolution and more. *Phys. Chem. Chem. Phys.* **14**, 11224–11233 (2012).

31. Dubouis, N. & Grimaud, A. The hydrogen evolution reaction: From material to interfacial descriptors. *Chem. Sci.* **10**, 9165–9181 (2019).

32. Hu, C., Zhang, L. & Gong, J. Recent progress made in the mechanism comprehension and design of electrocatalysts for alkaline water splitting. *Energy Environ. Sci.* **12**, 2620–2645 (2019).

33. Zhu, Y. *et al.* Metal oxide-based materials as an emerging family of hydrogen evolution electrocatalysts. *Energy Environ. Sci.* **13**, 3361–3392 (2020).

34. Xu, X. *et al.* A Perovskite Electrocatalyst for Efficient Hydrogen Evolution Reaction. *Adv. Mater.* **28**, 6442–6448 (2016).

35. Zhu, Y. *et al.* A Perovskite Nanorod as Bifunctional Electrocatalyst for Overall Water Splitting. *Adv. Energy Mater.* **7**, (2017).

36. Guan, D. *et al.* Searching General Sufficient-and-Necessary Conditions for Ultrafast Hydrogen-Evolving Electrocatalysis. *Adv. Funct. Mater.* **29**, 1900704 (2019).

37. Montoya, J. H., Doyle, A. D., Norskov, J. K. & Vojvodic, A. Trends in adsorption of electrocatalytic water splitting intermediates on cubic ABO3 oxides. *Phys. Chem. Chem. Phys.* **20**, 3813–3818 (2018).

38. Seh, Z. W. *et al.* Combining theory and experiment in electrocatalysis: Insights into materials design. *Science* **355**, eaad4998 (2017).

39. Jiao, Y., Zheng, Y., Jaroniec, M. & Qiao, S. Z. Design of electrocatalysts for oxygen- and hydrogen-involving energy conversion reactions. *Chem. Soc. Rev.* **44**, 2060–2086 (2015).

40. Nørskov, J. K. *et al.* Origin of the Overpotential for Oxygen Reduction at a Fuel-Cell Cathode. *J. Phys. Chem. B* **108**, 17886–17892 (2004).

41. Hong, W. T. *et al.* Toward the rational design of non-precious transition metal oxides for oxygen electrocatalysis. *Energy Environ. Sci.* **8**, 1404–1427 (2015).

42. Rossmeisl, J., Qu, Z.-W., Zhu, H., Kroes, G.-J. & Nørskov, J. K. Electrolysis of water on oxide surfaces. *J. Electroanal. Chem.* **607**, 83–89 (2007).

43. Huang, Z. F. *et al.* Strategies to Break the Scaling Relation toward Enhanced Oxygen Electrocatalysis. *Matter* **1**, 1494–1518 (2019).

44. Seh, Z. W. *et al.* Combining theory and experiment in electrocatalysis: Insights into materials design. *Science* **355**, eaad4998 (2017).

45. Fabbri, E., Habereder, A., Waltar, K., Kötz, R. & Schmidt, T. J. Developments and perspectives of oxide-based catalysts for the oxygen evolution reaction. *Catal. Sci. Technol.* **4**, 3800–3821 (2014).

46. Man, I. C. *et al.* Universality in Oxygen Evolution Electrocatalysis on Oxide Surfaces. *ChemCatChem* **3**, 1159–1165 (2011).

47. Shen, X. *et al.* Dual-Site Cascade Oxygen Reduction Mechanism on SnOx/Pt-Cu-Ni for Promoting Reaction Kinetics. *J. Am. Chem. Soc.* **141**, 9463–9467 (2019).

48. Mefford, J. T. *et al.* Water electrolysis on $La_{1-x}Sr_xCoO_{3-d}$ perovskite electrocatalysts. *Nat. Commun.* **7**, 11053 (2016).

49. Naito, T., Shinagawa, T., Nishimoto, T. & Takanabe, K. Recent advances in understanding oxygen evolution reaction mechanisms over iridium oxide. *Inorg. Chem. Front.* **8**, 2900–2917 (2021).

50. Suntivich, J., May, K. J., Gasteiger, H. A., Goodenough, J. B. & Shao-Horn, Y. A Perovskite Oxide Optimized for Oxygen Evolution Catalysis from Molecular Orbital Principles. *Science* **334**, 1383–1385 (2011).

51. Liang, Q., Brocks, G. & Bieberle-Hütter, A. Oxygen evolution reaction (OER) mechanism under alkaline and acidic conditions. *J. Phys. Energy* **3**, 026001 (2021).

52. Hardin, W. G. *et al.* Tuning the Electrocatalytic Activity of Perovskites through Active Site Variation and Support Interactions. *Chem. Mater.* **26**, 3368–3376 (2014).

53. Suntivich, J. *et al.* Design principles for oxygen-reduction activity on perovskite oxide catalysts for fuel cells and metal–air batteries. *Nat. Chem.* **3**, 647–647 (2011).

54. Wang, Y., Li, J. & Wei, Z. Transition-metal-oxide-based catalysts for the oxygen reduction reaction. *J. Mater. Chem. A* **6**, 8194–8209 (2018).

Chapter 3. Best Practices for the Use of Counter Electrodes in 3-Electrode Measurements of Hydrogen Evolution Electrocatalysts in Acidic Aqueous Electrolytes

3.1 Introduction

There is a large and growing interest in the development of electrocatalysts based on earth-abundant materials. Key to these materials is that their activities do not require expensive and rare metals or oxides such as platinum, iridium oxide, or ruthenium oxide.[1–3] The standard method for accurately assessing these materials is through rotating-disc electrode voltammetry with a three-electrode setup (i.e., working, reference, and counter electrodes).[3–12]

The working electrode (WE) comprises a substrate upon which the electrocatalyst of interest is coated. Typically, the substrate for testing electrocatalysts is glassy carbon (GC). GC is an ideal substrate as it has a wide electrochemical window in aqueous electrolytes and a very low intrinsic activity toward many reactions of interest to the hydrogen economy, namely the oxygen evolution (OER), oxygen reduction (ORR), hydrogen evolution (HER), and hydrogen oxidation (HOR) reactions.[9,13,14]

Details of reference electrode operation were given in the previous chapter along with a brief explanation of the need of a counter electrode. The rest of this chapter concerns the details of counter electrode choice and application.

3.1.1 Operation of a Counter Electrode

In a three-electrode setup, current flows between the working and counter electrodes. The potential of the counter electrode is undefined in most experimental setups, though it is possible to measure the potential of the counter electrode versus the reference electrode with some potentiostat setups.[15] Regardless of whether the potential of the counter electrode is measured, it is not controlled in the same way as the potential of the working electrode. The potential of the counter electrode is such that it allows for an equal and opposite current to the working electrode. For example, a reduction

current of −1 mA at the working electrode will require a corresponding oxidation of +1 mA at the counter electrode. More precisely, the counter electrode will induce the most facile oxidation reactions to facilitate a reductive current at the WE, and the most facile reduction reactions to drive oxidative currents at the WE.[16] To do this, the potentiostat applies a potential (relative to that of the reference electrode) to the counter electrode to cause a current to flow. The potential applied to the counter electrode is typically not a measured quantity. It will be as high or low (within the compliance voltage range of the potentiostat used) as is needed to bring about the current flow required for the desired potential between the WE and RE.

The resistance between the counter and reference electrodes is automatically compensated for by the way a counter electrode is connected to the potentiostat. If there is a high resistance, then the potential applied to the CE will simply increase to account for this. However, the same cannot be said for the resistance between the working and reference as the potentiostat circuitry is 'blind' to this, hence the need for iR-compensation.[17]

It is important to emphasise that it is the total current that is matched between the WE and CE, not the current density. However, the overpotential required to drive the reaction *is* dictated by the current density.[15] For example, there may be a reduction current density of −10 mA cm^{-2} at the working electrode. If the area of the CE is 10 times the surface area of the WE, then the current density will only be +1 mA cm^{-2} at the CE, despite the absolute currents being equal. If the counter electrode reaction is oxygen evolution, then this difference in current density could mean the potential at the counter electrode is considerably less than were it the same surface area, depending on the activity of the material towards the reaction.

3.1.2 Concerns Associated with the Counter Electrode

It is impossible for a potential to be applied to the CE and for a current to flow without in some way changing either the CE itself and/or the electrolyte in close proximity to it. For whatever current is demanded of the counter electrode,

there will be some electrochemical process which affords that current. This should lead any electrochemist to ask:

1. What is happening around the counter electrode?
2. What is happening to the counter electrode?

The discussion in the previous section stated that there is a reduction reaction at the WE, then a corresponding oxidation reaction will happen at the CE. This oxidation could be of some analyte in the solution or of the electrolyte itself. The oxidation process will change as the required current changes. At low currents, charging or discharging the double layer at the counter electrode may provide sufficient currents. To meet higher current requirements, it may be necessary to electrolyse the solvent through oxygen or hydrogen evolution reactions (in aqueous media). If an analyte or other redox-active species is undergoing oxidation or reduction at the CE, the concentration of this species may eventually deplete, forcing the reaction to change to another one to afford the required current. Clearly, even in a constant current experiment, the CE may undergo significant changes in potential, even if the working electrode under study is stable.

The second question is what the bulk of this chapter concerns. In all cases, the CE material is chosen due to its electrochemical inertness. Elements such as gold and platinum are commonly recommended as counter electrode materials because of their supposed superior inertness.[18]

The issue with blanket recommendations for CE materials is that inertness is a dynamic property that depends on the pH of the electrolyte, the potential at which the material is held, and the testing regime. This concept can be partially visualised through Pourbaix diagrams, which show phase boundaries as a function of pH and applied potential (vs RHE). These diagrams were popularised by Marcel Pourbaix in his *Atlas of Electrochemical Equilibria in Aqueous Solutions.*[19] The lines in a Pourbaix diagram represent equilibria. Above and to the right of such lines, the more oxidised form will be stable. Below and to the left of these lines, the reduced form will be more stable. The simplest of these

diagrams is for water, shown in Figure 3.1. Here, one can see two parallel lines separated by a constant potential difference of 1.23 V. Line a represents where the HER becomes spontaneous, and below this line H_2 is stable relative to water. Line b represents where the OER becomes spontaneous, and above this line O_2 is stable relative to water. Between these two lines, water is stable relative to both H_2 and O_2 and is thus known as the region of thermodynamic stability for water. Solving the Nernst equation for both the OER and HER demonstrates that the thermodynamic (for the derivation of this and an explanation of Nernstian systems see Chapter 2) potential for these reactions decreases with a slope of 59 mV per pH unit.

The ideal counter electrode material for testing water-splitting electrocatalysts will be stable above the top line if the CE will be undergoing OER and below the bottom-line if undergoing HER.

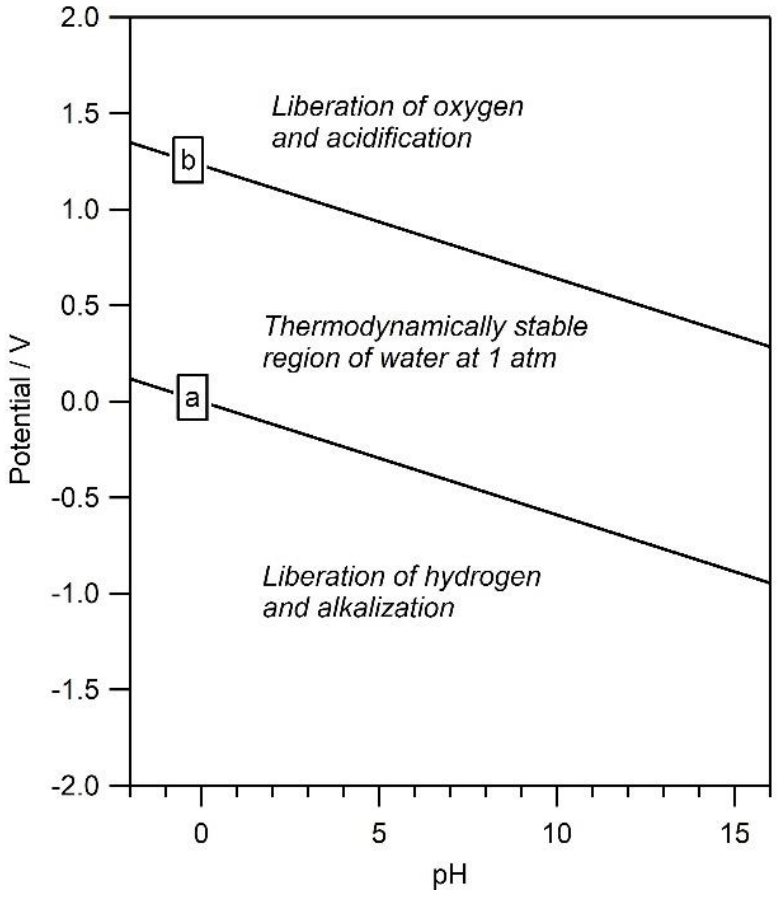


Figure 3.1 Pourbaix diagram of water. Potential is given vs an RHE, and the x-axis represents pH. Recreated from Pourbaix.[19]

If one evolves hydrogen in a hydrogen-free aqueous electrolyte, the counter electrode will be at a sufficiently positive potential that oxygen is evolved. At pH 0, this means the counter electrode will be at 1.2 V or higher. In Figure 3.2 the Pourbaix diagram for platinum is shown. The region of relevance is at pH 0, and ~1.2 V as this corresponds to the conditions a counter electrode will be under.

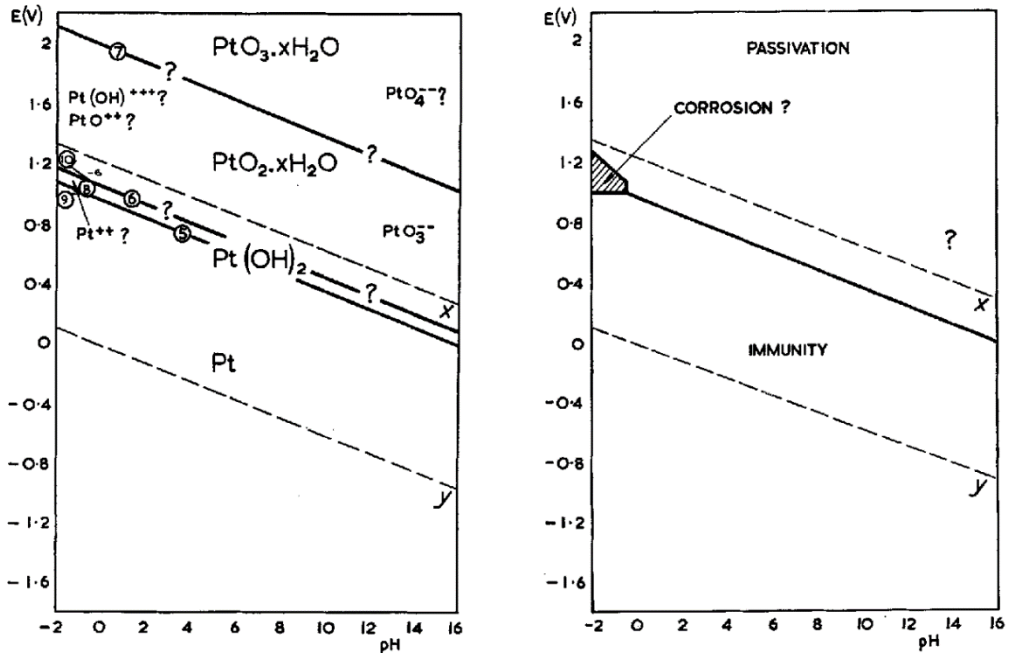


Figure 3.2 Left: Pourbaix diagram showing the equilibria for various forms of Pt and Pt ions as functions of pH and applied potential. Right: A simplified diagram in which the forms shown on the left are described in terms of immunity, passivation, and corrosion. In both, the dashed lines represent the thermodynamically stable region of water. Reproduced from Pourbaix et al.[20]

Although platinum is clearly stable at a wide range of pH value and potentials, there is a phase transition within the region of thermodynamic stability of water. At pH > 0, this transition is toward a passivating $Pt(OH)_2$ layer, which would slightly reduce the conductivity of the counter electrode. However, at pH 0, the counter electrode must pass through a corrosion-related phase transition, generating Pt^{2+} and potentially other charged species. In other words, the counter electrode will dissolve. Even if the corrosion region of the diagram is entered only briefly, or avoided entirely, it is still possible for PtO^{2+} or $Pt(OH)^{3+}$ to form alongside formation of the $PtO_2.xH_2O$ phase.[20] If these

dissolved species diffuse to the working electrode (which is at < 0 V), then they could deposit onto the surface as Pt.

Gold, although fully immune to dissolution within the thermodynamic stability window of water, almost immediately enters a corrosive regime when the potential goes above that of oxygen evolution as shown in Figure 3.3. This means gold would likely be a reasonable counter electrode for any electrochemical reactions requiring only small currents (and thus not pushing the Au CE towards dissolution potentials) but is clearly unsuitable for any measurements which would require significant water-splitting currents to pass given the increased potential at the counter electrode. At low pH the Au corrodes to form Au^{3+}, whereas above pH 1 it will form $Au(OH)_3$.[19,21]

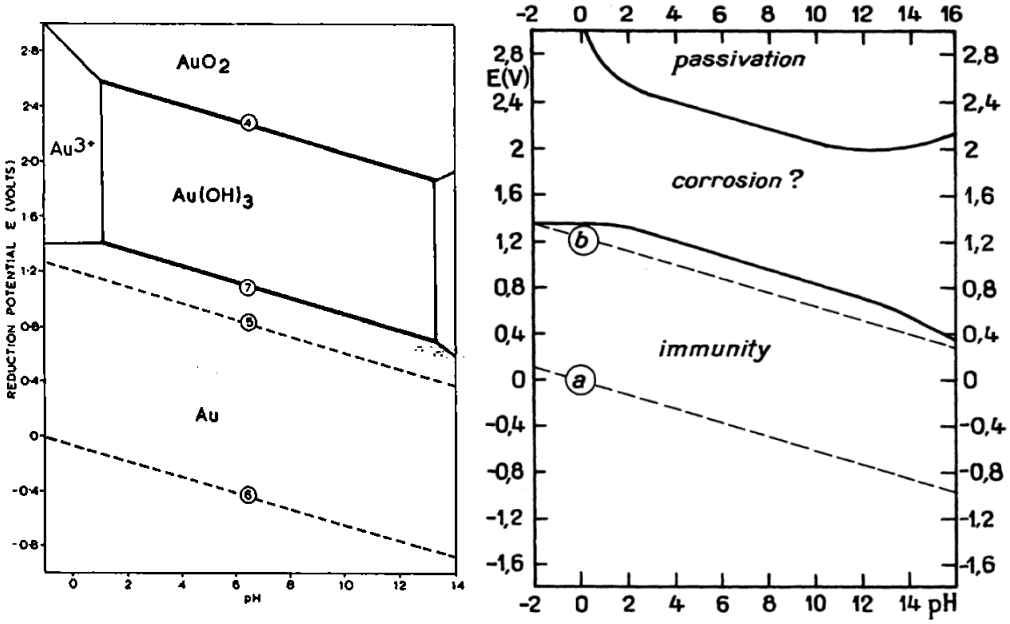


Figure 3.3 Left: Pourbaix diagram showing the equilibria for various forms of Au and Au ions as functions of pH and applied potential. Reproduced from Finkelstein et al.[21] *Right: Pourbaix diagram of gold in terms of passivating, corrosion, and immunity. Reproduced from Pourbaix.*[19] *The dotted lines relate to the thermodynamically stable region of water.*

Pourbaix diagrams are derived from the Nernst equation using the thermodynamic properties of the various species in equilibrium (i.e., standard reduction potentials) and are therefore purely thermodynamic in nature. As such, kinetic information relating to the rate of dissolution cannot be elucidated from the diagrams. Similarly, information on secondary interactions with counterions are not presented in these diagrams. The identity of the counterion can change the propensity of a metal to dissolve. For example, Cl^- ions from either the electrolyte or leaked from a reference electrode can form stable metal—chloride complexes, thus increasing the rate of metal dissolution from the counter electrode.[15,21,22] The diagrams also do not account for a dynamically changing system (such as potential sweeps), in which regions of passivation, corrosion, and immunity are cycled in and out of. For this reason, although Pourbaix diagrams are useful to demonstrate the variable nature of nobility, they should not be considered as absolute in terms of whether any given material should be used for the counter electrode.

Extra consideration should be given to the full potential regime. In cyclic voltammetry the potential is varied as a function of time, meaning the counter electrode will be transitioning repeatedly between many phases on the Pourbaix diagram. This may lead to the counter electrode material destabilising and being more prone to further dissolution.[15]

Chen *et al*, proposed a detailed mechanism by which a platinum counter electrode may dissolve under acidic conditions during a cyclic voltammetry experiment.[15] Initially, during oxygen evolution at the Pt counter electrode, the CE will be coated with a layer of PtO or PtO_2. Once a complete layer of oxide has formed, the O and Pt atoms can undergo place exchange, leading to a less stable surface oxide layer which can undergo dissolution to Pt^{2+} or Pt^{4+}, or reduction to Pt which is prone to later dissolve to Pt^{2+} when the potential scan changes direction.[15]

With dissolved Pt or Au species in solution, a third question becomes apparent.

3. Where are the dissolved species going?

Typically, during an electrocatalysis experiment the working electrode is rotating.[8] Assuming the counter electrode is in the same solution as the working electrode, any dissolved species will be well-mixed and quickly reach the proximity of the working electrode. Here, the dissolved species are able to deposit on to the working electrode and increase the electrocatalytic activity of the material being tested as Pt is itself a highly active HER electrocatalyst.[6,10,11,15,23–28]

3.1.3 Review of Mitigation Strategies

There are several approaches that have been taken in the literature to mitigate against the issue of counter electrode dissolution and subsequent deposition of those species onto the WE.

The first step to mitigation is proper experimental design. As discussed earlier, the counter electrode should be at least 10 times the surface area of the working electrode. Doing this minimises the current density at the CE and so leads to a lower magnitude potential at the CE.[15] A large surface area Pt counter electrode coupled with relatively short cycling experiments (<400 cycles) has been shown to be a reasonable setup.[29] Another experimental design to consider is saturating the electrolyte with hydrogen. This would allow a platinum counter electrode to carry out the HOR to oppose the HER currents, rather than using the OER. The HOR happens at close to 0 V, and so would keep the counter electrode at a safe and stable potential even with significant current flowing. However, it is not always possible to saturate the electrolyte with hydrogen.

One of the most common mitigation strategies is to physically separate the counter electrode from the working electrode solution with a Nafion membrane.[15,24,30–32] Nafion is a perfluorinated polymer cation-exchange membrane specifically designed for proton transport. Protons are transported through the membrane by shuttling via the -SO_3H groups.[33] Its ability to prevent gas crossover has made it a popular choice for PEM fuel cells and electrolysers.[34] Although it is commonly assumed to only allow for the transfer

of protons, it also allows the passage of Na^{+}[34] and, when lithiated, is able to transfer Li^{+}.[35] There is also much evidence in the fuel cell literature that Pt ions dissolved from the cathode can infiltrate the Nafion membrane.[22,36–38] The ability of Nafion to allow Pt to enter has been specifically used in the fabrication membrane-electrode assemblies.[39]

An alternative to blocking the dissolution products is to avoid their generation in the first place. This is typically done by using a graphite or glassy-carbon counter electrode.[6–8,10,11,14,26,40,41] Carbon is a poor electrocatalyst for the hydrogen evolution reaction, so any contamination from it would not activate most test electrocatalysts. However, deactivation is also not a desirable outcome. Despite the high number of papers in the literature recommending this solution, there is no strong evidence of its effectiveness except for the specific case of long-term cycling.[11,26]

Iridium-based counter electrode materials have also been explored. Given that the counter electrode is catalysing the OER, the potential of the counter electrode can be minimised by choosing a material that is highly active for the reaction and stable in the operating conditions. Lee at al. demonstrated that $IrO_2Ta_2O_5$ supported on Ti was suitable as a counter electrode for investigating the HER in acid as the CE material is extremely active to the OER.[42] This was supported by Dondapati *et al*, who showed the counter electrode is also stable for measuring the OER and other electrocatalytic reactions.[29] The material may be a stable and active counter electrode material, but it may struggle to gain wide use given the increased complexity of making the electrode. Such CEs are beyond the scope of the work presented in this chapter.

3.1.4 Context of the Work Presented in This Chapter

The first port-of-call for new electrochemists is likely an electrochemistry textbook. Different texts go into varying levels of details about counter electrode operation and have differing levels of depth in terms of the practical aspects of their deployment. The work presented in this chapter aims to fill in the gaps left by such electrochemical texts.

Compared to the reference electrode, which has been thoroughly treated and examined in textbooks since they were first developed,[43,44] the counter electrode is afforded relatively little space. For example, Bard and Faulkner's seminal textbook, *Electrochemical Methods*, gives the topic just half a page and states that the counter electrode's "electrochemical properties do not affect the behaviour of the electrode of interest".[45] Hamman, Hamnett, and Vielstich's *Electrochemistry* discusses the counter electrode in terms of its function, but with no reference to best practices.[46] Gileadi, in *Physical Electrochemistry*, makes the technically true statement that significant changes in the counter electrode potential "does not in any way influence the measured potential of the working electrode with respect to the reference," but does not go onto deal with what practically occurs when different materials go to high oxidative potentials.[47] Compton and Banks' *Understanding Voltammetry* correctly notes that a counter electrode will "electrolytically induce chemical changes in the solution in the vicinity of the counter electrode" and that one must design electrochemical experiments with these products in mind, but they simply recommend a frit rather than detail what should be considered when choosing a counter electrode material.[48] The only textbook I could find which makes specific note of the kinds of contamination discussed in this chapter was Pletcher's *A First Course in Electrode Processes*, which states "one needs to be cautious of low rate corrosion of the anode in long timescale experiments", mentioning, "reports of the transfer of Pt from counter to working electrode influencing experimental data."[16] Pletcher recommends carbon, nickel, or steel as alternatives to Pt counter electrodes.

The use of carbon- or iridium-based counter electrodes have been shown to be successful in the literature. However, all the studies presented only investigate cycling experiments.[11,26] In addition to cycling, long-term constant current tests are used to assess the stability of an electrocatalyst in conditions closer to a real device.[8] Similarly, although in an ideal experiment one would saturate the electrolyte with hydrogen, there are many reasons why this might not be the

case. For example, it is unlikely that an operational electrolyser would be entirely saturated with the gas.

This work fills in this gap in the literature and thoroughly investigates the effect of the counter electrode material and the deployed mitigation strategy on the measured activity of the working electrode. We first show that during a 24-hour constant current HER experiment, a Pt counter electrode dissolves and will deposit on a glassy carbon working electrode thus increasing its HER activity. This still occurs, albeit to a lesser extent, if a Nafion membrane or glass frit is present. We then show that a pristine active working electrode will be deactivated if a graphite counter electrode is used. A glass frit or Nafion is demonstrated to be effective at mitigating this. We then apply these findings to the electrocatalysis of the HER using a MoS_2 as the electrocatalyst material. Finally, the use of a glassy carbon counter electrode is demonstrated to be a far better choice than a Pt counter electrode in a cycling experiment in which HER was not a desirable reaction.

3.2 Experimental Section

3.2.1 Materials and Apparatus

Glassy carbon, platinum, or gold rotating disc electrodes with ⌀ = 5 mm (Pine Research, Durham, NC) were used as working electrodes. Pt- and Au-coils (CH Instruments, Austin, TX), and graphite or glassy carbon rods (Alfa Aesar) were used as counter electrodes. All reference electrodes were Ag/AgCl (CH Instruments) filled with saturated KCl solution. Nafion-117 membranes were supplied by Alfa Aesar. Unless otherwise stated, the electrolyte was 1.0 mol dm^{-3} H_2SO_4. Where specifically stated, 1.0 mol dm^{-3} HCl is also used. Standard solutions of 100 mg dm^{-3} Pt or Au in 2% HCl were provided by Fischer Scientific. MoS_2 (Alfa Aesar) was used as received.

Electrochemical testing was carried out using a model CHI760C potentiostat (CH Instruments) coupled with a modulated speed rotator from Pine Research. X-ray photoelectron spectroscopy (XPS) was carried out using a Kratos AXIS DLD instrument equipped with an Al Kα X-ray source (1486.6 eV). CasaXPS software

was used with Kratos sensitivity factors to determine atomic concentrations. A Shirley background correction was applied to all spectra prior to analysis. All spectra were charge corrected to the adventitious carbon peak at 284.8 eV. Fitting of spectral components used the asymmetrical line shapes LF(0.5,1,400,500) and DS(0.01,250) for Pt and Au, respectively. A Zeiss EVO MA10 scanning electron microscope equipped with secondary and backscattered-electron detectors and an energy-dispersive X-ray (Element, AMETEK) analyser was used for scanning electron microscopy (SEM) and elemental detection. The accelerating voltage was 20 kV. Diluted aliquots of the electrolyte were analysed for Pt and Au by inductively coupled plasma mass spectrometry (ICP-MS) using an iCAP-Q from Thermo Fisher Scientific (Bremen, Germany) with a collision cell charged with He. Kinetic energy discrimination (KED) was used to remove polyatomic interferences. Samples were introduced at 1.2 cm^3 min^{-1} from an autosampler (Cetac ASX-520) incorporating an ASXpress rapid uptake module through a perfluoroalkoxy (PFA) Microflow PFA-ST nebulizer (Thermo Fisher Scientific, Bremen, Germany).

3.2.2 Experimental Methods

The glassy carbon working electrode was cleaned by immersing briefly in aqua regia then rinsing with milli-Q water. The GC, Pt, and Au working electrodes were polished to a mirror finish with alumina (1.0, 0.3, 0.05 µm, Buehler, Coventry, UK). The polishing pads were replaced each experiment to eliminate cross contamination. Prior to use, Pt counter electrodes were flame treated, and Au electrodes were rinsed with milli-Q water. Graphite rods were polished with 0.05 µm alumina, rinsed with water, immersed in 1.0 mol dm^{-3} HNO_3 for at least 60 min, and then agitated ultrasonically in water. A 3-necked flask, a separable H-cell, or an H-cell containing a built-in glass frit was used for electrochemical measurements. All glassware was cleaned prior to use and between experiments by soaking in aqua regia then rinsing with ultra-pure Milli-Q water (18.2 MΩ·cm). In divided cells, one compartment contained the test electrocatalyst and the other contained the Ag/AgCl reference electrode and counter electrode. Membranes were immersed in 1.0 mol dm^{-3} H_2SO_4 for

at least 20 min before use. Each half of the H-cells contained 20 cm^3 of 1.0 mol dm^{-3} H_2SO_4, and approximately 3.14 cm^2 of the counter electrodes were submerged in the electrolyte. The electrolyte was purged with N_2 prior to use, and a N_2 atmosphere was maintained during the experiment through use of an Atmos bag.

MoS_2 electrodes were fabricated by dispersing MoS_2 in isopropyl alcohol and agitating the dispersion ultrasonically for 30 min. The dispersion (0.010 cm^3) was drop cast onto a 5 mm diameter GC electrode to give an approximate loading of 1.8 mg cm^{-2}. This material was tested in 1.0 mol dm^{-3} H_2SO_4 electrolyte.

The $K_6[P_2W_{18}O_{62}](H_2O)_{14}$@SWNT electrode was prepared by mixing a solution containing 1 wt % $K_6[P_2W_{18}O_{62}](H_2O)_{14}$@SWNT and 3 wt % PTFE binder ultrasonically for 20 min. The mixture (0.080 cm^3) was deposited onto a 3 mm diameter GC electrode surface and allowed to dry in air. Electrochemical testing of this electrocatalyst was carried out using Ar saturated 1.0 mol dm^{-3} HCl as electrolyte and a saturated calomel reference (SCE) electrode. A Pt CE was originally used with this setup. The CE was changed to a polished GC CE and the results compared.

Unless otherwise indicated, all potentials are reported on the reversible hydrogen electrode (RHE) scale. Constant-current stability tests were carried out by passing −10 mA cm^{-2} through the electrocatalysts for 24 h while the electrodes rotated at 1600 rpm.

3.3 Results and Discussion

3.3.1 Evidence for Contamination of the WE by CE species

Before assessing the effectiveness of any strategy to mitigate against the effects of contamination from the counter electrode, it was important to assess the level of contamination in a typical electrochemistry setup. −10 mA cm^{-2} was passed between a glassy carbon (GC) working electrode and either a Pt or Au counter electrode for 24 hours. Rotating electrode linear sweep voltammograms were measured before and after to show the change in the

activity of the working electrode. Figure 3.4A clearly shows that initially the GC electrode had negligible activity toward the hydrogen evolution reaction (HER). After 24 h of electrolysis, the activity had increased drastically such that −10 mA cm^{-2} was reached at 165 mV vs RHE. This is just 125 mV more negative than Pt-based electrocatalysts reported in the literature.[8] When a Au counter Figure 3.4B) electrode was used, an even larger activity increase was observed with the overpotential required for −10 mA cm^{-2} (η_{-10}) = 154 mV (accounting for the lower baseline).

To prove these increases were due to the counter electrode materials, SEM, EDX, and XPS analyses were carried out on the working electrode surface after the 24 h electrolysis. The SEM images in Figure 3.4C,D were taken in back-scatter detection mode such that the brightness correlates to atomic number. Pt islands, 700 – 1600 nm across, were identified across the GC electrode and their elemental identity was confirmed to be Pt using EDX analysis. Comparable SEM images of the GC electrode prior to the experiment were not taken.

In the case where Au was used as the counter electrode, a large quantity of dendrites were seen. These were similar in form to those created by Hau *et al via* electrodeposition.[49] Remarkably, these Au nanodendrites had a significantly higher HER activity than a pure Au disc. The η_{-10} of a polished Au disc was measured as −421 mV compared to −163 mV for the Au nanodendrites formed on the GC after a stability test using a Au counter electrode. Indeed, the post-stability electrode performed better than some recent Au-based electrocatalysts specifically designed for the HER (though it is important to note that further work would be needed to draw accurate comparisons).[50] Further investigation on the physical and electrocatalytic properties of this material could demonstrate whether this is a useful result for hydrogen production.

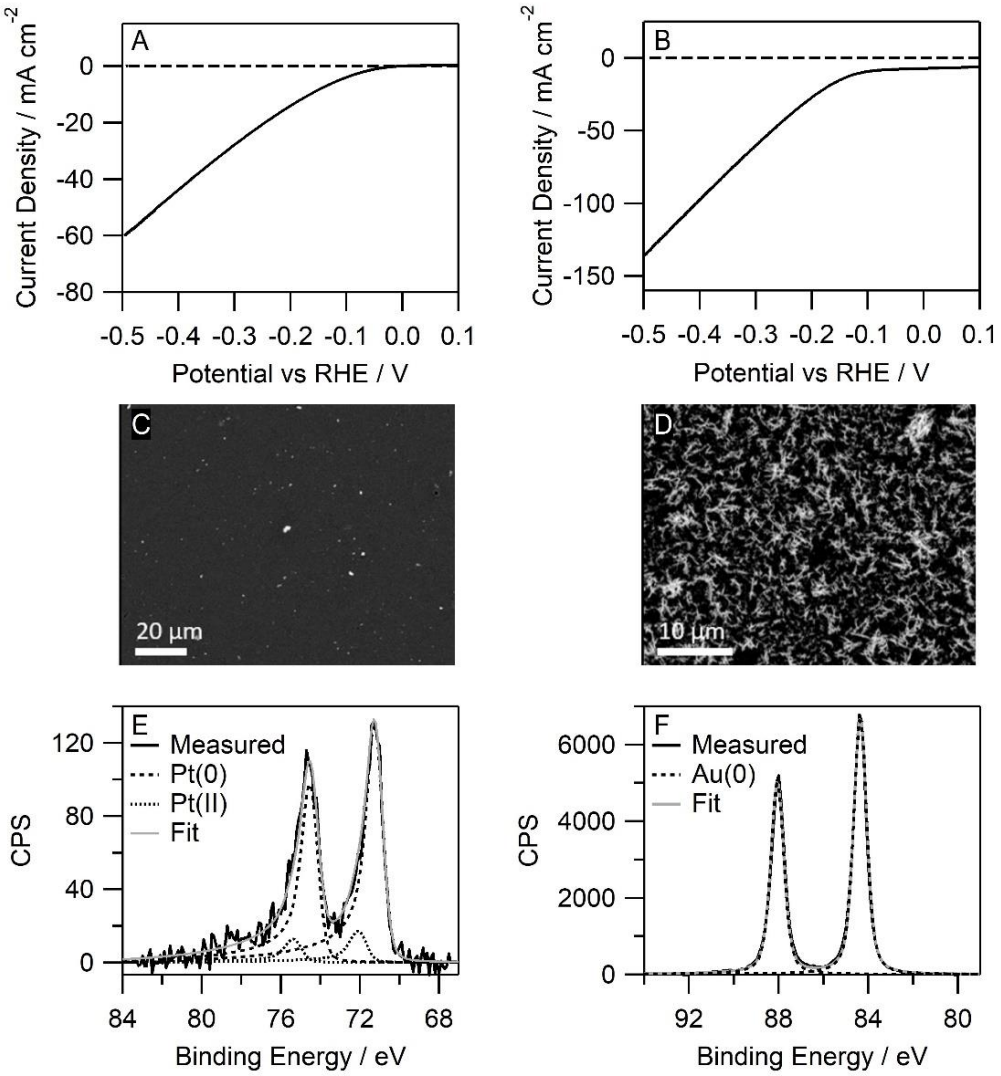


Figure 3.4 (A and B) Voltammograms recorded before (dashed line) and after (solid line) 24 h of HER at GC at −10 mA cm^{-2} in a cell containing a Pt and Au counter electrode, respectively. (C and D) Back-scattered scanning electron microscopy images of the GC surfaces after 24 h HER in a cell containing a Pt counter electrode and a Au counter electrode, respectively. (E and F) X-ray photoelectron spectra showing the presence of Pt and Au on the GC surface after the extended stability tests in which Pt and Au, respectively, were used as counter electrode.

The experiments were repeated, but rather than using a glassy carbon rotating disc electrode, a polished square of glassy carbon was used instead. To somewhat replicate the rotating electrode, a stirrer bar was set to 400 rpm throughout the experiment. As the GC RDE physically cannot enter the XPS instrument, the flat GC squares allowed for the electrode to be analysed with XPS. High-resolution XP spectra were taken at multiple spots on the GC carbon squares before and after electrochemical testing. As was to be expected, there

were no Pt or Au peaks in any of the 'before' spectra. As shown in Figure 3.4E, the GC after electrochemical testing with a Pt CE showed doublets characteristic of Pt $4f_{7/2}$ and Pt $4f_{5/2}$ signals. When deconvoluted and fitted using an asymmetrical line shape, it was seen that the deposited Pt was 93 % metallic Pt(0) (71.3 and 74.6 eV) with only 7 % Pt(II) (72.2 and 75.5 eV).[15,37,51] Similarly, a doublet characteristic of Au(0)[52,53] was observed when Au was used as the CE material (Figure 3.4F). Unlike in the Pt case, there was no evidence of Au in any non-zero oxidation state.

Comparing the areas under the Pt or Au peaks to the areas associated with C, O, N, and S gives an estimate of 0.21 and 10.0 atom % on GC of Pt and Au, respectively. This matches the qualitative images from the SEM analyses.

From the above results, it is clear that the issue of dissolution of Pt or Au is still present in constant current experiments and that without a suitable mitigation strategy, results cannot be reliably trusted.

3.3.2 Use of Divided Cells to Mitigate Contamination

A common strategy to prevent the dissolution products from the counter electrode contaminating the working electrode surface is to place the electrodes in two compartments separated by a membrane or frit. In this section the membrane material Nafion-117 and sintered glass frits will be compared for this application.

Nafion-117 is almost exclusively the form of Nafion used to form membranes to separate a divided cell. The 117 denotes that this form of Nafion has an equivalent weight of 1100 and a nominal thickness of 0.07 in.[34] Prior to use, the Nafion-117 membranes were hydrated in 1 mol dm^{-3} H_2SO_4. This hydration step ensured the volume of the membrane did not change significantly during the experiment, as this would lead to leakage at the join of the two halves of the cell setup.

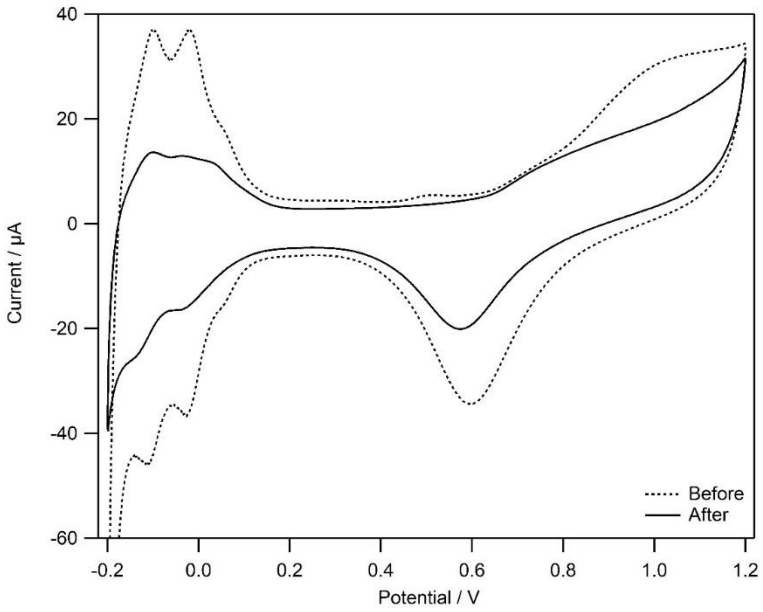


Figure 3.5 Before (dotted) and after (solid) cyclic voltammograms measured in 1 mol dm^{-3} H_2SO_4 with a Ag/AgCl RE with a stationary Pt working electrode. A Vycon® rubber O-ring was present in the electrolyte for the purpose of this test. After just 10s of cycles, a significant change in the voltammetry is observed.

The hydrated Nafion-117 membrane was sandwiched between two halves of an H-cell with PTFE O-rings ensuring a good seal. PTFE was chosen as the more common Vycon® O-ring material was not stable in the presence of acid for such long periods and thus added an additional source of contamination as shown in Figure 3.5. When a PTFE O-ring was used, the voltammograms did not change.

An H-cell assembly with a glass frit built-in was used. This setup ensured there was no leakage, but the frit is not able to be removed for post-mortem analyses in the same way that the Nafion membranes are.

The testing procedure was the same as before, with 24 hours of constant HER at the WE and voltammograms measured before and after. This time, the counter and reference electrodes were placed in a compartment separate to the working electrode. Typically, the reference electrode would be in the same compartment as the working electrode to minimise iR-drop. However, we opted to separate it from the working electrode to remove the reference as a potential contamination source. Given that the results discussed in this chapter are only being internally compared, and that the experiments are consistent

and carefully carried out to ensure reproducibility, we do not believe the additional iR-drop to be an issue.

The voltammograms in Figure 3.6 show the difference in HER activity before and after 24 h of constant current HER at −10 mA cm−2 when Nafion or a frit is used in conjunction with a Pt (A) or Au (B) CE. As is always the case, the voltammogram of the GC before the test showed negligible HER activity. After 24 hours using a Nafion-117 membrane, currents from the HER were visible, with onset potentials of −0.5 V and −0.4 V when using a Pt or Au CE, respectively. Although Pt is a more active material toward the HER than Au, the previous experiments showed that the Au CE dissolves to a greater extent than the Pt. The η_{-10} decreased to −0.67 V and −0.54 V, respectively. When using a glass frit as the separator and a Pt CE, η_{-10} decreased to −0.42 V suggesting the frit was worse at preventing Pt crossover than the Nafion membrane. Although these values do not represent excellent HER electrocatalysts, they are greater than should be expected from a GC electrode.

ICP-MS was used to measure the Pt concentration after 24 h of constant current at −10 mA cm^{-2} of HER with Pt as the counter electrode with a Nafion membrane separating the two compartments. 31 ppb Pt was found in the counter electrode compartment compared to just 0.10 ppb in the working electrode compartment. This is a significant decrease in the amount of Pt species present, but there is still non-negligible quantities present in the WE compartment meaning some Pt did cross through the Nafion membrane. When a glass frit was used, 3.1 ppb was found in the WE compartment demonstrating the frit to be far more permeable Pt ions than the Nafion-117 membrane.

When a Au counter electrode was used, the concentration of the Au was so high it led to contamination of subsequent MS measurements. This means that the measurements cannot be used quantitatively. However, it does clearly demonstrate that Au dissolution and passage across the membrane or frit occurs to a larger extent than for Pt.

XP spectra on GC squares were measured as in the previous section, but with a Nafion membrane separating the CE and WE. The spectra are shown in Figure 3.6. Doublets corresponding to the presence of Pt (C) and Au (D) were observed meaning a measurable quantity of the metals had deposited. A Nafion-117 membrane is clearly unable to reduce the transmission of counter electrode contaminants sufficiently to prevent appreciable deposition on the working electrode in the conditions tested.

In the case of Nafion-117 membranes, it is important to demonstrate that the passage of Pt or Au is through the membrane, and not a consequence of some physical defect or passageway due to a poor H-cell seal. If the passage of Pt and Au is around the outside of the membrane or through physical holes, then one would expect not to see metals dispersed throughout the membrane. The SEM, EDX, and XPS analyses presented in Figure 3.7 confirm that the transmission is through the membrane and not around it. As Au dissolution is greater, the distribution of the metal across the membrane is easier to see than with Pt. The Nafion-117 was imaged in back-scatter mode and with the side that was facing the WE compartment facing the detector. Bright spots are seen across the whole membrane, and EDX confirmed that these bright spots are due to Au. XPS analyses on a different section of the membrane was carried on three spots of the membrane. Again, the membrane was oriented such that the WE-side was exposed for analysis. A doublet like that seen in the previous XPS analyses was observed, confirming the presence of gold. As the spots analysed by XPS were randomly selected, the probability that the gold was only present at specific defects in the membrane is low and so it is highly likely that there is gold across the entirety of the membrane.

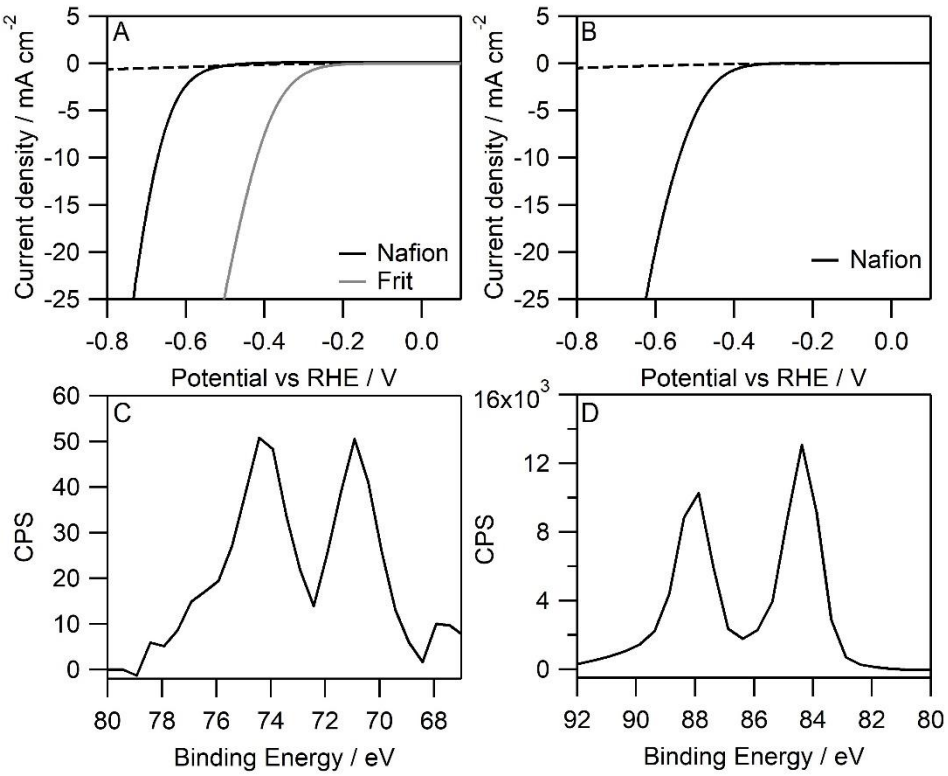


Figure 3.6 (A) Voltammograms recorded before (dashed line) and after (solid lines) 24 h of HER at −10 mA cm^{-2} at GC in cells containing a Pt counter electrode and a Nafion-membrane (black solid line) and glass-frit separator (grey solid line), respectively. (B) Voltammograms recorded before (dashed line) and after (solid line) 24 h of HER at −10 mA cm^{-2} at GC in a cell containing a Au counter electrode and Nafion-membrane separator. XP spectra of a GC surface after 24 h of HER at −10 mA cm^{-2} in cells containing (C) Pt and (D) Au counter electrodes, with a Nafion membrane separating the counter/reference electrodes from the GC.

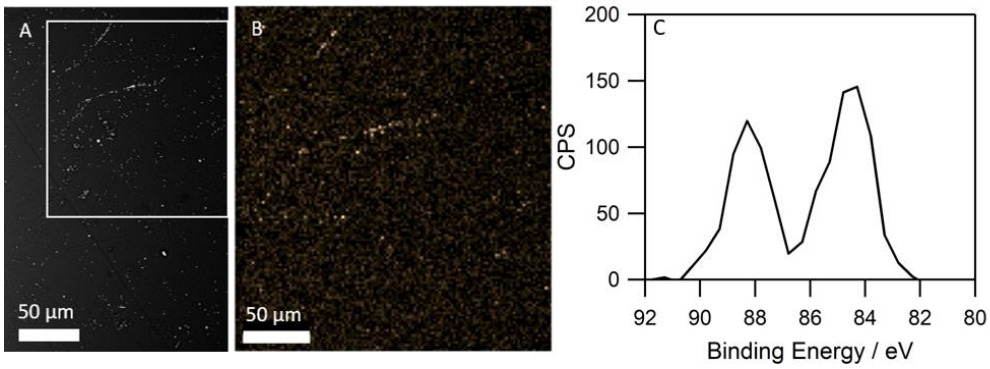


Figure 3.7 (A) Back-scattered SEM image of a Nafion membrane after 24 h of HER at −10 mA cm^{-2} at GC in a cell containing a Au counter electrode on the other side of the membrane. (B) EDX image of the boxed area in A, in which the orange spots correspond to Au. (C) High-resolution XP spectrum of the membrane surface in the Au region.

The same set of analyses was carried out for the case with Pt as the counter electrode (Figure 3.8). Given the smaller quantity of Pt dissolved, deposition across the membrane was more sporadic. Back-scatter SEM showed several bright spots on both sides of the membrane and EDX analysis on these bright spots confirm they are due to Pt. Due to the more localised nature of these deposits, XPS analysis failed to identify the presence of Pt peaks beyond the noise of the experiment. We propose the deposits may be localised to microscopic inhomogeneities of the membrane which could act as nucleation sites for the reduction of Pt^{2+} to Pt. The reduction is perhaps encouraged by the presence of H_2 gas present in the electrolyte as has been described in the fuel cell and membrane literature.[22,36–38,54,55]

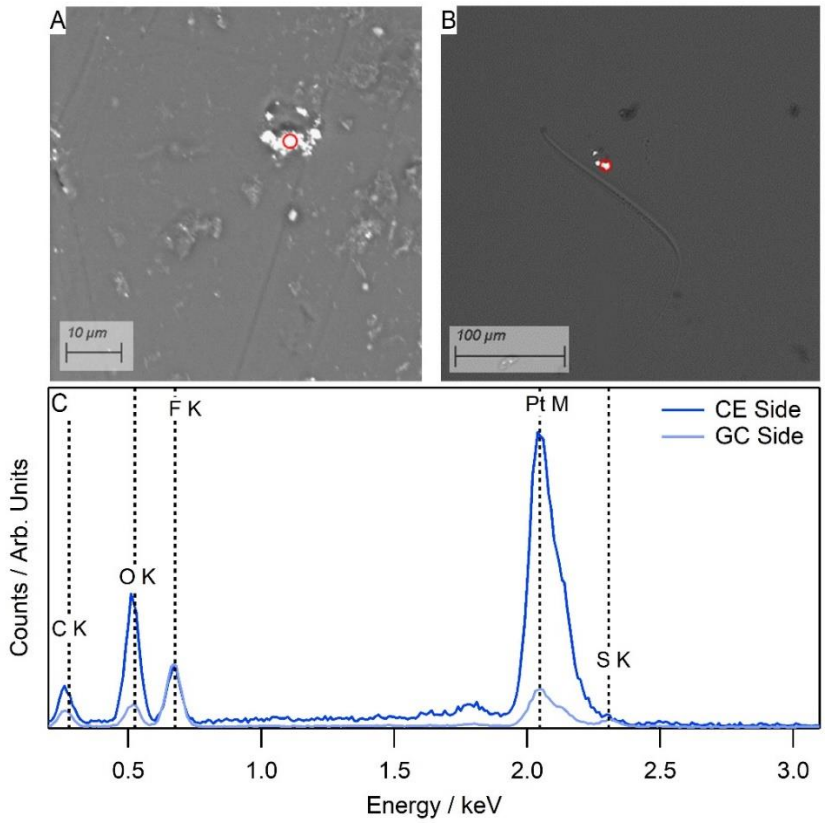


Figure 3.8 Back-scattered SEM images of Nafion after use in a divided cell containing a Pt counter electrode and in which the HER occurred for 24 h at GC at −10 mA cm^{-2}. (A) GC electrode (HER) side (B) counter-electrode (CE) side. (C) EDX spectra of both sides of the membrane. Red circles on the images show where EDX spectra were recorded. Spectra are normalised to the F K_α peak heights.

Combined, these data sets clearly demonstrate that neither glass frits nor Nafion-117 membranes are suitable for mitigating the activity increases observed when using Pt or Au counter electrodes.

3.3.3 Use of Carbon Counter Electrodes to Mitigate Metallic Contamination

Naturally, if preventing the cross-over of counter electrode contaminants is not easily achievable, then eliminating the source of contamination is a logical next step. So long as the active surface area of the counter electrode remains at least ten times bigger than that of the working electrode, the decreased activity of the CE material should not become a limiting factor.[56]

Graphite is generally considered a suitable CE material which should have a minimal effect on the activity of the test electrocatalyst.[11,24,26] However, as discussed in the introduction, the studies that do discuss carbon-based CEs, do not have strong electrochemical or spectrochemical evidence that the C CE does not influence the WE. Thus, the experiments presented herein serve to fill this gap in the literature.

The previous experiments used glassy carbon as the WE. This was chosen for its intrinsic inactivity toward the HER meaning any contamination by an active material would be clearly evident electrochemically. However, if a graphite counter electrode were to release contaminants, they would have a similar activity to the glassy carbon substrate and so identifying an increase or decrease in activity would be difficult. As such, the WEs for the following set of experiments are polished Pt or polished Au rotating disc electrodes. These can be polished to give a reproducible surface, and deposition of carbon-based contaminants would be expected to present as a decrease in electrochemical activity and be clearly visible as dark spots in back-scatter SEM images.

Other than the change in electrode material, the electrochemical testing was identical to before: 24 h of constant current HER at −10 mA cm^{-2} with rotating disc electrode voltammograms measured before and after.

When a graphite rod was used as the CE, and Pt as the WE, a drastic decrease in the activity of the electrode was observed after 24 hours as seen in Figure 3.9A. The onset of HER was initially ~0 V as expected for Pt, but then drops to 95 mV. The magnitude of η_{-10} increases by over 100 mV. This decrease in activity was correlated to carbon-based contamination by back-scatter SEM shown in Figure 3.10. The even dispersion of the dark spots shown in the SEM micrograph is representative of the whole electrode. Deposition does seem to be associated with the applied potential. A rotating ring disc electrode was used for the experiment with Pt as both the disc and ring material. The ring had no applied potential to it and was not connected during the experiment. The ring appeared to not be contaminated with carbon, whereas the disc was. Whether this is simple electrostatic attraction, or some form of electrochemical deposition process is not possible to discern from the collected data. Regardless of the process of deposition, it is clear use of a graphite CE leads to the opposite problem of Pt or Au CEs. For this reason, the use of Nafion-117 and frits were also tested in conjunction with graphite CEs.

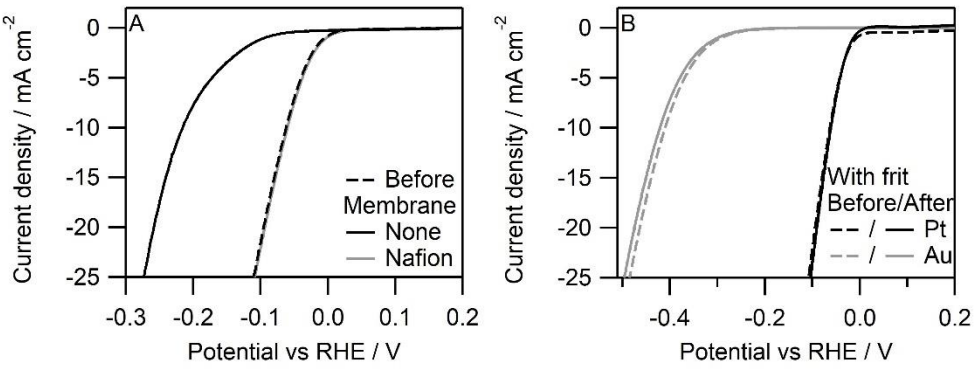


Figure 3.9 (A) Voltammograms recorded before (dashed line) and after (solid lines) 24 h of HER at −10 mA cm^{-2} at Pt in an undivided cell containing a graphite counter electrode. Gray line (which overlaps the black dashed line) shows the voltammogram recorded after the Pt electrocatalyst had been separated from the counter electrode by a Nafion membrane. (B) Voltammograms recorded before (dashed lines) and after (solid lines) 24 h of HER at −10 mA cm^{-2} in cells containing Pt (black) and Au (grey) electrocatalysts separated from a graphite counter electrode by a glass frit.

When Nafion-117 was used, there was no change in the RDE-LSVs indicating the membrane was able to sufficiently block the movement of carbon-based

contaminants from the CE compartment to the WE. This is shown as the grey line in Figure 3.9A. There was no noticeable change in either the onset or η_{-10} after the 24 h experiment. When a frit was used in place of the membrane a similar result was observed (Figure 3.9B). This setup is also consistent with the experimental setup by McCrory and co-workers in their highly cited OER and HER benchmarking papers.[7,8] To ensure this result remains true for less active electrocatalysts, the graphite rod and glass frit combination was also tested with a gold WE. As shown in Figure 3.9B, there was minimal change in the onset and η_{-10}, with the latter increasing by just 11 mV.

We also tested the use of a glassy carbon rod as a counter electrode. Similar to the graphite case, the best results were observed when a separator was used in conjunction with the GC CE. The GC CEs were likely flaking due to the graphitic domains of the material oxidising during use.[57]

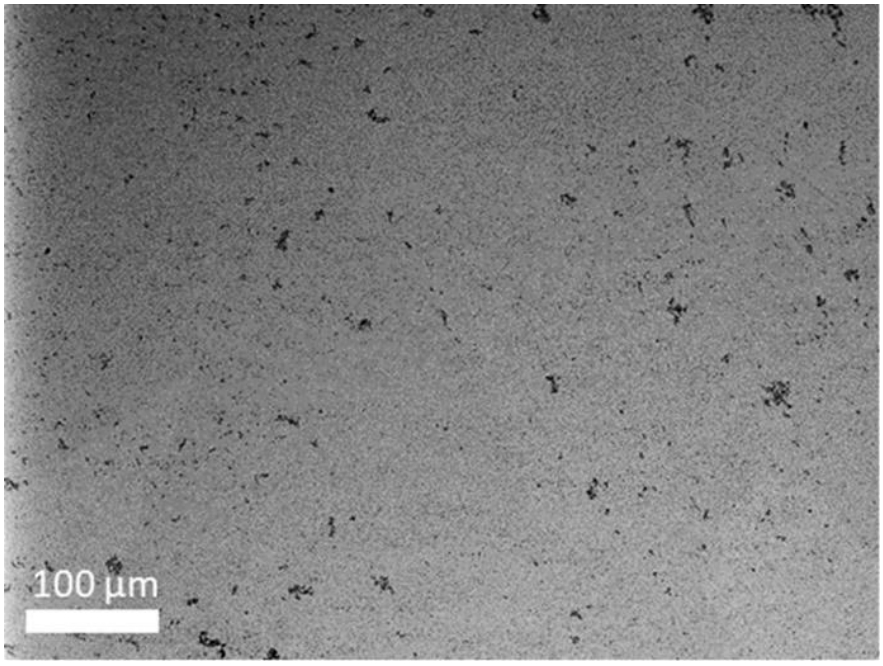


Figure 3.10 Back-scattered SEM image of a Pt surface after 24 h of HER at −10 mA cm^{-2} in an undivided cell containing a graphite counter electrode, showing contamination of the Pt with carbonaceous material (dark spots).

3.3.4 Application of Findings

The evidence and data presented above make a strong case for the use of carbon-based counter electrodes in conjunction with either a Nafion

membrane or a glass frit separator. This is the first time that this recommendation is supported by rigorous electrochemical evidence.

To further validate these findings, we applied our counter electrode recommendations to some real-life scenarios. First, is directly related to the conditions we have tested: the HER stability of a molybdenum sulfide electrocatalyst coated onto a GC electrode is assessed. Second, we apply the use of a carbon-based CE to a cycling experiment used to assess the stability of a redox system over time.

3.3.4.1 H_2 Evolution by MoS_2 at Constant Current

MoS_2 has been demonstrated to be a good electrocatalyst for the hydrogen evolution reaction.[58,59] Here we use it as a more realistic example of a test electrocatalyst than the polished metal and carbon surfaces used previously in the chapter. 10 µL of an ink consisting of MoS_2 dispersed in Nafion (5% in aliphatic alcohols) and ethanol was dropcast onto a glassy carbon rotating disc electrode. This ink formulation has not been optimised for performance as this experiment is being used as a demonstration of the effect of the counter electrode contamination mitigation strategy on the measured activity rather than of the material's electrocatalytic properties.

Figure 3.11 clearly demonstrates that when a Pt CE is used with no separating membrane the activity of the electrocatalyst increases significantly after 24 hours of testing at a constant current of −10 mA cm^{-2}. However, when a graphite rod is used as the counter electrode, the activity of the electrocatalyst does not change over the course of the 24-hour experiment. Unlike our idealised tests, we observed no difference between the use of a carbon CE with and without a separating frit. This may be because the increased surface area of the material makes it less susceptible to contamination from the counter electrode due to the high number of active sites available for the reaction to take place. Despite this, we believe it is still prudent to use a glass frit whenever possible to reduce any possible contamination.

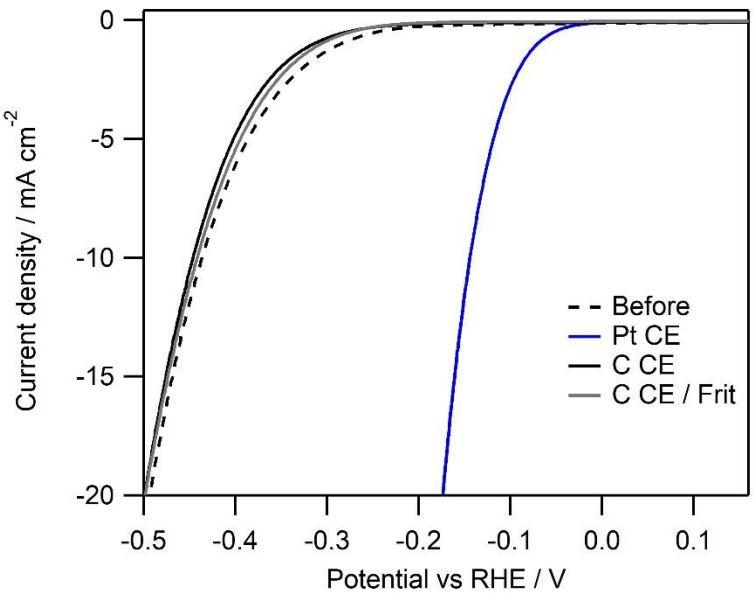


Figure 3.11 Voltammograms recorded before (dashed line) and after (solid lines) 24 h of HER at −10 mA cm^{-2} at a GC electrode coated with MoS_2 in divided (black/grey solid lines) and undivided (blue solid)

3.3.4.2 Potential-Cycling Experiments of Polyoxometalate Species

Up to this point, all the stability tests presented have been at a constant current. However, stability and durability can also be tested by repeatedly cycling the potential forward and back across a specified range. Specifically, we tested the redox-stability of the Wells-Dawson tungsten polyoxometalate (POM) $K_6[P_{12}W_{18}O_{62}](H_2O)_{14}$ encapsulated within a single-walled nanotube (SWNT), hereby referred to as POM@SWNT. This family of materials has well-defined redox chemistry and unique properties of relevance to energy-related applications.[60] A film of the material was dropcast onto a stationary GC working electrode and cycled in Ar-purged 1 mol dm^{-3} HCl at 100 mV s^{-1}. The resulting voltammogram is shown as Cycle 1 in Figure 3.12A. The electrochemistry is surface-confined leading to bell-shaped peaks with near 0 mV peak-to-peak separation between corresponding oxidation and reduction processes.

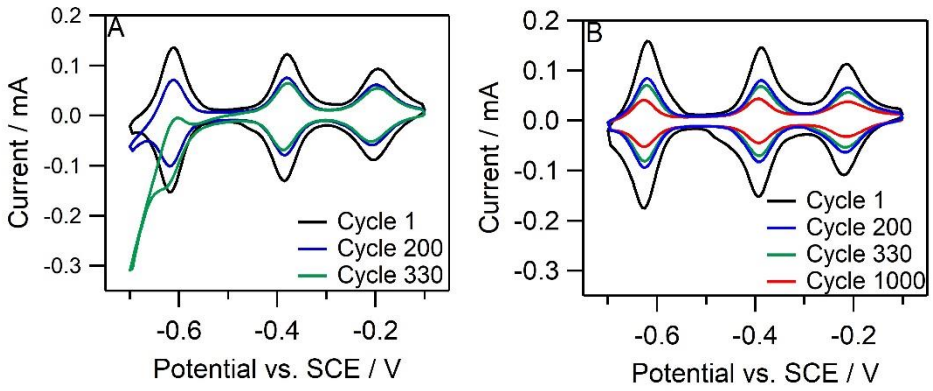


Figure 3.12 1st, 200th, and 330th cyclic voltammograms of $K_6[P_2W_{18}O_{62}](H_2O)_{14}$@SWNT deposited onto a stationary GC electrode and cycled at 100 mV s^{-1} in an undivided cell containing a (A) Pt CE or (B) GC rod CE.

The redox processes between −0.1 and −0.7 V (vs SCE) are attributed to (most positive to most negative):

$$[P_2W_{18}O_{62}]^{6-} + 2e^- \leftrightarrow [P_2W_{18}O_{62}]^{8-} \quad (1)$$

$$[P_2W_{18}O_{62}]^{6-} + 2e^- + 2H^+ \leftrightarrow [H_2P_2W_{18}O_{62}]^{8-} \quad (2)$$

$$[H_2P_2W_{18}O_{62}]^{8-} + 2e^- + 2H^+ \leftrightarrow [H_4P_2W_{18}O_{62}]^{8-} \quad (3)$$

After fewer than 200 cycles, in the system using a Pt CE, an increase in the cathodic current is clearly visible at potentials negative of −0.6 V. This current is clearly hydrogen evolution as it occurs concurrently with bubble formation which eventually covers the whole electrode and prematurely ends the experiment. This contamination is a vicious cycle as the more Pt coats onto the WE, the higher the reductive currents become and so the counter electrode is driven to ever higher oxidative currents.

Previously, this current has been attributed to the POMs forming an electrocatalytic material active towards the HER.[61,62] However, it was subsequently proven to be Pt dissolved from the CE and subsequently deposited onto the WE surface that led to the increase in HER activity.[28] Zhang *et al* even used this observation to generate a highly active HER electrocatalyst based on Pt co-deposited with POMs onto an electrode surface.[63] Despite this observation being made in the 1980s, Pt is still used as the CE in such systems by unwary electrochemists, so we wanted to definitively demonstrate that the observation vanishes when the CE material is changed.

To this end, we repeated the cycling experiments of the POM@SWNT coated on GC and used a GC rod as the counter electrode. As is clearly shown in Figure 3.12B there is no encroaching cathodic HER current. This allows the stability of the redox couples to be accurately assessed. In this case, the redox activity drops off during cycling due to a slow loss of material from the working electrode coating. The lack of HER also meant there was no bubble formation during the experiment. Another key experimental detail to note here is that the system was stationary, i.e., the electrode was not rotating. The significance of this is that Pt cations were able to diffuse to the WE and contaminate it sufficiently to drastically change the voltammetry without the necessity of forced convection. It is likely that this lack of forced convection also helped limit any possible contamination from the GC CE. Another factor reducing the contamination is that the currents reached were not particularly high (especially compared to the constant current HER experiments) so the GC CE would never reach particularly high oxidative potentials.

3.4 Conclusions

The work presented in this chapter has definitively shown that Pt- and Au-based counter electrodes release metallic cations which can migrate to and deposit on the working electrode. This contamination leads to an overestimation of electrocatalytic performance. The frequently suggested mitigation strategy of a glass frit or Nafion-117 membrane is not sufficient to prevent this contamination over the length of a 24-hour constant current experiment. Using a metal-free counter electrode such as a graphite or glassy carbon rod was shown lead to the opposite problem, in which an active working electrode surface is deactivated by contaminants from the counter electrode. To prevent this a Nafion-117 membrane or glass frit should be used to separate the working and counter electrodes. This work showed no difference between a membrane or frit for this purpose. This solution was shown to work to prevent contamination of a MoS_2 electrocatalyst under test conditions. However, use a carbon-based CE without a separating membrane or frit was shown to be just as effective in this case. Finally, erroneously attributed hydrogen evolution in a

POM-based was shown to no longer be present when the CE was changed from Pt to GC.

3.5 References

1. Hunter, B. M., Gray, H. B. & Müller, A. M. Earth-Abundant Heterogeneous Water Oxidation Catalysts. *Chem. Rev.* **116**, 14120–14136 (2016).

2. Roger, I., Shipman, M. A. & Symes, M. D. Earth-abundant catalysts for electrochemical and photoelectrochemical water splitting. *Nat. Rev. Chem.* **1**, 1–13 (2017).

3. Hong, W. T. *et al.* Toward the rational design of non-precious transition metal oxides for oxygen electrocatalysis. *Energy Environ. Sci.* **8**, 1404–1427 (2015).

4. Shao, M., Chang, Q., Dodelet, J. P. & Chenitz, R. Recent Advances in Electrocatalysts for Oxygen Reduction Reaction. *Chem. Rev.* **116**, 3594–3657 (2016).

5. Garsany, Y., Baturina, O. A., Swider-Lyons, K. E. & Kocha, S. S. Experimental Methods for Quantifying the Activity of Platinum Electrocatalysts for the Oxygen Reduction Reaction. *Anal. Chem.* **82**, 6321–6328 (2010).

6. Voiry, D. *et al.* Best Practices for Reporting Electrocatalytic Performance of Nanomaterials. *ACS Nano* **12**, 9635–9638 (2018).

7. McCrory, C. C. L., Jung, S., Peters, J. C. & Jaramillo, T. F. Benchmarking Heterogeneous Electrocatalysts for the Oxygen Evolution Reaction. *J. Am. Chem. Soc.* **135**, 16977–16987 (2013).

8. McCrory, C. C. L. *et al.* Benchmarking Hydrogen Evolving Reaction and Oxygen Evolving Reaction Electrocatalysts for Solar Water Splitting Devices. *J. Am. Chem. Soc.* **137**, 4347–4357 (2015).

9. Benck, J. D., Pinaud, B. A., Gorlin, Y. & Jaramillo, T. F. Substrate selection for fundamental studies of electrocatalysts and photoelectrodes: inert potential windows in acidic, neutral, and basic electrolyte. *PLoS One* **9**, e107942 (2014).

10. Chen, J. G., Jones, C. W., Linic, S. & Stamenkovic, V. R. Best Practices in Pursuit of Topics in Heterogeneous Electrocatalysis. *ACS Catal.* **7**, 6392–6393 (2017).

11. Li, J., Liu, H. Y., Lu, Y., Guo, X. W. & Song, Y. J. Influence of counter electrode material during accelerated durability test of non-precious metal electrocatalysts in acidic medium. *Chinese J. Catal.* **37**, 1109–1118 (2016).

12. Niu, S., Li, S., Du, Y., Han, X. & Xu, P. How to Reliably Report the Overpotential of an Electrocatalyst. *ACS Energy Lett.* **5**, 1083–1087 (2020).

13. Dekanski, A., Stevanovic, J., Stevanovic, R., Nikolic, B. Z. & Jovanovic, V. M. Glassy carbon electrodes I. Characterization and electrochemical activation. *Carbon* **39**, 1195–1205 (2001).

14. Bystron, T., Sramkova, E., Dvorak, F. & Bouzek, K. Glassy carbon electrode activation - A way towards highly active, reproducible and stable electrode surface. *Electrochim. Acta* **299**, 963–970 (2019).

15. Chen, R. *et al.* Use of Platinum as the Counter Electrode to Study the Activity of Nonprecious Metal Catalysts for the Hydrogen Evolution Reaction. *ACS Energy Lett.* **2**, 1070–1075 (2017).

16. Pletcher, D. *A First Course in Electrode Processes*. (RSC Pub., 2009).

17. Colburn, A. W., Levey, K. J., O'Hare, D. & Macpherson, J. V. Lifting the lid on the potentiostat: a beginner's guide to understanding electrochemical circuitry and practical operation. *Phys. Chem. Chem. Phys.* **23**, 8100–8117 (2021).

18. Elgrishi, N. *et al.* A Practical Beginner's Guide to Cyclic Voltammetry. *J. Chem. Educ.* **95**, 197–206 (2018).

19. Pourbaix, M. *Atlas of electrochemical equilibria in aqueous solutions*. (National Association of Corrosion Engineers, 1974).

20. Pourbaix, M. J. N. Electrochemical Properties of the Platinum Metals: A New Approach To Studies Of Corrosion Resistance And Cathodic Protection. *Platin. Met. Rev.* **3**, 47–53 (1959).

21. Finkelstein, N. P. & Hancock, R. D. A new approach to the chemistry of gold. *Gold Bull.* **7**, 72–77 (1974).

22. Yasuda, K., Taniguchi, A., Akita, T., Ioroi, T. & Siroma, Z. Platinum dissolution and deposition in the polymer electrolyte membrane of a PEM fuel cell as studied by potential cycling. *Phys. Chem. Chem. Phys.* **8**, 746–752 (2006).

23. Inoue, M., Nakazawa, A. & Umeda, M. Study of Pt electrode dissolution in H_2O_2-containing H_2SO_4 solution using an electrochemical quartz crystal microbalance. *J. Power Sources* **196**, 4579–4582 (2011).

24. Wei, R., Fang, M., Dong, G. & Ho, J. C. Is platinum a suitable counter electrode material for electrochemical hydrogen evolution reaction? *Sci. Bull. (Beijing)* **62**, 971–973 (2017).

25. Xing, L. Y. *et al.* Platinum Electro-dissolution in Acidic Media upon Potential Cycling. *Electrocatalysis* **5**, 96–112 (2014).

26. Dong, G. F. *et al.* Insight into the electrochemical activation of carbon-based cathodes for hydrogen evolution reaction. *J. Mater. Chem. A* **3**, 13080–13086 (2015).

27. Xu, X. X. *et al.* Revisiting the factors influencing gold electrodes prepared using cyclic voltammetry. *Sens. Actuators B Chem* **283**, 146–153 (2019).

28. Kulesza, P. J., Lu, W. & Faulkner, L. R. Cathodic fabrication of platinum microparticles via anodic dissolution of a platinum counter-electrode: Electrocatalytic probing and surface analysis of dispersed platinum. *J. Electroanal. Chem.* **336**, 35–44 (1992).

29. Dondapati, J. S., Thiruppathi, A. R., Salverda, A. & Chen, A. Comparison of Pt and IrO_2-Ta_2O_5/Ti as a counter electrode in acidic media. *Electrochem. commun.* **124**, 106946 (2021).

30. Popczun, E. J. *et al.* Nanostructured nickel phosphide as an electrocatalyst for the hydrogen evolution reaction. *J. Am. Chem. Soc.* **135**, 9267–9270 (2013).

31. Roy, C. *et al.* Trends in Activity and Dissolution on RuO_2 under Oxygen Evolution Conditions: Particles versus Well-Defined Extended Surfaces. *ACS Energy Lett.* **3**, 2045–2051 (2018).

32. Tian, M. *et al.* Influence of the Working and Counter Electrode Surface Area Ratios on the Dissolution of Platinum under Electrochemical Conditions. *ACS Catal.* **6**, 5108–5116 (2016).

33. Sagarik, K., Phonyiem, M., Lao-Ngam, C. & Chaiwongwattana, S. Mechanisms of proton transfer in Nafion®: Elementary reactions at the sulfonic acid groups. *Phys. Chem. Chem. Phys.* **10**, 2098–2112 (2008).

34. Mauritz, K. A. & Moore, R. B. State of Understanding of Nafion. *Chem. Rev.* **104**, 4535–4586 (2004).

35. Yu, X., Joseph, J. & Manthiram, A. Polymer lithium–sulfur batteries with a Nafion membrane and an advanced sulfur electrode. *J. Mater. Chem. A* **3**, 15683–15691 (2015).

36. Burlatsky, S. F. *et al.* The Dynamics of Platinum Precipitation in an Ion Exchange Membrane. *J. Electrochem. Soc.* **158**, B322–B330 (2011).

37. Peron, J., Nedellec, Y., Jones, D. & Roziere, J. The effect of dissolution, migration and precipitation of platinum in Nafion®-based membrane electrode assemblies during fuel cell operation at high potential. *J. Power Sources* **185**, 1209–1217 (2008).

38. Ohma, A., Suga, S., Yamamoto, S. & Shinohara, K. Membrane degradation behavior during open-circuit voltage hold test. *J. Electrochem. Soc.* **154**, B757–B760 (2007).

39. Hawut, W., Hunsom, M. & Pruksathorn, K. Platinum electroless deposition on Nafion membrane for PEM fuel cells. *Korean J. Chem. Eng.* **23**, 555–559 (2006).

40. Wu, G., More, K. L., Johnston, C. M. & Zelenay, P. High-performance electrocatalysts for oxygen reduction derived from polyaniline, iron, and cobalt. *Science* **332**, 443–447 (2011).

41. Lin, C., Gao, Z. F., Yang, J. H., Liu, B. & Jin, J. Porous superstructures constructed from ultrafine FeP nanoparticles for highly active and exceptionally stable hydrogen evolution reaction. *J. Mater. Chem. A* **6**, 6387–6392 (2018).

42. Lee, J. & Bang, J. H. Reliable counter electrodes for the hydrogen evolution reaction in acidic media. *ACS Energy Lett.* **5**, 2706–2710 (2020).

43. Ives, D. J. G. & Janz, G. J. *Reference electrodes, theory and practice*. (Academic Press, 1961).

44. Inzelt, G., Lewenstam, A. & Scholz, F. *Handbook of Reference Electrodes*. (Springer, 2013).

45. Bard, A. J. & Faulkner, L. R. *Electrochemical Methods*. (John Wiley & Sons, Inc., 2001).

46. Hamann, C. H., Hamnett, A. & Vielstich, W. *Electrochemistry*. (Wiley-VCH, 2007).

47. Gileadi, E. *Physical Electrochemistry: Fundamentals, Techniques and Applications*. (Wiley-VCH, 2011).

48. Compton, R. G. & Banks, C. E. *Understanding voltammetry*. (World Scientific, 2018).

49. Hau, N. Y. *et al.* Aminosilane-Assisted Electrodeposition of Gold Nanodendrites and Their Catalytic Properties. *Sci. Rep.* **7**, 39839 (2017).

50. Li, Y. *et al.* Hydrogen Evolution Electrocatalyst Design: Turning Inert Gold into Active Catalyst by Atomically Precise Nanochemistry. *J. Am. Chem. Soc.* **143**, 11102–11108 (2021).

51. Hammond, J. S. & Winograd, N. XPS Spectroscopic Study of Potentiostatic and Galvanostatic Oxidation of Pt Electrodes in H_2SO_4 and $HClO_4$. *J. Electroanal. Chem.* **78**, 55–69 (1977).

52. Casaletto, M. P., Longo, A., Martorana, A., Prestianni, A. & Venezia, A. M. XPS study of supported gold catalysts: the role of Au^0 and $Au^{+\delta}$ species as active sites. *Surf. Interface Anal.* **38**, 215–218 (2006).

53. Schneider, W. D. & Laubschat, C. Actinide-Noble-Metal Systems - an X-Ray-Photoelectron-Spectroscopy Study of Thorium-Platinum, Uranium-Platinum, and Uranium-Gold Intermetallics. *Phys. Rev. B* **23**, 997–1005 (1981).

54. Zatoń, M., Rozière, J. & Jones, D. J. Current understanding of chemical degradation mechanisms of perfluorosulfonic acid membranes and their mitigation strategies: A review. *Sustain. Energy Fuels* **1**, 409–438 (2017).

55. Macauley, N., Wong, K. H., Watson, M. & Kjeang, E. Favorable effect of in-situ generated platinum in the membrane on fuel cell membrane durability. *J. Power Sources* **299**, 139–148 (2015).

56. Jerkiewicz, G. Applicability of Platinum as a Counter-Electrode Material in Electrocatalysis Research. *ACS Catal.* **12**, 2661–2670 (2022).

57. Yi, Y. *et al.* Electrochemical corrosion of a glassy carbon electrode. *Catal. Today* **295**, 32–40 (2017).

58. Zhuang, Z., Huang, J., Li, Y., Zhou, L. & Mai, L. The Holy Grail in Platinum-Free Electrocatalytic Hydrogen Evolution: Molybdenum-Based Catalysts and Recent Advances. *ChemElectroChem* **6**, 3570–3589 (2019).

59. Benck, J. D., Chen, Z. B., Kuritzky, L. Y., Forman, A. J. & Jaramillo, T. F. Amorphous Molybdenum Sulfide Catalysts for Electrochemical Hydrogen Production: Insights into the Origin of their Catalytic Activity. *ACS Catal.* **2**, 1916–1923 (2012).

60. Jordan, J. W. *et al.* Host–Guest Hybrid Redox Materials Self-Assembled from Polyoxometalates and Single-Walled Carbon Nanotubes. *Adv. Mater.* **31**, 1904182 (2019).

61. Keïta, B. & Nadjo, L. Activation of electrode surfaces: Application to the electrocatalysis of the hydrogen evolution reaction. *J ElectroAnal. Chem. Interfacial Electrochem* **191**, 441–448 (1985).

62. Keita, B. & Nadjo, L. New oxometalate-based materials for catalysis and electrocatalysis. *Mater. Chem. Phys.* **22**, 77–103 (1989).

63. Zhang, C. *et al.* Highly Active Hydrogen Evolution Electrodes via Co-Deposition of Platinum and Polyoxometalates. *ACS Appl. Mater. Interfaces* **7**, 11648–11653 (2015).

Chapter 4. The Effect of Encapsulation on the Electrocatalytic Performance of Cobalt Oxide

4.1 Introduction

The electrolysis of water is typically achieved through the oxygen evolution reaction (OER) at the anode and the hydrogen evolution reaction (HER) at the cathode. The HER is relatively fast and very small overpotentials can be achieved, especially in acidic electrolytes.[1] In contrast, the OER is kinetically sluggish due to the multiple complex electron and proton transfer reactions involved.[2] To reach economically useful OER rates, rare and expensive metals (and their oxides) are required such as Pt, Ir, or Ru.[3–6] Thus, much effort has been devoted to designing electrocatalysts which either minimise the quantity of expensive metals or avoids their use altogether.[2,7–16]

Carbon nanotubes (CNTs) are often used in the design of novel electrocatalysts owing to their high electronic conductivity and large surface area making them ideal support materials allowing for rapid electron transfer.[17–20] Most examples of CNT-based electrocatalysts only utilise the external surface of the tube,[21–26] though some make use of the internal concave cavity of the tubes.[12,27,28] When the external surface of a tube is modified with a molecule or particle it is known as an exohedral hybrid, whereas when the internal cavity is used to encapsulate a material, it is an endohedral hybrid.[29] Even if the same molecule or particle is used in both cases, the curvature of the CNT wall leads to a difference in π-electron density meaning an externally adsorbed material may have different properties to an internally encapsulated one.[30] For endohedral hybrids, the size of the nanotube determines which molecules can be encapsulated, and an optimal relationship between the size of the cavity and size of the molecule will lead to encapsulation being favoured over surface adsorption.[31]

Endohedral hybrids (denoted M@CNT, where M is the encapsulated species) have been frequently used to enhance chemical reactions.[29,30,32–34] Typically, reactants will enter the tube and either chemically react within the tube (nanoreactor) or a reactant will enter the tube and then interact with the

encapsulated catalyst generating a product. This product can then remain in the tube or, if there is sufficient volume to allow for diffusion, leave the tube and enter the bulk.[32] Such catalysts have been used to, for example, enhance the stereoselectivity of asymmetric reactions,[34] improve the conversion of rate and stability of Suzuki coupling,[33] and allow the sensing of peroxide and glucose in biological applications.[35] In each of these cases, the improvement can be partially attributed to the confinement effect, which can both improve the stability of a catalyst but also lead to an enrichment of the reagents within the nanotube.[30,36] However, the benefits of confinement only go so far and it is important to note that multiwalled carbon nanotubes (MWNTs) were used in the given examples owing to their increased internal diameter. The catalytic reactions required reactants to enter the nanotubes, interact with the encapsulated catalyst, and the products to then leave the tube. If a narrower tube, such as a single-walled nanotube (SWNT) was used, then there may not be sufficient space for the flow of reagents and products.[32]

In electrochemical reactions, the location of the active site is less clear. It is well-known that redox active species can remain electrochemically active after encapsulation within a CNT as has recently been reviewed by our group.[37] There is strong evidence by McSweeney *et al* that the mechanism of a redox reaction is significantly altered by the extreme endohedral confinement of redox-active molecules within a SWNT.[38] Bulky ligands cannot enter the tube in order to electrochemically react with the confined organometallic complex and the ligand is unable to react with the surface of the tube. It is often assumed that generally electrocatalysis using endohedral hybrids favour an active site on the external surface of the CNT.[32,36] For example, Deng *et al* endohedrally modified CNTs with an iron-based electrocatalyst to enhance the ORR[39] and the HER[27]. Their DFT calculations strongly supported the active site being the electronically modified CNT surface, rather than the oxygen needing to directly interact with the encapsulated iron. However, this is not always the case; Sun *et al* suggested that the oxidation and reduction of peroxide by an endohedral ferrocene hybrid

electrocatalyst (Fc@SWNT) occurred inside the tube and not on the external surface.[40]

The discussion of whether the electrocatalytic active site may be at the endohedral metal surface or at the surface of the CNT is analogous to the discussion around carbon-coated electrocatalysts generally. Certainly, there can be considered some level of equivalence between a metal surrounded by the carbon wall of a CNT and a core metal coated in a shell of graphitic carbon layers. The shell imparts enhanced conductivity owing to the sp^2 conjugated carbons[36] in a similar way to the sp^2 carbons present in a CNT wall. Wen *et al* coated a platinum core with a carbon shell to generate nanoparticles which were active toward the electrocatalytic ORR.[41] They proposed that the active site was still the platinum, and that oxygen diffuses through micropores in the carbon that are large enough for oxygen but small enough to prevent methanol from fouling the platinum core. Despite this, the carbon itself is suggested to be active due to electron transfer from the metal core potentially leading to two active sites. The pore theory was furthered by Choi and co-workers who suggested the small size of the pores led to specificity for end-on adsorption of O_2 onto the platinum surface which then favoured the $2e^-$ ORR pathway.[42] However, the identity of the encapsulated material altered the electronics of the carbon shell which in turn altered the activity of the electrocatalyst suggesting the carbon also influenced the electrocatalysis beyond just stabilisation. Carbon-based shells and supports have been used to develop single-atom catalyst materials for the ORR in which the carbon is used to isolate metallic centres in an attempt to maximise the specific activity of each atom. The conflict over the identity of the active site can be seen in the two design strategies deployed to optimise such electrocatalyst materials. Some favour increasing the porosity of the carbon support to increase access to the single atom centre, whereas others opt for modulation of the electronic structure of the support, presumably under the assumption that the electrocatalysis is happening at the carbon rather than the metal centre.[43]

Careful experimental design can allow the elucidation of the active site(s). For example, Choi *et al* selectively poisoned the Pt with cyanide whilst leaving the carbon unchanged. The subsequent loss in activity strongly supported the Pt as being the active site.[42] Prato and co-workers recently suggested that more experimental effort should be given to discerning the active site and that one should not assume one site over another.[36]

We present a material for the OER in which cobalt oxide is encapsulated within single-walled nanotubes (Co_3O_4@SWNT). Cobalt-based oxide materials have shown promise as OER electrocatalysts in a variety of electrolytes.[16] This presents multiple angles of novelty. The majority of the discussion around the mechanism and active sites of electrocatalysts incorporating endohedral materials within CNTs has focused on reduction reactions owing to the CNTs intrinsic activity to these reactions as a result of the facile electron mobility in such systems,[36] and as such there is limited work on the OER. Additionally, although multi-walled CNTs (MWNTs) have been shown to easily encapsulate metal oxides,[44,45] it is harder to encapsulate such materials in SWNTs given the greater size constraints. The literature examples which do demonstrate MOx@SWNTs require harsh conditions that are not conducive to generating a sustainable material.[46] Our process is simple with relatively few steps.

The Co_3O_4@SWNT shows greater stability than the exohedrally modified Co_3O_4/SWNT. Such stability has been shown recently by Wang *et al* for Fe_3C@MWNTs, and though the nature of the active site was not sufficiently determined by their experiments the authors suggest the reactions take place at oxygen functionalities on the surface of the tubes.[47] In this chapter, the active site for the OER is experimentally determined. It is shown that the active site cannot be at the surface of the encapsulated Co_3O_4 material as there is no loss in electrocatalytic activity when the SWNTs are capped with fullerenes to prevent the movement of reagents and products in and out of the SWNTs. Further, the material shows remarkable mass activity with the activity per mass unit of endohedral Co_3O_4 massively outperforming that of the exohedral

material. This work represents significant advance in our understanding of OER electrocatalysis at endohedral hybrid materials.

4.2 Experimental Section

4.2.1 Materials

SWNTs (P2-SWNTs, arc discharge, Carbon Solutions, USA) were refluxed in nitric acid (3 mol dm^{-3}) for three hours and filtered with deionised water. They were then heated at 600 °C for 30 minutes to open the SWNT termini, giving a 50 % weight loss. All other chemicals were used as supplied (Sigma Aldrich).

4.2.2 Material Preparation

$Co_2(CO)_8$ (10 mg, 0.029 mmol) and freshly opened SWNTs (20mg) were sealed in a glass ampoule under reduced pressure (10-5 mbar) and heated to 38 °C for 72 hours. The ampoule was allowed to cool to room temperature before exposing the sample to air to give the Co_3O_4/SWNT composite. The Co_3O_4/SWNT composite was washed with 1 mol dm^{-3} HCl for 30 minutes and then MilliQ water to remove surface nanoparticles and give the Co_3O_4@SWNT composite.

4.2.3 Physical Characterisation

Transmission electron microscopy (TEM) micrographs were acquired using a JOEL 2100F TEM field emission gun microscope and JOEL JEM-2100+ microscope operated at 200 keV. Aberration corrected transmission electron microscopy (AC-TEM) was performed using the dedicated low voltage spherical (C_S) and chromatic (C_C) aberration corrected SALVE TEM microscope operated at 60 kV (Linck *et al* PRL 117 (2016) 076101, www.salve-project.de). Samples were prepared by dispersing in isopropyl alcohol and then were spotted on a copper grid mounted with a “lacey” carbon film (Agar Scientific UK) and allowed to dry. Micrographs were processed using Gatan DigitalMicrograh Software. Raman spectroscopy measurements were acquired using a Horiba–Jobin–Yvon LabRAM HR spectrometer, with a laser wavelength of 660 nm operating at a power of *ca.* 3 mW and a 600 lines mm^{-1} grating. The detector was a Synapse CCD detector. The Raman shift was calibrated using the Rayleigh peak and the

520.7 cm^{-1} silicon line from an Si(100) reference sample. Spectra were baseline corrected using a linear fitting model. Thermogravimetric analysis was performed using a TA Q500 Thermogravimetric Analyzer. All samples were analysed using a platinum pan and in the presence of air. The parameters for all experiments were: Ramp 5 °C min^{-1} from 20 to 1000 °C followed by an isotherm for 10 min at 1000 °C, air flow: 60 mL min^{-1}. X-ray photoelectron spectroscopy (XPS) was carried out using a Kratos AXIS DLD instrument equipped with an Al K_α X-ray source (1486.6 eV). A linear background correction was applied to all spectra prior to analysis. All spectra were charge corrected to the adventitious carbon peak at 284.8 eV.

4.2.4 Electrochemical and Electrocatalytic Characterisation

5.5 mg of the Co_3O_4/SWNT powder was suspended in 1 mL of ethanol and 100 µL of 5% Nafion (in aliphatic alcohols). A 10 µL drop of this ink was dropcast onto a 5 mm glassy carbon rotating disc electrode. The electrode was rotated at ~200 rpm for at least 1 h to allow the coated electrode to dry and the alcohols to evaporate. This gave a total mass loading of 0.25 mg cm^{-2} on the electrode. The loading of Co_3O_4 in the Co_3O_4/SWNT and Co_3O_4@SWNT samples was determined through TGA, as described above, to be 11.7% and 1.1% of the weight of the electrocatalyst, respectively. Oxygen evolution activity was measured in O_2-saturated 0.1 mol dm^{-3} or 1 mol dm^{-3} KOH at 1600 rpm. A Hg/HgO (0.1 mol dm^{-3} KOH) reference electrode and graphite rod counter electrode were used. The potential of the Hg/HgO (0.1 mol dm^{-3} KOH) reference electrode was measured against either a homemade RHE or a Gaskatel Hydroflex. All potentials are given versus RHE. Linear sweep voltammograms (LSVs) were measured at 20 mV s^{-1}. For stability measurements, the potential was cycled between the potentials given in the text at 100 mV s^{-1} with LSVs measured at 20 mV s^{-1} before and after. Stability measurements were taken in an O_2-free electrolyte sparged with N_2. O_2 saturation was determined by cycling between 0.9 V and 0.1 V until the O_2 reduction current observed at ~0.5 V no longer increased in magnitude. The

electrolyte was determined to be O_2 free when cycling in the same range showed no O_2 reduction currents.

4.3 Results and Discussion

4.3.1 Coating and Encapsulation of Co_3O_4 on and in SWNTs

The generation of oxide species inside and on the surface of nanotubes typically requires harsh oxidising conditions.[46] The use of organometallic precursors can help limit the harsh conditions as they can sublime at low temperatures.[48–50] However, the ligands on organometallics can leave residual contamination on and within the tubes which can affect the interface between the desired oxide and the walls of the nanotube. To this end, cobalt carbonyl ($Co_2(CO)_8$) was used as the metal precursor for the formation of the cobalt oxide in and on the single-walled nanotubes. It not only sublimes at a low temperature, but the only decomposition product is CO gas, leaving behind pure Co metal. The metal then spontaneously oxidises in the air at room temperature to form cobalt oxide. This allows for the synthesis of Co_3O_4/SWNT (that is, Co_3O_4 both on the exterior and in the interior of the SWNTs) material, without the need for harsh conditions or multiple steps, in a single-step synthetic procedure.

Prior to use, SWNTs were refluxed in HNO_3 for 3 hours to remove residual metals leftover from SWNT synthesis. The acid washed SWNTs were then washed in MilliQ water and opened by heating at 600 °C to allow access to their internal surfaces. $Co_2(CO)_8$ was added to the SWNTs under an Ar blanket to minimise exposure to air. The mixture was heated to 38 °C under reduced pressure for 72 hours to sublime $Co_2(CO)_8$ onto and into the carbon nanotubes. This was then cooled and exposed to air at room temperature, to allow spontaneous oxidation of metallic Co to an oxide, yielding the Co_3O_4/SWNT material, without any additional oxidation or processing typically required in preparation of such material. The Co_3O_4/SWNT composite was then washed with 1.0 mol dm^{-3} HCl for 30 mins to remove the surface nanoparticles while leaving the encapsulated cobalt oxide (Co_3O_4@SWNT). Wide area TEM images

are presented in Figure 4.1 showing the success of the washing procedure for removing particles from the surface of the nanotubes.

Encapsulation of Co_3O_4 within the tubes was confirmed with aberration corrected TEM (AC-TEM) which also showed that the surface Co_3O_4 particles had been removed (Figure 4.2). The encapsulated Co_3O_4 formed nanorods between 6-8 nm long and ~0.8 nm wide, which matches closely to the lattice parameter of cubic Co_3O_4 (JCPDS file No. 42-1467, space group *Fd-3m,* lattice parameter = 8.0837 Å), seen throughout the sample. The closeness of the Co_3O_4 size to its lattice parameter and the close fitting within the tube means the SWNT is on the threshold of the minimum acceptable size for a SWNT to encapsulate this material; a van der Waals gap of ~0.30-0.35 nm between Co_3O_4 and concave nanotube surface is required, hence the minimum diameter of SWNT capable of hosting Co_3O_4 is between 1.4-1.5 nm. Owing to damage to the structure from the electron beam (60 kV), the crystal structure of the encapsulated oxide could not be determined by TEM. This is a commonly occurring issue for metal oxides assessed using TEM.[51,52]

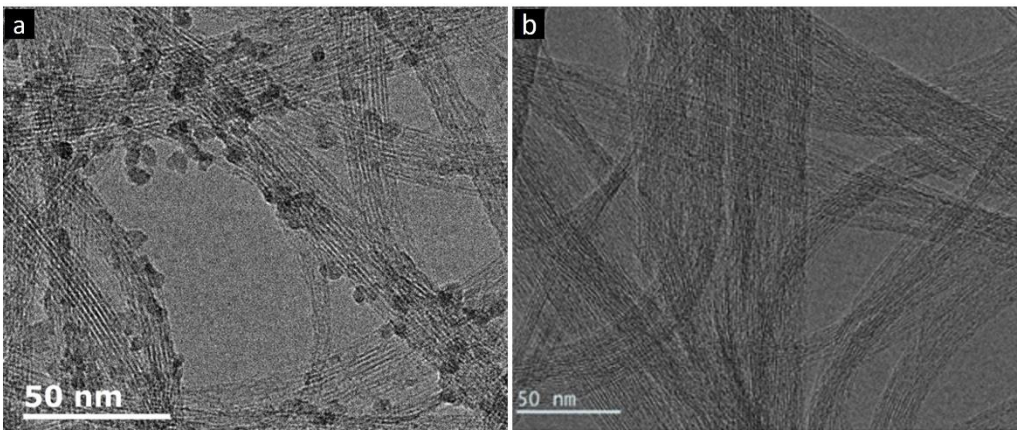


Figure 4.1 Wide area TEM images of (a) Co_3O_4/SWNT showing the presence of dark particles on the surface of the SWNTs and (b) Co_3O_4@SWNT showing the lack of particles on the SWNT surface.

Co_3O_4/SWNT and Co_3O_4@SWNT samples were compared by XPS (Figure 4.3). Cobalt peaks from the Co_3O_4/SWNT (Figure 4.3a) sample matched well to literature values of Co_3O_4, with Co $2p_{1/2}$ and Co $2p_{3/2}$ peaks at 796.8 eV and 780.9 eV respectively.[24] This match is to be expected as the Co_3O_4 in the that sample is largely on the outside of the tubes and so should not be affected by confinement within the tubes. For Co_3O_4@SWNT (Figure 4.3b), the Co 2p peaks shift negatively by ~0.6 eV. The peak shift is indicative of a stabilisation effect of the interior of the SWNTs on the encapsulated cobalt oxide, as suggested by Cui *et al.*[46] The octahedral Co^{3+} components of the 2p peaks are assigned at lower binding energies than the tetrahedral Co^{2+} components.[53] This is consistent with the literature investigating cobalt oxide with XPS.[53–58] A shoulder is seen in the spectrum for Co_3O_4/SWNT. This may be due to a mix of forms of cobalt oxide including CoO and Co_3O_4 on the surface of the tubes,[53,59] but without a pure sample of CoO on SWNTs this is not possible to definitively prove. The noise in the spectrum for Co_3O_4@SWNT may conceal a similar feature.

Raman Spectroscopy was performed on Co_3O_4@SWNT and compared to SWNTs. The bands observed at 1318 cm^{-1} and 1590 cm^{-1} are characteristic of the SWNT's radial breathing mode D band, and G band of the carbon lattice, respectively. A positive shift in the G band is seen when comparing SWNT to Co_3O_4@SWNT (1590.3 cm^{-1} and 1593.3 cm^{-1} respectively), indicating a charge transfer from the SWNT to the encapsulated metal oxide species, as has been seen previously for metal oxides encapsulated in SWNTs,[46] and for SWNTs doped with halogens.[60] The position of the G band at ~1590 cm^{-1} is indicative that the SWNTs are semiconducting in nature, as opposed to metallic which would have led to a G band measured at ~1567 cm^{-1}.[60] The G band shift for Co_3O_4@SWNT, as measured with 660 nm laser is explicitly labelled in Figure 4.4. Raman spectroscopy was not carried out on the Co_3O_4/SWNT material.

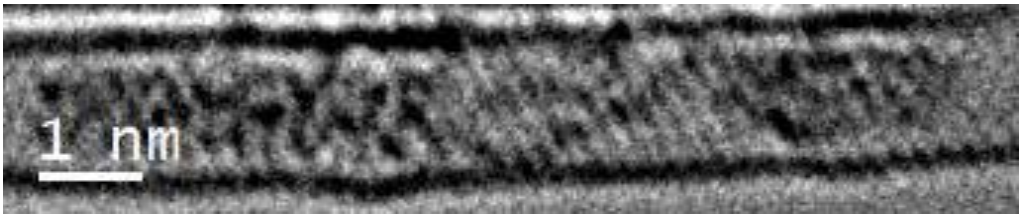


Figure 4.2 AC-TEM image showing Co_3O_4 (dark spots) encapsulated within a SWNT (Co_3O_4@SWNT).

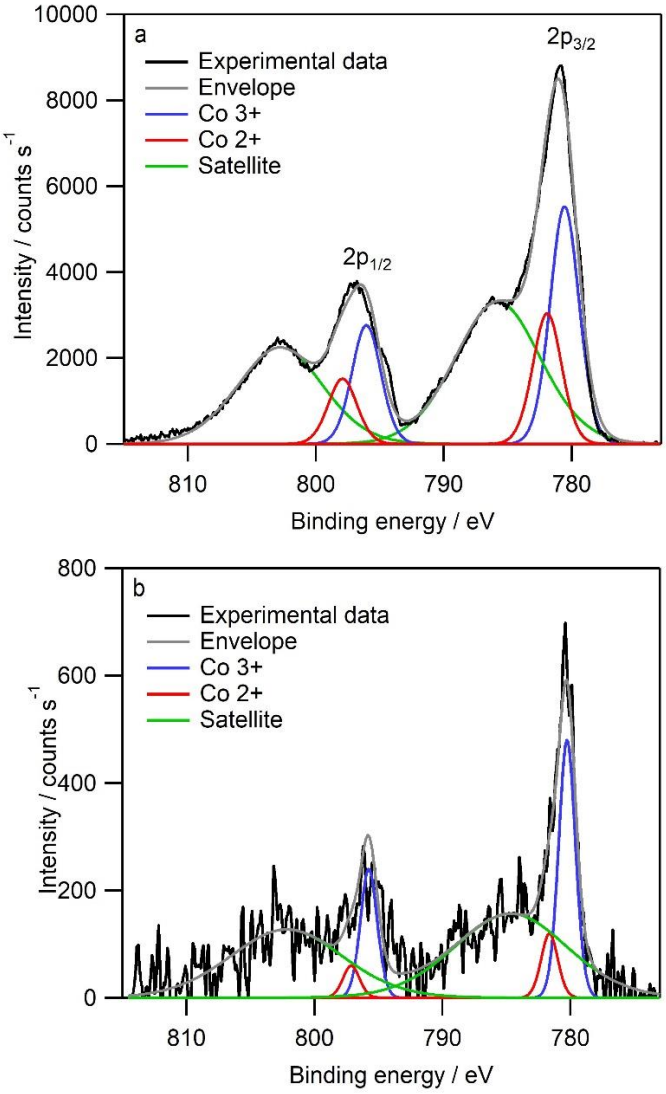


Figure 4.3 High resolution X-ray photoelectron spectra of the Co 2p region for (a) Co_3O_4/SWNT and (b) Co_3O_4@SWNT. The spectra are corrected with a linear background.

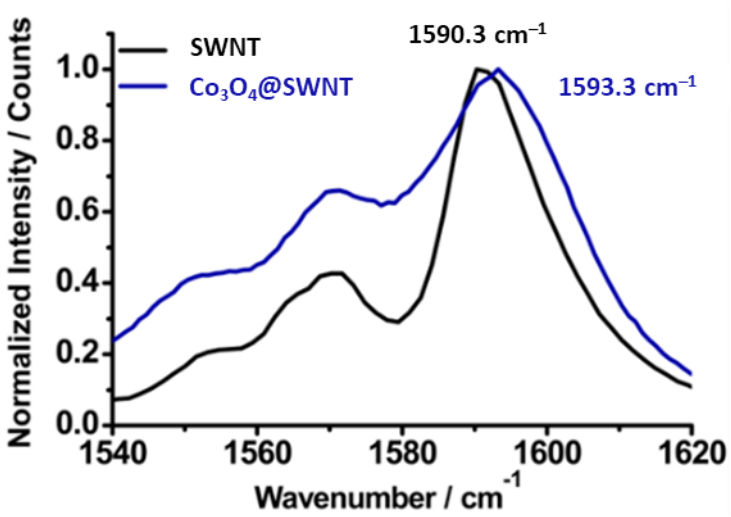


Figure 4.4 Raman spectra of Co_3O_4@SWNT (blue) compared to the G band of SWNT (black) excited at 660 nm. The values of the G band are explicitly labelled. The intensities of both lines were normalised to their respective G band maxima.

4.3.2 Effect of Encapsulation on the Oxygen Evolution Reaction

The oxygen evolution reaction is generally agreed to be the limiting reaction in overall electrolytic water-splitting. The activity of the composite materials Co_3O_4/SWNT and Co_3O_4@SWNT toward the OER was assessed through linear sweep voltammetry in 0.1 mol dm^{-3} KOH saturated with O_2 gas, which is standard practice.[4] Garcia *et al* have noted that O_2 saturation either lowers the OER activity of an electrocatalyst or has no impact.[61] They also note that such conditions can better replicate the environment of an electrolyser.[61] They go on to emphasise the importance of using a reference electrode that is insensitive to oxygen such as the Hg/HgO reference electrode used in this chapter. Bhandari *et al* showed that there is no difference in the measured OER activity using an electrolyte purged with O_2 or N_2.[62] They also demonstrated that purging with gas, regardless of whether that is O_2 or N_2, can improve the reproducibility of OER measurements.[62] 0.1 mol dm^{-3} KOH was chosen as the electrolyte was chosen as other oxide and carbon-based materials have been characterised toward the OER in this media.[63–69]

Inks of the composite materials were made by mixing the powder in ethanol and a Nafion solution (5%) to create a solids content of 5 g dm^{-3}. 10 µL of this

was deposited onto a polished glassy carbon rotating disc electrode (0.1965 cm^{-2}) resulting in a total mass loading of ~0.25 mg cm^{-2}.

The oxidation potential of a species is expected to shift when encapsulated.[37] The inset of Figure 4.5 highlights the peaks associated with the oxidation of Co_3O_4. Co_3O_4/SWNT has an oxidation peak at 1.10 V with a shoulder at 1.01 V. Co_3O_4@SWNT a smaller oxidation peak at 1.07 V, more negative than the main peak for Co_3O_4/SWNT. A negative shift in the oxidation potential is consistent with an electron withdrawing group being present, though the presence of material on both the interior and the exterior of the tubes makes qualification difficult in this case. The two peaks in the Co_3O_4/SWNT sample are likely due to differences in the internal and external cobalt oxide. A combination of electron withdrawal and confinement effects leads to the distinct peaks. Importantly, neither feature is seen in the plain SWNTs, confirming the peaks as being associated with Co_3O_4. Given the visibly different electrochemistry of the samples it is reasonable to expect different electrocatalytic behaviour.

A common metric used to compare OER electrocatalysts is the overpotential required to drive 10 mA cm_{geo}^{-2} of current (η_{10}).[4,9] As shown in Figure 4.5, η_{10} is almost the same for both Co_3O_4/SWNT and Co_3O_4@SWNT at 512 and 521 mV, respectively. SWNTs without any Co_3O_4 required an overpotential of 572 mV to afford the same current density. These overpotentials are higher than those of IrO_2 and Ir/C in the same conditions which require overpotentials of 450 mV[70] and 380 mV,[71] respectively, though our electrocatalyst materials do not require any precious metals. For single-site electrocatalysts, the scaling relationship for the OER means that 350 mV is the best achievable overpotential, however this can be lower in electrocatalysts with multiple types of active site.[8,72]

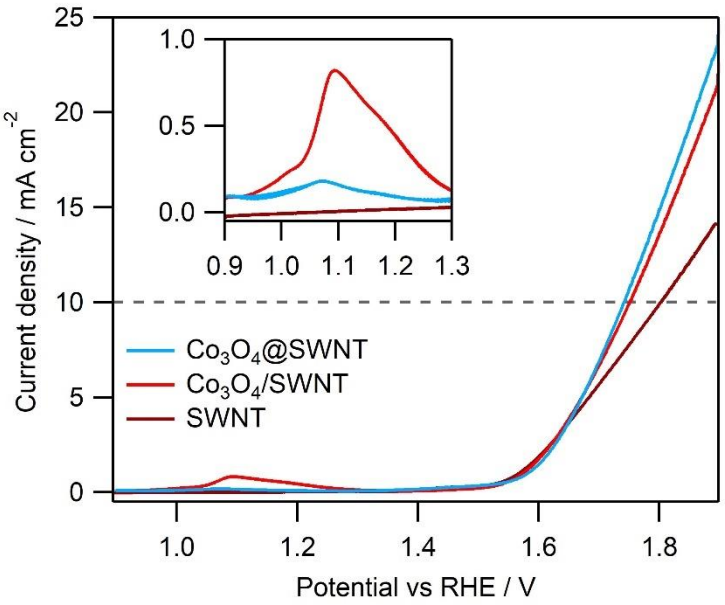


Figure 4.5 Linear sweep voltammograms measured in O_2-saturated 0.1 mol dm^{-3} KOH at a GC rotating disc electrode coated with an electrocatalyst ink containing Co_3O_4@SWNT, Co_3O_4/SWNT, or SWNT. Potential swept positive from 0.9 V to 1.9 V vs RHE at 20 mV s^{-1}. Measured against a Hg/HgO (0.1 mol dm^{-3} KOH) and then converted to RHE. A graphite rod behind a glass frit was used as the counter electrode. The dotted line shows 10 mA cm^{-2}. The inset is a magnified region of the voltammogram. Currents are normalised to the geometric area of the disc electrode (0.1965 cm^{-2}).

The geometric activity is an important metric when scaling up an electrocatalyst but gives little information about what the specific effect of the encapsulation is. To this end, we normalised the currents to the mass of cobalt oxide in the material which was calculated through TGA to be 11.7% the mass of the Co_3O_4/SWNT sample and 1.1% the mass of the Co_3O_4@SWNT sample. It is significant that despite having almost ten-times less Co_3O_4, Co_3O_4@SWNT displays a similar electrocatalytic activity to Co_3O_4/SWNT by the traditional geometrically normalised current metric.

Figure 4.6 shows the enhancement in mass activity of Co_3O_4@SWNT compared to Co_3O_4/SWNT with a remarkable 2460 A g_{Co3O4}^{-1} at 1.70 V (compared to 224 A g_{Co3O4}^{-1} for Co_3O_4/SWNT). The massive increase in current per mass of cobalt oxide highlights how much the encapsulation affects the activity. When normalised to the geometric area (as in Figure 4.5) both materials outperformed bare SWNTs by a similar amount. This mass activity metric shows

that the performance gains can almost entirely be attributed to the encapsulated material.

The improvement in the activity of the material can be attributed to the Co_3O_4 withdrawing electron density away from the surface of the SWNTs as observed through Raman spectroscopy as explained previously. By making the surface of the tubes more positive, the OH^- intermediate can bind more easily and more strongly. However, the Sabatier principle states that the binding of intermediates should be neither too strong nor too weak. Thus, further analysis is required to assess whether the increased positivity of the tube surface is beneficial.

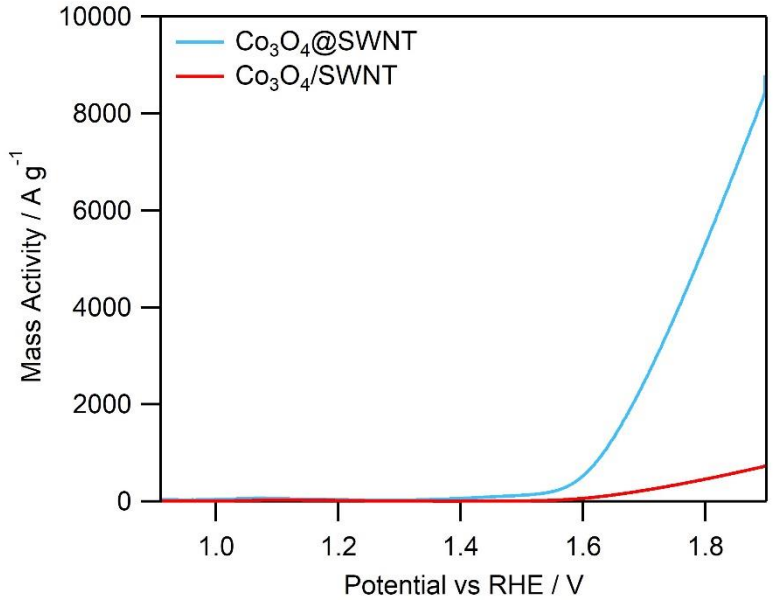


Figure 4.6 The voltammograms for Co_3O_4/SWNT and Co_3O_4@SWNT from Figure 4.5 normalised to the mass of cobalt oxide as determined by TGA.

To this end, Tafel analysis was carried out. A plot of the potential versus the log current density is referred to as a Tafel plot. The gradient of a linear portion of this line is the Tafel slope (with units of mV dec^{-1}) and provides information on the kinetics of the reaction. Small Tafel slopes are preferable as this means smaller overpotentials are required to bring about a decadal increase in current density. The value of the slope also gives insight into the rate determining step of the reaction. The Tafel slope is related to the number of electrons *n* transferred in the steps preceding the RDS, the number of electrons *q* in the

RDS (1 for an electrochemical step, 0 for a chemical step) and the charge transfer coefficient α of the RDS (assumed to be α = 0.5).[73]

A Tafel plot of Co_3O_4@SWNT, Co_3O_4/SWNT, and SWNT is presented in Figure 4.7. The region of this plot was chosen to be at low enough overpotentials that bubble formation would not alter the surface of the electrode, but a sufficient overpotential was applied that the Tafel equation is valid (at very low overpotentials the Butler-Volmer equation must be used to account for the reverse reaction).

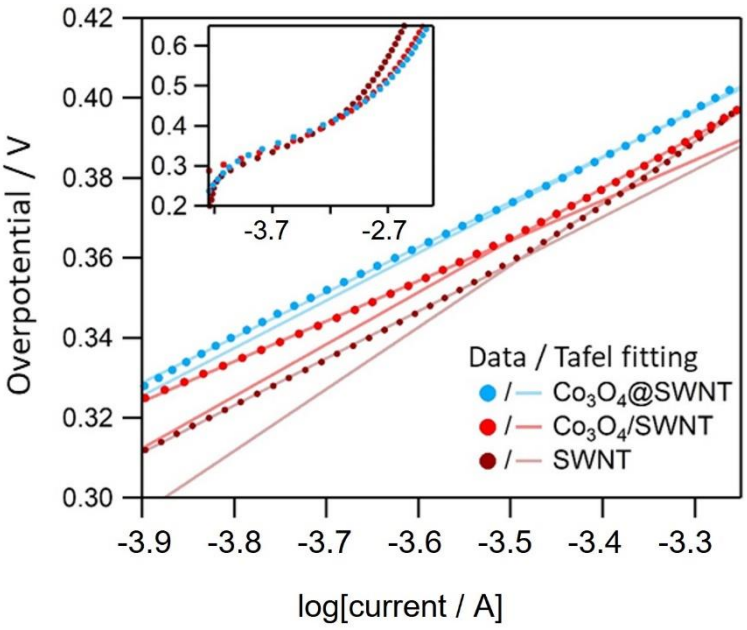


Figure 4.7 Plot of log[current / A] vs overpotential in the region used for Tafel analysis. For each electrocatalyst two Tafel slopes are shown. (Inset) A wider view of the Tafel plot showing the deviation from linear at very low and high current densities.

Multiple Tafel regions can be seen in the full Tafel plot (inset). Those at high overpotentials with very high Tafel slopes were not analysed as visible bubble formation occurred at these potentials. Two Tafel slopes are plotted in the lower current density region. The first is plotted between $-0.2 < \log(j) < 0.2$, and the second between $0.2 < \log(j) < 0.45$. All Tafel slopes plotted in these regions had $R_2 > 0.998$ indicating a good linear fit. Log(j) was used as the range decider for the Tafel slopes to ensure the rate of oxygen evolution was the same in all

cases allowing for better comparison of the slopes than if it was defined by overpotential.

At the lower current density, Co_3O_4/SWNT had the lowest Tafel slope (see Table 4.1 for comparison) followed by Co_3O_4@SWNT and SWNTs. At close to the onset potential, the kinetics of Co_3O_4/SWNT were more favourable. However, as the OER progresses, the Tafel slopes change. The slopes associated with Co_3O_4/SWNT increases by 29 % and SWNT by 31 %. Co_3O_4@SWNT, by contrast, changes by a very small amount (5.3 %). Assuming there is no bubble formation on the surface, a change in Tafel slope can mean the rate determining step has changed or the adsorption of reaction intermediates onto the surface is potential dependant.[74] Given that these Tafel slopes are defined by the current density, it can be assumed that amount of bubble formation is the same at all three electrocatalysts. That Co_3O_4@SWNT did not exhibit a significant increase in Tafel slope implies that bubble formation is not the cause for the increase in the other two materials.

Table 4.1 Comparison of Tafel slopes b and the transfer coefficient α in the two different Tafel regions in Figure 4.7. α is calculated by $\frac{1}{b}\frac{2.303RT}{F}$.[74]

	$-0.20 < \log(j) < 0.20$		$0.20 < \log(j) < 0.45$	
	b / mV dec^{-1}	α	b / mV dec^{-1}	α
Co_3O_4@SWNT	113	0.52	119	0.50
Co_3O_4/SWNT	101	0.59	130	0.46
SWNT	118	0.50	155	0.38

A slope of ~120 mV dec^{-1} is indicative of the first electrochemical step ($M + OH^- \rightleftharpoons MOH + e^-$) being the RDS (n=0, q=1, α=0.5).[75] At lower overpotentials, Co_3O_4@SWNT and SWNTs were associated with Tafel slopes very close to that value and so this is very likely the RDS. Co_3O_4/SWNT had a lower Tafel slope, though higher than 60 mV dec^{-1} which is the next highest 'standard' Tafel slope associated with the OER.[75] The ~100 mV dec^{-1} Tafel slope for Co_3O_4/SWNT suggests that at low overpotentials the adsorption of OH^- and

the first electrode transfer is more favourable than it is for Co_3O_4@SWNT. However, at higher overpotentials, the exposed oxide on the surface of the tubes may be unstable, resulting in a higher Tafel slope.

Similarly, the large increase in the Tafel slope between the two regions associated with the SWNTs could be due to oxidation of the tubes. The presence of Co_3O_4 within the tubes may lead to a synergistic stabilisation of both the oxide and the tubes as shown by Cui *et al.*[46] This may translate into the active sites being more stable active site for Co_3O_4@SWNT than Co_3O_4/SWNT.

The identity of the active site for Co_3O_4@SWNT cannot be determined from Tafel analysis. There are two possible options: the active site could be the Co_3O_4 surface inside the SWNT, or it could be the exterior carbon surface of the Co_3O_4@SWNT material. There are precedents for both in the literature, as discussed in the introduction.[27,32,36,39,40] In the preceding discussion it has been assumed that the tube surface is the active site, however this should be proven experimentally. To this end, the tubes for Co_3O_4@SWNT were filled with inactive C_{60} fullerenes. The diameter of C_{60} is sufficiently close to the size of the nanotube interior diameter that it is no longer possible for reactants and products to diffuse in and out of the ends of the tubes. Thus, the only available active sites would be on the exterior carbon surface. The electrocatalyst material was coated onto the GC RDE as before. A mixture of C_{60} and toluene was then dropped onto the coated electrode surface and allowed to dry. Excess C_{60} (that which did not enter the tubes) was rinsed off with more toluene. Parts a and b in Figure 4.8 present TEM images in which C_{60} molecules are observable throughout the full interior of the tubes up to the tips showing that the SWNTs in Co_3O_4@SWNT-C_{60} are successfully capped.

Figure 4.8c shows the OER voltammograms measured in the same conditions as before for Co_3O_4@SWNT and Co_3O_4@SWNT-C_{60}. The two materials show very similar activity. If the active site was the Co_3O_4 inside the tubes, then the activity would have been expected to drop off to near that of plain SWNTs.

Given that this is not the case, the active site is therefore confirmed not to be in the interior of the SWNTs and instead on the exterior surface.

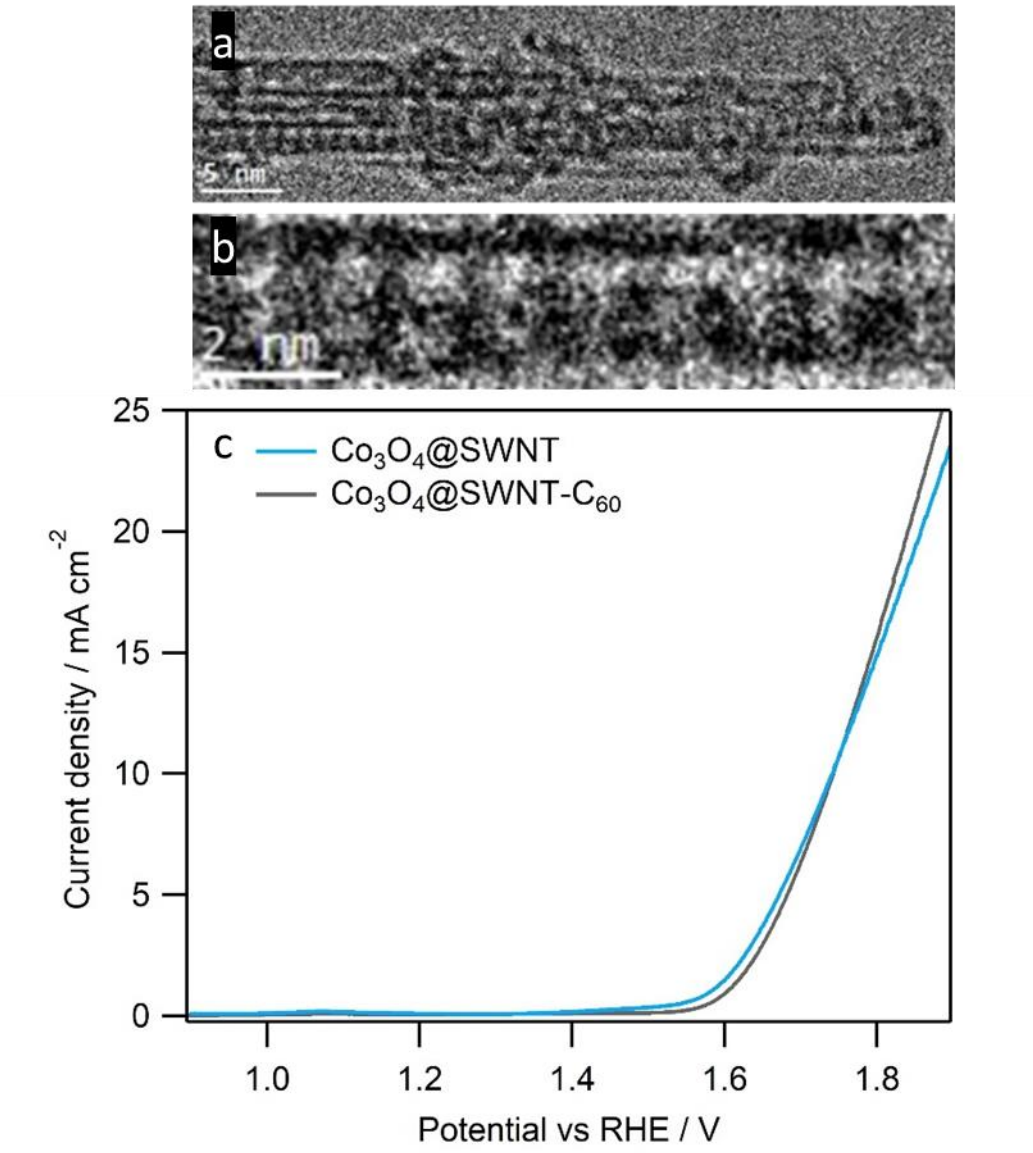


Figure 4.8 (a, b) AC-TEM images showing the successful capping of Co_3O_4@SWNT with C_{60} fullerenes as seen by the regular circular dark areas within the SWNTs. (a) also shows the presence of C_{60} fullerenes conglomerated on the surface of the tubes. (c) Linear sweep voltammograms measured in 0.1 mol dm^{-3} KOH at a GC rotating disc electrode coated with either Co_3O_4@SWNT or Co_3O_4@SWNT-C_{60}. Potential swept positive from 0.9 V to 1.9 V vs RHE at 20 mV s^{-1}. Measured against a Hg/HgO (0.1 mol dm^{-3} KOH) and then converted to RHE. A graphite rod behind a glass frit was used as the counter electrode. Currents are normalised to the geometric surface area of the electrode.

The Tafel and capping experiment results provides evidence that the active site of the hybrid electrocatalyst is the exterior carbon surface and strongly suggests a synergistic interaction between the interior Co_3O_4 and the SWNT wall which enhances OER electrocatalysis. With the active site identified, more detailed experiments can be used to elucidate how this active site changes over the course of an oxygen evolution cycle.

Between 0 V and 0.6 V vs Ag/AgCl, a small change is observed in the A_D:A_G ratio when SWNT is used as the electrocatalyst (0.023 to 0.025). In contrast, the initial ratio is higher for Co_3O_4@SWNT and a decrease is observed between 0 V and 0.4 V. This decrease is in line with the Co oxidation feature seen in the CV at $E_{1/2}$= 0.17 V. This suggests that the oxidation of the encapsulated material affects the carbon surface of the SWNTs. Between 0.6 V and 0.8 V vs Ag/AgCl, in line with the onset of the OER, an increase from 0.025 to 0.034 in the A_D:A_G ratio is observed when SWNT is used. This increase in the A_D:A_G between 0.6 V and 0.8 V is also seen in the Co_3O_4@SWNT hybrid material, from 0.029 to 0.038, suggesting that the OER in the Co_3O_4@SWNT hybrid is also happening on the carbon surface, rather than on the encapsulated cobalt oxide surface.

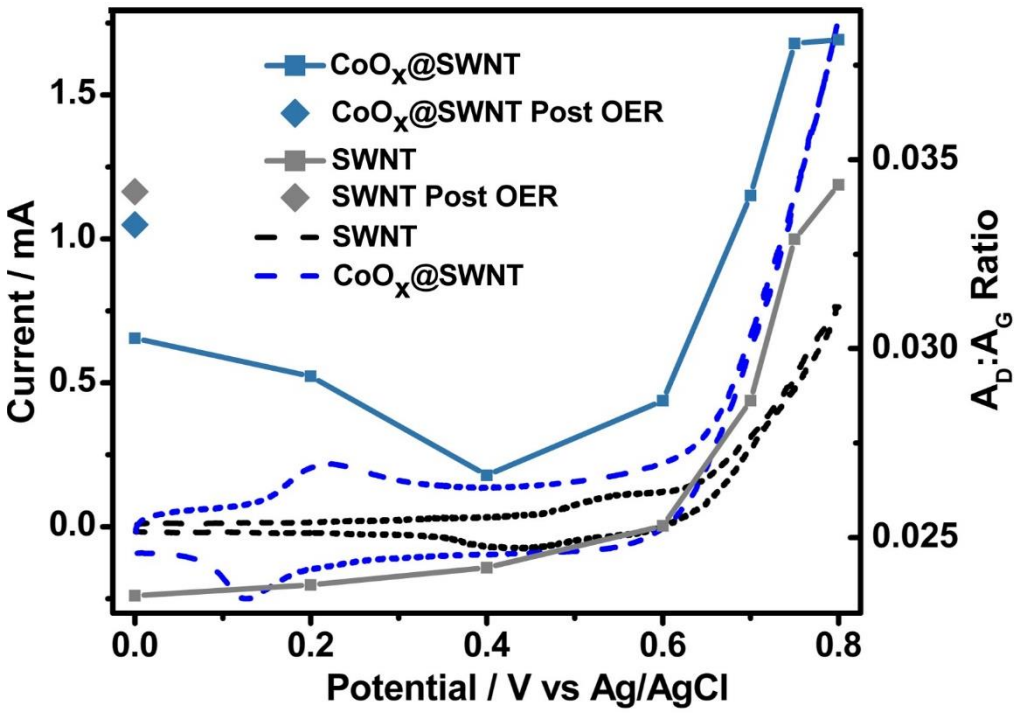


Figure 4.9 In-situ Raman spectroelectrochemistry performed in 0.1 mol dm^{-3} KOH. A GC stationary electrode was coated in Co_3O_4@SWNT or SWNT and OER carried out vs a Ag/AgCl reference electrode. A graphite rod was used as the CE. The dashed lines correspond to the CV measured at 50 mV s^{-1} and relate to the left y-axis. The solid lines correspond to the A_D:A_G ratio measured using Raman spectroscopy during a 15 mins potential hold at each given potential and relate to the right y-axis. The diamond data points at 0 V were measured after the OER Raman measurements.

The increase in the A_D:A_G ratio is indicative of a decrease in the *sp*^{2} character (and increase in *sp*^{3} character) of the carbon atoms in the SWNT.[79–81] This gives further validity to the active site being on the surface of the tubes as a more *sp*^{3}-like carbon environment is suggestive of an intermediate bonding on the surface of the tubes.[80] After the OER measurements are carried out, the A_D:A_G ratio is higher than the start of the experiment. This is likely due to the presence of strongly adsorbed oxygen species on the surface of the tubes that did not participate in the OER. The adsorption of these species leads to increased *sp*^{3} character of the tubes. Future repeats of this experiment could be improved by doing multiple potential cycles in which ORR potentials are reached to remove such adsorbed species. This would also show if the changes in the A_D:A_G ratio are consistent across multiple cycles or if they change over time.

The position of the G band was also monitored during OER (Figure 4.10). While the G band position of both SWNT and Co_3O_4@SWNT shifted to higher wavenumbers as positive potential was applied, as seen in previous SWNT in situ Raman studies,[82] the shift for Co_3O_4@SWNT was far greater, increasing by 11.8 cm^{-1} compared to 2.3 cm^{-1} for SWNT. A blue-shift of the G band suggests a loss of electron density from SWNT,[82] so this result supports the idea that the encapsulated Co_3O_4 is withdrawing electron density from the tube surface, increasing the favourability of OH^- adsorption in line with the Tafel analysis presented earlier.

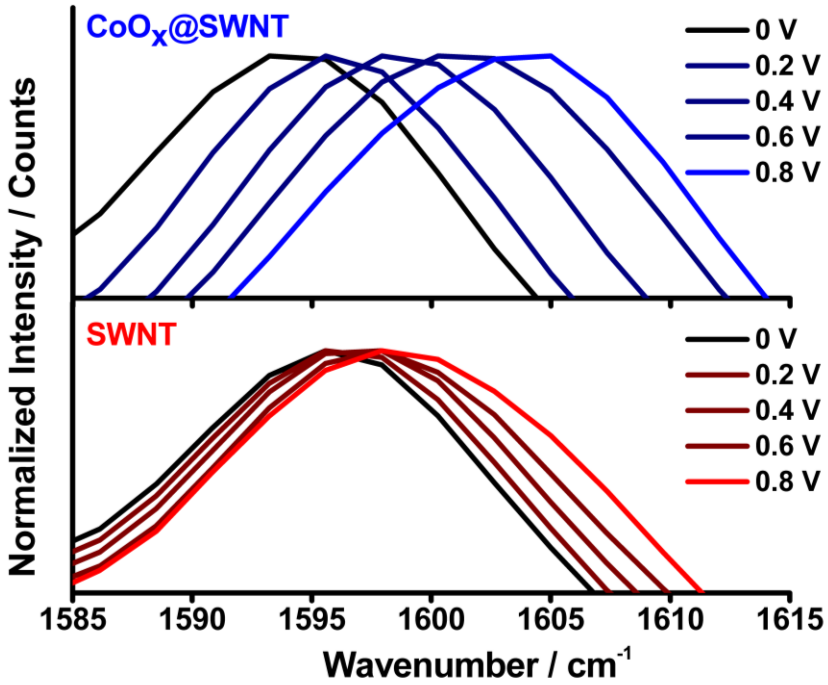


Figure 4.10 The position of the G band for Co_3O_4@SWNT and SWNT electrocatalysts measured using in-situ Raman spectroelectrochemistry as described in the main text and Figure 4.9. The intensity is normalised such that the peaks have equal intensity as it is the position of the band that is of interest.

4.3.3 Effect of Encapsulation on the Stability of the Electrocatalyst

Often, good OER electrocatalysts are let down by their inability to maintain a high level of activity over many cycles in and out of the reaction. Layers of carbon surrounding an active material have previously been shown to enhance the stability of the electrocatalyst enabling them to be used for longer.[83–85] It is demonstrated that the single carbon layer that surrounds the encapsulated

Co_3O_4 provides a similar level of protection. The potentials of GC electrodes coated with Co_3O_4/SWNT and Co_3O_4@SWNT were cycled 2000 times between 0.8 and 1.7 V (vs RHE) in 0.1 mol dm^{-3} KOH at 100 mV s^{-1}. Rotating linear sweep voltammograms were measured before and after cycling to assess the stability of the system. Figure 4.11b demonstrates the enhanced stability of Co_3O_4@SWNT (η_{10} increases by 7 mV) compared to Co_3O_4/SWNT (η_{10} increases by 35 mV, Figure 4.11a) which confirms the stabilising role of the SWNTs. For plain SWNTs the activity increases over the course of repeated OER cycles such that the η_{10} is 19 mV higher than before. For comparison, Co_3O_4 was mixed with activated carbon (AC) using the same procedure as used to create the Co_3O_4/SWNT material. Figure 4.11d clearly demonstrates the inferior stability of such a material showing that Co_3O_4, although initially as active towards the OER as the SWNT-based materials (with currents normalised to the electrode's geometric area as described previously), the activity rapidly drops off over the course of 2000 cycles and is unable to reach 10 mA cm^{-1} before 1.9 V.

The origin of the stability can be seen through the XPS and ex-situ Raman. The XPS data presented previously (Figure 4.3) suggested a stabilisation of the cobalt oxide within the confines of the SWNT and the Raman (Figure 4.4) suggested an electron withdrawing effect (further evidenced in Figure 4.10), which would further enhance the intimate interaction between the oxide and the carbon. It is also interesting to note the A_D:A_G ratio measured at 0 V after the OER is far close to the starting ratio than for SWNTs (diamonds in Figure 4.9). This suggests the surface oxygen species are less strongly adsorbed on the SWNT surface when Co_3O_4@SWNT is the electrocatalyst than when Co_3O_4 is not present. This further supports the stability being associated with the interaction between the encapsulated species and the SWNTs.

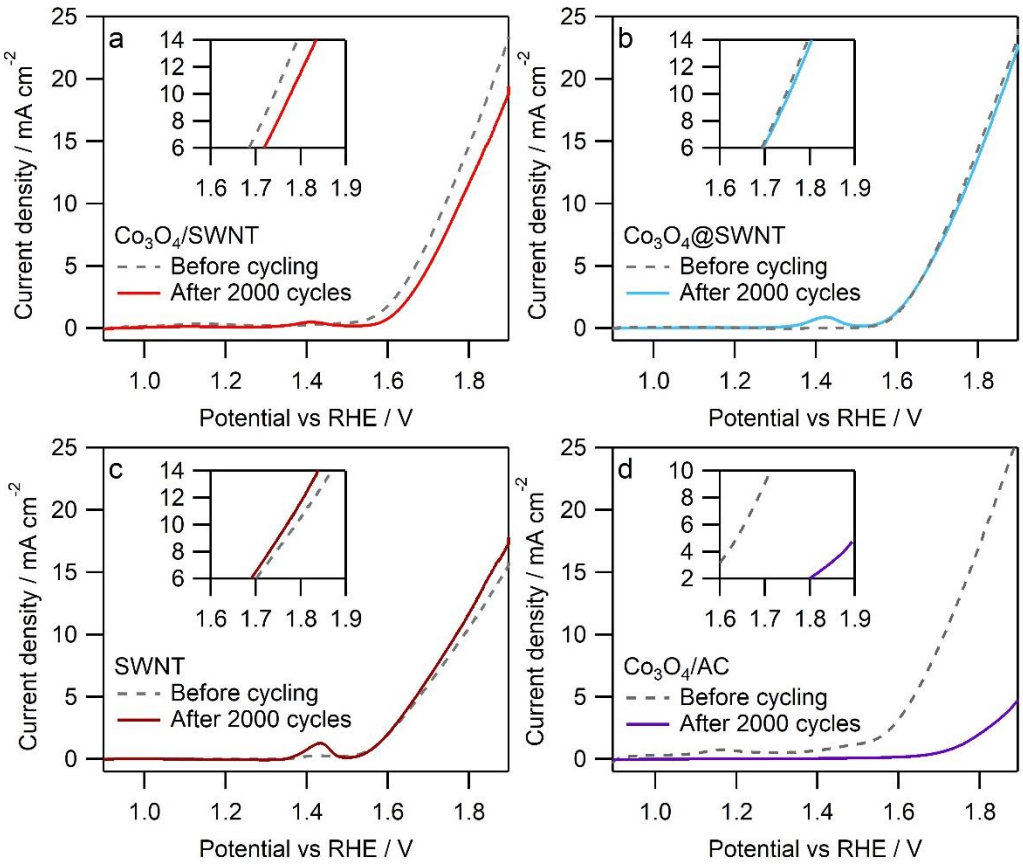


Figure 4.11 Rotating disc voltammograms measured in the same conditions as previously described for (a) Co_3O_4/SWNT, (b) Co_3O_4@SWNT, (c) SWNT, and (d) Co_3O_4 supported on AC (Co_3O_4/AC). In all cases, voltammograms are presented from before (dotted lines) and after (solid lines) 2000 cycles between 0.9 and 1.7 V vs RHE in N_2-purged 0.1 mol dm^{-3} KOH. The insets show magnified regions around 10 mA cm^{-2} (note that in d, the magnified region is at a lower current density).

The stability data presented in Figure 4.11 unfortunately highlight a complication to the interpretation of the presented data which was only truly appreciated after the completion of this work. The presence of an encroaching oxidation peak just after 1.4 V suggests the presence of a contaminant. Its association with the SWNTs rather than the Co_3O_4 is suggested by the lack of such a peak in Figure 4.11d in which AC was used instead of SWNTs. Initially, this peak was thought to be associated with the oxidation of the SWNTs. However, the peak is associated with the oxidation of nickel hydroxide.[86] Nickel is used as the catalyst in the synthesis of SWNTs and a residual amount must have been present, despite the use of an acid washing step to remove such contamination. When nickel contamination is present within SWNTs, its

presence is not immediately observed electrochemically, rather it becomes apparent only after many successive scans.[86]

It is important to note that as all the samples using SWNTs were prepared in the same way, it is expected that the level of contamination in all samples will be the same. As such, the trends observed are expected to hold true and so the analysis and discussion presented thus far can be considered valid. However, the only way to truly be sure of this is to repeat the work with an enhanced cleaning regime.

4.3.4 OER with Co_3O_4@SWNT in 1 mol dm^{-3} KOH

The work thus far presented was carried out in 0.1 mol dm^{-3} KOH. This is a relatively low concentration of KOH compared to that used in commercial electrolysers which can have concentrations as high as 20 – 30 %.[87] Using a lower concentration of KOH generally lowers the activity of an electrocatalyst. For the purposes of elucidating the active site and proving the concept, this was beneficial as it reduced the amount of bubble formation. The less harsh environment also minimises potential damage to the electrocatalyst which could influence the conclusions. However, to confirm whether encapsulation generates an electrocatalytic material with potentially practical applications, the activity, Tafel slope, and stability of Co_3O_4@SWNT was assessed in 1 mol dm^{-3} KOH.

The activity was significantly higher in 1 mol dm^{-3} KOH (~pH 14) as shown in Figure 4.12a. This is to be expected as electrocatalytic activity typically increases with increasing pH within alkaline electrolytes. The material remains stable in higher pH electrolyte as shown in Figure 4.12b; after 2000 cycles the η_{10} decreased by just 9 mV.

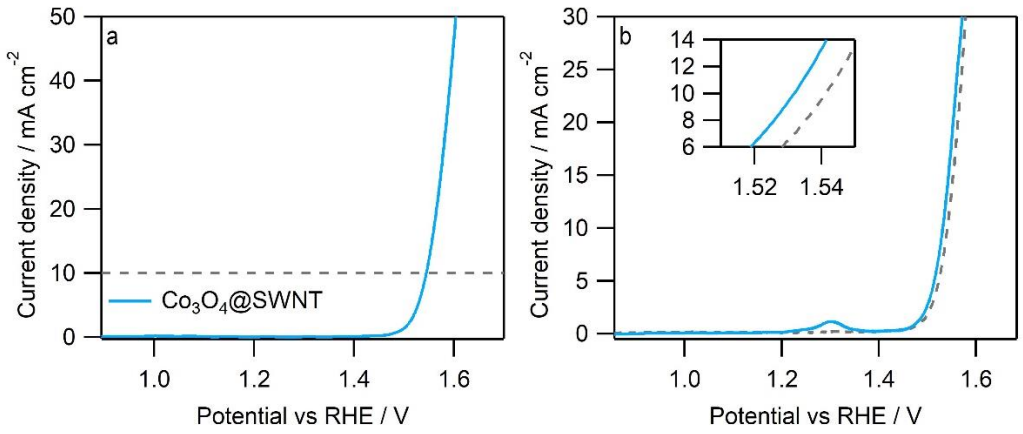


Figure 4.12 (a) Linear sweep voltammogram measured in O_2-saturated 1 mol dm^{-3} KOH at a GC rotating disc electrode coated with an electrocatalyst ink containing Co_3O_4@SWNT. Potential swept positive from 0.9 V to 1.9 V vs RHE at 20 mV s^{-1}. Measured against a Hg/HgO (1 mol dm^{-3} KOH) and then converted to RHE. A graphite rod behind a glass frit was used as the counter electrode. The dotted line shows 10 mA cm^{-2}. (b) Rotating disc voltammograms before and after 2000 cycles between 0.85 and 1.54 V vs RHE in N_2-purged 1 mol dm^{-3} KOH. The inset shows magnified region around 10 mA cm^{-2}.

The RDS of the mechanism in 1 mol dm^{-3} KOH is different than in 0.1 M KOH. The higher concentration leads to far more rapid kinetics and the first step is no longer rate determining. As seen in Figure 4.13, three Tafel slopes are observed. At low, mid, and high overpotentials the Tafel slopes are 51 mV dec^{-1}, 75 mV dec^{-1}, and 108 mV dec^{-1}, respectively. The complexity of the OER mechanism and the non-standard values of these Tafel slopes makes it difficult to ascribe a specific RDS. The first step can be eliminated as the RDS given the variation in the Tafel slope with potential. From the modelling done by Shinagawa *et al*, and given that the observed Tafel slopes are greater than 30 mV dec−1, it is likely that the final O_2 release is rate determining ($*OO^- \rightleftharpoons * + O_2 + e^-$).[75]

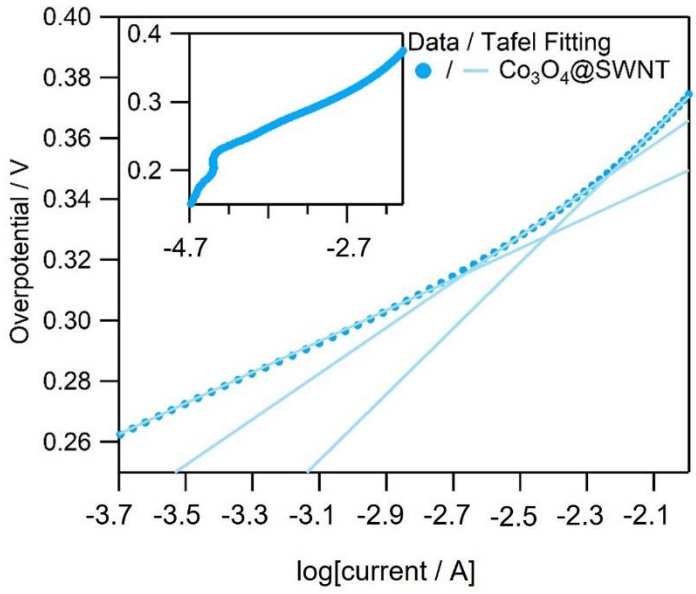


Figure 4.13 Plot of log[current / A] vs overpotential in the region used for Tafel analysis with the Co_3O_4@SWNT electrocatalyst used in 1 mol dm^{-3} KOH. Three Tafel slopes were identified. The inset shows the wider Tafel plot.

4.4 Conclusions

Co_3O_4 was successfully encapsulated within SWNTs using a method employing less harsh oxidation conditions than previously seen in the literature. After washing, the Co_3O_4 on the exterior of the SWNTs was removed and the encapsulated material remained. This material exhibits enhanced electrocatalytic properties compared to empty tubes. Co_3O_4@SWNT contains significantly less Co_3O_4 than Co_3O_4/SWNT, and so on a per gram of Co_3O_4 basis, the activity is far higher. The nature of the mechanism towards the OER was explored using Tafel analysis, capping experiments, and in-situ Raman spectroelectrochemistry. Through these experiments it was ascertained that the active site for electrocatalysis was on the surface of the SWNTs, and not inside the tubes at the surface of the encapsulated material. Given that the active site is on the carbon surface, it can be assumed that the OER proceeds via the adsorbate evolution mechanism (AEM) as described in Chapter 2 as it is not possible for the lattice oxygen in the Co_3O_4 to participate as would be required by the lattice oxygen mediated (LOM) mechanism. The first step of the OER reaction was rate limiting in all cases, though the adsorption of the OH^- was closer to optimal with Co_3O_4@SWNT than with empty tubes. Encapsulation

significantly enhanced the stability of the material to repeated cycles in and out of the OER owing to the strong interaction between the oxide and the interior cavity of the tubes. The stability benefits of encapsulation remain even at pH 14 though the kinetics of the reaction at the high pH leads to a different RDS.

The work presented here demonstrates a route to designing electrocatalysts with enhanced stability whilst requiring minimal active material.

4.5 Future Work

The electron-withdrawing nature of the cobalt oxide on the SWNTs appears to be beneficial to the electrocatalytic activity and stability. Further work exploring this relationship could be carried out. By systematically encapsulating materials with different electron-withdrawing and -donating properties, an optimal level could be found. Preliminary experiments along this line of reasoning have been carried out using ferrocene and cobaltocene encapsulated in SWNTs (Fc@SWNT and CoCp@FC, respectively). As previously described by McSweeney *et al*, the HOMO of Fc is positioned such that electron transfer from Fc to the pristine tube is not possible, whereas CoCp has a SOMO significantly higher in energy, meaning it can donate electrons to the empty nanotube states.[50] Thus, from the work presented in this chapter, it would be expected that CoCp@SWNT would have worse electrocatalytic properties than Fc@SWNT. Figure 4.14 shows this is indeed the case. Further exploration of this area could be achieved by encapsulating substituted Fc and CoCp molecules (as in McSweeney *et al*[50]) or through different molecules with intermediate properties.

The work presented in this chapter highlights how large changes in the electrocatalytic activity can be achieved through just 1.1 wt% Co_3O_4 encapsulated within in the SWNTs. However, this work did not ascertain whether further reducing the quantity, or indeed increasing the quantity, of encapsulated material could further enhance the activity of the electrocatalyst. A systematic study on the loading would provide insights into this area.

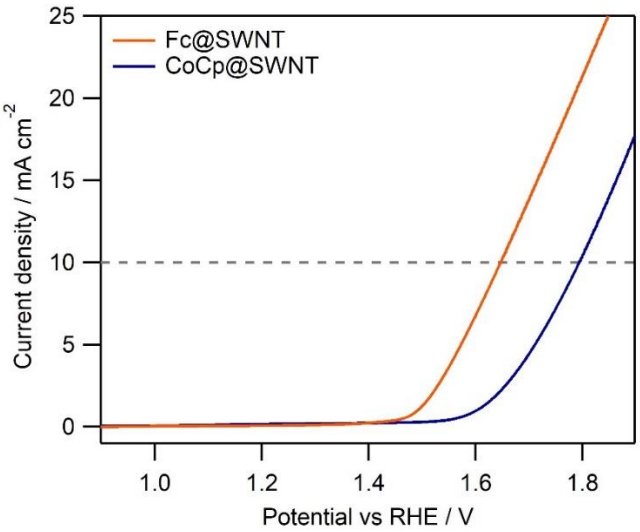


Figure 4.14 Linear sweep voltammograms measured in 0.1 mol dm^{-3} KOH at a GC rotating disc electrode coated with an electrocatalyst ink containing Fc@SWNT or CoCp/SWNT. Potential swept positive from 0.9 V to 1.9 V vs RHE at 20 mV s^{-1}. Measured against a Hg/HgO (0.1 mol dm^{-3} KOH) and then converted to RHE. A graphite rod behind a glass frit was used as the counter electrode. The dotted line shows 10 mA cm^{-2}.

The presence of contaminants in the SWNTs highlights the strong need for better washing procedures. Without them, the trends and conclusions reached in this chapter cannot be asserted with confidence. Thus, the full set of experiments should be repeated including a more thorough washing step and a method by which to confirm nickel contamination has been eliminated.

Given the highly oxidative potentials, it is possible that the currents ascribed to the OER could come from the oxidation of residual alcohols in the ink formulation or of the SWNTs themselves. Further investigations in this area should quantify the amount of O_2 produced to allow the Faradaic efficiency of the reaction to be calculated. This could be done via rotating-ring disc electrode experiments in which a gold ring is held at a potential to reduce the O_2 produced during the OER or using a differential electrochemical mass spectrometer.[88]

4.6 References

1. Dubouis, N. & Grimaud, A. The hydrogen evolution reaction: From material to interfacial descriptors. *Chem. Sci.* **10**, 9165–9181 (2019).

2. Man, I. C. *et al.* Universality in Oxygen Evolution Electrocatalysis on Oxide Surfaces. *ChemCatChem* **3**, 1159–1165 (2011).

3. Stamenkovic, V. R., Strmcnik, D., Lopes, P. P. & Markovic, N. M. Energy and fuels from electrochemical interfaces. *Nat. Mater.* **16**, 57–69 (2017).

4. McCrory, C. C. L., Jung, S., Peters, J. C. & Jaramillo, T. F. Benchmarking Heterogeneous Electrocatalysts for the Oxygen Evolution Reaction. *J. Am. Chem. Soc.* **135**, 16977–16987 (2013).

5. Shi, Z., Wang, X., Ge, J., Liu, C. & Xing, W. Fundamental understanding of the acidic oxygen evolution reaction: mechanism study and state-of-the-art catalysts. *Nanoscale* **12**, 13249–13275 (2020).

6. Naito, T., Shinagawa, T., Nishimoto, T. & Takanabe, K. Recent advances in understanding oxygen evolution reaction mechanisms over iridium oxide. *Inorg. Chem. Front.* **8**, 2900–2917 (2021).

7. Suen, N.-T. T. *et al.* Electrocatalysis for the oxygen evolution reaction: recent development and future perspectives. *Chem. Soc. Rev.* **46**, 337–365 (2017).

8. Seh, Z. W. *et al.* Combining theory and experiment in electrocatalysis: Insights into materials design. *Science* **355**, eaad4998 (2017).

9. Hu, C., Zhang, L. & Gong, J. Recent progress made in the mechanism comprehension and design of electrocatalysts for alkaline water splitting. *Energy Environ. Sci.* **12**, 2620–2645 (2019).

10. Exner, K. S. Design Criteria for Oxygen Evolution Electrocatalysts from First Principles: Introduction of a Unifying Material-Screening Approach. *ACS Appl. Energy Mater.* **2**, 7991–8001 (2019).

11. Exner, K. S. Universality in Oxygen Evolution Electrocatalysis: High-Throughput Screening and a Priori Determination of the Rate-Determining Reaction Step. *ChemCatChem* **12**, 2000–2003 (2020).

12. Wang, J. *et al.* Recent Progress in Cobalt-Based Heterogeneous Catalysts for Electrochemical Water Splitting. *Adv. Mater.* **28**, 215–230 (2016).

13. Shiva Kumar, S. & Himabindu, V. Hydrogen production by PEM water electrolysis – A review. *Mater. Sci. Energy Technol* **2**, 442–454 (2019).

14. Byers, J. C., Güell, A. G. & Unwin, P. R. Nanoscale electrocatalysis: Visualizing oxygen reduction at pristine, kinked, and oxidized sites on individual carbon nanotubes. *J. Am. Chem. Soc.* **136**, 11252–11255 (2014).

15. Zhao, Q., Yan, Z., Chen, C. & Chen, J. Spinels: Controlled Preparation, Oxygen Reduction/Evolution Reaction Application, and beyond. *Chem. Rev.* **117**, 10121–10211 (2017).

16. Roger, I., Shipman, M. A. & Symes, M. D. Earth-abundant catalysts for electrochemical and photoelectrochemical water splitting. *Nat. Rev. Chem.* **1**, 1–13 (2017).

17. Sun, L., Wang, X., Wang, Y. & Zhang, Q. Roles of carbon nanotubes in novel energy storage devices. *Carbon* **122**, 462–474 (2017).

18. Liang, Y. *et al.* Oxygen Reduction Electrocatalyst Based on Strongly Coupled Cobalt Oxide Nanocrystals and Carbon Nanotubes. *J. Am. Chem. Soc.* **134**, 15849–15857 (2012).

19. Al-Hakemy, A. Z. *et al.* Facile and simple deposition of cobalt oxide onto oxidized multiwall carbon nanotubes for electrocatalytic oxygen reduction. *J. Mater. Sci. Mater. Electron.* **31**, 1391–1402 (2020).

20. Chai, Y., Du, Y., Li, L. & Wang, N. Dual metal oxides interconnected by carbon nanotubes for high-capacity Li- and Na-ion batteries. *Nanotechnology* **31**, 215402 (2020).

21. Xiao, Y. *et al.* Plum-like and octahedral Co_3O_4 single crystals on and around carbon nanotubes: large scale synthesis and formation mechanism. *RSC Adv.* **2**, 3496–3501 (2012).

22. Qian, Y., Huang, S., Chen, Z., Huang, Y. & Li, D. Facile synthesis of cobalt nanoparticles embedded nitrogen-doped carbon nanotubes as electrocatalyst of hydrogen evolution reaction. *Fullerenes, Nanotub. Carbon Nanostructures* **27**, 808–815 (2019).

23. Raoof, J. B., Chekin, F. & Ehsani, V. Cobalt oxide nanoparticle-modified carbon nanotubes as an electrocatalysts for electrocatalytic evolution of oxygen gas. *Bull. Mater. Sci.* **38**, 135–140 (2015).

24. Wu, J. *et al.* Co_3O_4 nanocrystals on single-walled carbon nanotubes as a highly efficient oxygen-evolving catalyst. *Nano Res.* **5**, 521–530 (2012).

25. Fu, L. *et al.* Beaded Cobalt Oxide Nanoparticles along Carbon Nanotubes: Towards More Highly Integrated Electronic Devices. *Adv. Mater.* **17**, 217–221 (2005).

26. Nassr, A. B. A. A., Kottakkat, T. & Bron, M. A simple microwave process for the preparation of cobalt oxide nanoparticles supported on carbon nanotubes for electrocatalytic applications. *J. Solid State Electrochem.* **24**, 131–136 (2020).

27. Deng, J. *et al.* Highly active and durable non-precious-metal catalysts encapsulated in carbon nanotubes for hydrogen evolution reaction. *Energy Environ. Sci.* **7**, 1919–1923 (2014).

28. Cui, T. *et al.* Enhanced hydrogen evolution reaction over molybdenum carbide nanoparticles confined inside single-walled carbon nanotubes. *J. Energy Chem.* **28**, 123–127 (2019).

29. Vizuete, M., Barrejón, M., Gómez-Escalonilla, M. J. & Langa, F. Endohedral and exohedral hybrids involving fullerenes and carbon nanotubes. *Nanoscale* **4**, 4370–4381 (2012).

30. Pan, X. & Bao, X. The Effects of Confinement inside Carbon Nanotubes on Catalysis. *Acc. Chem. Res.* **44**, 553–562 (2011).

31. Miners, S. A., Rance, G. A. & Khlobystov, A. N. Chemical reactions confined within carbon nanotubes. *Chem. Soc. Rev.* **45**, 4727–4746 (2016).

32. Iglesias, D. & Melchionna, M. Enter the Tubes: Carbon Nanotube Endohedral Catalysis. *Catalysts* **9**, 128 (2019).

33. Liu, H., Zhang, L., Wang, N. & Su, D. S. Palladium Nanoparticles Embedded in the Inner Surfaces of Carbon Nanotubes: Synthesis, Catalytic Activity, and Sinter Resistance. *Angew. Chemie Int. Ed.* **53**, 12634–12638 (2014).

34. Chen, Z., Guan, Z., Li, M., Yang, Q. & Li, C. Enhancement of the Performance of a Platinum Nanocatalyst Confined within Carbon Nanotubes for Asymmetric Hydrogenation. *Angew. Chemie Int. Ed.* **50**, 4913–4917 (2011).

35. Wang, T. *et al.* Filling Carbon Nanotubes with Prussian Blue Nanoparticles of High Peroxidase-Like Catalytic Activity for Colorimetric Chemo- and Biosensing. *Chem. – A Eur. J.* **20**, 2623–2630 (2014).

36. Melchionna, M., Fornasiero, P. & Prato, M. Into the carbon: A matter of core and shell in advanced electrocatalysis. *APL Mater.* **8**, 20905 (2020).

37. Jordan, J. W. *et al.* Electrochemistry of redox-active molecules confined within narrow carbon nanotubes. *Chem. Soc. Rev.* **50**, 10895–10916 (2021).

38. McSweeney, R. L., Chamberlain, T. W., Davies, E. S. & Khlobystov, A. N. Single-walled carbon nanotubes as nano-electrode and nano-reactor to control the pathways of a redox reaction. *Chem. Commun.* **50**, 14338–14340 (2014).

39. Deng, D. *et al.* Iron Encapsulated within Pod-like Carbon Nanotubes for Oxygen Reduction Reaction. *Angew. Chemie Int. Ed.* **52**, 371–375 (2013).

40. Sun, N. *et al.* Ferrocene Peapod Modified Electrodes: Preparation, Characterization, and Mediation of H2O2. *Anal. Chem.* **78**, 6050–6057 (2006).

41. Wen, Z., Liu, J. & Li, J. Core/Shell Pt/C Nanoparticles Embedded in Mesoporous Carbon as a Methanol-Tolerant Cathode Catalyst in Direct Methanol Fuel Cells. *Adv. Mater.* **20**, 743–747 (2008).

42. Choi, C. H. *et al.* Hydrogen Peroxide Synthesis via Enhanced Two-Electron Oxygen Reduction Pathway on Carbon-Coated Pt Surface. *J. Phys. Chem. C* **118**, 30063–30070 (2014).

43. Wang, X. *et al.* Review of Metal Catalysts for Oxygen Reduction Reaction: From Nanoscale Engineering to Atomic Design. *Chem* **5**, 1486–1511 (2019).

44. Seo, B. *et al.* Size-Dependent Activity Trends Combined with in Situ X-ray Absorption Spectroscopy Reveal Insights into Cobalt Oxide/Carbon Nanotube-Catalyzed Bifunctional Oxygen Electrocatalysis. *ACS Catal.* **6**, 4347–4355 (2016).

45. Gu, D. *et al.* Controllable Synthesis of Mesoporous Peapod-like Co_3O_4@Carbon Nanotube Arrays for High-Performance Lithium-Ion Batteries. *Angew. Chemie Int. Ed.* **54**, 7060–7064 (2015).

46. Cui, T. *et al.* A versatile method for the encapsulation of various non-precious metal nanoparticles inside single-walled carbon nanotubes. *Nano Res.* **11**, 3132–3144 (2018).

47. Wang, M. *et al.* Endohedral Fe_3C decorated multi-walled CNTs as an efficient electrocatalyst for oxygen evolution. *Diam. Relat. Mater.* **118**, 108508 (2021).

48. Botos, A. *et al.* Carbon Nanotubes as Electrically Active Nanoreactors for Multi-Step Inorganic Synthesis: Sequential Transformations of Molecules to Nanoclusters and Nanoclusters to Nanoribbons. *J. Am. Chem. Soc.* **138**, 8175–8183 (2016).

49. Stoppiello, C. T. *et al.* A one-pot-one-reactant synthesis of platinum compounds at the nanoscale. *Nanoscale* **9**, 14385–14394 (2017).

50. McSweeney, R. L. *et al.* Direct Measurement of Electron Transfer in Nanoscale Host-Guest Systems: Metallocenes in Carbon Nanotubes. *Chem. – A Eur. J.* **22**, 13540–13549 (2016).

51. Jiang, N. Electron beam damage in oxides: a review. *Reports Prog. Phys.* **79**, 016501 (2015).

52. Jordan, J. W. *et al.* Single-molecule imaging and kinetic analysis of intermolecular polyoxometalate reactions. *Chem. Sci.* **12**, 7377–7387 (2021).

53. Chuang, T. J., Brundle, C. R. & Rice, D. W. Interpretation of the x-ray photoemission spectra of cobalt oxides and cobalt oxide surfaces. *Surf. Sci.* **59**, 413–429 (1976).

54. Li, Y. *et al.* Co3O4@carbon with high Co2+/Co3+ ratios derived from ZIF-67 supported on N-doped carbon nanospheres as stable bifunctional oxygen catalysts. *Mater. Today Energy* **21**, 100737 (2021).

55. Li, J. *et al.* Ultrathin Mesoporous Co3O4 Nanosheet Arrays for High-Performance Lithium-Ion Batteries. *ACS Omega* **3**, 1675–1683 (2018).

56. Zhu, J., Kailasam, K., Fischer, A. & Thomas, A. Supported cobalt oxide nanoparticles as catalyst for aerobic oxidation of alcohols in liquid phase. *ACS Catal.* **1**, 342–347 (2011).

57. Zhou, M. *et al.* Enhancing Catalytic CO Oxidation over Co3O4 Nanowires by Substituting Co2+ with Cu2+. *ACS Catal.* **5**, 4485–4491 (2015).

58. Cui, B. *et al.* Photophysical and photocatalytic properties of core-ring structured NiCo2O4 nanoplatelets. *J. Phys. Chem. C* **113**, 14083–14087 (2009).

59. Biesinger, M. C. *et al.* Resolving surface chemical states in XPS analysis of first row transition metals, oxides and hydroxides: Cr, Mn, Fe, Co and Ni. *Appl. Surf. Sci.* **257**, 2717–2730 (2011).

60. Ghosh, S., Yamijala, S. R. K. C. S., Pati, S. K. & Rao, C. N. R. The interaction of halogen molecules with SWNTs and graphene. *RSC Adv.* **2**, 1181–1188 (2012).

61. Garcia, A. C. & Koper, M. T. M. Effect of Saturating the Electrolyte with Oxygen on the Activity for the Oxygen Evolution Reaction. *ACS Catal.* **8**, 9359–9363 (2018).

62. Bhandari, S., Narangoda, P. V., Mogensen, S. O., Tesch, M. F. & Mechler, A. K. Effect of Experimental Parameters on the Electrocatalytic Performance in Rotating Disc Electrode Measurements: Case Study of Oxygen Evolution on Ni−Co-Oxide in Alkaline Media. *ChemElectroChem* **9**, e202200479 (2022).

63. Vigil, J. A. & Lambert, T. N. Nanostructured cobalt phosphide-based films as bifunctional electrocatalysts for overall water splitting. *RSC Adv.* **5**, 105814–105819 (2015).

64. Yang, J., Shao, Q., Huang, B., Sun, M. & Huang, X. pH-Universal Water Splitting Catalyst: Ru-Ni Nanosheet Assemblies. *iScience* **11**, 492–504 (2019).

65. Wang, H. *et al.* Bifunctional non-noble metal oxide nanoparticle electrocatalysts through lithium-induced conversion for overall water splitting. *Nat. Commun.* **6**, (2015).

66. Zhou, H. *et al.* Highly active catalyst derived from a 3D foam of $Fe(PO_3)_2/Ni_2P$ for extremely efficient water oxidation. Proc. Natl. Acad. Sci. **114**, 5607–5611 (2017).

67. Wygant, B. R. *et al.* Structural and Catalytic Effects of Iron-and Scandium-Doping on a Strontium Cobalt Oxide Electrocatalyst for Water Oxidation. *ACS Catal.* **6**, 1122–1133 (2016).

68. Han, B. H. *et al.* Iron-Based Perovskites for Catalyzing Oxygen Evolution Reaction. *J. Phys. Chem. C* **122**, 8445–8454 (2018).

69. Zhao, Y. *et al.* Graphene-Co_3O_4 nanocomposite as electrocatalyst with high performance for oxygen evolution reaction. *Sci. Rep.* **5**, 1–7 (2015).

70. Sun, H. *et al.* B-Site Cation Ordered Double Perovskites as Efficient and Stable Electrocatalysts for Oxygen Evolution Reaction. *Chemistry* **23**, 5722–5728 (2017).

71. Mattick, V. F., Jin, X., White, R. E. & Huang, K. A perovskite/noble-metal composite as a bifunctional oxygen electrocatalyst for alkaline electrochemical cells. *J. Energy Storage* **23**, 537–543 (2019).

72. Huang, Z. F. *et al.* Strategies to Break the Scaling Relation toward Enhanced Oxygen Electrocatalysis. *Matter* **1**, 1494–1518 (2019).

73. Fang, Y. H. & Liu, Z. P. Tafel Kinetics of Electrocatalytic Reactions: From Experiment to First-Principles. *ACS Catal.* **4**, 4364–4376 (2014).

74. Negahdar, L., Zeng, F., Palkovits, S., Broicher, C. & Palkovits, R. Mechanistic Aspects of the Electrocatalytic Oxygen Evolution Reaction over Ni-Co Oxides. *ChemElectroChem* **6**, 5588–5595 (2019).

75. Shinagawa, T., Garcia-Esparza, A. T. & Takanabe, K. Insight on Tafel slopes from a microkinetic analysis of aqueous electrocatalysis for energy conversion. *Sci. Rep.* **5**, 1–21 (2015).

76. Joya, K. S. & Sala, X. In situ Raman and surface-enhanced Raman spectroscopy on working electrodes: spectroelectrochemical characterization of water oxidation electrocatalysts. *Phys. Chem. Chem. Phys.* **17**, 21094–21103 (2015).

77. Campion, A. & Kambhampati, P. Surface-enhanced Raman scattering. *Chem. Soc. Rev.* **27**, 241–250 (1998).

78. Zwaschka, G. *et al.* Imaging the Heterogeneity of the Oxygen Evolution Reaction on Gold Electrodes Operando: Activity is Highly Local. *ACS Catal.* **10**, 6084–6093 (2020).

79. Tuinstra F & Koenig JL. Raman Spectrum of Graphite. *J. Chem. Phys.* **53**, 1126 (2003).

80. Campos-Roldán, C. A. *et al.* Influence of sp3-sp2 carbon nanodomains on metal/support interaction, catalyst durability, and catalytic activity for the oxygen reduction reaction. *ACS Appl. Mater. Interfaces* **8**, 23260–23269 (2016).

81. Lin, Y., Sun, X., Su, D. S., Centi, G. & Perathoner, S. Catalysis by hybrid sp2/sp3 nanodiamonds and their role in the design of advanced nanocarbon materials. *Chem. Soc. Rev.* **47**, 8438–8473 (2018).

82. Kavan, L., Rapta, P. & Dunsch, L. In situ Raman and Vis-NIR spectroelectrochemistry at single-walled carbon nanotubes. *Chem. Phys. Lett.* **328**, 363–368 (2000).

83. Yan, X. H. *et al.* Recent Progress of Metal Carbides Encapsulated in Carbon-Based Materials for Electrocatalysis of Oxygen Reduction Reaction. *Small Methods* **4**, 1900575 (2020).

84. Wan, W. *et al.* Transition metal electrocatalysts encapsulated into N-doped carbon nanotubes on reduced graphene oxide nanosheets: efficient water splitting through synergistic effects. *J. Mater. Chem. A* **7**, 15145–15155 (2019).

85. Jose, V., Jayakumar, A. & Lee, J. M. Bimetal/Metal Oxide Encapsulated in Graphitic Nitrogen Doped Mesoporous Carbon Networks for Enhanced Oxygen Electrocatalysis. *ChemElectroChem* **6**, 1485–1491 (2019).

86. Ambrosi, A. & Pumera, M. Redox-Active Nickel in Carbon Nanotubes and Its Direct Determination. *Chem. – A Eur. J.* **18**, 3338–3344 (2012).

87. Brauns, J. & Turek, T. Alkaline Water Electrolysis Powered by Renewable Energy: A Review. *Processes* **8**, 248 (2020).

88. Kempler, P. A. & Nielander, A. C. Reliable reporting of Faradaic efficiencies for electrocatalysis research. *Nat. Commun.* **14**, 1–4 (2023).

Chapter 5. The Influence of the Phase and Morphology of Titanate Materials on the Reduction of Oxygen

5.1 Introduction

In recent years, awareness of the climate crisis has been growing.[1] As a result, battery and fuel cell technologies are becoming increasingly important.[2] Oxygen reduction is a key reaction for both.[3–6] However, the state-of-the-art fuel cells use precious metals to overcome the sluggish kinetics of the ORR.[3,6–9] As such, research into novel ORR electrocatalysts aim to either eliminate the precious metals entirely[10–12] or significantly reduce the loading of them.[6,8] This can be achieved through changing the morphology of the material to alter the surface area and increase the number of exposed active sites, or by designing the chemistry of the material to have active sites with higher intrinsic activity.[3,5,7]

The morphology and surface chemistry of electrocatalysts are key characteristics that influence their activity. It is well known that increasing the surface area of a material will increase its activity per unit area. However, simply increasing the number of active sites does not mean the material is intrinsically more active.[13] A material which packs more active sites into a given geometric area may be useful at the device level, but from a scientific perspective it can be more useful to consider how active those sites are. Reporting both the geometric and specific activity of a material can give a better picture of how the material functions as an electrocatalyst as chemical and surface area effects can be separated.[13–15]

Titanium is more abundant than platinum-group metals and so has the potential to be an attractive material for electrocatalysis. Although not an extremely common element in novel ORR electrocatalysts (compared to, say, cobalt or nickel), it has been used by some researchers. TiO_2 has a bandgap of 3.2 eV, allowing it to be used in photocatalysis,[16] is cheap,[17] and is stable in the environments used for electrocatalysis.[18]

Despite these advantages, electrocatalysts based on Ti and TiO_2 are typically combined with other elements to bring about more enhanced properties. For example, Yang *et al* added strontium to create a strontium titanate material as a supercapacitor material. [19]

TiO_2 on its own has several forms: tetragonal anatase, tetragonal rutile, and orthorhombic brookite are all stable in ambient conditions; TiO_2 (B), (H), and (R) are metastable forms. Titanates are salts with TiO_6 octahedra and form from polytitanic acids.[20] Titanates commonly also form part of perovskite structures. They can also form part of layered titanate structures with the formula $M_{2n}Ti_mO_{2m+n}$. The M cation is often Na^+, K^+, or H^+, though, in much the same way as perovskites, the structure is versatile and can take many different cations.[20]

When an alkaline metal cation is used the structure is known as a layered alkaline titanate. Such titanate structures have a large ion-exchange capacity, fast ion-diffusion, and a high surface charge density.[21] This is due to the crystal structure allowing for cations to be exchanged within the negatively charged Ti-containing sheets. These properties make them useful for energy storage applications such as capacitors and lithium intercaltors.[19–21] There are examples hydrogen and alkaline titanates being used in synergy with Pt for methanol oxidation in methanol fuel cell applications. Beyond tailoring the chemistry of titanate materials, the morphology can also be tailored to maximise the number of exposed active sites for electrocatalytic applications or increase the surface area for energy storage.

Work by Wadge and co-workers has investigated alternative synthesis routes of alkaline titanate species. Specifically, the use of a wet chemical method as opposed to the more standard sintering method. They found that by synthesising such materials through a wet-chemical method, the resulting material had a greater degree of porosity.[22–24] Such materials have primarily been due to their biocompatibility owing to the material forming a similar structure to the apatite mineral component of bone. This allows them to be used as a coating on titanium-based implants.[20–25] As yet, wet-chemical sodium

titanate has not been assessed for its electrocatalytic properties toward the ORR.

Microspheres have previously been deployed as the morphology for oxygen reduction electrocatalyst. For example, Wang *et al* created hollow porous microspheres based on $ZnMnCoO_4$ which could be optimised to give ORR activities close to that of Pt/C electrocatalysts.[12] The best of these materials had a half-wave-potential towards the ORR just 50 mV lower than that of Pt/C and showed superior stability[26]. Lei *et al* created a similar morphology from Ni_2P and demonstrated good bifunctional oxygen electrocatalysis (*i.e.,* good at both OER and ORR) which was also more stable than Pt/C.[11] The hollow nature of these materials yields high surface-to-volume ratios and maximises mass transfer of reactant oxygen to, and products from, the active sites of the material.

Carbon-boron core-shell microspheres synthesised by Periasamy *et al* had faster ORR kinetics than the carbon counterpart with no boron present.[10] However, the material electrocatalysed a mix of the direct 4 electron and the 2x2 electron ORR pathways resulting in an electron transfer number of ~3 electrons, which results in a material that cannot be efficiently used for either route. However, the authors use this to demonstrate boron doping as a potential avenue for tuning the pathway followed by a carbon-based material.[10]

Microspheres have also been used as support materials for more active electrocatalysts. Balgis *et al* coated N-doped carbon microspheres with Pt and improved the onset potential of the ORR and increased the mass utilisation of the Pt meaning less Pt could be used without lowering the activity of the material.[8]

Wadge *et al* recently showed that TiO_2 and Ti6Al4V microspheres can be used as a substrate, which can be chemically converted using a wet chemical method to create microspheres with a nanoporous alkaline titanate surface layer allowing accessibility to the underlying microsphere.[27] The numbers in Ti6Al4V

are not stoichiometric and refer to the percentage of the alloy by weight of the element (i.e., Ti alloy with 6 wt% of Al and 4 wt% of V). “Ti6Al4V microspheres” is abbreviated to Ti6_MS.

Given that the electrocatalytic reactions are sensitive to the surface area of the electrocatalyst material,[9,13–15] the above-described material had the potential to show interesting properties towards the ORR. Ti6_MS is compared to converted microspheres. The converted microspheres featured a sodium titanate layer on the surface of the underlying spheres. An additional heat-treatment process was carried out to enhance the surface area of the converted microspheres. It was found that the surface sodium titanate layer altered the specificity of the mechanism through which the reaction proceeded compared to the untreated microspheres, and that the heat-treatment enhanced the rate of the reaction.

5.2 Experimental Section

The work presented in this chapter represents a collaboration between me and Matthew Wadge from the Engineering Department, University of Nottingham as the lead researchers. The non-heat-treated materials had been synthesised prior to the project along with their physical characterisation (XPS, XRD, Raman, and some SEM). All electrochemical and electrocatalytic work was carried out by me and the direction of the project was then discussed collaboratively based on these results. TEM was carried out by Andrzej Sankowski under the instruction of both lead researchers.

5.2.1 Materials and Apparatus

5.2.2 Powder synthesis

Three different powders were assessed. Ti6Al4V (Timet Ti 6-4 PREP® Powder; [-140+270] MESH; equivalent 53-105 µm) was used as the base powder and is denoted Ti6_MS. To convert this powder, it was suspended in 5.0 M NaOH solution (NaOH pellets, 99.9% purity; Sigma-Aldrich, dissolved in distilled water). The suspensions were stored in Falcon™ 15 mL (17 mm diam.; 120 mm length) Conical Sterile Polypropylene Graduated Centrifuge Tubes. The tubes

were sealed and heated in a low temperature Lenton® furnace at 60 ± 2 ^{o}C for 24 h. After heating, the powder was washed *via* filtration is deionised water to remove excess NaOH and then dried in a furnace at 100 ^{o}C in air for 1 h. This material was stored in a desiccator until use and is denoted Ti6_TC. Portions of this powder were further converted *via* heat-treatment in a Lenton® furnace in air with a ramp rate of 5 °C min^{-1} to 100 °C at first leaving them to dwell for 1 h, followed by heating at the same ramp rate to 450 °C with a dwell time of 1 hour then left to cool naturally to room temperature. The resulting powder is denoted Ti6_TC_HT.

5.2.2.1 Ink and electrode preparation

20 mg of the titanate powders were mixed with 5 mg of Vulcan carbon (VC) to increase the conductivity of the material and dispersed in ethanol (1 mL) and a 5% solution of Nafion in aliphatic alcohols (100 µL). The solution was then mixed with a magnetic stir bar (1400 rpm) for 30 mins or using ultrasonication for 5 or 30 mins.

A 5 mm rotating disc electrode (RDE; Pine Research, Durham, NC) was polished with 1, 0.3, and 0.05 µm alumina (Buehler, Coventry, UK) to a reproducible mirror finish. 10 µL of the ink was dropcast onto the rotating electrode (100-200 rpm) and left to dry for ~1 hour at room temperature at 500 rpm.

5.2.3 Physical Characterisation

5.2.3.1 Scanning electron microscopy (SEM) and energy dispersive spectroscopy (EDS)

Image acquisitions for high resolution micrographs were conducted on a Field-Emission Gun Scanning Electron Microscope (JEOL 7100 FEG-SEM). Surface compositional analysis was determined *via* an Energy-Dispersive X-ray spectrometer (EDX) (Oxford Instruments) at a working distance of 10 mm, a beam voltage of 15 kV, whilst maintaining a minimum X-ray count of 250,000 counts.

Additional micrographs were obtained using a Zeiss EVO MA10 SEM with a W-filament. Elemental analysis within this instrument was carried out with an Energy-Dispersive X-ray spectrometer (Element, AMETEK) with an accelerating voltage of 15 kV, working distance of ~8 mm and counts of at least 2000.

5.2.3.2 X-ray photoelectron spectroscopy (XPS)

All samples were mounted onto stainless steel stubs using carbon sticky tabs. X-ray Photoelectron Spectroscopy (XPS) was conducted using a VG ESCALab Mark II X-ray photoelectron spectrometer with a monochromatic Al Kα X-ray source incident to the sample surface at *ca.* 30°. Survey and high-resolution scans were conducted in addition to the measurement of adventitious C 1s for calibration: charge corrected to 284.8 eV. Parameters for acquisition were as follows: step size of 1.0 eV; number of scans set at 5; dwell time 0.2 s for survey scans, and 0.4 s for high-resolution scans. Binding energies were measured over a range of 0–1200 eV. All spectra were analysed in Casa XPS constraining the Full Width at Half Maximum (FWHM) to the same value for all deconvoluted spectral peaks for the same element. When fitting curves for $2p_{1/2}$ and $2p_{3/2}$, spin-orbit coupling relationships were used as constraints.

5.2.3.3 X-ray diffraction (XRD)

Sample crystallinity of all powders were analysed using a Bruker D8 ADVANCE with DaVinci diffractometer (Cu Kα source, λ = 1.5406 Å, 40 kV, 40 mA) with a LYNXEYE 1D detector, in Bragg-Brentano mode. Powders were mounted into Perspex (polymethyl methacrylate; PMMA; Bruker) holders, ensuring the powder sits flush. Measurements were taken over a 2θ range from 10 to 100°; with a step size of 0.02° (2θ); and a step time of 0.2 s.

5.2.3.4 Raman spectroscopy

Raman spectroscopy was conducted using a HORIBA Jobin Yvon LabRAM HR spectrometer. Spectra were acquired using a Quantum Ignis 660 nm Laser (100 mW power), 100× objective, and a 300 µm confocal pinhole. A 600 lines/mm rotatable diffraction grating along a path length of 800 mm was used for simultaneous scanning of multiple Raman shifts. Spectra detection was

achieved using a SYNAPSE CCD detector (1024 pixels) thermoelectrically cooled to −60 °C. Instrument calibration using the Rayleigh line at 0 cm^{-1} and a standard Si (100) reference band at 520.7 cm^{-1}, was employed prior to spectra acquisition. A constrained time window of 10 s was employed for each spectra recording with 10 accumulations per sample.

5.2.4 Electrochemical Characterisation

Electrochemical testing was carried out using a model CHI760C potentiostat (CH Instruments) coupled with a modulated speed rotator from Pine Research. A graphite rod counter electrode was used and kept separate from the working electrode electrolyte with a fritted glass tube. A Hg/HgO (0.1 mol dm^{-3} KOH) reference electrode was used. The reference potential was checked either against a home-made RHE or a Gaskatel RHE. The electrolyte was 0.1 mol dm^{-3} KOH.

The ECSA of the coated electrode was determined by measuring CVs at difference scan rates with a 100 mV window in a region with no faradaic processes. When using O_2-saturated electrolyte, 20 cycles at 500 mV s^{-1} were carried out in the ORR region until a reproducible CV was observed to ensure saturation. Similarly, with N_2-sparged electrolyte CVs in the same region were measured until no oxygen electrochemistry could be observed.

The oxygen reduction reaction (ORR) activity was measured by cyclic voltammetry between 0.8 and −0.2 V at 5 mV s^{-1}. The rotation rate was varied between 400 and 2500 rpm. Blank CVs were recorded in N_2-saturated electrolytes and were subtracted from those recorded in O_2-saturated electrolyte to ensure only oxygen-related electrochemistry was investigated. For the K-L analyses the following constants were used (as defined in Chapter 2): $D_{O2} = 1.93\times10^{-5}$ cm^2 s^{-1}, $C_{02} = 1.26\times10^{6}$ mol cm^{-3}, $v = 1.09\times10^{-2}$ cm^2 s^{-1}, A is the geometric area of the electrode (0.19635 cm^{-2}).

5.3 Results and Discussion

5.3.1 Physical Characterisation

Ti6Al4V microspheres (Ti6_MS) were used as the starting material to create new spherical morphologies. This starting material is an alloy with Ti as the primary element, and 6 wt% Al and 4 wt% V alloyed with the Ti. Ti6_MS was converted to Ti6_TC *via* heating in 5 mol dm^{-3} NaOH for 24 hours at low temperature (60 °C), rinsed and then dried for 1 h at 100 °C. This material was further converted to Ti6_TC_HT by heat treating in a furnace to 100 °C for 1 hour followed by heating for a further hour at 450 °C.

SEM characterisation (Figure 5.1a-c) shows that the Ti6_MS are smooth with relatively few surface features. After the alkaline titanate conversion (Figure 5.1d-f), the surfaces of the microspheres are coated with dendritic structures. The dendritic features are still present after heat-treatment (Figure 5.1g-i), though they are more densely packed with less definition between individual titanate struts. The modification of the dendritic structure could be due to the formation of rutile crystals within the anatase titanate film, or just an increase in the anatase crystal size. Further analysis by XRD, Raman, and TEM are required to confirm which is the case. These analyses are presented later.

Fortuitous regions of delamination on some of the Ti6_TC and Ti6_TC_HT microspheres allowed the thickness of the titanate layer to be measured. No difference between the two samples was observed, so only a representative region of Ti6_TC is shown in Figure 5.2. The layer thickness was ~822 nm, consistent with previous observations.[27] It is notable that the thickness of this layer is consistent with layers formed on non-spherical materials[27–29] meaning the gross morphology of the underlying material has little influence over the microscale formation of the titanate layer.[27]

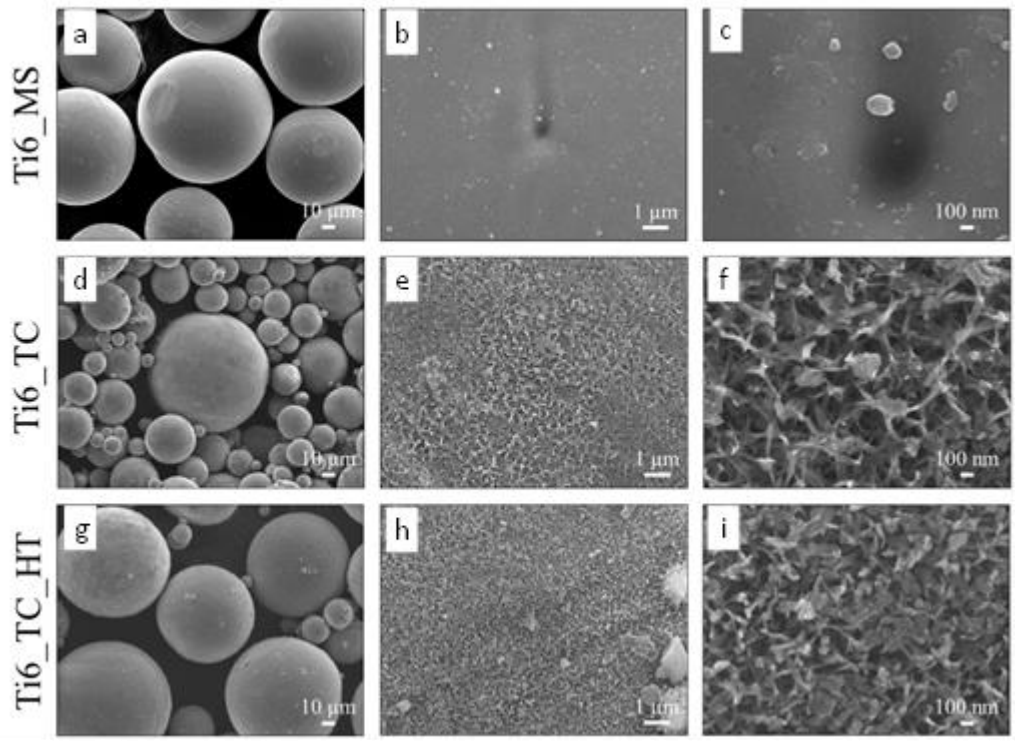


Figure 5.1 SEM micrographs of Ti6_MS (a-c), Ti6_TC (d-f), and Ti6_TC_HT (g-i). Micrographs show the overall structure (a, d, g), the general surface texture (b, e, h), and high magnification of the surface structure (c, f, i).

EDX mapping of representative areas of SEM micrographs (Figure 5.3) shows the distribution of the constituent elements is homogeneous in all cases. Elemental quantification from the EDX data is presented in Table 5.1. The Ti6_MS material contains only Ti, Al, and V which is to be expected given the alloy's composition. Furthermore, the lack of O observed is expected, since the only O present should be in the form of TiO_2 as a passivated oxide layer (a few nms thick). Within error, the ratio of these elements from EDX is consistent with the alloy weights (note that the table gives at.%,).

After conversion in which the alkaline titanate layer forms, the presence of Na and O is observed by EDX. It can further be seen that the heat treatment increases the O content of the material whilst reducing the percentage of Ti and V. The increase in O content is to be expected as the heat-treatment occurred in air allowing for oxidation of the material. It is not possible to determine the titanate phase from EDX data of this sort.

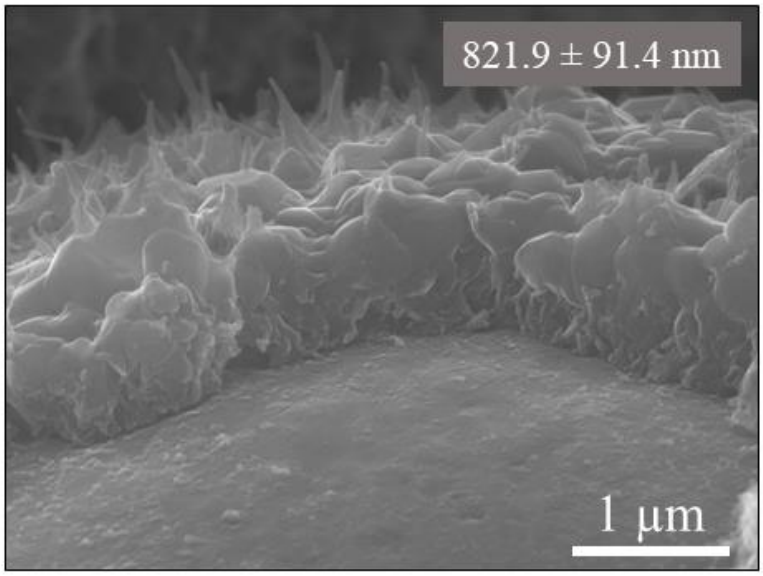


Figure 5.2 SEM micrograph of a representative region of the Ti6_TC surface where delamination had occurred. Multiple such regions were used to assess the thickness of the layer which is given in the top right corner as the mean with a standard error (n = 15).

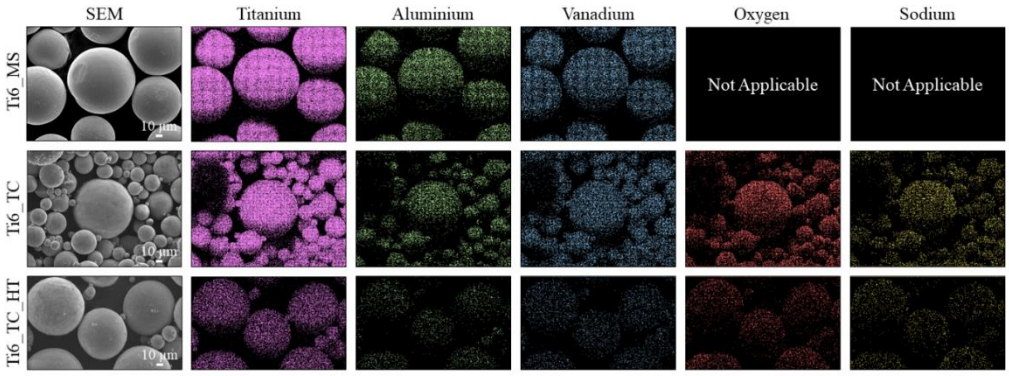


Figure 5.3 SEM micrographs and EDX maps of Ti6_MS, Ti6_TC, and Ti6_TC_HT showing the homogeneous distribution of Ti, Al, V, O, and Na. Relative brightness can only be compared within maps of the same sample. No information can be gleaned from the apparent lower brightness of the maps for Ti6_TC_HT.

Table 5.1 Elemental composition of Ti6_MS, Ti6_TC, and Ti6_TC_HT as determined by EDX and XPS. Standard errors calculated with n = 5. Dash (-) means no suitable peak detected or useable.

	Elemental Composition / at.%									
	Na		Ti		O		Al		V	
	EDX	XPS	EDX	XPS	EDX	XPS	EDX	XPS	EDX	XPS
Ti6_MS	-	-	86.5 ± 0.2	25.7 ± 1.2	-	74.3 ± 1.2	9.8 ± 0.3	-	3.7 ± 0.1	-
Ti6_TC	3.9 ± 0.3	19.9 ± 0.6	34.5 ± 1.3	19.2 ± 0.4	57.0 ± 1.3	60.9 ± 0.7	2.5 ± 0.4	-	2.1 ± 0.6	-
Ti6_TC_HT	5.4 ± 0.3	20.8 ± 0.6	31.3 ± 0.4	15.6 ± 0.4	59.1 ± 0.3	63.6 ± 0.7	2.9 ± 0.1	-	1.4 ± 0.1	-

To aid in that, X-ray diffraction (Figure 5.4) was used to probe the microspheres before and after the conversion and heat-treatment processes. All three samples are clearly similar in terms of peak positions and relative intensities. The peak positions (2θ = 35.5, 38.6, 40.5, 53.4, 63.6, 71.1, 74.9, 77.0, 78.2, 82.8, 87.7, and 93.3°) match that of hexagonal close-packed titanium (HCP Ti; ICDD: 00-044-1294). The narrowing of the peaks observed for Ti6_TC_HT is consistent with crystallite growth. This corroborates the observation through SEM that the titanate struts had expanded after the heat-treatment.

It should be possible to identify oxide phases and distinguish between anatase and rutile phases of titanium dioxide phases with XRD. Given the oxidation processes that occur at the surface of the microsphere it is expected that some amount of anatase formation will have occurred, and that heat-treatment may lead to a minor quantity of the rutile phase (phase formation follows: anatase < 600°C < rutile). There is a peak at 2θ ~ 43.6° (Figure 5.4 inset) present in Ti6_TC and larger in Ti6_TC_HT which may correspond to the phase TiO_2-B, but there are no other distinguishing peaks to corroborate this.[30] From the above presented analyses, it is considered that there were no changes to the bulk phase of the material upon conversion to Ti6_TC nor following the heat-treatment of the material. This suggests the conversion process was purely confined to the surface of the microspheres and so any changes in the

properties of the material can be ascribed to this layer, rather than bulk changes in the material.

X-ray photoelectron spectroscopy (XPS) is more surface sensitive than XRD and so is better suited to give information about the chemistry of the surface layer on the microspheres.[31] The spectra presented in Figure 5.5 were used to quantify the elemental constituents and are presented alongside the quantification data from EDX in Table 5.1. Discrepancies between the two quantification methods primarily come from the difference in the depths the two techniques work at. The electron beam for EDX can have a penetration depth of 10s of µm, whereas for XPS it is 10s of nm (depending, of course, on the experimental and sample conditions).[32,33] There was no suitable XPS peak for V or Al for those to be included in the quantification.

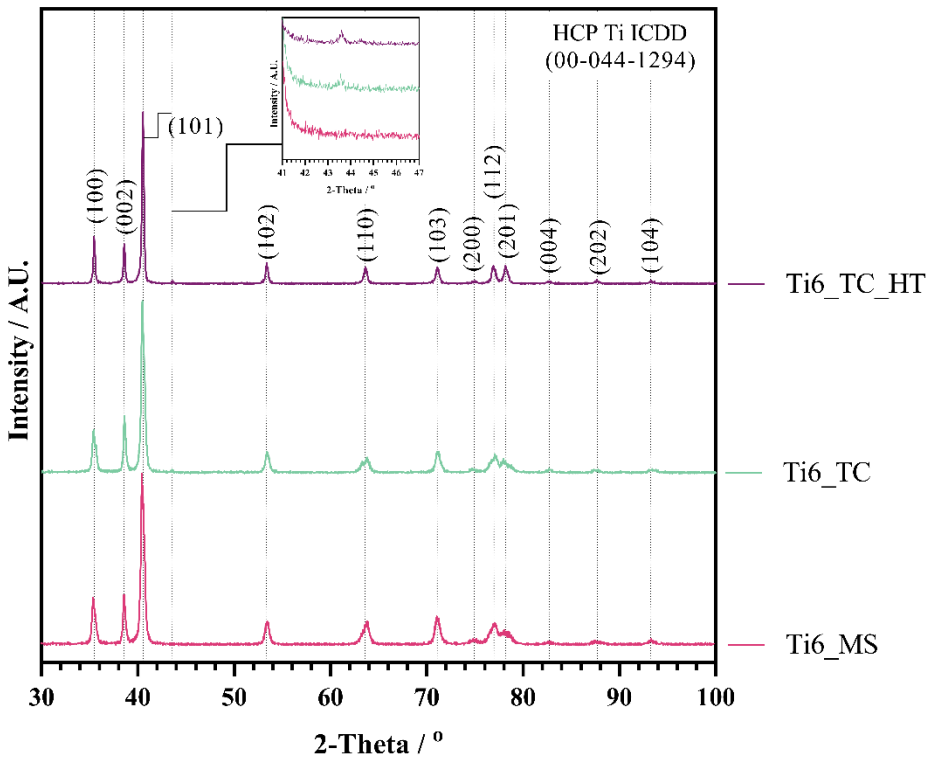


Figure 5.4 XRD spectra of Ti6_MS, Ti6_TC, and Ti6_TC_HT. Grey lines correspond to HCP Ti (ICDD 00-044-1294). (Inset) Magnified region showing the peak located at ~43.6°.

The spectra show significant differences between the three samples. As expected, there are no peaks associated with Na in the spectra for Ti6_TC. The two peaks observed within the high-resolution Na 1s window (Figure 5.5d) are due to Ti LMM. A peak due to the Na—O bond is only seen in the spectra for Ti6_TC and Ti6_TC_HT and is located at 1071.6 and 1071.4 eV, respectively, as expected for Na within titanate structures.

The high-resolution O 1s spectra (Figure 5.5b) can be deconvoluted into two forms: O^{2-} and OH^{-}. The proportion of the peak areas associated with O^{2-} and OH^{-} in the starting material was 67 and 33 %, respectively. This changed to 83 and 17 % for Ti6_TC and 79 and 21 % for Ti6_TC_HT.

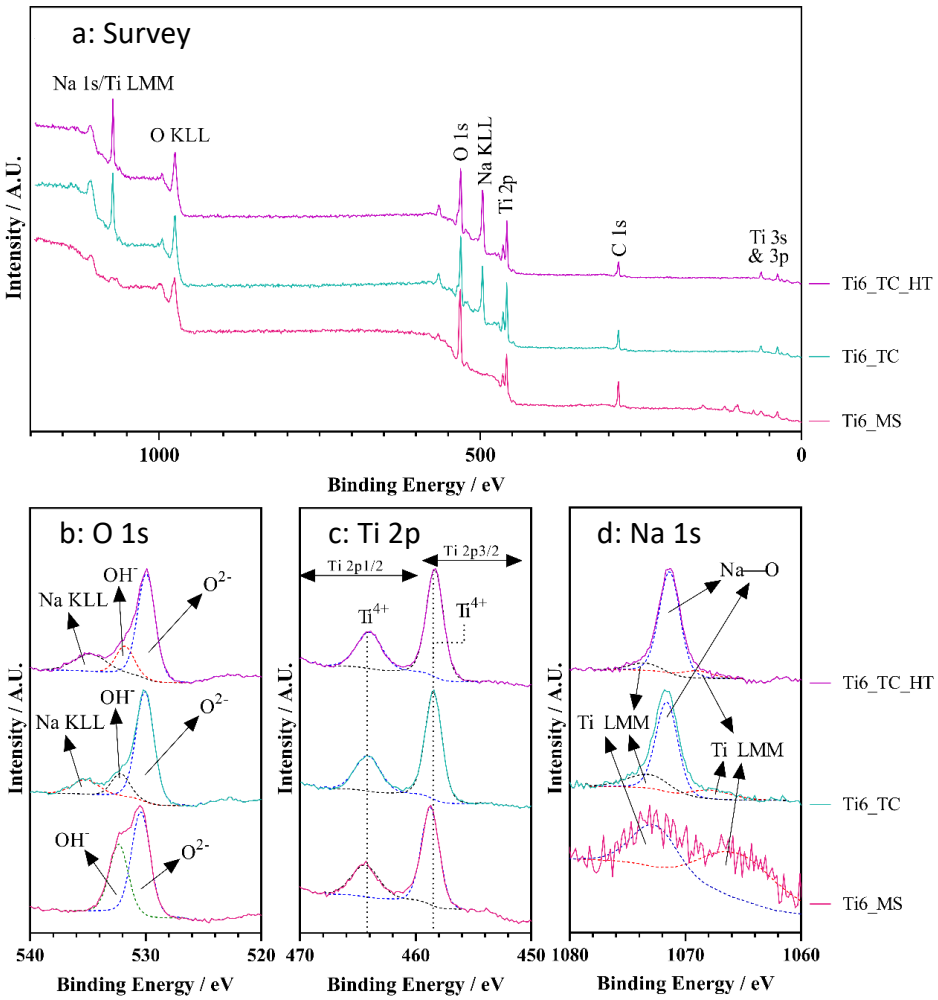


Figure 5.5 (a) Survey and high-resolution (b) O 1s, (c) Ti 2p, (d) Na 1s XP spectra of Ti6_MS, Ti6_TC, and Ti6_TC_HT. Dotted lines represent individual components.

The high-resolution Ti 2p spectra (Figure 5.5c) can be deconvoluted into one species with 2 components: Ti^{4+} $2p_{1/2}$ and $2p_{3/2}$ and indicates TiO_2 chemistry. There is little variation between samples for this doublet suggesting the chemical and heat treatments do not shift the chemistry away from that of TiO_2. This is consistent with the other analytical data and that found within the literature.

Finally, Raman analysis (Figure 5.6) was used to show the differences in the bonding on the microsphere surfaces before and after the alkaline titanate conversion and heat-treatment. All three samples featured a peak at 123 cm^{-1} which is attributed to the B_{1g} and E_g modes of anatase. The species present in the Ti6_MS sample were mostly Raman-inactive, with the only distinct feature being a small peak at 180 cm^{-1}, which we have not been able to identify, though it is consistently present. After the alkaline titanate conversion process additional peaks at 285, 440, and 900 cm^{-1} were observed. These features are consistent with sodium hydrogen titanate ($Na_xH_{2-x}Ti_3O_7$) and titanate species being present in the surface layer of the microspheres. The broad feature at 630–850 cm^{-1} suggests Ti—O—Ti stretching within the edge-shared TiO_6 octahedra.

After heat-treatment a new peak formed at 610 cm^{-1} in addition to those seen in Ti6_TC. The peak at 285 cm^{-1} disappeared and was replaced by a broader feature at 255 cm^{-1}. Peaks at 255, 440, 610, and 900 cm^{-1} in both the TC and TC_HT sample correspond to the E_g, A_{1g}, and Ti—O stretching vibrations (TiO_4 tetrahedra) modes, respectively, for rutile Ti_2O_3.[34,35] The broadening of the features at 255 and 900 cm^{-1} in Ti6_TC_HT is likely due to overlapping titanate and TiO_2.

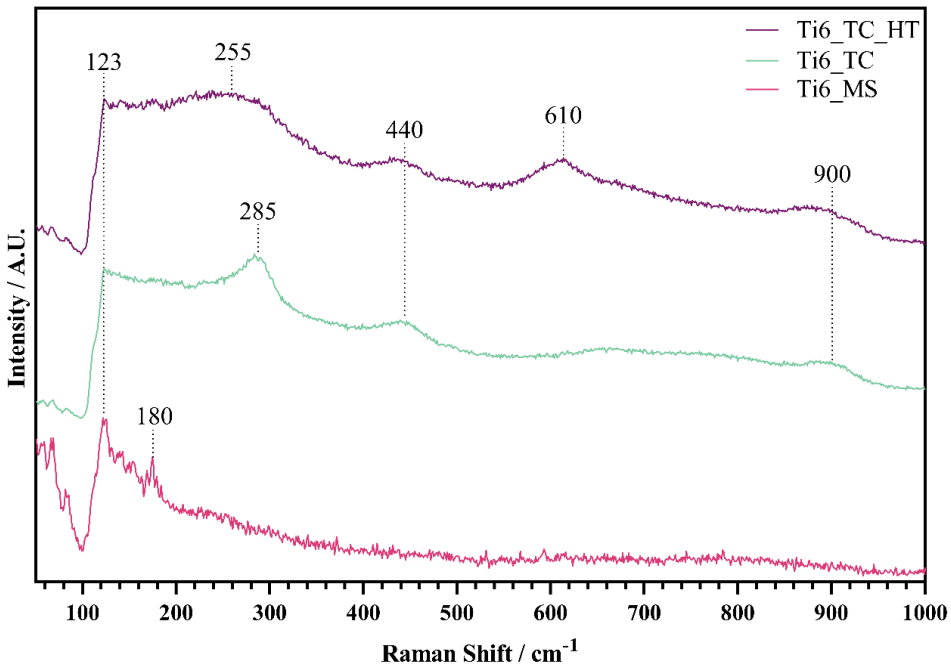


Figure 5.6 Raman spectra for Ti6_MS, Ti6_TC, and Ti6_TC_HT. Lines indicate notable features on the spectra as discussed in the main text.

The differences between the Raman spectra of Ti6_TC and Ti6_TC_HT are consistent with an increase in TiO_2 formation during the heat-treatment stage. This is likely in the form of anatase as rutile formation requires higher temperatures. The growth of anatase crystals must be relatively small as it is not observed within the XRD data, though it is consistent with the SEM micrographs in Figure 5.1 which showed some growth within the titanate structures.

5.3.2 Ink Optimisation for Electrochemical Testing

Before the material can be assessed for its activity towards electrochemical reactions, the ink used to coat it onto the electrode must be optimised. Initially, similar inks to those used for the perovskite electrochemistry (see Chapter 6) was used. However, it transpired that this was not suitable for two key reasons. First, the active electrocatalyst was far harder to disperse than the Vulcan carbon (VC) used to support it. This meant that after mixing, the microspherical electrocatalysts would sink to the bottom of the ink leading to a non-homogeneous solution. This results in the electrocatalyst coating containing a

significantly lower amount of active material that expected from the masses used to make the ink.

The second major issue with the ink formulation used in that chapter is the use of ultrasonication. Ultrasonication is a common technique to create homogeneous electrocatalyst inks,[36] and long exposure to ultrasonic irradiation can give inks which stay well dispersed after mixing.[37] It has also been shown that ultrasonication can reduce dissolved metals to form metallic nanoparticles,[38] alter the morphology of electrocatalysts,[39] and depolymerise macromolecules.[40] Pollet and co-workers systematically showed that the time, power, and temperature of the sonication of the ink can alter the ECSA of an otherwise identical electrocatalyst coating.[41] They have also argued that the use of ultrasonication as an ink homogenisation method is not given enough attention in the literature and is often used without sufficient thought.[42] Within the fuel cell literature, Kuroki *et al* demonstrated that sonication can damage the triple phase boundary (that between Nafion, Pt, and the substrate), reducing cell performance.[43]

Given this, it is important, therefore, to check that the ultrasonication method does not change the morphology of the material under study in a detrimental way. In the next chapter, the bulk perovskite powders were not influenced by this process as they did not possess any specifically designed structure. However, the titanate microspheres have a relatively fragile nanostructure. As such, sonication can damage the microspheres and the conversion layers at their surface. This was first observed whilst preparing samples for TEM analysis. The standard preparation procedure requires sonication of the sample in IPA to then coat onto the TEM grid. However, as can be seen in Figure 5.7, this destroyed the microspheres. When the TEM sample preparation procedure was altered such that the no ultrasonication was used, the microspherical structure was maintained and analysis possible as shown in Figure 5.8.

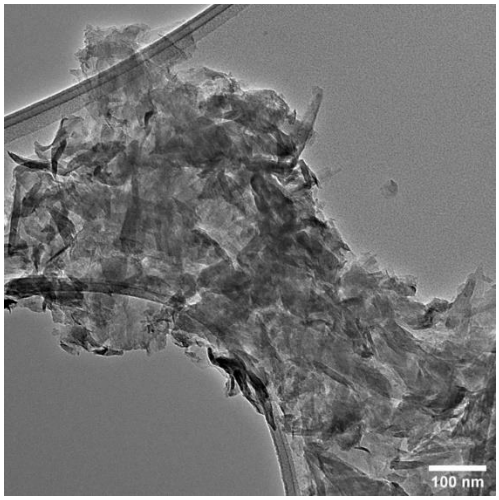


Figure 5.7 TEM micrograph (200 kV) of Ti6_TC showing the complete loss of the microspherical structure after ultrasonication. Scale bar shows 100 nm.

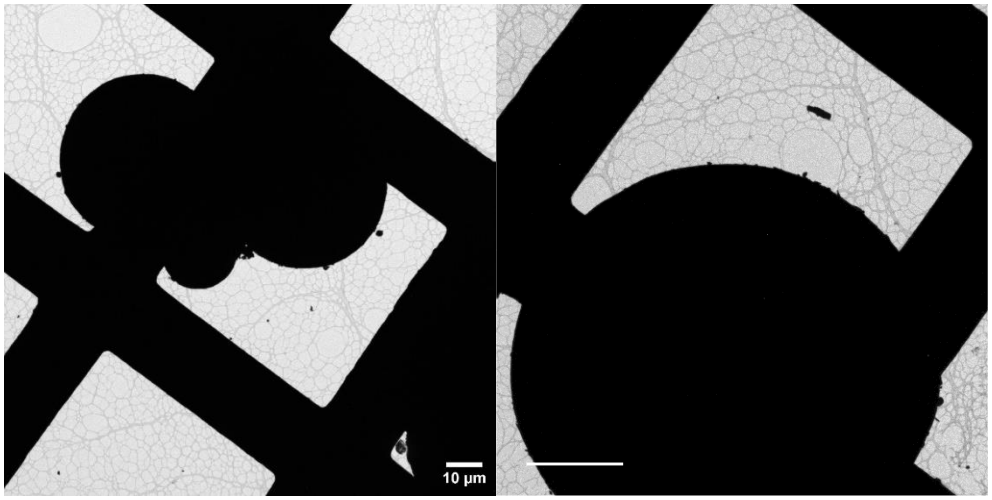


Figure 5.8 TEM micrographs at 200 kV showing the Ti6_TC sample showing the preservation of the titanate microspheres when the ink is prepared without ultrasonication. Scale bars are (a) 10 µm and (b) 200 µm.

Moving away from ultrasonication may reduce the homogeneity of the electrocatalyst ink. Though researchers have demonstrated that alternative homogenization methods such as ball-milling, magnetic stirrer-bars, and hydrodynamic cavitation can work effectively.[42] Mixing of the inks with a stirrer-bar would eliminate the risk of ultrasonic cavitation damaging the structures. If the aliquot required for the ink coating is taken whilst the solution is still being stirred, then there will not be sufficient time of the electrocatalyst to settle. Thus, it was hoped that this method would give a more representative loading of the electrocatalyst. Figure 5.9 compares SEM micrographs after

various mixing techniques were deployed. In all cases a 4:1 electrocatalyst:VC ratio was used. For the SEM analyses, the samples were dropcasted onto sticky carbon applied to stainless steel stubs. When 30 mins of sonication was used, almost no microspheres could be seen in the Ti6_TC sample. 30 mins of stirrer bar mixing gave the most consistent results.

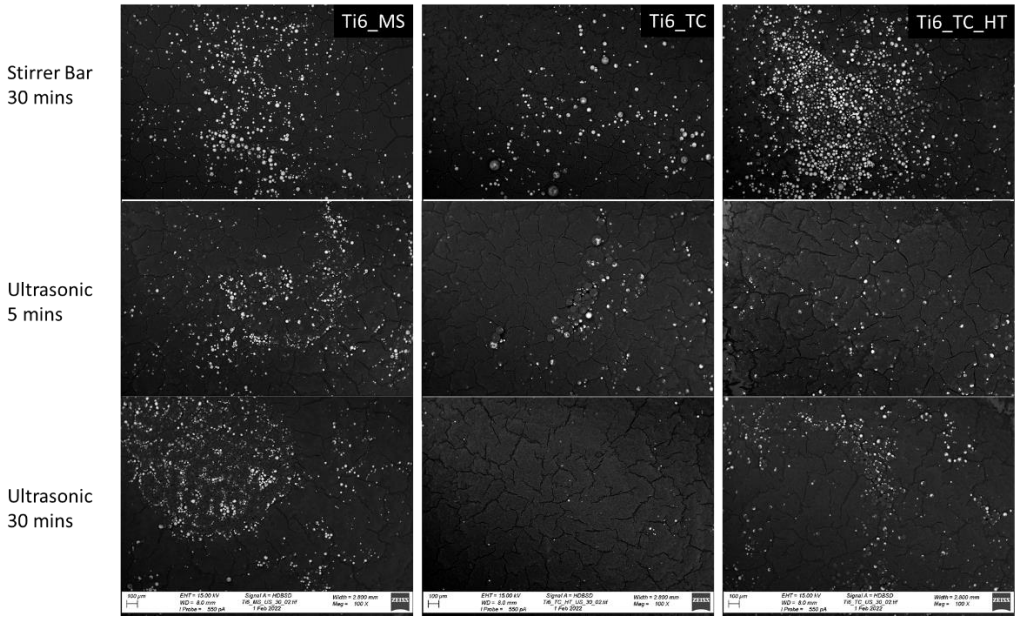


Figure 5.9 Back-scatter detection SEM images of Ti6_MS, Ti6_TC, and Ti6_TC_HT with VC inks homogenised either with a stirrer bar for 30 minutes, or ultrasonicated for 5 or 30 minutes. With BSD-SEM the contrast relates to the atomic number with heavier elements showing brighter. Scale bars show 100 µm.

5.3.3 General Electrochemical Characterisation

The titanate materials are not, in and of themselves, sufficiently conductive to be used as an electrocatalyst ink, hence Vulcan carbon (VC) was used as highly conductive support. The ink formulation used was 5 mg of VC and 20 mg of titanate mixed in 1 mL of ethanol and 100 µL of Nafion (5%wt in aliphatic alcohols). 10 µL of this ink was dispersed onto a GC rotating disc electrode. This resulted in a total mass loading of 1.16 mg cm^{-2} (0.92 $mg_{electrocatalyst}$ cm^{-2}, 0.23 mg_{VC} cm^{-2}) on the 5 mm GC electrode (area = 0.19635 cm^{-2}). Materials were tested in 0.1 mol dm^{-3} KOH in line with previous ORR reports in the literature.[44,45]

As discussed in Chapter 2, it is important to assess materials with a variety of metrics. In order to do this, the surface area of the mixed material must be measured to allow the specific activity (mA cm^{-2}) to be calculated. A non-Faradaic region of the CV was identified, and a scan rate study carried out in that region. The capacitive current at 0.86 V (the centre point of the 100 mV region measured) was plotted against scan rate. Two lines are produced from the positive and negative currents. The average of the magnitudes of these slopes gives the capacitance of the material. This is then divided by the specific capacitance (22 µF cm^{-2} is used for carbon materials in basic electrolytes in the literature[46,47]) to give the electrochemically active surface area (ECSA). A representative set of CVs showing the different scan rates in the region used is given in Figure 5.10A and the capacitance slopes obtained from the experiment in Figure 5.10B. These data are summarised in Table 5.2.

The alkaline conversion (MS→TC) increased the surface area by 25 %. The heat-treatment process (TC→TC_HT) further increased the surface area by 45 %. Relative to the initial Ti6_MS formulation, Ti6_TC_HT had an 81 % higher surface area. This is in line with the SEM images in Figure 5.1 and Figure 5.2 in which the sodium titanate layer clearly has a higher surface area than the relatively smooth underlying microsphere.

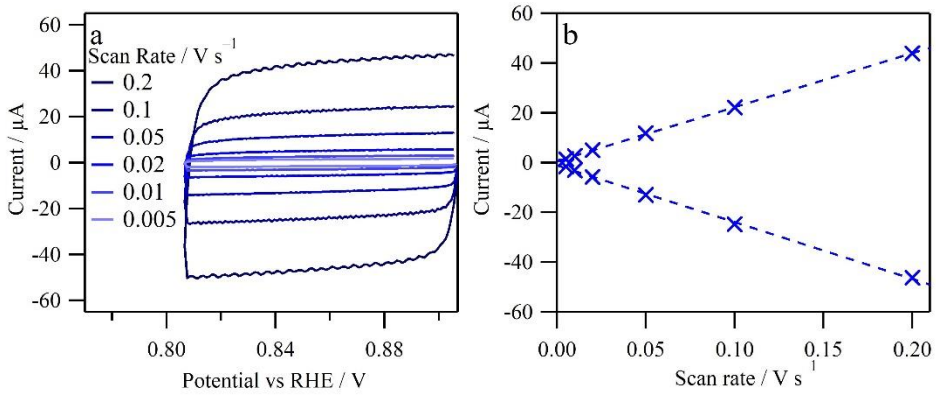


Figure 5.10 (a) Cyclic voltammograms of a GC working electrode coated with an ink of Ti6_TC with VC (4:1 ratio) in 0.1 mol dm^{-3} KOH at scan rates between 0.005 and 0.2 V s^{-1}. (b) Plot showing the linear relationship between the scan rate and the positive and negative non-Faradaic current measured at 0.86 V. Potentials converted from Hg/HgO (0.1 mol dm^{-3} KOH) to RHE.

Table 5.2 Mass loading, capacitance, and calculated ECSA of the tested electrocatalyst formulations. Except for VC, all materials are a 4:1 mixture of electrocatalyst:VC. A specific capacity of 22 µF cm^{-2} was used to calculate the ECSA from the measured capacitance.

	Mass Loading / mg cm^{-2}				
Ink	Total	Electrocatalyst	Carbon	Capacitance / µF	ECSA / cm^{-2}
Ti6_MS	1.16	0.926	0.231	179	8.11
Ti6_TC	1.16	0.926	0.231	223	10.11
Ti6_TC_HT	1.16	0.926	0.231	323	14.66
VC	0.231	-	0.231	383	17.42

5.3.4 Oxygen Reduction Reaction (ORR)

The electrocatalyst/VC formulations were tested were tested in alkaline (0.1 mol dm^{-3} KOH) conditions for activity towards the ORR. Rotating disc electrode voltammetry was used to extract kinetic information about the electrocatalytic ORR ability of each of the tested materials.

As discussed previously, oxygen reduction can take place through different mechanisms. The most common in aqueous media are the 1x4e and 2x2e mechanism. The former directly reduces oxygen to water, whereas the latter goes *via* a peroxide intermediate. For fuel cell applications, the 1x4e mechanism is preferred.[48] If H_2O_2 is the desired product, then the 2x2e mechanism is desirable.[49] For battery applications, the 2x2e route is also preferred.[50]

All the electrocatalysts resulted in voltammograms with 2 distinct regions. There is an initial plateau between 0.5 and 0.3 V, and then a second plateau from 0 V. This indicates the oxygen reduction is taking place in two steps, consistent with the 2x2e mechanism in which oxygen is first reduced to peroxide in a 2-electron step and then to water in a final 2-electron step.

Koutecký-Levich (K-L) analyses were carried out to verify the number of electrons transferred throughout the ORR. The high ECSA of the coated

electrode relative to the geometric area of the electrode ($\frac{A_{ECSA}}{A_{geo}} \gg 1$) means that the extraction of kinetic parameters from the mixed kinetic-diffusion controlled region of the RDE voltammogram (*i.e.,* the sloped region) would lead to erroneous results, in which electrocatalytic properties may be ascribed to properties solely arising from surface area effects.[51–53] However, work by Masa *et al* showed that the mass-transport controlled region of the voltammogram (*i.e.,* the plateau region) is unaffected by the effects of a high surface area, thus the region can be used to extract information on the number of electrons transferred.[51]

A full set of RDE voltammograms are shown in Figure 5.11 at varying rotation rates. Figure 5.12 presents a comparison of voltammograms measured at 1600 rpm for each electrocatalyst. K-L slopes were extracted from these plots at 0.4 V for the first plateau and −0.1 V for the second plateau. The K-L slopes calculated for the electrocatalyst materials and for the VC support are presented in Figure 5.13. The theoretical K-L slopes for n = 2 and n = 4 are presented in each for comparison.

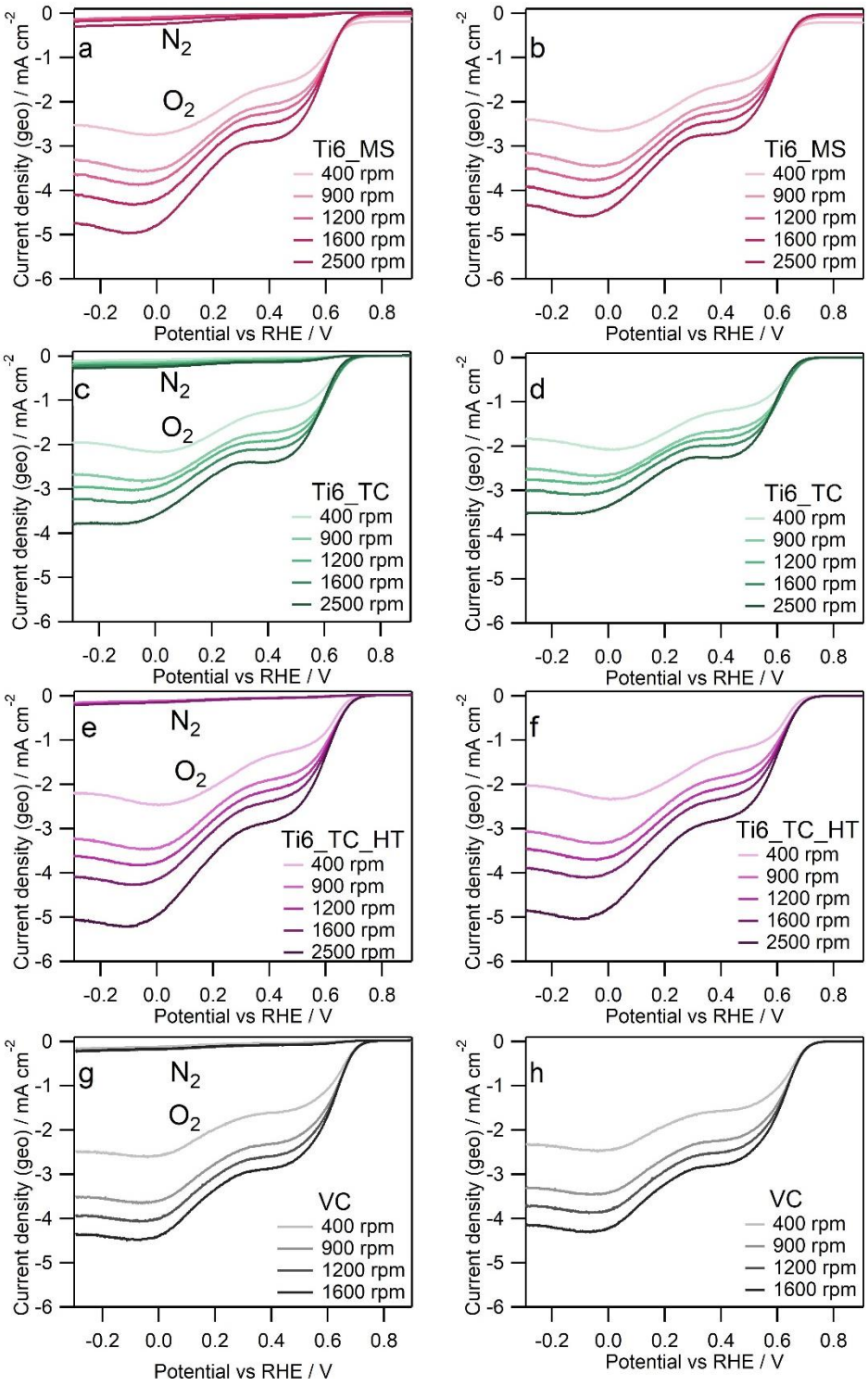


Figure 5.11 RDE voltammograms measured in 0.1 mol dm^{-3} KOH for a GC electrode coated in an ink containing (a, b) Ti6_MS, (c, d) Ti6_TC (AM), (e, f) Ti6_TC_HT each with VC (4:1 ratio) or (g, h) an ink containing VC and no electrocatalyst. LSVs measured in (a, c, e, g) O_2 saturated or N_2 purged electrolyte were subtracted from the O_2 saturated LSVs to give the (b, d, f, h) final LSVs used for K-L analyses. Rotation rate: 400 rpm to 2500 rpm. Scan rate: 5 mV s^{-1}, positive to negative. Potentials converted to RHE from Hg/HgO (0.1 mol dm^{-3} KOH). Geometric area of the electrode: 0.19635 cm^2

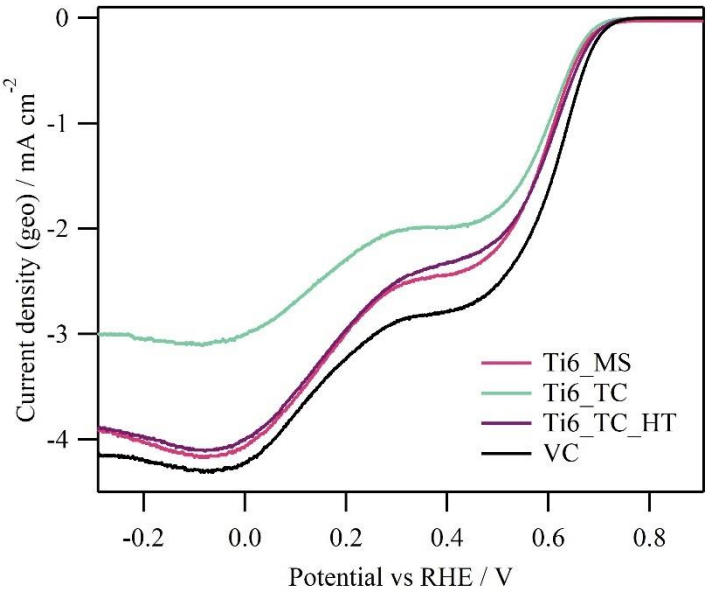


Figure 5.12 RDE voltammograms measured in 0.1 mol dm^{-3} KOH saturated with O_2 for a GC electrode coated with an ink containing Ti6_MS, Ti6_TC or Ti6_TC_HT with VC in a 4:1 ratio, or just VC. Rotation rate: 1600 rpm, scan rate: 5 mV s^{-1}. Scanning in the negative direction. Potentials converted to RHE from Hg/HgO (0.1 mol dm^{-3} KOH). LSVs in N_2 purged electrolyte were subtracted from the O_2 saturated LSVs. Currents normalised to the geometric area of the electrode (0.19635 cm^2).

Although K-L slopes extracted from the plateau region would be expected to pass through the origin, it is clearly observed that this is not the case. This may be due to the high mass loading.[54] As such, it is suggested that future work should first begin with an electrocatalyst loading study. This would allow the loading to be minimised and hence reduce the impact of mass loading on the mass transport properties of the electrode coating and allow for more effective extraction of kinetic parameters.[51]

Values for n were extracted using K-L analyses as previously described from a 100 mV region of the plateau and the average taken in order to get an error for the value (taken as 2 standard deviations). These results are presented in Table 5.3.

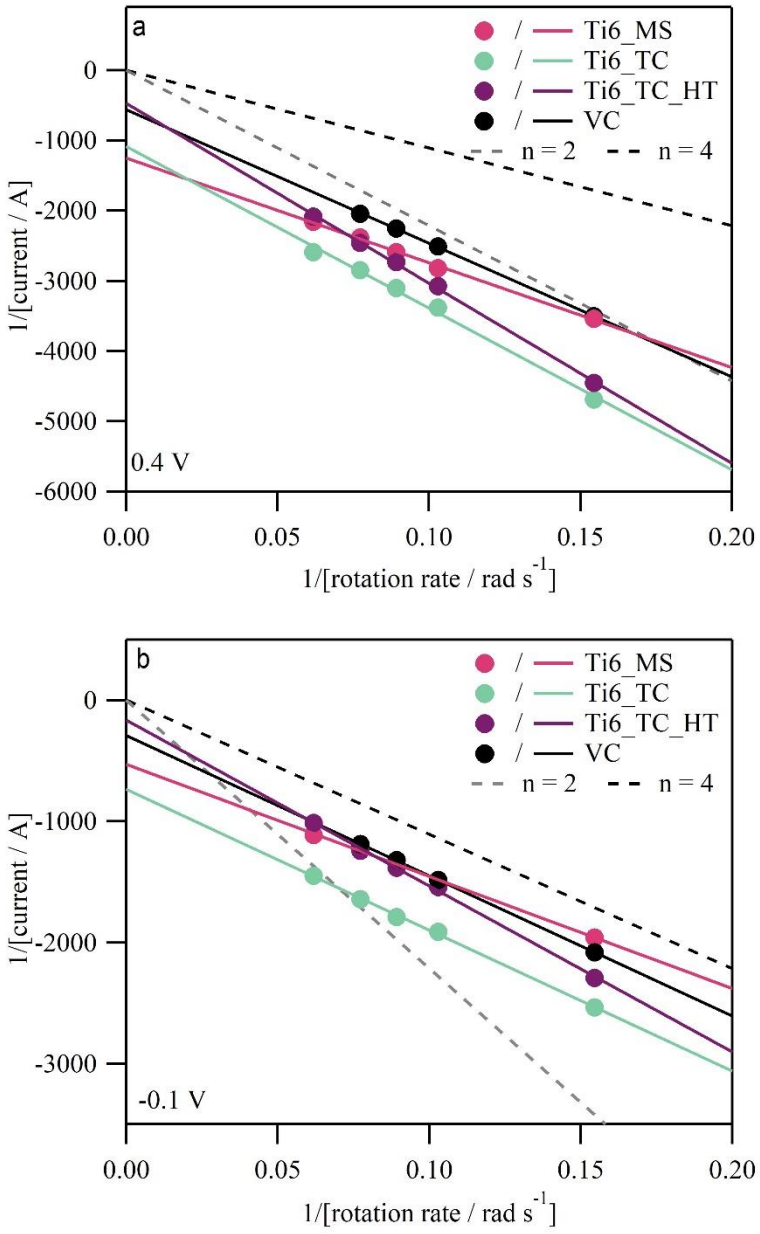


Figure 5.13 K-L analyses at the (a) first (0.4 V) and (b) second (−0.1 V) plateaus. The black dotted line is the theoretical K-L slope for n=4 and the grey dotted line is the theoretical K-L slope for n=2.

Table 5.3 Comparison of J_L at 1600 rpm for the electrocatalysts and the VC support at 0.4 V and −0.1 V, where the first and second plateaus are observed, respectively. Values for n across each plateau are extracted by K-L analyses and the average value across the plateau is presented ±2 standard deviation.

	First plateau (0.4 V)		Second plateau (−0.1 V)	
	J_L / mA cm^{-2}	n ± 2 s.d.	J_L / mA cm^{-2}	n ± 2 s.d.
Ti6_MS	−2.44	3.1 ± 0.2	−4.16	4.5 ± 0.2
Ti6_TC	−1.99	2.0 ± 0.1	−3.09	3.9 ± 0.2
Ti6_TC_HT	−2.32	1.8 ± 0.1	-4.10	3.0 ± 0.2
VC	−2.79	2.38 ± 0.04	-4.29	3.7 ± 0.1

It is expected that the first plateau would correspond to the transfer of 2 electrons and the second would correspond to the transfer of 4 electrons. For Ti6_MS, the plateau deviates strongly from this value with an electron transfer number of 3. This suggests that a mix of the 2x2e and 1x4e mechanisms are at play. The addition of the sodium titanate layer appears to increase the specificity of electrocatalyst towards the 2e process, with Ti6_TC and Ti6_TC_HT having electron transfer numbers of 2.0 and 1.8, respectively. The VC support shows a mix of the two mechanisms. Carbon materials typically follow the 2x2e ORR route and have been investigated for their use in electrochemical H_2O_2 production,[55] but some researchers have optimised the nitrogen doping of VC towards the 1x4e route.[44]

The onset potentials (defined here as the potential required to achieve −0.2 mA cm^{-2}) for the first plateau are all about equal. For VC this it is 0.697 V, whereas for Ti6_MS, Ti6_TC, and Ti6_TC_HT the onset potentials are 0.680 V, 0.672 V, and 0.686 V, respectively. This is indicative that the RDS occurs on the same active site. The only active site that is the same across all the samples is the carbon in the VC support. Synergistic interactions between the VC support and electrocatalyst material have been previously reported in the literature with MoO_2,[44] precious metal electrocatalysts,[56] and CeO_2,[57] and $LaNiO_3$.[58]

The second plateau should give rise to an electron transfer number of 4 in all cases, though this is not observed. Inspection of the voltammograms in Figure 5.12 shows that the plateau region is not flat and instead appears to peak. This suggests that mass-transport control is not fully achieved, and that kinetic and diffusional issues may be impacting the measurement.[51,52,59,60] This is likely due to the thickness of the coating blocking the efficient diffusion of O_2. For this reason, deep analytical insights into the electron transfer in this region is not possible.

Further insights into how the change in surface chemistry impacts the electrochemistry can be gained from Tafel analyses. As noted previously, the large ECSA relative to the geometric surface area means that kinetic parameters extracted from outside the plateau region may not be reliable.[51] However, in the interest of completeness, values for the kinetic current density (i_k) are calculated from the rotation rate studies presented in Figure 5.11 between 610 mV and 673 mV whereby the ORR is partially kinetically controlled and is prior to the plateau. The fitting of Tafel slopes to this region is shown in Figure 5.14. Ti6_MS, Ti6_TC, and Ti6_TC_HT have Tafel slopes (± standard error) of −76 mV dec^{-1} ± 3 mV dec^{-1}, −80 mV dec^{-1} ± 3 mV dec^{-1}, and −84 mV dec^{-1} ± 2 mV dec^{-1}, respectively. For VC, the Tafel slope is −86 mV dec^{-1} ± 2 mV dec^{-1}. Tafel slopes of between 85 and 95 mV dec^{-1} were previously reported for Co-based electrocatalysts on a nanocarbon support by Wu *et al.*[61]

A slope of 60 mV dec^{-1} is suggestive of the $MO_2^- + H_2O \rightarrow MO_2H + OH^-$ being the rate limiting step (where M is a metal).[62] The next archetypal Tafel slope for the ORR is 120 mV dec^{-1} and is associated the first electron transfer being the RDS.[62] All four tested systems have Tafel slopes between these values indicating a rate is determined by a combination of this first electron transfer and the dissociation of the H_2O as with the other materials. However, it should again be stressed that these Tafel slopes are derived from regions of the RDE voltammograms that are likely to be unduly influenced by surface area.[51]

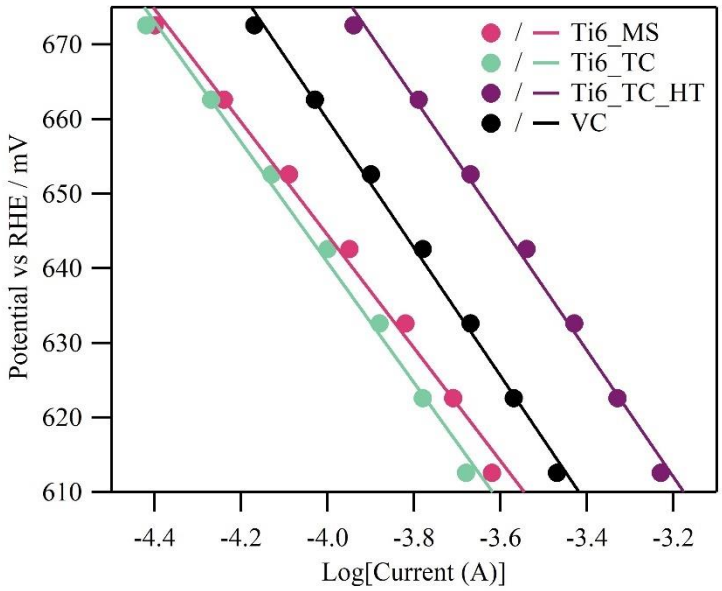


Figure 5.14 Tafel slopes (solid lines) fitted to kinetic current values (circles) extracted by K-L analysis from the rotation rate study described previously. Potential is given in mV against the log of the current in A to give Tafel slopes with values in mV dec^{-1}.

5.4 Conclusions

The work presented in this chapter demonstrates that the wet chemical method for sodium titanate formation can be applied to Ti6Al4V microspheres and doing so increases the ECSA of the material. Further enhancement of the ECSA is achieved through heating the material such that the crystal size increases, but minimal rutile formation occurs.

It was found that the Ti6_MS microspheres had low specificity towards either the 2x2e or 1x4e ORR pathways. The introduction of a sodium titanate layer to form Ti6_TC improved the specificity towards the 2x2e pathway as noted by an electron transfer number close to 2 being measured for the first plateau (compared to 3 for Ti6_MS). Heat treatment of this coated material to form Ti6_TC_HT maintained this improved specificity, whilst also greatly enhancing the surface area of the material. Thus, this work has shown that the gross morphology (microspheres) of a material can be maintained whilst inducing mechanistic changes through chemical means. Coupled to the ability to increase the surface area of the material without altering the mechanistic specificity, this work showcases a potential electrocatalyst design strategy.

5.5 Future Work

Further evidence of the mechanistic change due to the presence of the sodium titanate layer could be gained through rotating-ring disc voltammetry. In this experiment a Au ring surrounds the coated GC disc. As oxygen is reduced at the disc electrode the products are flung out across the ring (when rotating laminar flow is achieved). The ring is poised at a potential to oxidise peroxide. Thus, if the product of the reduction is peroxide, and oxidative current will be measured at the ring. The potential at which the second 2e step begins is characterised by a decrease in the oxidative current at the ring.

It is possible that further heat-treatment could induce rutile formation within the sodium titanate structure. This would greatly disrupt the layered titanate structure, potentially increasing the intrinsic activity as well as the surface area.

5.6 References

1. Deutch, J. Is Net Zero Carbon 2050 Possible? *Joule* **4**, 2237–2240 (2020).

2. HM Government. *The Ten Point Plan for a Green Industrial Revolution*. https://www.gov.uk/government/publications/the-ten-point-plan-for-a-green-industrial-revolution/title (2020).

3. Wang, X. *et al.* Review of Metal Catalysts for Oxygen Reduction Reaction: From Nanoscale Engineering to Atomic Design. *Chem* **5**, 1486–1511 (2019).

4. Bhuvanendran, N., Ravichandran, S., Xu, Q., Maiyalagan, T. & Su, H. A quick guide to the assessment of key electrochemical performance indicators for the oxygen reduction reaction: A comprehensive review. *Int. J. Hydrogen Energy* **47**, 7113–7138 (2022).

5. Li, Y. *et al.* Recent Progresses in Oxygen Reduction Reaction Electrocatalysts for Electrochemical Energy Applications. *Electrochem. Energy Rev.* **2**, 518–538 (2019).

6. Gao, R. *et al.* Pt/Fe2O3 with Pt–Fe pair sites as a catalyst for oxygen reduction with ultralow Pt loading. *Nat. Energy* **6**, 614–623 (2021).

7. Wang, Y., Zheng, X. & Wang, D. Design concept for electrocatalysts. *Nano Res.* **15**, 1730–1752 (2022).

8. Balgis, R., Anilkumar, G. M., Sago, S., Ogi, T. & Okuyama, K. Ultrahigh oxygen reduction activity of Pt/nitrogen-doped porous carbon microspheres prepared via spray-drying. *J. Power Sources* **229**, 58–64 (2013).

9. Mayrhofer, K. J. J. *et al.* Measurement of oxygen reduction activities via the rotating disc electrode method: From Pt model surfaces to carbon-supported high surface area catalysts. *Electrochim. Acta* **53**, 3181–3188 (2008).

10. Periasamy, A. P. *et al.* Carbon–boron core–shell microspheres for the oxygen reduction reaction. *J. Mater. Chem. A* **4**, 12987–12994 (2016).

11. Lei, H. *et al.* Ni2P hollow microspheres for electrocatalytic oxygen evolution and reduction reactions. *Catal. Sci. Technol.* **8**, 2289–2293 (2018).

12. Wang, H. *et al.* Durable and Efficient Hollow Porous Oxide Spinel Microspheres for Oxygen Reduction. *Joule* **2**, 337–348 (2018).

13. Sun, S., Li, H. & Xu, Z. J. Impact of Surface Area in Evaluation of Catalyst Activity. *Joule* **2**, 1024–1027 (2018).

14. Ren, H., Pan, Y., Sorrell, C. C. & Du, H. Assessment of electrocatalytic activity through the lens of three surface area normalization techniques. *J. Mater. Chem. A* **8**, 3154–3159 (2020).

15. Wei, C. *et al.* Approaches for measuring the surface areas of metal oxide electrocatalysts for determining their intrinsic electrocatalytic activity. *Chem. Soc. Rev.* **48**, 2518–2534 (2019).

16. Serpone, N. Is the Band Gap of Pristine TiO_2 Narrowed by Anion- and Cation-Doping of Titanium Dioxide in Second-Generation Photocatalysts? *J. Phys. Chem. B* **110**, 24287–24293 (2006).

17. Lv, Q. *et al.* Promotion effect of TiO2 on catalytic activity and stability of Pt catalyst for electrooxidation of methanol. *J. Power Sources* **218**, 93–99 (2012).

18. Huang, S. Y., Ganesan, P., Park, S. & Popov, B. N. Development of a titanium dioxide-supported platinum catalyst with ultrahigh stability for polymer electrolyte membrane fuel cell applications. *J. Am. Chem. Soc.* **131**, 13898–13899 (2009).

19. Yang, H., Yan, F., Lin, Y. & Wang, T. Novel Strontium Titanate-Based Lead-Free Ceramics for High-Energy Storage Applications. *ACS Sustain. Chem. Eng.* **5**, 10215–10222 (2017).

20. Kordás, K., Mohl, M., Kónya, Z. & Kukovecz, Á. Layered titanate nanostructures: perspectives for industrial exploitation. *Transl. Mater. Res.* **2**, 015003 (2015).

21. Zhang, Y. *et al.* Titanate and titania nanostructured materials for environmental and energy applications: a review. *RSC Adv.* **5**, 79479–79510 (2015).

22. Wadge, M. D., Stuart, B. W., Thomas, K. G. & Grant, D. M. Generation and characterisation of gallium titanate surfaces through hydrothermal ion-exchange processes. *Mater. Des.* **155**, 264–277 (2018).

23. Wadge, M. D. *et al.* Tailoring the degradation rate of magnesium through biomedical nano-porous titanate coatings. *J. Magnes. Alloy.* **9**, 336–350 (2021).

24. Wadge, M. D. *et al.* Developing highly nanoporous titanate structures via wet chemical conversion of DC magnetron sputtered titanium thin films. *J. Colloid Interface Sci.* **566**, 271–283 (2020).

25. Yamaguchi, S. *et al.* Two-in-One Biointerfaces—Antimicrobial and Bioactive Nanoporous Gallium Titanate Layers for Titanium Implants. *Nanomaterials* **7**, 229 (2017).

26. Wang, H. *et al.* Direct synthesis of bimetallic PtCo mesoporous nanospheres as efficient bifunctional electrocatalysts for both oxygen reduction reaction and methanol oxidation reaction. *Nanotechnology* **29**, 175403 (2018).

27. Wadge, M. D. *et al.* Characterization of potential nanoporous sodium titanate film formation on Ti6Al4V and TiO_2 microspherical substrates via wet-chemical alkaline conversion. *Mater. Charact.* **185**, 111760 (2022).

28. Rastegari, S. & Salahinejad, E. Morphological Optimization of Chemical-Conversion Sodium Titanate and Chitosan/Glass Nanocomposite Dip Coatings Deposited on a Titanium Alloy. *Met. Mater. Int.* **26**, 188–195 (2020).

29. Yamaguchi, S., Takadama, H., Matsushita, T., Nakamura, T. & Kokubo, T. Cross-sectional analysis of the surface ceramic layer developed on Ti metal by NaOH-heat treatment and soaking in SBF. *J. Ceram. Soc. Japan* **117**, 1126–1130 (2009).

30. Rutar, M. *et al.* Transformation of hydrogen titanate nanoribbons to TiO_2 nanoribbons and the influence of the transformation strategies on the photocatalytic performance. *Beilstein J. Nanotechnol.* **6**, 831–844 (2015).

31. Hantsche, H. Comparison of basic principles of the surface-specific analytical methods: AES/SAM, ESCA (XPS), SIMS, and ISS with X-ray microanalysis, and some applications in research and industry. *Scanning* **11**, 257–280 (1989).

32. Kawai, J. *et al.* Inelastic Mean Free Path of Photoelectrons in Ag Determined by Total Reflection X-Ray Photoelectron Spectroscopy. *Anal. Sci.* **13**, (1997).

33. Scheithauer, U. Application of the analytical methods REM/EDX, AES and SNMS to a chlorine induced aluminium corrosion. *Fresenius J. Anal. Chem.* **341**, 445–448 (1991).

34. Ocaña, M., Garcia-Ramos, J. v. & Serna, C. J. Low-Temperature Nucleation of Rutile Observed by Raman Spectroscopy during Crystallization of TiO2. *J. Am. Ceram. Soc.* **75**, 2010–2012 (1992).

35. Porto, S. P. S., Fleury, P. A. & Damen, T. C. Raman spectra of TiO_2, MgF_2, ZnF_2, FeF_2, and MnF_2. *Phys. Rev.* **154**, 522–526 (1967).

36. Pollet, B. G. The use of ultrasound for the fabrication of fuel cell materials. *Int. J. Hydrogen Energy* **35**, 11986–12004 (2010).

37. Garsany, Y., Baturina, O. A., Swider-Lyons, K. E. & Kocha, S. S. Experimental methods for quantifying the activity of platinum electrocatalysts for the oxygen reduction reaction. *Anal. Chem.* **82**, 6321–6328 (2010).

38. Okitsu, K. *et al.* Formation of noble metal particles by ultrasonic irradiation. *Ultrason. Sonochem.* **3**, S249–S251 (1996).

39. Jafari Foruzin, L. & Rezvani, Z. Ultrasonication construction of the nano-petal NiCoFe-layered double hydroxide: An excellent water oxidation electrocatalyst. *Ultrason. Sonochem.* **64**, 104919 (2020).

40. Adamski, M., Peressin, N., Holdcroft, S. & Pollet, B. G. Does power ultrasound affect Nafion® dispersions? *Ultrason. Sonochem.* **60**, 104758 (2020).

41. Pollet, B. G. & Goh, J. T. E. The importance of ultrasonic parameters in the preparation of fuel cell catalyst inks. *Electrochim. Acta* **128**, 292–303 (2014).

42. Pollet, B. G. & Kocha, S. S. Using Ultrasound to Effectively Homogenise Catalyst Inks: Is This Approach Still Acceptable? *Johnson Matthey Technol. Rev.* **66**, 61–76 (2021).

43. Kuroki, H., Onishi, K., Asami, K. & Yamaguchi, T. Catalyst Slurry Preparation Using a Hydrodynamic Cavitation Dispersion Method for Polymer Electrolyte Fuel Cells. *Ind. Eng. Chem. Res.* **58**, 19545–19550 (2019).

44. Liu, W., Cai, J., Huang, B., Zhang, X. & Lin, S. Synergistic catalytic effects of MoO2 and Vulcan carbon on the oxygen reduction reaction. *New J. Chem.* **45**, 2775–2780 (2021).

45. Ma, Y. *et al.* Highly active Vulcan carbon composite for oxygen reduction reaction in alkaline medium. *Electrochim. Acta* **133**, 391–398 (2014).

46. Centeno, T. A. & Stoeckli, F. On the specific double-layer capacitance of activated carbons, in relation to their structural and chemical properties. *J. Power Sources* **154**, 314–320 (2006).

47. McCrory, C. C. L., Jung, S., Peters, J. C. & Jaramillo, T. F. Benchmarking Heterogeneous Electrocatalysts for the Oxygen Evolution Reaction. *J. Am. Chem. Soc.* **135**, 16977–16987 (2013).

48. Shimizu, K., Sepunaru, L. & Compton, R. G. Innovative catalyst design for the oxygen reduction reaction for fuel cells. *Chem. Sci.* **7**, 3364–3369 (2016).

49. Tong, Y., Wang, L., Hou, F., Dou, S. X. & Liang, J. Electrocatalytic Oxygen Reduction to Produce Hydrogen Peroxide: Rational Design from Single-Atom Catalysts to Devices. *Electrochem. Energy Rev.* **5**, 1–34 (2022).

50. Rai, V., Lee, K. P., Safanama, D., Adams, S. & Blackwood, D. J. Oxygen Reduction and Evolution Reaction (ORR and OER) Bifunctional Electrocatalyst Operating in a Wide pH Range for Cathodic Application in Li-Air Batteries. *ACS Appl. Energy Mater.* **3**, 9417–9427 (2020).

51. Masa, J., Batchelor-McAuley, C., Schuhmann, W. & Compton, R. G. Koutecky-Levich analysis applied to nanoparticle modified rotating disk electrodes: Electrocatalysis or misinterpretation. *Nano Res.* **7**, 71–78 (2014).

52. Ward, K. R., Gara, M., Lawrence, N. S., Hartshorne, R. S. & Compton, R. G. Nanoparticle modified electrodes can show an apparent increase in electrode kinetics due solely to altered surface geometry: The effective electrochemical rate constant for non-flat and non-uniform electrode surfaces. *J. Electroanal. Chem.* **695**, 1–9 (2013).

53. Gara, M., Ward, K. R. & Compton, R. G. Nanomaterial modified electrodes: evaluating oxygen reduction catalysts. *Nanoscale* **5**, 7304–7311 (2013).

54. Zhong, G. *et al.* Effect of Experimental Operations on the Limiting Current Density of Oxygen Reduction Reaction Evaluated by Rotating-Disk Electrode. *ChemElectroChem* **7**, 1107–1114 (2020).

55. Cordeiro-Junior, P. J. M. *et al.* Catalysis of oxygen reduction reaction for H2O2 electrogeneration: The impact of different conductive carbon matrices and their physicochemical properties. *J. Catal.* **392**, 56–68 (2020).

56. Tzorbatzoglou, F., Brouzgou, A. & Tsiakaras, P. Electrocatalytic activity of Vulcan-XC-72 supported Pd, Rh and Pd_xRh_y toward HOR and ORR. *Appl. Catal. B* **174–175**, 203–211 (2015).

57. Hota, I., Debnath, A. K., Muthe, K. P., Varadwaj, K. S. K. & Parhi, P. A synergistic approach of Vulcan carbon and CeO2 in their composite as an efficient oxygen reduction reaction catalyst. *J. Appl. Electrochem.* **50**, 1069–1077 (2020).

58. Alexander, C. T., Abakumov, A. M., Forslund, R. P., Johnston, K. P. & Stevenson, K. J. Role of the Carbon Support on the Oxygen Reduction and Evolution Activities in LaNiO3 Composite Electrodes in Alkaline Solution. *ACS Appl. Energy Mater.* **1**, 1549–1558 (2018).

59. Chen, W. *et al.* Reconsidering the Benchmarking Evaluation of Catalytic Activity in Oxygen Reduction Reaction. *iScience* **23**, 101532 (2020).

60. Mayrhofer, K. J. J. *et al.* Measurement of oxygen reduction activities via the rotating disc electrode method: From Pt model surfaces to carbon-supported high surface area catalysts. *Electrochim. Acta* **53**, 3181–3188 (2008).

61. Wu, X. *et al.* Mixed-valence cobalt oxides bifunctional electrocatalyst with rich oxygen vacancies for aqueous metal-air batteries. *Chem. Eng. J.* **453**, 139831 (2023).

62. Shinagawa, T., Garcia-Esparza, A. T. & Takanabe, K. Insight on Tafel slopes from a microkinetic analysis of aqueous electrocatalysis for energy conversion. *Sci. Rep.* **5**, 1–21 (2015).

Chapter 6. Perovskites as Electrocatalysts for the Hydrogen Economy

6.1 Introduction

6.1.1 Perovskite Materials

Perovskites are a class of functional materials with crystal structures related to that of the mineral *perovskite*, with the prototypical formula $CaTiO_3$. The generalised perovskite formula is ABX_3, where the A-cation is 12-fold coordinated, and the B-site is coordinated to 6 anions. A is generally a rare-earth (lanthanoids plus Sc and Y) or alkali earth metal (especially Ca, Sr and Ba), B is typically a transition metal, and X is often an oxide anion, though halides and organic moieties can be used.

The idealised perovskite structure is cubic (Figure 6.1A) as is taken by $SrTiO_3$ at room temperature. Perovskites can be doped at both the A and B sites, and doped materials are represented by the formula $A_{1-x}A'_xB_{1-y}B'_yO_{3\pm\delta}$, where x is the proportion of A replaced by dopant A', and y is the proportion of B replaced by dopant B'.

In many cases, the dopant replaces an ion of different charge, resulting in oxygen non-stoichiometry which is represented by $\pm\delta$ (where $\delta > 0$ represents an excess of oxygen and $\delta < 0$ represents an oxygen deficiency). Part of the interest in perovskites stems from the large degree of flexibility in their compositions, which can accommodate almost every element in the periodic table, giving rise to wide range of properties and applications.[1–5] Hybrid perovskites, such as $(CH_3NH_3)PbI_3$, feature both inorganic and organic cations and are typically used in photovoltaic applications.[6] This chapter will focus on purely inorganic perovskite structures.

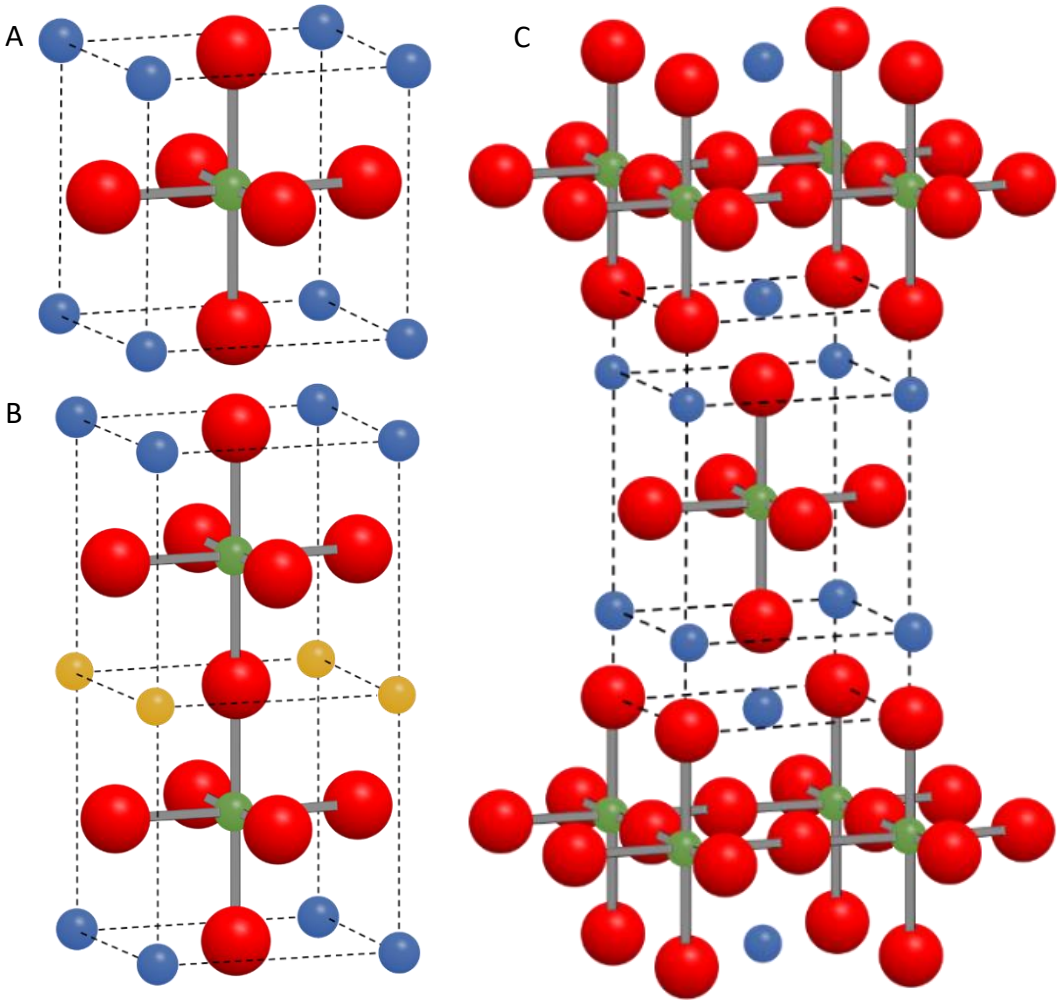


Figure 6.1 A) The cubic perovskite structure. B) Layered double perovskite. C) n=1 Ruddlesden-Popper structure. The dotted lines are guides to show alignment. Note in all cases, the idealised structure is presented with no defects or vacancies. A-site (blue/gold), B-site (green), oxygen (red). Original diagrammatic representations created based on descriptions and diagrams by Tilley[7] and Xu[8].

The structures of perovskites depend on their compositions. The Goldschmidt tolerance factor (t) is used to describe how far a structure deviates from an ideal cubic structure:[6,7]

$$t = \frac{r_a + r_O}{\sqrt{2}(r_b + r_O)} \qquad [6.1]$$

where r_A and r_B are the radii of the A and B cations, respectively. When $0.9 < t \leq 1$, the structure is likely cubic. Orthorhombic and other distorted structures occur for $0.71 < t < 0.9$. When $t > 1$, hexagonal structures occur.[7] Significantly

high or low values of t lead to non-perovskite structures.[6] For perovskite structures with multiple A and/or B cations (A' and B'), the average of the radii can be used in calculation of *t*. In addition, ionic radii can be replaced with the bond lengths A—O and B—O (if known), and *t* is then referred to as the observed tolerance factor (t_{obs}).[7] The lowest limits for cationic radii are $r_A > 0.09$ nm and $r_B > 0.051$ nm.

The cubic perovskite structure is the most-strict definition of a perovskite. There are several alternative perovskite structures which will be briefly discussed here. A double perovskite structure is one in which the dopant cations are of sufficiently different size that rather than randomly arranging amongst the A-sites, the most stable lattice configuration is one in which alternating layers of A and A' form (Figure 6.1B). In the schematic example given in Figure 6.1B it is the A-site with different dopants, though a similar phenomenon is observed with B-site doping, whereby the B-site cation represented by the green circle would alternate between B and B' down the O—B—O—B—O axis. The general formula for a double perovskite is $AA'BB'O_{5.5\pm\delta}$. For A-site doped double perovskites B = B' and vice versa for B-site doped double perovskites.[7]

Note how in the layered structure the B-site cations maintain vertical alignment. This is contrary to the Ruddlesden-Popper (RP) structure in which layers of perovskite oxide are displaced from each other and separated by a rock-salt-like layer (AO). The RP structure is based on the general formula of $A_{n+1}B_nO_{3n+1}$, whereby n dictates the structure that forms. For n=1 (Figure 6.1C), only a single layer of ABO_3 occurs before the next layer is displaced. For n=2, each slab would be 2 layers deep and so on for $n \rightarrow \infty$. In some cases, the slabs can have different structures (for instance alternating cubic and orthorhombic slabs). It is due to the wide variety of structures that perovskites can take that make them excellent candidates for optimising towards such a variety of applications.[9]

Kröger-Vink notation is used to describe defects and vacancies within perovskites.[7] The notation has the form Y_X^Z, where *X* is the ion being replaced; if *X* = i, then it is an interstitial site. *Y* is the species that replaces *X*. Vacancies are represented by the term *V*. *Z* describes the valence difference of the defect; × denotes that *X* and *Y* have the same valence, a higher valence is denoted by •, and a lower valence is denoted by ′. For example, when Sr^{2+} is added as an A-site dopant to $LaMnO_3$ to form $La_{1-x}Sr_xMnO_3$ (or LSM), the A-site occupants are denoted as $La_{La}^{\times}$, Sr_{La}', and V_{La}'''. B-site occupants are described as $Mn_{Mn}^{\times}$, $Mn_{Mn}^{\bullet}$, Mn_{Mn}', V_{Mn}'''. Most of the B sites in LSM are occupied by Mn^{3+} ions ($Mn_{Mn}^{\times}$), with a significant proportion of Mn^{4+} ($Mn_{Mn}^{\bullet}$) to maintain electroneutrality. The lower valence Mn^{2+} in unlikely to be present in a large proportion, as its formation provides no charge balancing to counter the addition of Sr^{2+}. Finally, the oxygen site is occupied by either $O_O^{\times}$ or $V_O^{\bullet\bullet}$.[7]

The electronic conductivity of perovskites is affected by the presence of oxygen- and cation-vacancy defects, and by differences in the valences of the A and/or B cations.[7] Oxygen vacancies can be formed by heating the material under vacuum or in O_2-poor environments, resulting in a change in cation valence (Equation 6.2), or (when a change in valence is not possible) the release of electrons (Equation 6.3).[10]

$$O_O^{\times} + 2B_B \leftrightarrow \frac{1}{2}O_2 + V_O^{\bullet\bullet} + 2B_B' \qquad [6.2]$$

$$O_O^{\times} \leftrightarrow \frac{1}{2}O_2 + V_O^{\bullet\bullet} + 2e' \qquad [6.3]$$

The release of a charge-balancing sea of electrons results in electronic (n-type) conductivity. The magnitude of the conductivity is proportional to the number of free electrons, which depends on the partial pressure of O_2. Where a change of valence is possible, electronic conduction can occur through electron hopping between adjacent ions. For example, Mn^{3+} in $LaMnO_3$ is reduced to Mn^{2+} upon formation of oxygen vacancies. Electronic charge propagates through the system by electron hopping from Mn^{2+} to Mn^{3+} centres. In doped

systems, such as LSM, the electrical conductivity can arise from electron transfer between Mn^{4+} and Mn^{3+} centres.

6.1.2 Synthesis of Perovskites

Two of the most common methods used to synthesise perovskites are the sol-gel and traditional solid-state routes.[11] The solid-state route involves stoichiometric mixing of metal oxides or carbonates, such as $SrCO_3$ and Fe_2O_3.[12,13] The mixtures are milled, then calcined at high temperatures (typically about 1000 °C) for many hours.

A typical sol-gel method involves stoichiometric mixing of metal nitrates (acetates, carbonates, halides, and oxides are sometimes used) are dissolved in water. Ethylenediaminetetraacetic acid (EDTA) and citric acid are then added as complexing and gelation agents. Ammonia or ammonium hydroxide is then added to adjust the pH to a suitable level, which varies with the target composition. This mixture is heated slightly to form a gel. The gel is then heated to remove volatile organics, before calcination near 1000 °C to obtain the solid perovskite powder.[14,15] The sol-gel route often allows for a lower calcination temperature to be used. Amirfakhri *et al* used a variant of the sol-gel method without EDTA to synthesise $LaNiO_3$ using a final calcination temperature of only 700 °C for 2 hours.[16]

6.1.3 Cation choice as a Design Strategy

An overview of some of a variety of methods that can be used for enhancing electrocatalysts were explored in Chapter 1. Here, perovskite-specific examples are explored.

6.1.3.1 A-site Cation Choice

The intrinsic activity of a perovskite material can be enhanced by substituting and doping the basic perovskite structure with additional elements. We define doping as the inclusion of additional elements to influence structure or chemistry of the perovskite to affect its activity, without the dopant itself acting as an active site for the electrocatalysis. In this sense, A-site doping does not

change the identity of the active site but can influence the valence of the B-site cations, introduce oxygen vacancies, and/or change the crystal structure.

One of the most well-studied perovskites for the oxygen evolution reaction is $(Ba_{0.5}Sr_{0.5})(Co_{0.8}Fe_{0.2})O_{3-\delta}$ (BSCF) which was brought to prominence by Suntivich *et al* in a 2011 paper showing that near unity e_g orbital filling is a strong predictor of OER performance.[17] BSCF has a cubic structure with the B-site cations having an average valence of 3.13. Without additional dopants, BSCF has an overpotential of 342 mV for −10 mA cm^{-2} of HER,[18] significantly worse than that of a platinum electrocatalyst supported on carbon (Pt/C). One of the papers that sparked the recent interest in perovskites as HER catalysts was by Xu *et al* in 2016.[18] They doped the A-site of BSCF with varying levels of Pr (i.e. $Pr_x(Ba_{0.5}Sr_{0.5})_{1-x}(Co_{0.8}Fe_{0.2})O_{3-\delta}$). Given the small size of the Pr^{3+} cation, inclusion of the dopant led to lattice shrinkage, characterised by a decrease in the lattice parameter *a*. Within $0 \leq x \geq 0.5$ the structure remains cubic and reaches a near perfect cubic perovskite structure at x = 0.5 as shown through XRD and with the oxygen non-stoichiometry $\delta = 0$. In addition to this, the presence of the Pr^{3+} was shown, through XPS, to somewhat increase the oxidation state of the Co present in the B-site and increase the Lewis acidity of the surface oxygen which could improve the adsorption, and thus dissociation, of H_2O. The conductivity of the doped BSCF increased compared to the undoped material. These factors combine to give activity towards the HER η_{-10} = 237 mV, which is over 100 mV better than the undoped BSCF. Further substitution of the A-site with Pr led to an orthorhombic structure and a dramatic loss in activity. When x = 1, η_{-10} = 456 mV meaning the electrocatalyst has no use for the HER. The increase in conductivity of the Pr-doped BSCF is somewhat surprising given the material has fewer oxygen vacancies than the un-doped counterpart. Other studies (discussed later) have shown that an increase in oxygen vacancies (characterised by an increase in δ) increases the activity.[19,20] Xu *et al* do note, however, that although they observed trends associated with the Pr-doping, there is no evidence to suggest these trends are universal.[18] Hua *et al* also doped BSCF with lanthanoids and found that La^{3+} produced similar

performance to Pr^{3+}, though overpotentials are not reported for the bulk material.[21]

Given the sheer quantity of potential A-site dopants, a rational approach to this method is required. Guan *et al* synthesised a large number of cobalt-based single and double perovskite materials systematically doped at the A-site.[22] They identified that although the B-site is the primary active site for most perovskite electrocatalysts, it exists within the influence of the A-site and so both sites are linked. The valence of the B-site can be changed by doping the A-site with cations of varying ionic electronegativity. As shown in Figure 6.2 (left), the authors had previously shown that the HER activity of oxide electrocatalysts (and specifically perovskites) shows a volcano-plot dependence to the B-site valence,[23] and this later work demonstrated an effective way to control this is via the A-site.[22] The optimal A-site ionic electronegativity (AIE) was ~2.33 was linked to the optimal B-site valence. They also demonstrated that this AIE led to a d-band which crossed the Fermi level which, as discussed previously, is a requirement of a good HER catalyst.

She *et al* demonstrated the importance of oxygen non-stoichiometry, specifically that of the concentration of surface oxygen vacancies.[24] They varied the Sr fraction in the material $La_{1-x}Sr_xFeO_{3-\delta}$ between $0 \leq x \geq 1$. The authors noted that the oxygen ion diffusion rate did not correlate to the activity of the catalyst, but the surface vacancy concentration did with x = 0.8 having both the highest concentration and the highest activity (η_{10} = 0.37).[24] Indeed, this is amongst the highest activities reported for a perovskite material towards the OER. Additionally, the concentration of Fe^{4+} was found to have a slight volcano-like relationship to the activity. This is expected as Fe^{4+} binds strongly to the OH intermediate in the OER. Too much Fe^{4+} would lead to poor release of the intermediate, and too little to poor binding.[24]

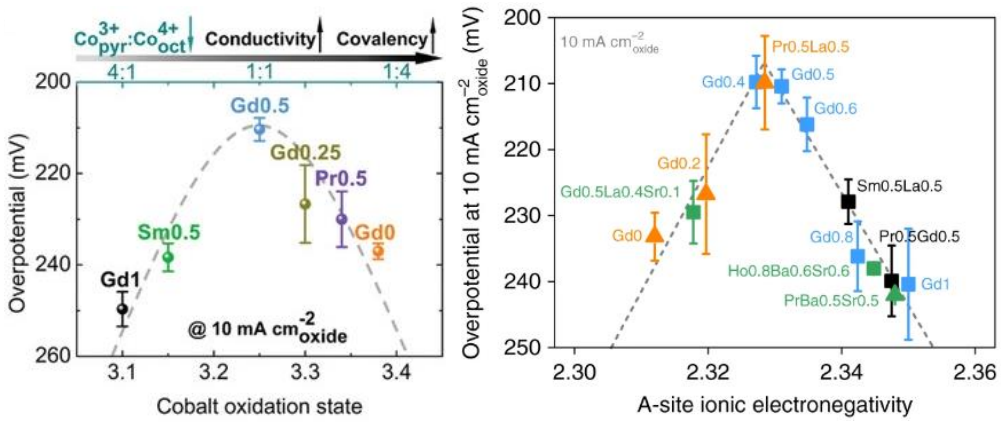


Figure 6.2 Volcano relationship between the intrinsic HER activity and (left) B-site oxidation state and (right) A-site ionic electronegativity. Triangles and squares in right represent single and double perovskites, respectively. The colours represent different dopant elements. Reproduced from Guan et al[23] *and Hua et al.*[22]

6.1.3.2 B-site Cation Choice

Where A-site doping gives indirect control over the B-site valency, doping at the B-site gives direct control over the active site. Careful choice of B-site cation can lead to interactions within the site as Dai *et al* demonstrated.[25] By bringing into close proximity sites that were either suitable for water dissociation, OH desorption, or H adsorption the activity is significantly increased compared to a material with one type of active site that compromised on some or all of those abilities. In the case of Dai *et al* the B-site was co-doped with Ti^{3+} and Ru^{5+} ($SrTi_{1-x}Ru_xO_{3-\delta}$). With x = 0.3, they found the activity of the material was orders of magnitude better than STO and ~1.5 times better than SRO. This suggests a synergy between the Ti^{3+} and Ru^{5+} centres.[25] Individually both cations would be expected to exist in the 4+ state, but charge redistribution and super-exchange mediated through the shared oxygen anion leads to the tri- and pentavalent states observed. This STRO perovskites displays the best activity towards the HER of any perovskite in terms of overpotential for −10 mA $cm_{(geo)}^{-2}$ at just 46 mV. The Tafel slope of 40 mV dec^{-1} is the similar to that of Pt/C and the durability is much better with very little change in the voltammogram even after 1000 cycles.[25]

6.2 Aims of the chapter

The work presented herein explores some trends with a variety of different perovskite materials. First Pr-doped BSCF is explored for use on the OER and ORR. This material was chosen as doping half the A-site of BSCF with Pr has previously been shown by Xu *et al* to enhance the HER.[8] Doping Pr into the A-site doping changes the crystal structure of the perovskite and decreases its activity towards the OER.

Further, the impact of the arc-melt synthesis of $BaTiO_3$ is investigated in comparison to a commercial $BaTiO_3$ powder. Arc-melting rapidly heats a material between two electrodes in an Ar atmosphere to generate a melt.[26] This then rapidly cools down to room temperature. This process can introduce a significant number of defects into the structure and thus change its physical and electrocatalytic properties. La is doped into the arc-melted $BaTiO_3$ to further investigate cationic doping as a design strategy for electrocatalysts.

Such a process has previously been done on $SrTiO_3$ by Yu *et al*.[26] Arc melting did not change its crystal structure (seen through XRD) but did narrow its bandgap and enhance its photocatalytic performance.[26] Liu *et al* doped Ba into $SrTiO_3$ leading to an enhancement in its photocatalytic performance on a Au substrate.[27]

6.3 Experimental Section

The work presented in chapter was carried out in collaboration with PhD researchers in the Ming Li group in the School of Engineering at the University of Nottingham. The perovskites were synthesised by members of the Li group and the XRD was measured by them. Matthew Cliffe and Andrew Jones assisted with XRD data analysis. Data interpretation is my own. Post-processing (grinding and ink prep) and all electrochemical and electrocatalytic work was carried out by me.

6.3.1 Perovskite Synthesis

The Pr-doped BSCF perovskites were synthesised by the Ming group. $(Ba_{0.5}Sr_{0.5})_{1-x}Pr_x(Co_{0.8}Fe_{0.2})O_3$ with x values of 0, 0.1, 0.25, 0.5 and 0.75 were

produced. Stoichiometric quantities of barium oxide, strontium oxide, cobalt oxide, iron oxide and praseodymium oxide were mixed with a pestle and mortar in acetone. The acetone was left to evaporate, then a pellet of the mixed oxides was made. The pellet was calcined in a furnace at 1000-1300 °C. The perovskite pellet was then crushed in a pestle and mortar. The perovskite powders were characterised by powder X-ray diffraction (PXRD, PANlytical). Tolerance factors are calculated using ionic radii from Shannon.[28] An equivalent method was used to create $BaTiO_3$, La-doped $BaTiO_3$. These materials were arc melted between two electrodes and rapidly cooled to room temperature.

6.3.2 Ink Preparation

Catalyst ink formulations were adapted from Xu *et al*[8] For the perovskite catalysts, 10 mg of the perovskite and 10 mg of Vulcan XC72R carbon were dispersed in a solution of 1 mL ethanol and 100 µL 5 wt% Nafion solution and sonicated for at least 30 mins to form a homogenous ink. For the Pt/C, 10 mg of platinum on carbon (20 % nominal, Alfa) was sonicated with 1 mL of ethanol and 100 µL of Nafion to form a homogenous ink. A 5 µL aliquot of the ink was drop cast onto a 5 mm (area = 0.196 cm^{-2}) glassy carbon electrode (Pine Research) that was rotating at ~100 rpm. The ink was dried under ambient conditions with rotation. Prior to coating, the electrode was polished to a mirror finish with Al_2O_3 (0.05 µm) paste and rinsed with deionised water. The perovskite ink formulations yield ~0.232 mg_{oxide} cm^{-2}. The Pt/C ink formulation yields ~0.046 mg_{Pt} cm^{-2}.

6.3.3 Electrochemical and Electrocatalytic Measurements

For oxygen evolution and reduction measurements, oxygen-saturated 0.1 mol dm^{-3} KOH was used as the electrolyte. The electrode measurements were made with the coated glassy carbon rotating disk electrode as the working electrode, graphite rod as the CE and Hg/HgO (0.1 mol dm^{-3} KOH) as the RE. The reference potential was measured against a platinised platinum electrode with hydrogen bubbling over the surface in 0.1 mol dm^{-3} KOH. Measurements were made at 100 and 10 mV s^{-1} in the region 0 – 1.2 V (vs Hg/HgO) for oxygen evolution and -0.7 to 0 V for oxygen reduction. Activity measurements are made at 1600 RPM.

The oxygen reduction reaction (ORR) activity was measured by cyclic voltammetry between 0.8 and −0.2 V at 5 mV s^{-1}. The rotation rate was varied between 400 and 2750 rpm. When using O_2-saturated electrolyte, 20 cycles at 500 mV s^{-1} were carried out in the ORR region until a reproducible CV was observed, to ensure that saturation of the electrolyte had occurred. Similarly, with N_2-sparged electrolyte CVs in the same region were measured until no oxygen electrochemistry could be observed. Blank CVs were recorded in N2-saturated electrolytes and were subtracted from those recorded in O2-saturated electrolyte to ensure only oxygen-related electrochemistry was investigated. For the K-L analyses the following constants were used (as defined in Chapter 2): $D_{O2} = 1.93\times10^{-5}$ cm^2 s^{-1}, $C_{02} = 1.26\times10^{6}$ mol cm^{-3}, $v = 1.09\times10^{-2}$ cm^2 s^{-1}, A is the geometric area of the electrode (0.19635 cm^{-2}).

6.4 Results and Discussion

6.4.1 Praseodymium-doped BSCF

6.4.1.1 Physical Characterisation

The A-site of BSCF is the equimolar $Ba_{0.5}Sr_{0.5}$ moiety. This position can be doped with a Pr^{3+} cation to bring about change in the perovskite structure. The amount of Pr doped into the structure is denoted x giving the overall structure the formula $(Ba_{0.5}Sr_{0.5})_{1-x}Pr_xCo_{0.8}Fe_{0.2}O_{3-\delta}$.

The XRD spectra presented in Figure 6.3 show that the undoped BSCF conforms well with *Pm*-3m cubic perovskite system as shown by the ICDD BSCF pattern measured by Yaremchenko *et al.*[29] Further, the Pr-doped BSCF systems doped with Pr up to x = 0.5 are consistent with the *Pm-3m* cubic perovskite phase and match that seen in the literature.[1,8] It is observed that all peaks shift to higher angles as the Pr content increases, with the greatest rate of increase between x = 0 and 0.5. The Pr^{3+} A-site dopant is smaller (r = 1.286 Å) than the Ba^{2+} and Sr^{2+} (1.61 Å and 1.44 Å).[1,8] As the amount of Pr increases, the changes in the lattice due to this size mismatch are greater. Between x=0.1 and 0.5 the (110) peak at ~31° shifts more positive with increasing x. The increasing angle of the peaks is consistent with lattice shrinkage.[8] At x=0.75 some of the peaks split

from a clear singlet to a slight doublet and the intensity of the peak drops compared to the other perovskites. This implies there is a change in the structure of the perovskite with x=0.75, likely to orthorhombic.

The shift to orthorhombic is supported by the tolerance factor as defined in literature review. Undoped BSCF and doped BSCF with x up to 0.5 all have average tolerance factors relatively close to 1 (an average tolerance factor is used as the ratio of 3+/4+ in the B-site is unknown) which is in line with a cubic structure. However, the tolerance factor for x = 0.75 is between 0.8979 and 0.9114. Tolerance factors close to and below 0.9 are typical of orthorhombic structures.[6]

Pawley refinement of the Pr-doped BSCF perovskites was carried out to establish the lattice parameters. The refinements confirm the above discussion and found that between x = 0 and x = 0.5 were cubic, whereas x = 0.75 refined to a orthorhombic phase. These data are summarised in Table 6.1.

Energy dispersive X-ray (EDX) analysis was carried out on the undoped and Pr-doped BSCF materials. The SEM and EDX maps of these are shown in Figure 6.4, and show increasing Pr content (yellow).

Table 6.1 Space group and lattice parameters from the Pawley refinement for $(Ba_{0.5}Sr_{0.5})_{1-x}Pr_xCo_{0.8}Fe_{0.2}O_{3-\delta}$. x = 0 to x = 0.5 refined as cubic structures and have just one lattice parameter, whereas x = 0.75 refined as orthorhombic and as three lattice parameters.

x	Space group	a / Å	b / Å	c / Å
0	Pm-3m	3.9839± 0.0002	-	-
0.10	Pm-3m	3.9425± 0.0003	-	-
0.25	Pm-3m	3.8903± 0.0001	-	-
0.50	Pm-3m	3.8438± 0.0001	-	-
0.75	Pnma	5.42± 0.03	5.41± 0.02	7.64± 0.02

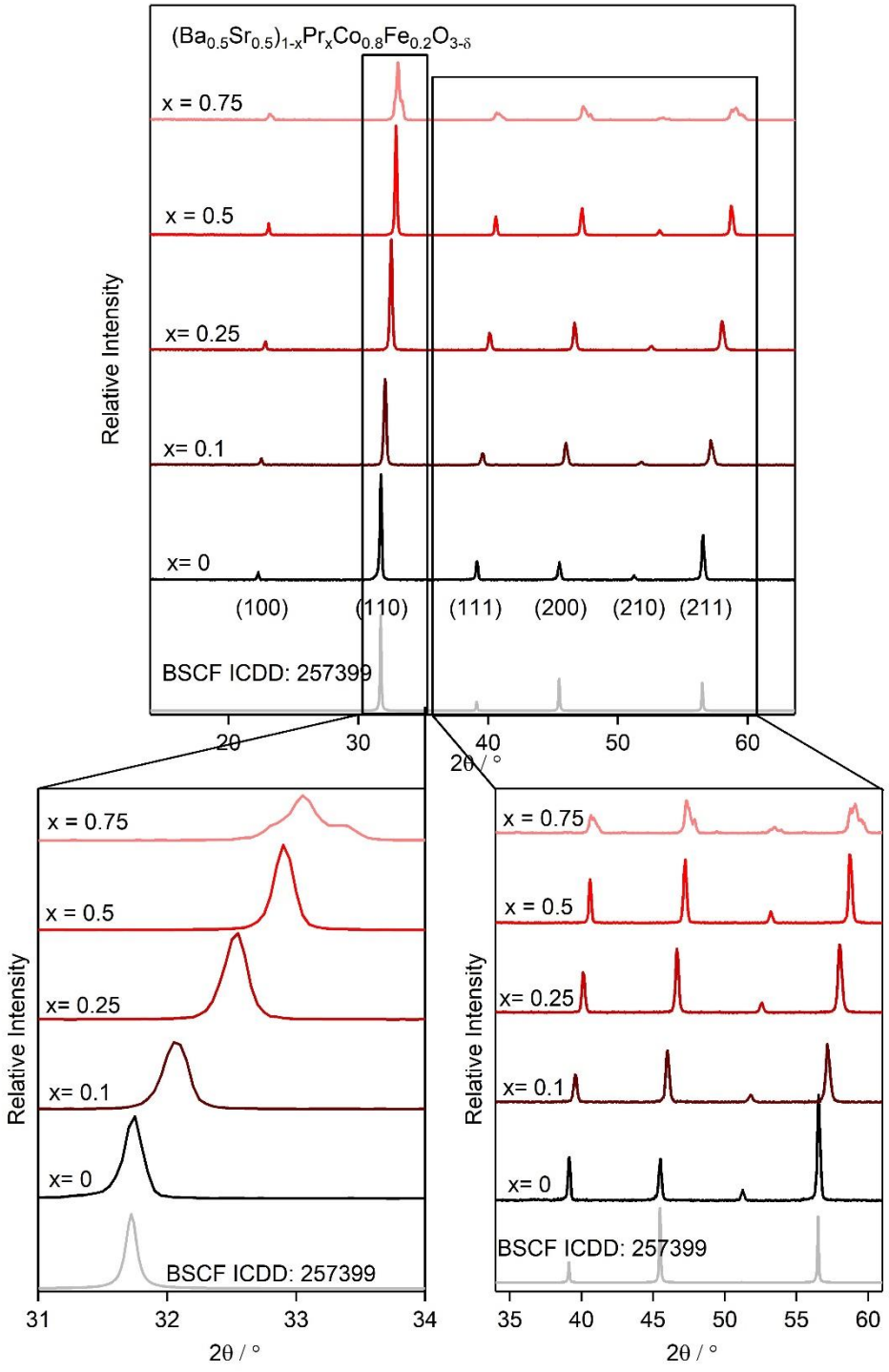


Figure 6.3 XRD spectra for the 4 Pr-doped BSCF examined in this report and for undoped BSCF. The BSCF reference ICDD pattern 257399 and peak assignments are from Yaremchenko et al.[29] *Magnified regions are given for the peaks contained within the boxed areas.*

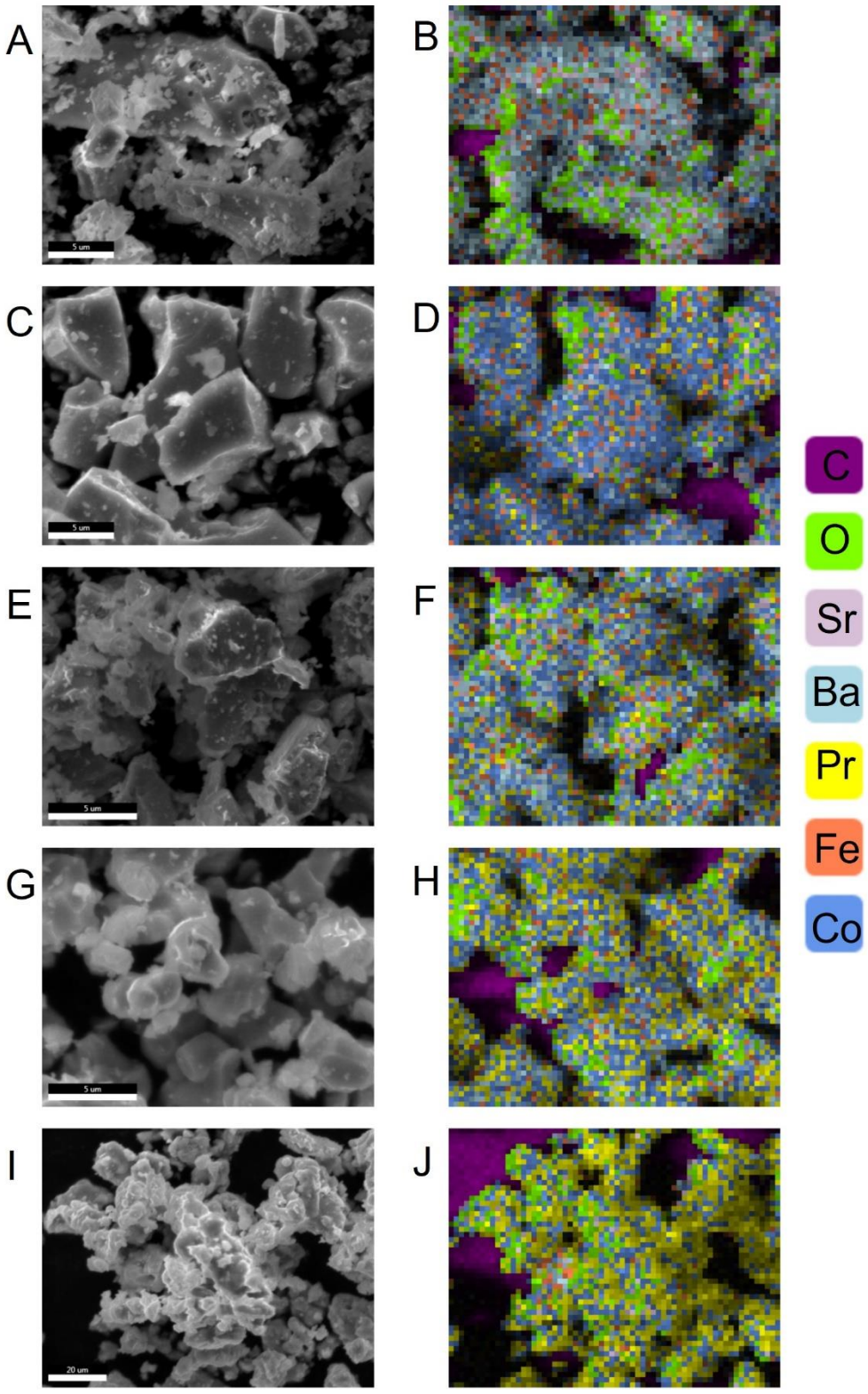


Figure 6.4 SEM (left) and EDX (right) images of Pr_x-doped BSCF with x=0 (A,B), 0.1 (C,D), 0.25 (E,F), 0.5 (G,H), and 0.75 (I,J). The white scale bars for the SEM images are all 5 µm except for (I) which is 20 µm.

6.4.1.2 Oxygen Evolution Reaction

The OER is typically the limiting reaction in an electrolyser system. Previous work has shown that Pr-doped BSCF (with x = 0.5) can enhance the perovskite towards the hydrogen evolution reaction.[8] It would be beneficial if both the cathode and anode electrocatalysts could be made from the same material, so this section investigates Pr-doped BSCF for the OER. OER testing was carried out in 0.1 mol dm^{-3} KOH as this is the standard electrolyte used when testing perovskite electrocatalysts.[30]

The perovskites are not sufficiently conductive on their own for electrocatalysis. Thus, they are mixed with Vulcan carbon in a 1:1 ratio to provide the needed conductivity to allow efficient charge transfer.

Figure 6.5 shows the OER activity for the Pr-doped BSCF perovskites. Clearly, increasing the amount of Pr doped into the A-site, decreases the activity of the material towards the OER. This contrasts with the observation for the HER by Xu *et al* who demonstrated at x = 0.5 enhanced the HER activity compared to the undoped BSCF.[8]

The overpotential to afford 10 mA cm^{-2} of current density increases with increasing x up to x = 0.5. For x = 0.75, the overpotential does not increase any more.

The (110) peak in the XRD around $2\theta = 32°$ correlates strongly with the activity of the perovskite toward the OER as shown in Figure 6.6. The position of the peak corresponds to the extent of lattice shrinking, and thus demonstrates that deviation from the cubic BSCF is detrimental to the OER performance. Between x = 0.5 and 0.75, the peak position changes only slightly, which is in line with the observed OER activity.

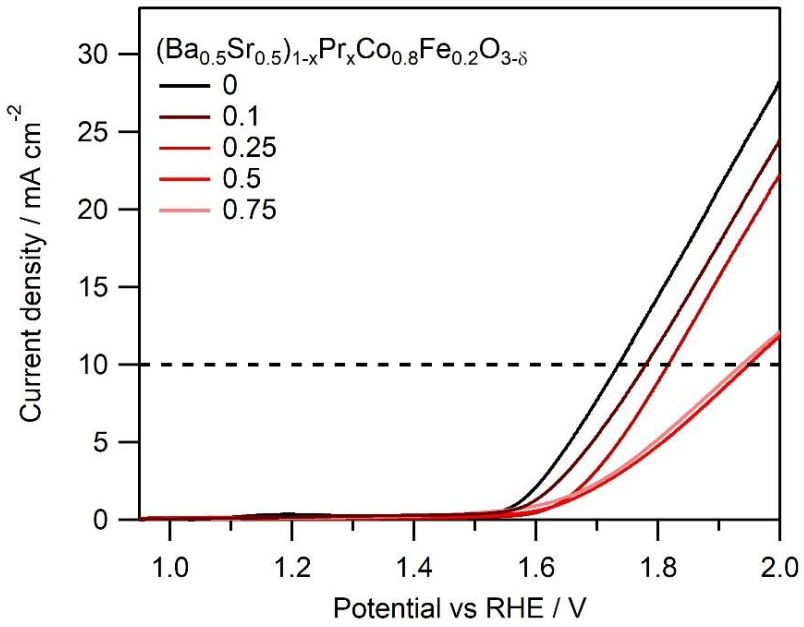


Figure 6.5 Linear sweep voltammograms measured in O_2-saturated 0.1 mol dm−3 KOH at a GC rotating disc electrode coated with an electrocatalyst ink containing Pr_x-doped BSCF with Vulcan carbon. Potential swept positive from 0.9 V to 2 V vs RHE at 10 mV s^{-1}. Measured against a Hg/HgO (0.1 mol dm−3 KOH) and then converted to RHE. A graphite rod was used as the counter electrode. The dotted line shows 10 mA cm^{-2}. Current is normalised to the geometric area of the electrode (0.196 cm^{-2})

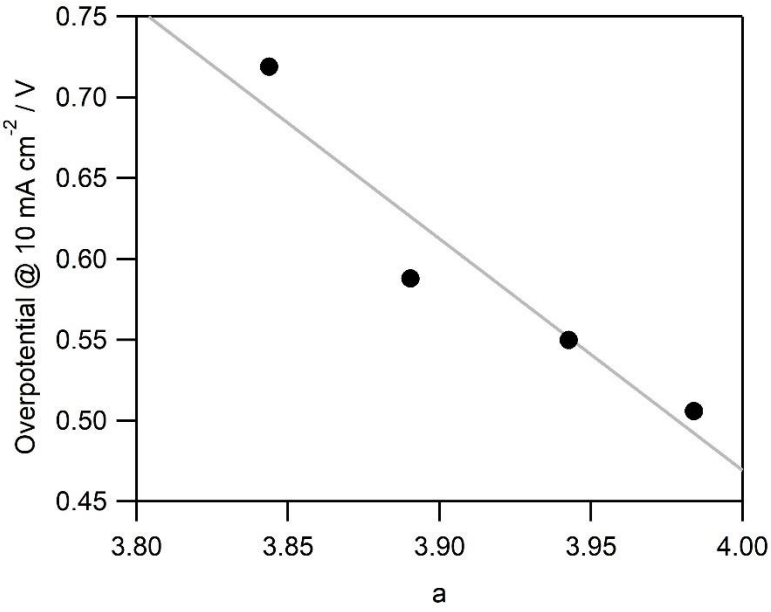


Figure 6.6 Correlation between the lattice parameter, a, and the overpotential at 10 mA cm^{-2} for the cubic Pr-doped BSCF perovskites with a Pr^{3+} : $(Ba_{0.5}Sr_{0.5})^{2+}$ ratio between 0 and 0.5.

Fits of the data to Tafel slopes are presented in Figure 6.7 and summarised in Table 6.2. The region chosen for the Tafel analysis was sufficiently beyond the onset that the reverse reaction would not interfere, but not so high a potential that transport of oxygen away from the surface could pose an issue. As expected, BSCF exhibits the fastest kinetics with the lowest Tafel slope of 98 mV dec^{-1}. Generally, the Tafel slopes increase with increasing x. For x = 0.1 and 0.25, the Tafel slopes are close enough to archetypal slope of 120 mV dec^{-1} that the charge transfer coefficient (α) is effectively 0.5. This means the RDS is the first electron transfer associated with the adsorption of OH^- onto the B-site active site.[31] For x = 0 (*i.e.,* BSCF), the Tafel slope of 98 mV dec^{-1} suggests that the OH^- adsorption is still rate determining, but the adsorption energy is more optimal than for the doped perovskites.[31] The BSCF Tafel slope is close to the 84 mV dec^{-1} slope reported by Chen *et al* for bulk BSCF in the same conditions,[32] giving validity to the other Tafel slopes reported in this section. The Pr-doping leads a change in oxidation states of the CoFe B-site along with a change in the perovskite structure such that the site is less active.

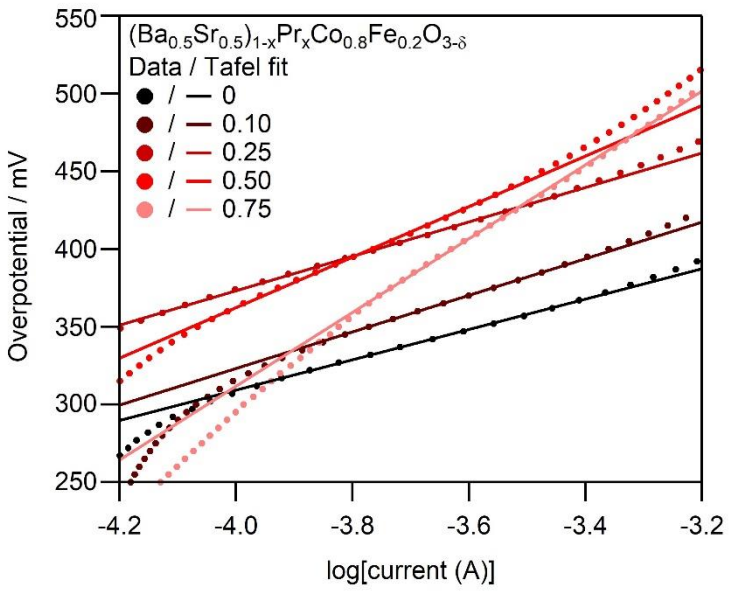


Figure 6.7 Plot of log(current / A) vs overpotential in the region used for Tafel analysis. For each electrocatalyst, the data are shown as dots and the Tafel slopes as solid lines. The slopes are plotted from linear regions of the data.

Table 6.2 Comparison of Tafel slopes b and the transfer coefficient α as x changes for the perovskite $(Ba_{0.5}Sr_{0.5})_{1-x}Pr_xCo_{0.8}Fe_{0.2}O_{3-\delta}$. α is calculated by $\frac{1}{b}\frac{2.303RT}{F}$.[33] *The fitted Tafel slopes are given ± the standard error of the slope fit.*

x	b / mV dec^{-1} ± standard error	α
0	98 ± 0.3	0.60
0.10	118 ± 0.3	0.50
0.25	111 ± 0.4	0.53
0.50	162 ± 0.6	0.37
0.75	237 ± 0.6	0.25

6.4.2 Lanthanum-doped $BaTiO_3$

$BaTiO_3$ and the La-doped $La_{0.2}Ba_{0.8}TiO_3$ have been compared to further investigate the role of cation doping on electrocatalysis. The commercial form of the material is compared to the arc-melted form (AM). The AM perovskite is then doped with La to create $La_{0.2}Ba_{0.8}TiO_3$.

6.4.2.1 Physical Characterisation

XRD spectra are shown in Figure 6.8 for $BaTiO_3$(AM) and $La_{0.2}Ba_{0.8}TiO_3$. The measured spectra are compared to the spectra for disordered tetragonal $BaTiO_3$ reported by Aoyagi *et al*,[34] and for hexagonal $BaTiO_3$ reported by Akimoto *et al*.[35] The $BaTiO_3$(AM) spectra is clearly most similar to the hexagonal reference 1. The La-doped perovskite more closely resembles the disordered tetragonal reference spectra. Pawley refinement agrees with these assignments, with $BaTiO_3$(AM) refining well to the $P6_3/mmc$ space group. Doping this structure with La to form $La_{0.2}Ba_{0.8}TiO_3$ yielded a structure that was and refinement places it in the P4mm tetragonal space group, though the lattice constants a and b are similar suggesting it is close to being cubic. The lattice parameters are summarised in Table 6.3.

Table 6.3 Space group and lattice parameters from the Pawley refinement for $BaTiO_3$(AM) and $La_{0.2}Ba_{0.8}TiO_3$.

	Space group	a / Å	b / Å	c / Å
$BaTiO_3$(AM)	$P6_3/mmc$	5.72867 ± 0.00002	-	13.9896± 0.00008
$La_{0.2}Ba_{0.8}TiO_3$	P4mm	3.9811± 0.0004	3.9715± 0.0004	-

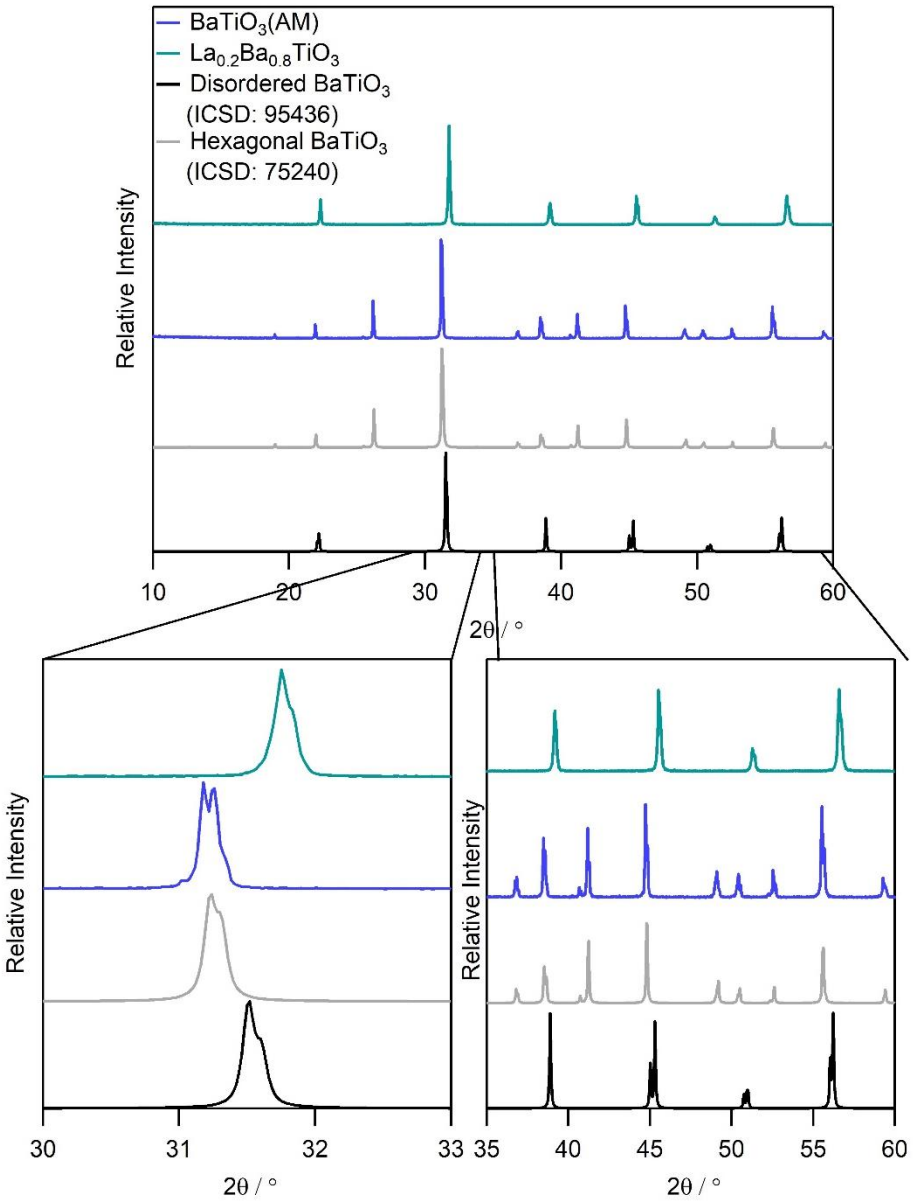


Figure 6.8 XRD spectra for $BaTiO_3$(AM) $La_{0.2}Ba_{0.8}TiO_3$. Magnified regions are given for the peaks contained within the boxed areas. Disordered $BaTiO_3$ (ICSD:95436) from Aoyagi et al[34] *and hexagonal $BaTiO_3$ (ICSD: 75240) from Akimoto* et al[35] *spectra are given for comparison.*

6.4.2.2 Oxygen Evolution

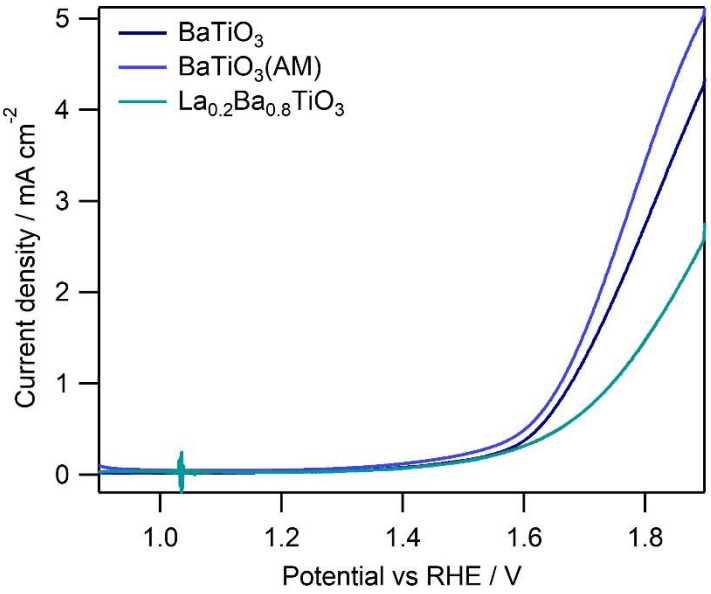


Figure 6.9 Linear sweep voltammograms measured in O_2-saturated 0.1 mol dm^{-3} KOH at a GC rotating disc electrode coated with an electrocatalyst ink containing $BaTiO_3$, $BaTiO_3$ (AM), or $La_{0.2}Ba_{0.8}TiO_3$, with Vulcan carbon (2:1 ratio). Potential swept positive from 0.9 V to 1.9 V vs RHE at 10 mV s^{-1}. Measured against a Hg/HgO (0.1 mol dm^{-3} KOH) and then converted to RHE. A graphite rod was used as the counter electrode. Currents are normalised to the geometric area of the electrode.

None of the tested materials showed good activity towards the OER given that 10 mA cm^{-2} was not reached within the test potential window. Chen *et al* previously observed that the hexagonal form of $BaTiO_3$ performed better for the OER than the tetragonal form, though neither form was as good as IrO_2.[36] This is in agreement with the data presented in Figure 6.9, in which the tetragonal $La_{0.2}Ba_{0.8}TiO_3$ required an overpotential of 516 mV to reach 1 mA cm^{-2} compared to 430 mV for the hexagonal $BaTiO_3$(AM) and 448 mV for $BaTiO_3$. The disorder generated by the arc-melting appears to slightly enhance the OER activity.

To establish whether the trends in the measured OER activities are intrinsic to the electrocatalyst, Figure 6.10 normalises the current density to the ECSA of the electrocatalysts. In this case, a value of 22 µF cm^{-2} was used.[37,38] Although these currents still do not represent highly active electrocatalysts, it is interesting to note that the hexagonal $BaTiO_3$(AM) remains the most active and

the cubic $La_{0.2}Ba_{0.8}TiO_3$ remains least active. This further highlights the role of the crystal structure in electrocatalysis.

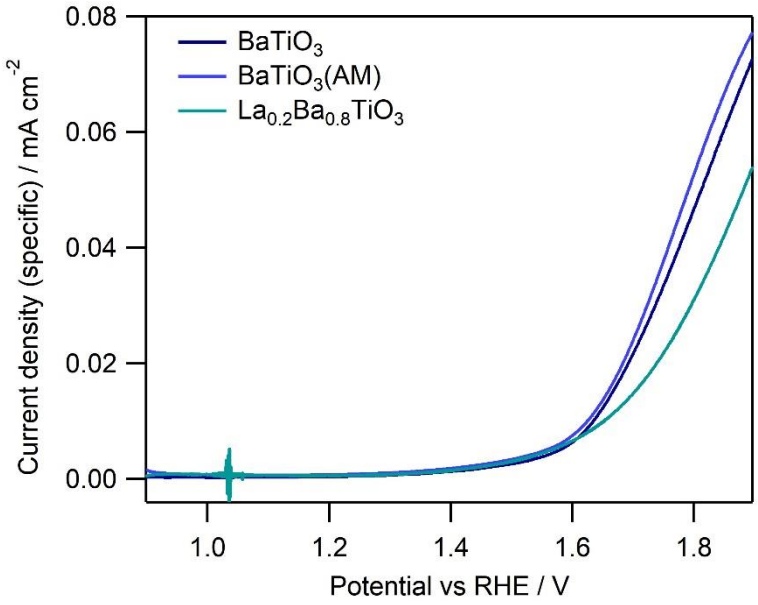


Figure 6.10 The currents from Figure 6.9 are normalised to the ECSA as determined by the double-layer capacitance of the material using a specific capacity of 22 µF cm^{-2}.

6.4.2.3 Oxygen Reduction

The oxygen reduction reaction (ORR) is the reverse reaction of the OER. Thus, some bad OER electrocatalysts can be good ORR electrocatalysts as the optimisation of one reaction can be at the detriment to the other. Figure 6.11 shows the activity of the perovskites towards the ORR reaction normalised to the geometric area of the material.

Scanning in the negative direction from 0.8 V vs RHE, the onset potential of the ORR is similar for all three materials. The potential required to reach −0.2 mA cm^{-2} is 0.68 V for $BaTiO_3$ and 0.67 V for both $BaTiO_3$(AM) and $La_{0.2}Ba_{0.8}TiO_3$. A plateau is reached between 0.5 V and 0.4 V. Given that after this plateau increasingly reductive currents are measured, it is likely the plateau corresponds to a 2 electron transfer, indicating a 2x2e ORR mechanism.

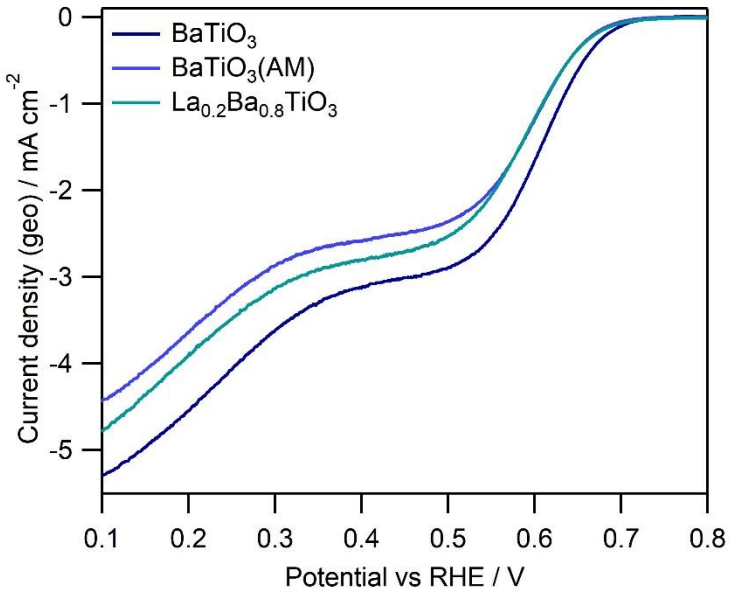


Figure 6.11 Linear sweep voltammograms measured in O_2-saturated 0.1 mol dm^{-3} KOH at a GC rotating disc electrode coated with an electrocatalyst ink containing $BaTiO_3$, $BaTiO_3$ (AM), or $La_{0.2}Ba_{0.8}TiO_3$ with Vulcan carbon (2:1 ratio). Potential swept positive from 0.9 V to 0.1 V vs RHE at 10 mV s^{-1}. Measured against a Hg/HgO (0.1 mol dm^{-3} KOH) and then converted to RHE. A graphite rod was used as the counter electrode. N_2-purged electrolyte was used for blank measurements which were subtracted from the oxygen-containing voltammograms. Currents are normalised to the geometric area of the electrode.

K-L analysis was carried out on a series of RDE voltammograms measured at varying rotation rates in the same way as in the previous chapter. The full set of RDE voltammograms can be seen in Figure 6.12.

The resulting K-L plots from the middle of the plateau at 0.45 V are presented in Figure 6.13. 0.45 V was chosen as it is in the plateau region whereby the current is not kinetically controlled and is limited by mass transport. As in the previous chapter, the surface area of the coated electrode is far greater than the geometric area of the electrode meaning extraction of kinetic data from kinetically controlled region of the RDE voltammograms would be invalid.[39]

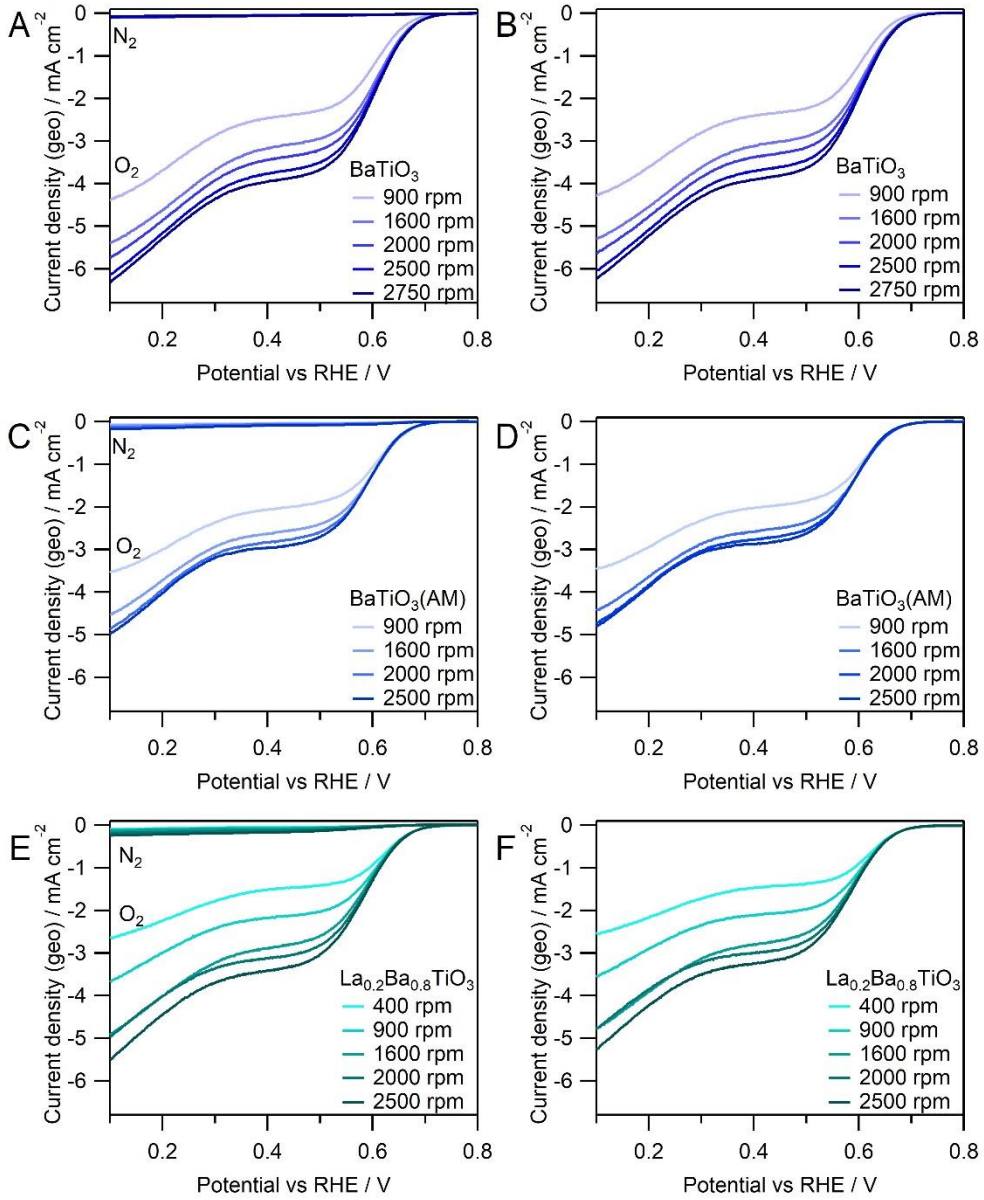


Figure 6.12 Rotating disc voltammograms measured in 0.1 mol dm^{-3} KOH for a GC electrode coated in (A, B) $BaTiO_3$, (C, D) $BaTiO_3$ (AM), or (E, F) $La_{0.2}Ba_{0.8}TiO_3$ with Vulcan carbon (2:1 ratio). LSVs measured in (a, c, e) O_2 saturated or N_2 purged electrolyte were subtracted from the O_2 saturated LSVs to give the (b, d, f) final LSVs used for K-L analyses. Rotation rate: 400 rpm to 2750 rpm. Scan rate: 5 mV s^{-1}, positive to negative. Potentials converted to RHE from Hg/HgO (0.1 mol dm^{-3} KOH). Geometric area of the electrode: 0.19635 cm^2

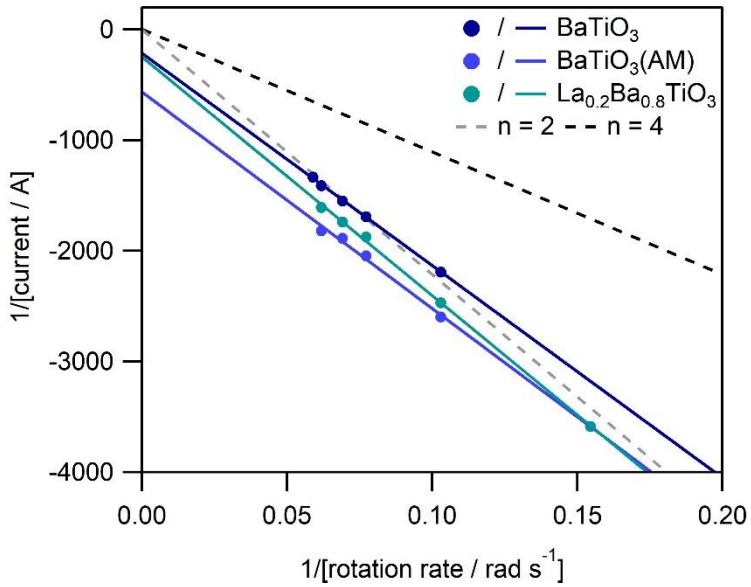


Figure 6.13 K-L analyses for $BaTiO_3$, $BaTiO_3$(AM), and $La_{0.2}Ba_{0.8}TiO_3$ carried out at 0.45 V. The circles represent data points, with the solid lines showing the slope used for K-L analysis. The dotted grey and dotted black lines show the theoretical slopes for 2 and 4 electron processes, respectively.

All three perovskites have a value of n close to 2 across the plateau region (Table 6.4). The La-doped perovskite has the highest specificity towards the 2 electron process, whereas both $BaTiO_3$ and $BaTiO_3$(AM) higher values of n suggesting a level of mixing between the 2x2e and 1x4e ORR routes may be at play. This may suggest that the nature of the active site for the undoped $BaTiO_3$ electrocatalysts is similar for the ORR, despite the difference the arc-melting process may cause. La-doping appears to change the nature of the active site n preference of the 2e reaction. A value of n between 2 and 3 is consistent with other perovskites supported on carbon in the literature for La-doped perovskites.[40]

Table 6.4 Comparison of the overpotentials required for 0.5 mA cm^{-2} and 3 mA cm^{-2}. The number of electrons (n) at each point along the plateau is calculated using K-L analysis and the average reported ± 2 standard deviations (s.d.). Currents used to define the overpotentials are normalised to the geometric current density.

Perovskite	$\eta_{0.2}$ /mV	η_3 / mV	n ± 2 s.d.
$BaTiO_3$	680	737	2.32 ± 0.03
$BaTiO_3$(AM)	670	950	2.26 ± 0.06
$La_{0.2}Ba_{0.8}TiO_3$	670	902	2.04 ± 0.02

6.4.2.4 Hydrogen Evolution

The HER is the more facile of the water-splitting reactions owing to the fewer electron transfers and intermediate adsorptions needed. Despite the reaction being kinetically more favourable, the series of perovskites tested did not have activity competitive with other materials in the literature. The standard electrolyte for testing the HER is 1 mol dm^{-3} KOH.[41]

The overpotentials required to reach −10 mA cm^{-2} of current towards the HER were similar for all the tested materials as seen in Figure 6.14 and summarised in Table 6.5. From these data, the La-doped perovskite performs slightly better for the HER than the others, though it should be noted that none of these materials showed HER activities close to state-of-the-art perovskites reported in the literature for the HER. In the literature, Pr-doped BSCF is able to achieve the same current density with just 237 mV of overpotential.[8] The Ruddlesden-Popper perovskite Sr_2RuO_4 requires just 61 mV of overpotential, though it does use a platinum-group metal.[42]

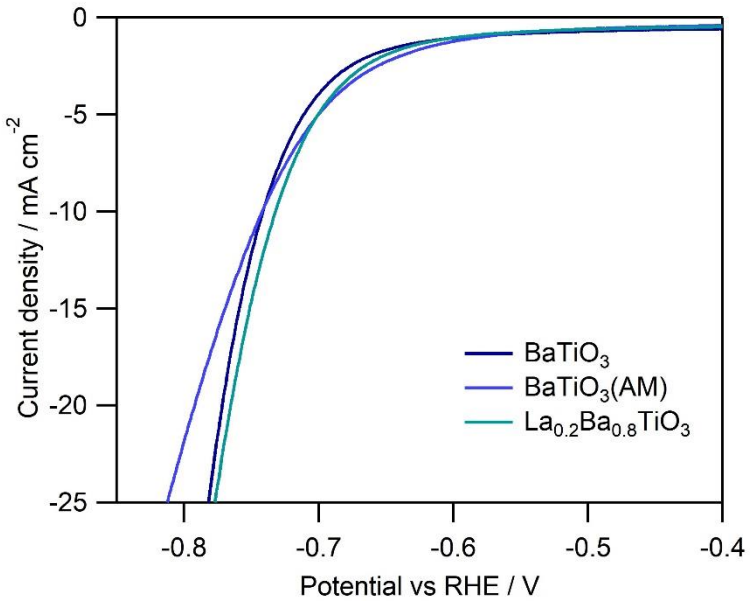


Figure 6.14 Linear sweep voltammograms measured in H_2-saturated 1 mol dm^{-3} KOH at a GC rotating disc electrode coated with an electrocatalyst ink containing $BaTiO_3$, $BaTiO_3$ (AM), or $La_{0.2}Ba_{0.8}TiO_3$ with Vulcan carbon (2:1 ratio). Potential swept negative 10 mV s^{-1}. Measured against a Hg/HgO (1 mol dm^{-3} KOH) and then converted to RHE. A graphite rod was used as the counter electrode. Currents are normalised to the geometric area of the electrocatalysts.

Tafel analyses were carried out on the data to establish the RDS. All 3 perovskites have a Tafel slope of at least 100 mV dec^{-1} (Figure 6.15) which indicates the Volmer step is rate limiting. However, the more intrinsically poor perovskites are those with α < 0.5 and the better performing perovskites have α > 0.5. This suggests that the higher activity materials are better able to dissociate the water and adsorb the first *OH intermediate.[31]

Table 6.5 Comparison of the fitted HER Tafel slopes, b, from Figure 6.15 and the transfer coefficient α for the different perovskites. α is calculated by $\frac{1}{b}\frac{2.303RT}{F}$.[33] The overpotentials required to reach −10 mA cm^{-2} *and −20 mA* cm^{-2} *are also given.*

Perovskite	Tafel slope / mV dec^{-1}	α	η_{-10}	η_{-20}
$BaTiO_3$	100	0.61	741	772
$BaTiO_3$ (AM)	138	0.43	742	792
$La_{0.2}Ba_{0.8}TiO_3$	111	0.54	732	765

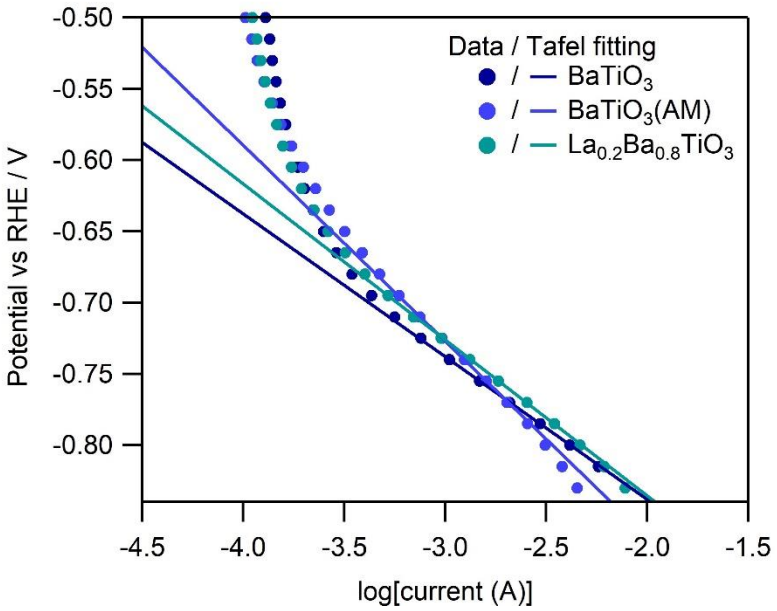


Figure 6.15 Plot of log[current (A)] vs overpotential in the region used for Tafel analysis. For each electrocatalyst, the data are shown as dots and the Tafel slopes as solid lines. The slopes are plotted from linear regions of the data.

6.5 Conclusions

The Pr-doped BSCF perovskites clearly demonstrated the influence of crystal structure on electrocatalytic activity. As the Pr-doping increased, the perovskite deviated further from the ideal cubic structure and the OER activity dropped off correspondingly. This highlights the role cationic doping of a perovskite can play as a design strategy for electrocatalysts.

The effect of cationic doping was further revealed through La-doping $BaTiO_3$. Doping the arc-melted $BaTiO_3$ shifted the crystal structure from hexagonal to tetragonal. This had the effect of increasing the specificity of the electrocatalyst system towards the 2x2e ORR mechanism. The disordered nature of the arc-melted $BaTiO_3$ led to slightly enhanced OER activity, but generally decreased its activity towards the ORR and HER.

As noted in the previous chapter, a synergistic relationship between the Vulcan carbon support and the perovskite cannot be ruled out. All materials had similar onset potentials, suggesting the same material could be initiating the reactions. However, notable trends were observed relating to the properties of the

perovskite electrocatalysts showing the activity was related to the perovskite and cannot be wholly attributed to the carbon support.

6.6 References

1. Chen, D., Chen, C., Baiyee, Z. M., Shao, Z. & Ciucci, F. Nonstoichiometric Oxides as Low-Cost and Highly-Efficient Oxygen Reduction/Evolution Catalysts for Low-Temperature Electrochemical Devices. *Chem. Rev.* **115**, 9869–9921 (2015).

2. Hwang, J. *et al.* Perovskites in catalysis and electrocatalysis. *Science* **358**, 751–756 (2017).

3. Choi, J. J. & Billinge, S. J. Perovskites at the nanoscale: from fundamentals to applications. *Nanoscale* **8**, 6206–6208 (2016).

4. Kostopoulou, A., Kymakis, E. & Stratakis, E. Perovskite nanostructures for photovoltaic and energy storage devices. *J. Mater. Chem. A* **6**, 9765–9798 (2018).

5. Bocher, L. *et al.* $CaMn_{(1-x)}Nb_{(x)}O_3$ (x < or = 0.08) perovskite-type phases as promising new high-temperature n-type thermoelectric materials. *Inorg. Chem.* **47**, 8077–8085 (2008).

6. Li, Z. *et al.* Stabilizing Perovskite Structures by Tuning Tolerance Factor: Formation of Formamidinium and Cesium Lead Iodide Solid-State Alloys. *Chem. Mater.* **28**, 284–292 (2016).

7. Tilley, R. J. D. *Perovskites: structure-property relationships*. (John Wiley & Sons, Inc., 2016).

8. Xu, X. *et al.* A Perovskite Electrocatalyst for Efficient Hydrogen Evolution Reaction. *Adv. Mater.* **28**, 6442–6448 (2016).

9. Zhang, M. *et al.* Recent development of perovskite oxide-based electrocatalysts and their applications in low to intermediate temperature electrochemical devices. *Mater. Today* **49**, 351–377 (2021).

10. Mefford, J. T. *et al.* Water electrolysis on $La_{1-x}Sr_xCoO_{3-d}$ perovskite electrocatalysts. *Nat. Commun.* **7**, 11053 (2016).

11. Chandler, C. D., Roger, C. & Hampdensmith, M. J. Chemical Aspects of Solution Routes to Perovskite-Phase Mixed-Metal Oxides from Metal-Organic Precursors. *Chem. Rev.* **93**, 1205–1241 (1993).

12. Bernardo, M. S., Jardiel, T., Peiteado, M., Caballero, A. C. & Villegas, M. Reaction pathways in the solid state synthesis of multiferroic BiFeO3. *J. Eur. Ceram. Soc.* **31**, 3047–3053 (2011).

13. Cheng, J., Navrotsky, A., Zhou, X.-D. & Anderson, H. U. Enthalpies of Formation of $LaMO_3$ Perovskites (M = Cr, Fe, Co, and Ni). *J. Mater. Res.* **20**, 191–200 (2011).

14. Shao, Z. Investigation of the permeation behavior and stability of a $Ba_{0.5}Sr_{0.5}Co_{0.8}Fe_{0.2}O_{3-\delta}$ oxygen membrane. *J. Memb. Sci.* **172**, 177–188 (2000).

15. Rousseau, S. *et al.* $La_{(1-x)}Sr_xCo_{1-y}Fe_yO_3$ perovskites prepared by sol–gel method: Characterization and relationships with catalytic properties for total oxidation of toluene. *Appl. Catal. B* **88**, 438–447 (2009).

16. Amirfakhri, S. J., Meunier, J. L. & Berk, D. Electrocatalytic activity of LaNiO3 toward H2O2 reduction reaction: Minimization of oxygen evolution. *J. Power Sources* **272**, 248–258 (2014).

17. Suntivich, J., May, K. J., Gasteiger, H. A., Goodenough, J. B. & Shao-Horn, Y. A Perovskite Oxide Optimized for Oxygen Evolution Catalysis from Molecular Orbital Principles. *Science* **334**, 1383–1385 (2011).

18. Xu, X. *et al.* A Perovskite Electrocatalyst for Efficient Hydrogen Evolution Reaction. *Adv. Mater.* **28**, 6442–6448 (2016).

19. Zhu, Y. *et al.* A Perovskite Nanorod as Bifunctional Electrocatalyst for Overall Water Splitting. *Adv. Energy Mater.* **7**, (2017).

20. Wang, J. *et al.* Water Splitting with an Enhanced Bifunctional Double Perovskite. *ACS Catal.* **8**, 364–371 (2018).

21. Hua, B., Li, M., Zhang, Y., Sun, Y. & Luo, J. All-In-One Perovskite Catalyst : Smart Controls of Architecture and Composition toward Enhanced Oxygen / Hydrogen Evolution Reactions. *Adv. Energy Mater.* **7**, 1700666 (2017).

22. Guan, D. *et al.* Screening highly active perovskites for hydrogen-evolving reaction via unifying ionic electronegativity descriptor. *Nat. Commun.* **10**, 1–8 (2019).

23. Guan, D. *et al.* Searching General Sufficient-and-Necessary Conditions for Ultrafast Hydrogen-Evolving Electrocatalysis. *Adv. Funct. Mater.* **29**, 1900704 (2019).

24. She, S. X. *et al.* Systematic Study of Oxygen Evolution Activity and Stability on $La_{1-x}Sr_xFeO_{3-delta}$ Perovskite Electrocatalysts in Alkaline Media. *ACS Appl. Mater. Interfaces* **10**, 11715–11721 (2018).

25. Dai, J. *et al.* Single-phase perovskite oxide with super-exchange induced atomic-scale synergistic active centers enables ultrafast hydrogen evolution. *Nat. Commun.* **11**, 1–10 (2020).

26. Yu, W., Ou, G., Si, W., Qi, L. & Wu, H. Defective $SrTiO_3$ synthesized by arc-melting. *Chem. Commun.* **51**, 15685–15688 (2015).

27. Liu, H., Zhao, G., Meng, X. & Ye, J. Doping Ba into strontium titanate for enhanced photocatalytic oxygen evolution over its supported Au-based catalysts. *Catal. Commun.* **99**, 127–130 (2017).

28. Shannon, R. D. Revised effective ionic radii and systematic studies of interatomic distances in halides and chalcogenides. *Acta Crystallogr. Sect. A* **32**, 751–767 (1976).

29. Yaremchenko, A. A., Khalyavin, D. D. & Patrakeev, M. V. Uncertainty of oxygen content in highly nonstoichiometric oxides from neutron diffraction data: example of perovskite-type $Ba_{0.5}Sr_{0.5}Co_{0.8}Fe_{0.2}O_{3-\delta}$. *J. Mater. Chem. A* **5**, 3456–3463 (2017).

30. Wygant, B. R. *et al.* Structural and Catalytic Effects of Iron-and Scandium-Doping on a Strontium Cobalt Oxide Electrocatalyst for Water Oxidation. *ACS Catal.* **6**, 1122–1133 (2016).

31. Shinagawa, T., Garcia-Esparza, A. T. & Takanabe, K. Insight on Tafel slopes from a microkinetic analysis of aqueous electrocatalysis for energy conversion. *Sci. Rep. 2015 5:1* **5**, 1–21 (2015).

32. Chen, G. *et al.* Two orders of magnitude enhancement in oxygen evolution reactivity on amorphous $Ba_{0.5}Sr_{0.5}Co_{0.8}Fe_{0.2}O_{3-\delta}$ nanofilms with tunable oxidation state. *Sci. Adv.* **3**, (2017).

33. Negahdar, L., Zeng, F., Palkovits, S., Broicher, C. & Palkovits, R. Mechanistic Aspects of the Electrocatalytic Oxygen Evolution Reaction over Ni-Co Oxides. *ChemElectroChem* **6**, 5588–5595 (2019).

34. Aoyagi, S., Kuroiwa, Y., Sawada, A., Yamashita, I. & Atake, T. Composite Structure of $BaTiO_3$ Nanoparticle Investigated by SR X-Ray Diffraction. *J. Physical Soc. Japan* **71**, 1218–1221 (2002).

35. Akimoto, J., Gotoh, Y. & Oosawa, Y. Refinement of hexagonal $BaTiO_3$. *Acta Crystallogr. C* **50**, 160–161 (1994).

36. Chen, C.-F. *et al.* Oxygen-deficient $BaTiO_{3-x}$ perovskite as an efficient bifunctional oxygen electrocatalyst. *Nano Energy* **13**, 423–432 (2015).

37. Centeno, T. A. & Stoeckli, F. On the specific double-layer capacitance of activated carbons, in relation to their structural and chemical properties. *J. Power Sources* **154**, 314–320 (2006).

38. McCrory, C. C. L., Jung, S., Peters, J. C. & Jaramillo, T. F. Benchmarking Heterogeneous Electrocatalysts for the Oxygen Evolution Reaction. *J. Am. Chem. Soc.* **135**, 16977–16987 (2013).

39. Masa, J., Batchelor-McAuley, C., Schuhmann, W. & Compton, R. G. Koutecky-Levich analysis applied to nanoparticle modified rotating disk electrodes: Electrocatalysis or misinterpretation. *Nano Res.* **7**, 71–78 (2014).

40. Safakas, A., Bampos, G. & Bebelis, S. Oxygen reduction reaction on $La_{0.8}Sr_{0.2}Co_xFe_{1-x}O_{3-\delta}$ perovskite/carbon black electrocatalysts in alkaline medium. *Appl. Catal. B* **244**, 225–232 (2019).

41. McCrory, C. C. L. *et al.* Benchmarking Hydrogen Evolving Reaction and Oxygen Evolving Reaction Electrocatalysts for Solar Water Splitting Devices. *J. Am. Chem. Soc.* **137**, 4347–4357 (2015).

42. Zhu, Y. L. *et al.* Unusual synergistic effect in layered Ruddlesden - Popper oxide enables ultrafast hydrogen evolution. *Nat. Commun.* **10**, 9 (2019).

Chapter 7. Conclusions

The aim of thesis was to explore a variety of design strategies for the investigation of novel electrocatalysts. The electrocatalysts were tested for their activity towards the OER, ORR, and/or HER. All three of these reactions are pertinent to the Hydrogen Economy with the OER and HER being the two sides of an electrolyser, and the ORR being one side of a fuel cell.

Prior to exploring electrocatalyst design strategies, Chapter 3 first investigated the best practice when measuring electrocatalysts, with a focus on the use and choice of counter electrode. The work presented showed that although Pt and Au are considered inert, within the context of an electrochemical experiment this is not necessarily always the case. It was observed that the dissolution products of Pt and Au counter electrodes in a three-electrode setup can migrate to the working electrode whereupon they can deposit. This artificially enhances the measured electrocatalytic activity leading to erroneous interpretation of electrocatalytic performance. A Nafion membrane is sometimes used to avert this, but it was shown that this is insufficient for long duration experiments. Rather, it is best practice to use a carbon counter electrode behind a frit or membrane for the lowest risk of contamination of the working electrode.

Contamination was unfortunately identified within the work presented in Chapter 4. The process by which SWNTs are synthesised can leave behind Ni contaminants which can be observed in the electrochemistry, especially after multiple cycles. As emphasised in that chapter, it is not believed that the presence of Ni contamination impacts the trends observed, as the presence of the contaminant was consistent throughout the materials tested. However, further work is needed to optimise the process by which the SWNTs are cleaned prior to use. Before electrocatalytic testing commences, the SWNTs should be checked for the presence of contaminants. Comparison of the cleaned SWNT's OER activity with that of SWNTs with small amounts of Ni contamination would prove a useful investigation. If it is found that such small amounts of contamination can significantly influence the activity, in much the same way

that small amounts of Pt or Au from the counter electrode can, then this could be used in a controlled manner as another strategy for electrocatalyst design.

This thesis set out to investigate three design strategies: the introduction of a synergistic interaction; the control of morphology; and the choice of cation.

Co_3O_4 was used as the underlying electrocatalyst to explore synergistic electrocatalytic relationships in Chapter 4. The mass activity of the Co_3O_4 encapsulated within a SWNT was higher than the electrocatalyst with Co_3O_4 on the outside of the tubes. The presence of a synergistic interaction was confirmed by comparison with Co_3O_4 supported on a non-structured activated carbon substrate which had significantly lower activity. SWNTs without Co_3O_4 present were also shown to have a lower activity than the tubes with Co_3O_4 present. Both of these results point to a synergistic interaction as neither the Co_3O_4 nor the SWNTs showed as good an activity separately as they do when combined. Further to improving the mass activity, the synergistic interaction enhanced the stability of the electrocatalyst.

Titanate-based microspheres supported on Vulcan carbon were used as the underlying electrocatalysts for an investigation into how morphology impacts electrocatalytic activity in Chapter 5. The addition of a sodium titanate layer changed the specificity of the electrocatalytic reaction in favour of the 2x2 electron ORR pathway as opposed to the mixed 2x2 and 4x1 electron pathways observed through KL analysis for the unmodified microspheres. Heat treatment enhanced the surface area of the modified microspheres without adjusting the mechanistic specificity. This work showed that the underlying morphology of a material can be maintained whilst changing the mechanism by which the ORR proceeds. In turn, this mechanistic preference can be maintained whilst modifying the surface area of the material to improve its overall activity.

The work presented in both chapters 4 and 5 can be considered jointly through the lens of surface modification. In both cases an underlying morphology, that of a SWNT or a microsphere, had its surface chemistry altered through a chemical operation. In the case of the SWNTs, modification of the tube's external surface was achieved through the addition of Co_3O_4 on the inside of

the tube, whereas the microsphere surface was modified through the addition of a chemical layer. In both cases, the advantages of the underlying morphology were maintained whilst electrocatalytic properties were changed. These strategies could prove useful in further enhancing known electrocatalysts with specific morphologies through changing the surface chemistry without impacting the underlying structure.

A series of perovskite modifications were carried out as part of an investigation into the effect of cation choice and doping. The strongest correlation between activity and A-site cation choice was observed by doping BSCF with increasing amounts of Pr in the perovskite $(Ba_{0.5}Sr_{0.5})_{1-x}Pr_xCo_{0.8}Fe_{0.2}O_{3-\delta}$. This doping increasingly shifted the perovskite away from its ideal cubic structure. This strongly correlated to decreasing activity towards the OER. When the ratio of Pr^{3+} : $(Ba_{0.5}Sr_{0.5})^{2+}$ reached 0.75, the perovskite took on an orthorhombic structure which corresponded to the lowest OER performance and a significant change in the Tafel slope was observed. Further evidence for the influence of cationic doping was seen in the exploration of La-doped $BaTiO_3$ whereby La-doping shifted the structure from hexagonal to tetragonal and changed the specificity of the reaction towards the ORR.

Although the individual chapters focused on separate strategies, synergistic relationships were observed in each of Chapters 4, 5, and 6. This synergy was purposefully induced in Chapter 4. However, the Vulcan carbon support used in chapters 5 and 6 was observed to interact synergistically with the electrocatalyst when tested for the ORR owing to the intimate connection between the two materials. In both cases, the similarity of onset potentials across the variations tested indicated that the carbon from the support acted as the active site for the initial 2 electron reduction, with the titanate-based microspheres and perovskites then influencing the activity towards the second 2 electron reduction of peroxide.

Overall, this thesis has further demonstrated the usefulness of these electrocatalyst design strategies. Future work could combine these strategies, for example by varying the cation of the oxide encapsulated within a SWNT to increase or decrease the electron withdrawing nature of the material.